Seismic Load Path Effects in Reinforced Concrete Bridge Columns and Wall Piers

Volume 3: Out-of-plane buckling instability of Pier walls (APPENDIX)

(Ana Gabriela Haro – Constructed Facilities Laboratory - NCSU)
June 2017

Prepared By:
Ana Gabriela Haro Báez, Research Assistant (NCSU)
Dr. Mervyn J. Kowalsky, Principal Investigator (NCSU)
Dr. Y.H. Chai, Co-Principal Investigator (UC DAVIS)

Prepared For:
Alaska Department of Transportation & Public Facilities
Research, Development, and Technology Transfer
P.O. Box 112500
3132 Channel Drive
Juneau, Alaska 99811-2500

and

Federal Highway Administration
P.O. Box 21648
709 West 9th Street
Juneau, Alaska 99802-1648

REPORT DOCUMENTATION PAGE	Form approved OMB No.

Public reporting for this collection of information is estimated to average 1 hour per response, including the time for reviewing instructions, searching existing data sources, gathering and maintaining the data needed, and completing and reviewing the collection of information. Send comments regarding this burden estimate or any other aspect of this collection of information, including suggestion for reducing this burden to Washington Headquarters Services, Directorate for Information Operations and Reports, 1215 Jefferson Davis Highway, Suite 1204, Arlington, VA 22202-4302, and to the Office of Management and Budget, Paperwork Reduction Project (0704-1833), Washington, DC 20503

1. AGENCY USE ONLY (LEAVE BLANK)	2. REPORT DATE	3. REPORT TYPE AND DATES COVERED
4000(134)	June 30, 2017	Final Report / February 28, 2015 – June 30, 2017

4. TITLE AND SUBTITLE	5. FUNDING NUMBERS
Seismic Load Path Effects in Reinforced Concrete Bridge Columns and Wall Piers Volume 3: Out-of-plane buckling instability of Pier walls (Appendix)	Federal# 4000(134) IRIS# Z642030000
6. AUTHOR(S) Ana Gabriela Haro Báez, Research Assistant (NCSU) Dr. Mervyn J. Kowalsky, Principal Investigator (NCSU) Dr. Y.H. Chai, Co-Principal Investigator (UC DAVIS)	
7. PERFORMING ORGANIZATION NAME(S) AND ADDRESS(ES) North Carolina State University Raleigh, NC 27695	8. PERFORMING ORGANIZATION REPORT NUMBER 4000(134)
9. SPONSORING/MONITORING AGENCY NAME(S) AND ADDRESS(ES) Alaska Department of Transportation and Public Facilities Research, Development &Technology Transfer 3132 Channel Drive Juneau, Alaska 99811-2500	10. SPONSORING/MONITORING AGENCY REPORT NUMBER 4000(134)

11. SUPPLEMENTARY NOTES

12a. DISTRIBUTION / AVAILABILITY STATEMENT	12b. DISTRIBUTION CODE
Copies available online at http://www.dot.alaska.gov/stwddes/research/search_lib.shtml	

13. ABSTRACT (Maximum 200 words)

(Appendix) Buckling instability of reinforced concrete structural walls (RCSW) reported after the 2010 Chile and 2011 New Zealand earthquakes in addition to prior observations during laboratory tests have emphasized the importance of understanding this mode of structural response. Experimental tests on reinforced concrete prisms representative of boundary elements of prototype typical planar RC walls were conducted at the Constructed Facility Laboratory at North Carolina State University. The effects on out-of-plane instability due to a combination of selected longitudinal reinforcement ratios and various load paths were evaluated. As has been observed in past studies, when the buckled deformation is enough to cause instability, loss of vertical load carrying capacity occurred. The results of the study indicate that imposed out-of-plane displacements do not affect stability; however, in-plane loading history does impact the onset of the local buckling limit state.

14. KEYWORDS:	15. NUMBER OF PAGES
Out-of-plane buckling stability, pier walls, structural walls, maximum tensile strain, minimum thickness, boundary elements	199
	16. PRICE CODE N/A

17. SECURITY CLASSIFICATION OF REPORT	18. SECURITY CLASSIFICATION OF THIS PAGE	19. SECURITY CLASSIFICATION OF ABSTRACT	20. LIMITATION OF ABSTRACT
Unclassified	Unclassified	Unclassified	None

NSN 7540-01-280-5500

STANDARD FORM 298 (Rev. 2-98)
Prescribed by ANSI Std. 239-18 298-102

Notice

This document is disseminated under the sponsorship of the U.S. Department of Transportation in the interest of information exchange. The U.S. Government assumes no liability for the use of the information contained in this document.

The U.S. Government does not endorse products or manufacturers. Trademarks or manufacturers' names appear in this report only because they are considered essential to the objective of the document.

Quality Assurance Statement

The Federal Highway Administration (FHWA) provides high-quality information to serve Government, industry, and the public in a manner that promotes public understanding. Standards and policies are used to ensure and maximize the quality, objectivity, utility, and integrity of its information. FHWA periodically reviews quality issues and adjusts its programs and processes to ensure continuous quality improvement.

Author's Disclaimer

Opinions and conclusions expressed or implied in the report are those of the author. They are not necessarily those of the Alaska DOT&PF or funding agencies.

SI* (MODERN METRIC) CONVERSION FACTORS

APPROXIMATE CONVERSIONS TO SI UNITS

Symbol	When You Know	Multiply By	To Find	Symbol
		LENGTH		
in	inches	25.4	millimeters	mm
ft	feet	0.305	meters	m
yd	yards	0.914	meters	m
mi	miles	1.61	kilometers	km
		AREA		
in^2	square inches	645.2	square millimeters	mm^2
ft^2	square feet	0.093	square meters	m^2
yd^2	square yard	0.836	square meters	m^2
ac	acres	0.405	hectares	ha
mi^2	square miles	2.59	square kilometers	km^2
		VOLUME		
fl oz	fluid ounces	29.57	milliliters	mL
gal	gallons	3.785	liters	L
ft^3	cubic feet	0.028	cubic meters	m^3
yd^3	cubic yards	0.765	cubic meters	m^3
	NOTE: volumes greater than 1000 L shall be shown in m^3			
		MASS		
oz	ounces	28.35	grams	g
lb	pounds	0.454	kilograms	kg
T	short tons (2000 lb)	0.907	megagrams (or "metric ton")	Mg (or "t")
		TEMPERATURE (exact degrees)		
^oF	Fahrenheit	5 (F-32)/9 or (F-32)/1.8	Celsius	^oC
		ILLUMINATION		
fc	foot-candles	10.76	lux	lx
fl	foot-Lamberts	3.426	candela/m^2	cd/m^2
		FORCE and PRESSURE or STRESS		
lbf	poundforce	4.45	newtons	N
lbf/in^2	poundforce per square inch	6.89	kilopascals	kPa

APPROXIMATE CONVERSIONS FROM SI UNITS

Symbol	When You Know	Multiply By	To Find	Symbol
		LENGTH		
mm	millimeters	0.039	inches	in
m	meters	3.28	feet	ft
m	meters	1.09	yards	yd
km	kilometers	0.621	miles	mi
		AREA		
mm^2	square millimeters	0.0016	square inches	in^2
m^2	square meters	10.764	square feet	ft^2
m^2	square meters	1.195	square yards	yd^2
ha	hectares	2.47	acres	ac
km^2	square kilometers	0.386	square miles	mi^2
		VOLUME		
mL	milliliters	0.034	fluid ounces	fl oz
L	liters	0.264	gallons	gal
m^3	cubic meters	35.314	cubic feet	ft^3
m^3	cubic meters	1.307	cubic yards	yd^3
		MASS		
g	grams	0.035	ounces	oz
kg	kilograms	2.202	pounds	lb
Mg (or "t")	megagrams (or "metric ton")	1.103	short tons (2000 lb)	T
		TEMPERATURE (exact degrees)		
^oC	Celsius	1.8C+32	Fahrenheit	^oF
		ILLUMINATION		
lx	lux	0.0929	foot-candles	fc
cd/m^2	candela/m^2	0.2919	foot-Lamberts	fl
		FORCE and PRESSURE or STRESS		
N	newtons	0.225	poundforce	lbf
kPa	kilopascals	0.145	poundforce per square inch	lbf/in^2

*SI is the symbol for the International System of Units. Appropriate rounding should be made to comply with Section 4 of ASTM E380.
(Revised March 2003)

TABLE OF CONTENTS

TABLE OF CONTENTS v

Appendix A Individual reports of the experimental tests 1

Test 1 2

Test 2 18

Test 3 34

Test 4 48

Test 5 63

Test 6 80

Test 7 96

Test 8 113

Test 9 129

Test 10 144

Test 11 162

Test 12 179

Appendix A Individual reports of the experimental tests

This appendix comprises the reports generated after each experiment, which include additional information related to the structural response of the twelve tested specimens.

Stability of Ductile RC Structural Walls – Assessment of the Local Buckling Failure Mode

Test 1

18 – February – 2016

Summary Report

Prepared for:

Alaska Department of Transportation

Prepared by:

RA – Ana Gabriela Haro

PIs – Mervyn Kowalsky and Rob Chai

North Carolina State University

Raleigh – NC

1. Executive Summary

Test 1 was conducted at the Constructed Facilities Laboratory on Thursday, February 18, 2016, as part of the load path project. The specimen was designed and built simulating boundary elements from prototype walls. Monotonic lateral and axial tensile and compressive loads were applied to the specimen to capture its structural performance and to determine preliminary critical parameters associated with lateral instability of RC walls. The first part of the results are presented in this report. Further analyses will be elaborated.

2. Introduction

Recent earthquakes in New Zealand and Chile have illustrated the importance of out-of-plane stability of concrete wall elements due to in-plane loading. Pier walls are occasionally employed by Alaska DOT for their in-plane lateral stiffness. While these walls are normally thicker than the walls typically found in building applications, their clear heights are also larger, giving rise to height-to-thickness ratios which may be larger than that of buildings. Some analyses have demonstrated that walls as thick as 20 in. may be prone to buckling, depending on their length and height.

Noticing the concentration of damage in the boundary elements of rectangular reinforced concrete structural walls due to higher stress and strain demands, some past investigations by others have been carried out on prisms, which was found to be an economical way to study the inelastic instability of structural walls. In general, the main objective of these tests focuses on subjecting specimens to cyclic tension and compression actions to simulate vertical components of actual seismic loading.

While past tests on prisms has shown existing models to be promising, missing from the models is the interaction with out-of-plane loading. The existing models correlate tensile strain from in plane loading to out-of-plane deformation, assuming a prescribed curvature distribution. If loading occurs in the out-of-plane direction, the relationship between tensile strain and out-of-plane deformations must be adjusted to reflect this. In its simplest form, this would be an addition of an out-of-plane displacement to the existing equation. However, out-of-plane displacement may impact the distribution of curvature with height, thus requiring additional adjustments to the models.

A total of 12 prisms will be experimentally tested in the Constructed Facilities Laboratory (CFL) during this project. The support conditions for the 12 prisms are conceived as fixed-fixed. The first testing phase will involve controlled load paths where the specimens are subjected to tension/compression cycles in addition to lateral loading to mimic the effects of out-of-plane displacements. In the second phase, longitudinal reinforcement ratios will be varied – between the two phases, reinforcement ratios will span the typical values employed by Alaska DOT for pier walls. The details associated with the two phases are presented in Table A-1.

This first phase consists of testing six 1/2-scale identical specimens. The thickness of the prisms is 5 in. since the cover was excluded from the construction. The geometry used is 5x12x60 in, corresponding to an aspect ratio (*h/b = height/thickness*) of 10 (including the missing cover). The longitudinal reinforcement ratio is 2.6% (6 bars #5). Transverse reinforcement consists of #3 diameter rebar spaced at 2 in. and was placed as shown in Figure A-1.

Table A-1. Test 1: Description of the experimental phases

Phase	Tests	Geometry	Reinforcement	Loading
1	6	Thickness and Height (based on prototype wall). (6”x12” ; actual geometry = 5”x12”)	Longitudinal (6bars#5) and transverse (#3@2in) reinforcement ratios similar for the 6 specimens.	Controlled 3D load path
2	6	Same as phase 1 (Based on actual pier walls formerly used by the Alaska DOT)	Longitudinal reinforcement ratio varies. (3 specimens 6bars#3 and 3 specimens 6bars#4)	Controlled 3D load path

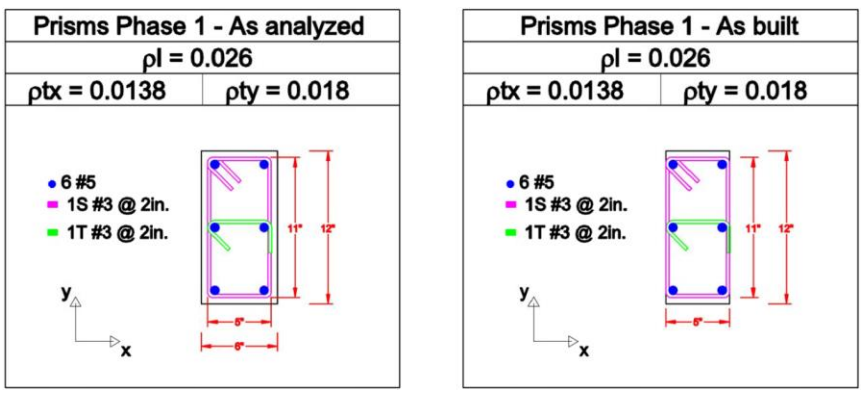

Figure A-1. Test 1: Phase 1 - Cross section of the prisms

Table A-2. Test 1: Phase 1 - Steel tensile test properties for bars #3 and #5

Sample No.	Bar #	fy (ksi)	εy = fy/Es	fu (ksi)	εu
1	3	74.7	0.0026	103.3	0.0916
2	3	74.8	0.0026	100.6	0.0750
3	3	79.6	0.0027	105.0	0.0927
4	3	76.8	0.0026	103.4	0.0770
5	3	77.0	0.0027	103.3	0.0736
6	3	77.1	0.0027	103.2	0.1040
#3 Average		**76.7**	**0.0026**	**103.1**	**0.0856**
1	5	69.4	0.0024	96.4	0.1100
2	5	68.2	0.0024	95.6	0.1124
3	5	68.7	0.0024	97.7	0.0981
4	5	70.1	0.0024	97.4	0.1128
5	5	70.0	0.0024	98.0	0.1326
#5 Average		**69.3**	**0.0024**	**97.0**	**0.1132**

Regarding the material properties, an unconfined concrete strength of 6 ksi and reinforcement yielding strength of 69.3 ksi were determined. Table A-2 shows the steel tensile test properties for the #3 and #5 bars. The reinforcement detailing was established according to the ACI 318 and NEHERP guidelines for ductile columns and boundary elements.

3. Test Setup

The test setup consisted of a 14 ft long steel loading beam placed on the top of the specimen and connected to three actuators: two vertically inclined 440 kips actuators which induce axial loads and one horizontal 55 kips actuator to apply out-of-plane displacements. Two steel frames are used to restrain torsion in the loading beam. Two concrete blocks attached to the strong floor support the specimen to reach the required height associated with the effective length of the 440 kips actuators. Figure A-2 depicts the test setup drawings and Figure A-3 shows some pictures of the area where the components of the project were placed.

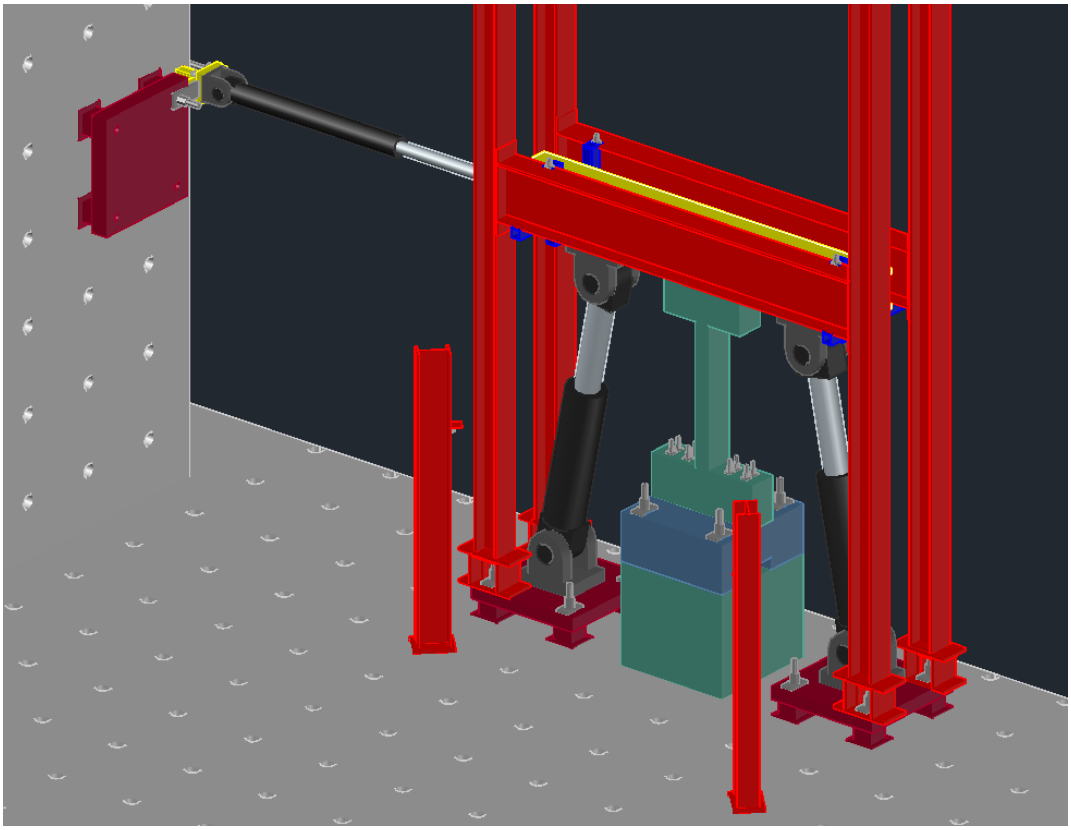

Figure A-2. Test 1: Test setup drawings

The horizontal actuator is controlled by displacements. The vertically inclined actuator located at the left hand side of the specimen, Figure A-2, is controlled by rotations captured throughout an

inclinometer attached to the loading beam. The actuator placed at the right hand of the specimen is controlled by a combination of forces and displacements. Loads and strokes in the actuators are measured through integrated LVDTs and loads cells.

Relative displacements resulting from the interaction between the loading beam, the specimen, and the support concrete block were obtained through 4 linear potentiometers. In addition, axial deformations of the prism were registered through 4 string potentiometers. Another string potentiometer was used to capture the lateral displacement of the loading beam.

Figure A-3. Test 1: Test setup in the CFL at NC State

A total of 114 infrared LEDs from the optical tracking system Optotrak Certus developed by Northern Digital Inc. were placed directly on the steel reinforcement of the prism. The objective was to establish longitudinal and transverse strains in real time throughout a MATLAB code recently developed for this purpose at the CFL. Figure A-4 shows the distribution of the LEDs in the right face of the prism and the overall allocation of the markers obtained from the Optotrak spatial coordinate output.

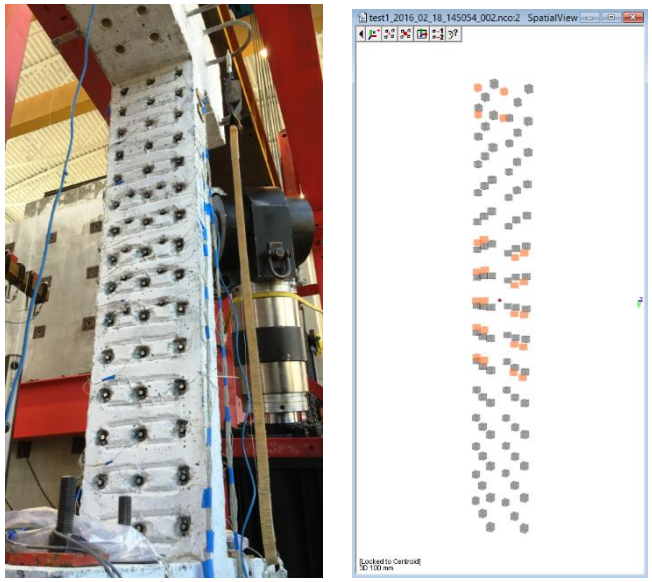

Figure A-4. Test 1: Instrumentation – Optotrak LEDs distribution on right face of the specimen and Spatial coordinate output

4. Test Summary

The first part of the test consisted of applying monotonic increasing lateral displacements followed by a second part where axial tensile and compressive displacements were induced to the specimen, identified as P1-P1 (Phase 1 – Prism 1), after it returned to the initial position.

4.1 Lateral Monotonic Loading

Specimen P1-P1, was subjected to monotonic increasing out-of-plane displacements to a 10 in. target, equivalent to 16.7% drift. The purpose of this part of the test was to confirm that the wall could sustain this level of drift in the absence of axial load. Consider Figure A-5 which shows the expected interaction between lateral deformations and axial compression loads. Future tests will consist of an application of a fixed lateral displacement followed by tension/compression cycles until buckling. Specimen P1-P1 is shown as ‘x’ in Figure A-5. While the specimen could have been pushed further, the level of out of plane displacement was felt to be more than would ever by achieved in a wall.

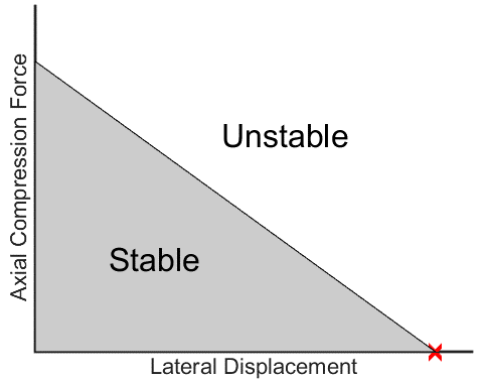

Figure A-5. Test 1: Response Representation

The test began with a 0.25 in. displacement and continued with the same increment up to 1 in. displacement. Next an increment of 0.5 in. was used up to 2 in., and finally 1 in. increment was used up to 10 in., Figure A-6. During the 0.5 in. displacement cycle, cracks appeared on the bottom left (BL) and top right (TR) regions of the prism, Figure A-7. Experimental first yielding was expected at 0.7 in. Upon loading to 0.75 in., more small cracks formed and extended to the beam-column connections, Figure A-8. After stage 3, the cracks became wider and more numerous. Concrete flaking occurred at 2 in. on the left top (LT) region, Figure A-9. By the time 3 in. displacement was completed, concrete flaking was observed on the bottom right (BR) region, Figure A-10. Crack widths close to 3/32 in. were measured on the BL region. When the specimen deformed 5 in., Figure A-11, slight concrete crushing on both compression regions was captured. In addition, concrete spalling was observed on the BR region. For the next displacements damage continued propagating and more cracks appeared on the connections. Figure A-12 and Figure A-13 show details of the damage visualized at the end of the lateral monotonic loading test. The deformed shape is depicted in Figure A-14.

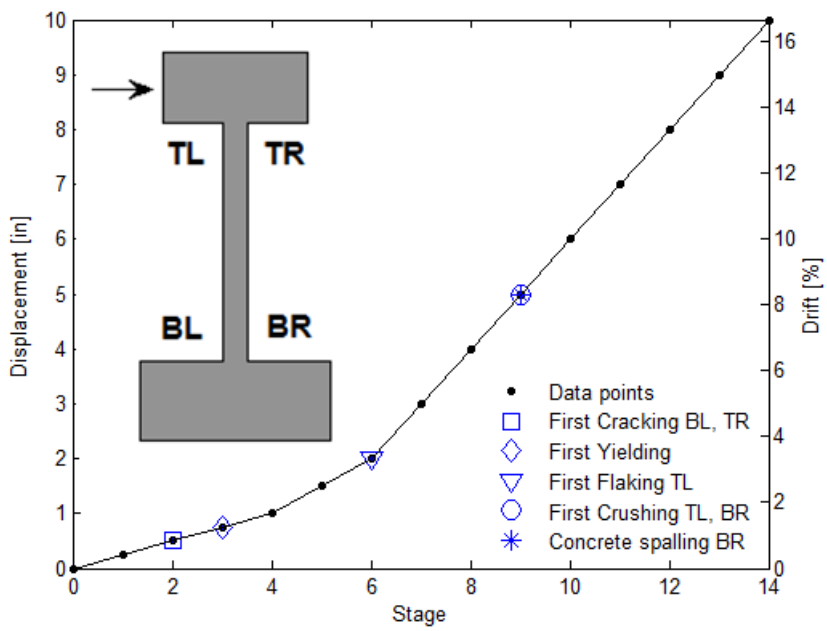

Figure A-6. Test 1: Out-of-Plane Lateral Displacement History

Figure A-15 includes Force - Displacement (F-D) diagrams from the experiment and the analysis prediction. The lateral loading applied to the specimen through the horizontal actuator and the displacement from the string potentiometer installed just below this actuator is first plotted. The response for the elastic range is close to the predicted shape. The first yielding point was established at 0.7 in. Both F-D curves tend to separate in the plastic range. The difference is attributed to the horizontal components of the forces developed by the vertical inclined actuators, as can be confirmed with the third curve that represents the force developed by the specimen.

Figure A-7. Test 1: First cracks at 0.5 in.

Figure A-8. Test 1: Crack propagation on the beam-column connections at 0.75 in.

Figure A-9. Test 1: Concrete flaking at 2in. on (TL); Propagation of cracks

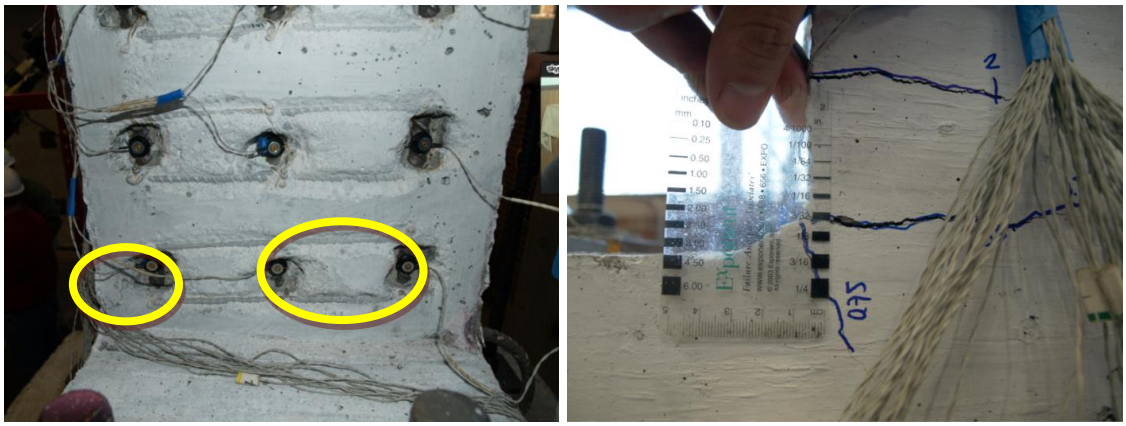

Figure A-10. Test 1: Concrete flaking at 3 in. on BR; Crack width

Figure A-11. Test 1: Concrete crushing at 5 in.; Concrete spalling

Figure A-12. Test 1: Bottom Left (BL) and Top Left (TL) Damage at 10in.

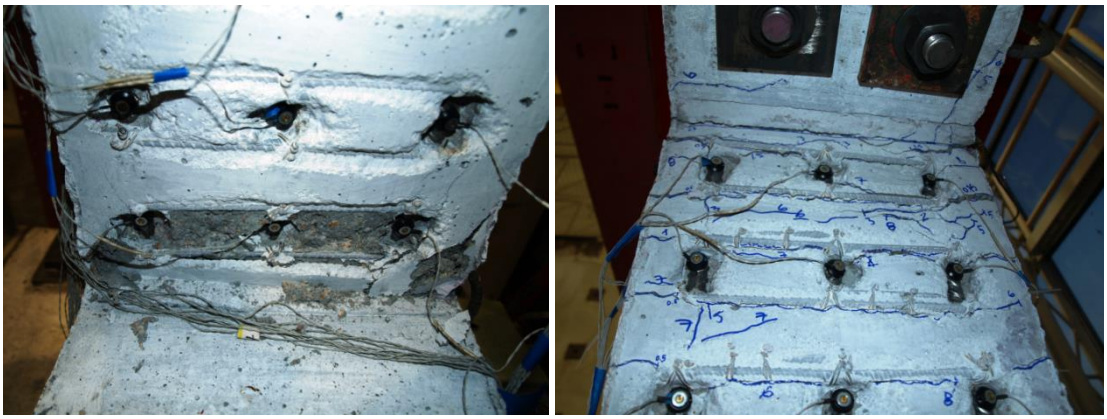

Figure A-13. Test 1: Bottom Right (BR) and Top Right (TR) Damage at 10 in.

Figure A-14. Test 1: Deformed shape at 10 in. lateral displacement

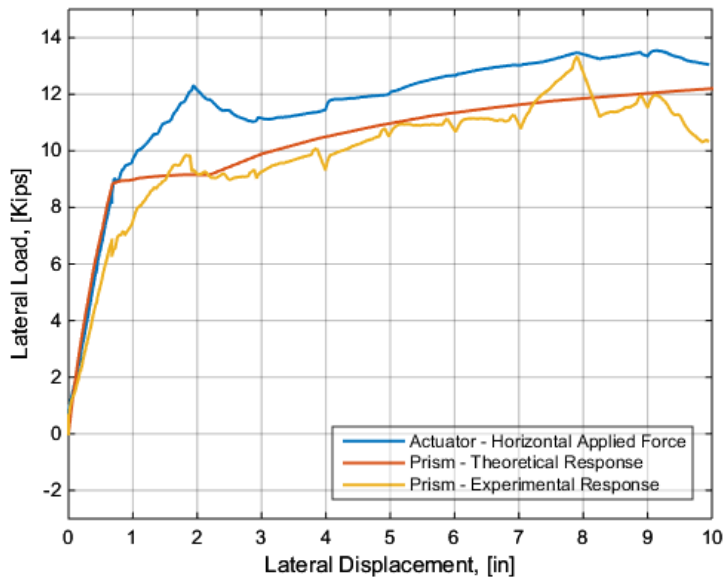

Figure A-15. Test 1: Force - Displacement response

Strains profiles at 10 in. displacement for each reinforcement line and for each face are displayed in Figure A-16. A total of 14 gages were established for each longitudinal bar along the 60 in. height, Y axis. The maximum tensile strain value reached at this stage was 5.6% obtained from the farthest gages located on the BL and TR regions.

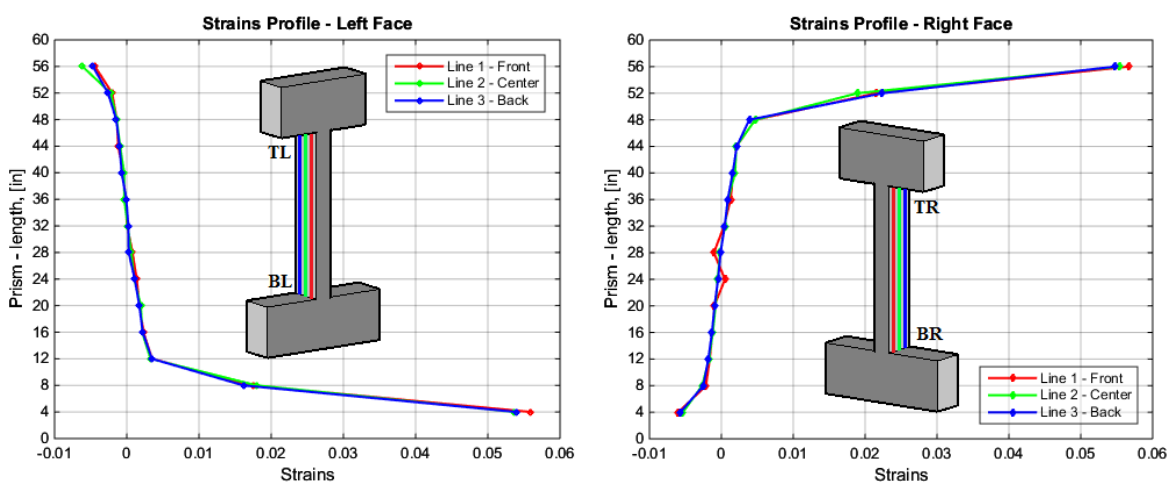

Figure A-16. Test 1: Strains profiles for the Left and Right Faces at 10in. lateral displacement

4.2 Axial Loading

Once the lateral monotonic loading was concluded, it was decided to take advantage of the same specimen and obtain a preliminary notion of the structural behavior of an RC wall boundary element affected by important combinations of out-of-plane displacements and axial deformations. The specimen returned to a zero lateral displacement and was subjected to axial monotonic tensile

displacements equivalent to 3% tensile strain. Three steps with an increment of 0.7 in. were induced in the vertical actuator controlled by displacements up to 2.1 in. The maximum axial tensile force captured for the prism was 155 Kips. Strain values in the six reinforcement lines were determined at this point, Figure A-17. It can be noted how the previous loading pattern applied to the specimen influenced the distribution of the strains along the height of the prism. An average of 3% strain is visible for the intermediate gages, as expected. The crack distribution along the prism in the central region was observed to be mostly uniform, Figure A-18.

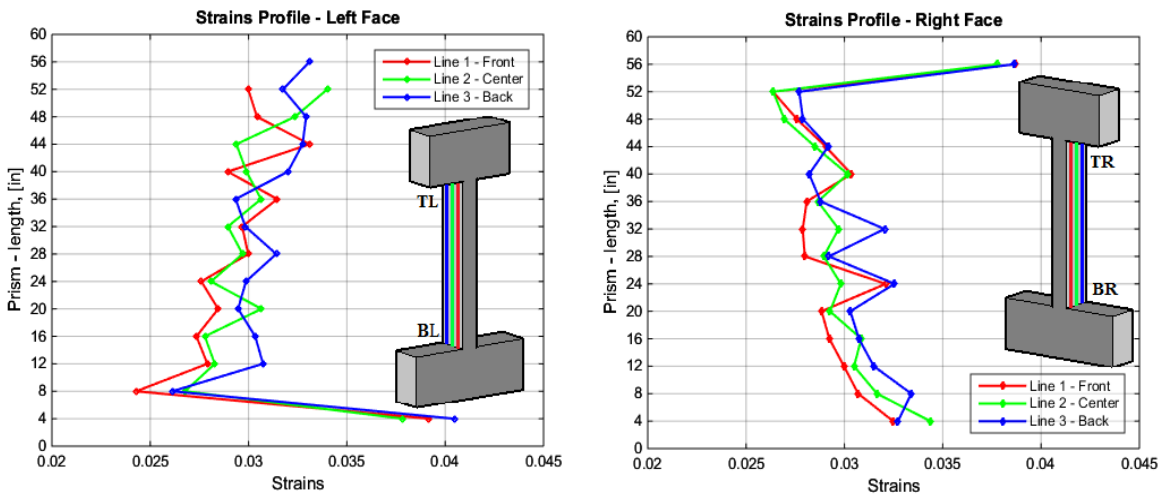

Figure A-17. Test 1: Strains profiles at maximum tensile deformation

Figure A-18. Test 1: Deformed shape at maximum tensile input

Subsequently, a 2.1 in. axial compressive displacement was induced to the actuator to return to the initial position. Before reaching the target, buckling was captured. The buckled shape of the prism by the time the target was accomplished is displayed in Figure A-19. Concrete crushing and concrete spalling were observed in the central part of the buckled region. After analyzing the data, it was determined that the vertical actuators were extended, approximately 0.8 in., beyond the zero position (i.e. still in tension) and the load that caused buckling was 96 kips (compressive), which represents 22% of the nominal compressive capacity of the prism, *Pn* = 423 kips.

Figure A-19. Test 1: Buckling deformation at 0in. axial displacement

The strains profiles at the onset of buckling are presented in Figure A-20. The strain distribution indicates maximum values greater than 3% reached in the BL and TR regions. In the central part, on the face subjected to tensile stresses due to the buckled shape, strains reached values greater than the opposite face, which coincides with the developed shape. An additional 0.5 in. compressive displacement was applied to the specimen and consequently concrete crushing and concrete spalling propagated along the central compressed region. The maximum axial load captured at this stage was 236 kips, close to 60% of *Pn*.

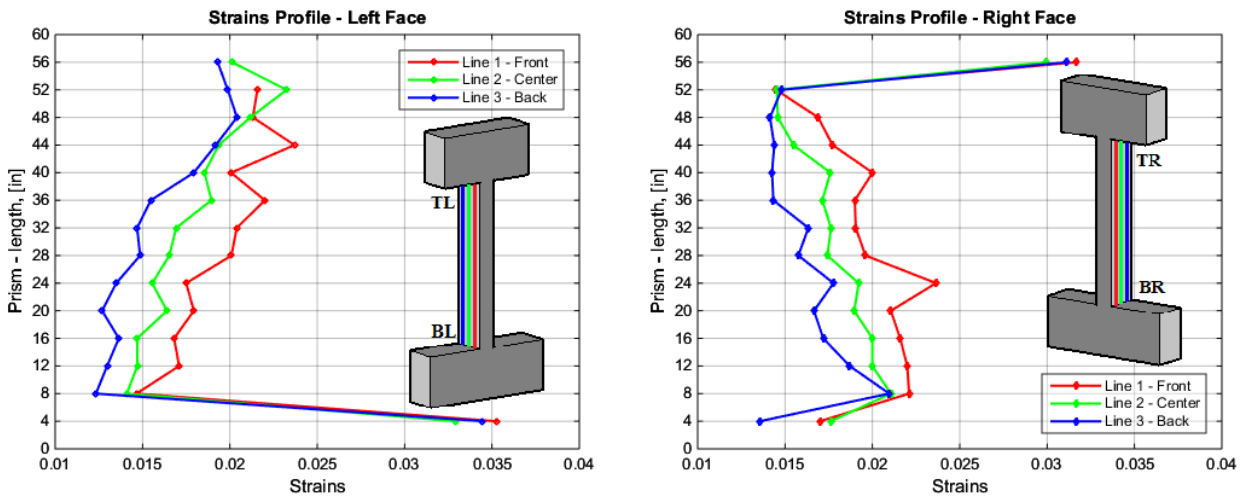

Figure A-20. Test 1: Strains profiles at buckling onset

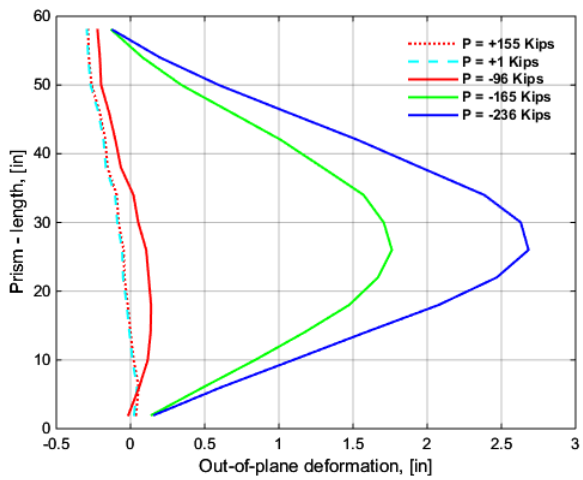

Figure A-21. Test 1: Evolution of out-of-plane deformations

Out-of-plane deformations due to the axial loads applied to the specimen are plotted in Figure A-21. Starting from the stage when maximum tensile strains were captured, a total of five stages were considered to display the evolution of out-of-plane displacements computed all along the prism height. The right face (RF) of the prism was selected for this purpose. The loads illustrated in Figure A-21 are characterized as follows: maximum tensile load, 155 kips; transition stage where axial loads change from tension to compression, +1 kip; onset of buckling, -96 kips; specimen returned to 0 in., -165 kips; and, maximum compressive load, -236 kips. Maximum relative out-of-plane displacements were captured at 26 in. height, 4in. below the center. The values registered for the last two stages were 1.8 in. and 2.7 in., respectively. The last one represents 54% of the prism thickness.

At the end of the test, the specimen was recovered to a zero loading position. The loading pattern established for this second part is depicted in Figure A-22. The final deformed shape of the prism, once the instrumentation was removed, is illustrated in Figure A-23.

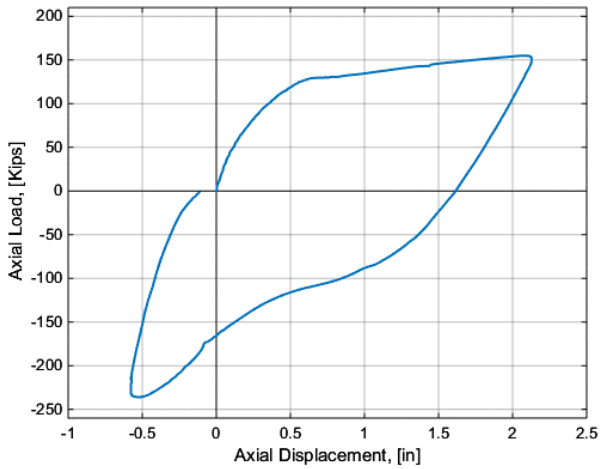

Figure A-22. Test 1: Displacement pattern - Axial Loading

Figure A-23. Test 1: Deformed shape at the end of the test

5. Conclusions

Specimen P1-P1 was tested during 4 hours where different loading patterns were applied. The first part of the test indicates the prism reached the 10 in. displacement with minor loss of capacity. Initial signs of concrete crushing and concrete spalling were noticed at 5in. Maximum strain values of 5.6%

were computed on the BL and TR regions by the end of the final stage related to the lateral monotonic loading.

In the second part of the test, axial tensile displacements equivalent to 3% strain were induced. Values close to the target were observed in the central region of the prism. However, the BL and TR showed higher values, demonstrating the influence of the previous loading pattern. The onset of buckling was captured by the time the prism was still elongated. The strains registered in the intermediate gages were close to 2%. The buckling load represented 22% of the nominal compressive capacity, *Pn*, predicted for the prism. An out-of-plane deformation greater than 50% of the prism thickness was determined at 26 in. height for a compressive load equivalent to 60% of *Pn*.

Neither bar buckling nor bar fracture were detected during or after the test. The stirrups remained as originally constructed. Analysis of the data from this test will continue, as a consequence the material presented here should be considered preliminary. Further experiments will reveal more information about the effectiveness of the reinforcement detailing recommended in guidelines to prevent lateral instability in RC structural walls.

Stability of Ductile RC Structural Walls – Assessment of the Local Buckling Failure Mode

Test 2

22 – March – 2016

Summary Report

Prepared for:

Alaska Department of Transportation

Prepared by:

RA – Ana Gabriela Haro

PIs – Mervyn Kowalsky and Rob Chai

North Carolina State University

Raleigh – NC

1. Executive Summary

Test 2 was conducted at the Constructed Facilities Laboratory on Thursday, March 22, 2016, as part of the load path project. The specimen was designed and built simulating boundary elements from prototype walls. An axial compression load followed by cyclic axial tensile displacements and compressive loads were applied to the specimen to capture its structural performance and to determine additional critical parameters associated with lateral instability of RC walls. The first part of the results are presented in this report. Further analyses will be elaborated.

2. Introduction

Recent earthquakes in New Zealand and Chile have illustrated the importance of out-of-plane stability of concrete wall elements due to in-plane loading. Pier walls are occasionally employed by Alaska DOT for their in-plane lateral stiffness. While these walls are normally thicker than the walls typically found in building applications, their clear heights are also larger, giving rise to height-to-thickness ratios which may be larger than that of buildings. Some analyses have demonstrated that walls as thick as 20 in. may be prone to buckling, depending on their length and height.

Noticing the concentration of damage in the boundary elements of rectangular reinforced concrete structural walls due to higher stress and strain demands, some past investigations by others have been carried out on prisms, which was found to be an economical way to study the inelastic instability of structural walls. In general, the main objective of these tests focuses on subjecting specimens to cyclic tension and compression actions to simulate vertical components of actual seismic loading.

While past tests on prisms has shown existing models to be promising, missing from the models is the interaction with out-of-plane loading. The existing models correlate tensile strain from in plane loading to out-of-plane deformation, assuming a prescribed curvature distribution. If loading occurs in the out-of-plane direction, the relationship between tensile strain and out-of-plane deformations must be adjusted to reflect this. In its simplest form, this would be an addition of an out-of-plane displacement to the existing equation. However, out-of-plane displacement may impact the distribution of curvature with height, thus requiring additional adjustments to the models.

A total of 12 prisms are being experimentally tested in the Constructed Facilities Laboratory (CFL) during this project. The support conditions for the 12 prisms are conceived as fixed-fixed. The first testing phase will involve controlled load paths where the specimens are subjected to tension/compression cycles in addition to lateral loading to mimic the effects of out-of-plane displacements. In the second phase, longitudinal reinforcement ratios will be varied – between the two phases, reinforcement ratios will span the typical values employed by Alaska DOT for pier walls. The details associated with the two phases are presented in Table A-3.

This first phase consists of testing six 1/2-scale identical specimens. The thickness of the prisms is 5 in. since the cover was excluded from the construction. The geometry used is 5x12x60 in, corresponding to an aspect ratio (*h/b = height/thickness*) of 10 (including the missing cover). The longitudinal reinforcement ratio is 2.6% (6 bars #5). Transverse reinforcement consists of #3 diameter rebar spaced at 2 in. and was placed as shown in Figure A-24.

Table A-3. Test 2: Description of the experimental phases

Phase	Tests	Geometry	Reinforcement	Loading
1	6	Thickness and Height (based on prototype wall). (6”x12” ; actual geometry = 5”x12”)	Longitudinal (6bars#5) and transverse (#3@2in) reinforcement ratios similar for the 6 specimens.	Controlled 3D load path
2	6	Same as phase 1 (Based on actual pier walls formerly used by the Alaska DOT)	Longitudinal reinforcement ratio varies. (3 specimens 6bars#3 and 3 specimens 6bars#4)	Controlled 3D load path

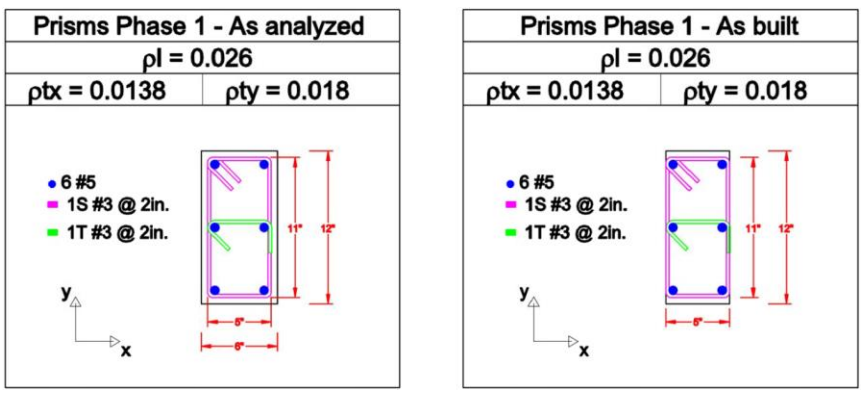

Figure A-24. Test 2: Phase 1 - Cross section of the prisms

Table A-4. Test 2: Phase 1 - Steel tensile test properties for bars #3 and #5

Sample No.	Bar #	fy (ksi)	εy = fy/Es	fu (ksi)	εu
1	3	74.7	0.0026	103.3	0.0916
2	3	74.8	0.0026	100.6	0.0750
3	3	79.6	0.0027	105.0	0.0927
4	3	76.8	0.0026	103.4	0.0770
5	3	77.0	0.0027	103.3	0.0736
6	3	77.1	0.0027	103.2	0.1040
#3 Average		**76.7**	**0.0026**	**103.1**	**0.0856**
1	5	69.4	0.0024	96.4	0.1100
2	5	68.2	0.0024	95.6	0.1124
3	5	68.7	0.0024	97.7	0.0981
4	5	70.1	0.0024	97.4	0.1128
5	5	70.0	0.0024	98.0	0.1326
#5 Average		**69.3**	**0.0024**	**97.0**	**0.1132**

Regarding the material properties, an unconfined concrete strength of 5 ksi and reinforcement yielding strength of 60 ksi were considered as design values to define the load/displacement history for the test. Table A-4 shows the actual steel tensile test properties for the #3 and #5 bars. The reinforcement detailing was established according to the ACI 318 and NEHERP guidelines for ductile columns and boundary elements.

3. Test Setup

The test setup consisted of a 14 ft long steel loading beam placed on the top of the specimen and connected to three actuators: two vertically inclined 440 kips actuators which induce axial loads and one horizontal 55 kips actuator to apply out-of-plane displacements. Two steel frames are used to restrain torsion in the loading beam. Two concrete blocks attached to the strong floor support the specimen to reach the required height associated with the effective length of the 440 kips actuators. Figure A-25 depicts the test setup drawings and Figure A-26 shows a picture of the area where the components of the project are placed.

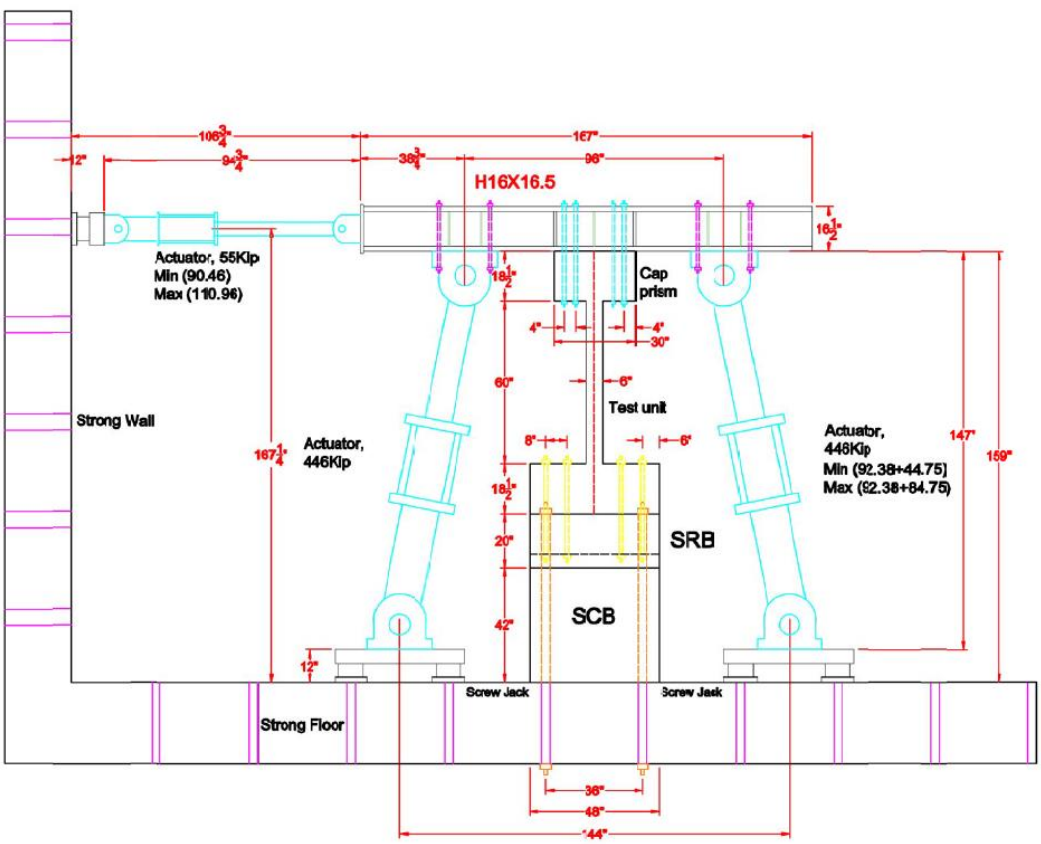

Figure A-25. Test 2: Test setup drawings

Figure A-26. Test 2: Test setup in the CFL at NC State

The horizontal actuator is controlled by displacements. The vertically inclined actuator located at the left hand side of the specimen, Figure A-25, is controlled by rotations captured throughout an inclinometer attached to the loading beam. The actuator placed at the right hand of the specimen is controlled by a combination of forces and displacements. Loads and strokes in the actuators are measured through integrated LVDTs and loads cells.

Relative displacements resulting from the interaction between the specimen and the connecting concrete block were obtained through 2 linear potentiometers. In addition, axial deformations of the prism were registered through 4 spring potentiometers. Another string potentiometer was used to capture the lateral displacement of the loading beam.

A total of 110 infrared LEDs from the optical tracking system Optotrak Certus developed by Northern Digital Inc. were placed directly on the steel reinforcement of the prism. The objective was to establish longitudinal and transverse strains in real time throughout a MATLAB code recently developed for this purpose at the CFL. Four additional infrared LEDs were positioned on the front face of the prism cap as a plane of reference. Figure A-27 shows the distribution of the LEDs on the left face of the prism and the overall allocation of the markers obtained from the Optotrak spatial coordinate output.

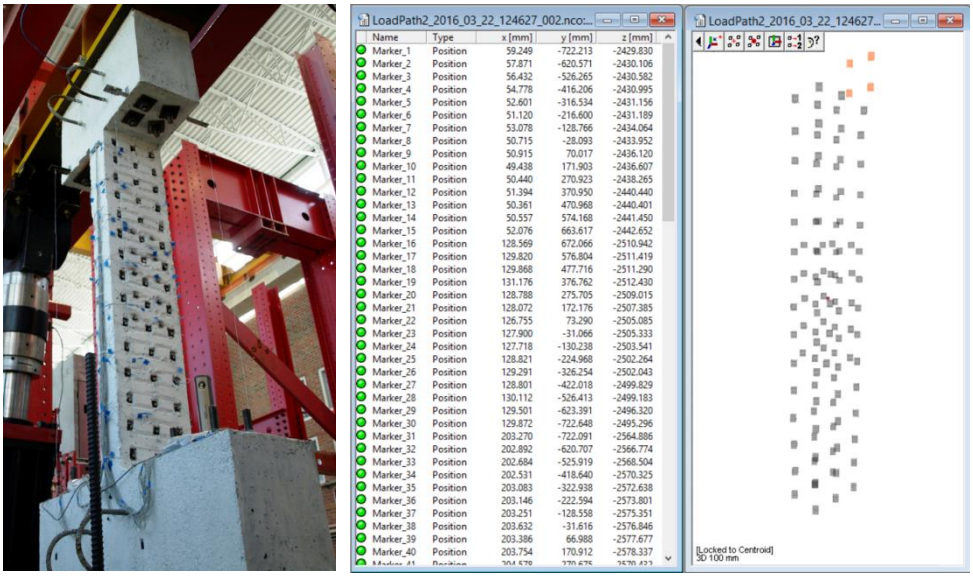

Figure A-27. Test 2: Instrumentation – Optotrak LEDs distribution on left face of the specimen and Spatial coordinate output

4. Test Summary

The first part of the test consisted of applying an axial compressive load followed by a second part where cyclic axial tensile displacements and compressive loads were induced to the specimen, identified as P1-P2 (Phase 1 – Prism 2), after it returned to the initial position.

4.1 Monotonic Compressive Loading

Specimen P1-P2, first was subjected to an axial load equivalent to the design axial compression capacity of the prism, *Po* = -358 kips. The purpose of this part of the test was to confirm that the boundary element of the wall could sustain this level of compressive load in the absence of lateral displacements. Consider Figure A-28, which shows the expected interaction between lateral deformations and axial compression loads. Future tests will consist of an application of a fixed lateral displacement followed by tension/compression cycles until buckling. Specimen P1-P2 is shown as 'x' in Figure A-28.

The test was successfully conducted with no signs of damage. An axial displacement of -0.43in. was measured at the time the target load was achieved. Strain profiles captured at this stage for each reinforcement line and for each face are displayed in Figure A-29. A total of 14 gages were established for each longitudinal bar along the 60 in. height, Y axis. The average compressive strain in both faces is close to -0.15%, which is less than the yielding strain, 0.238%.

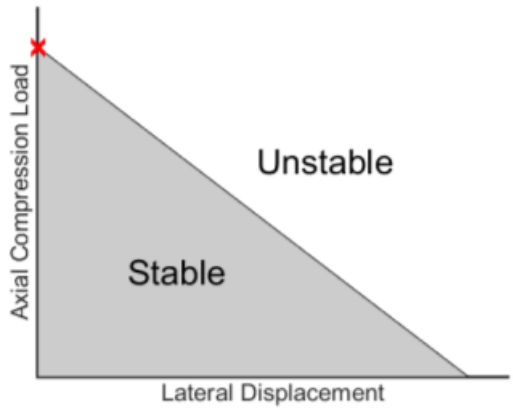

Figure A-28. Test 2: Response Representation

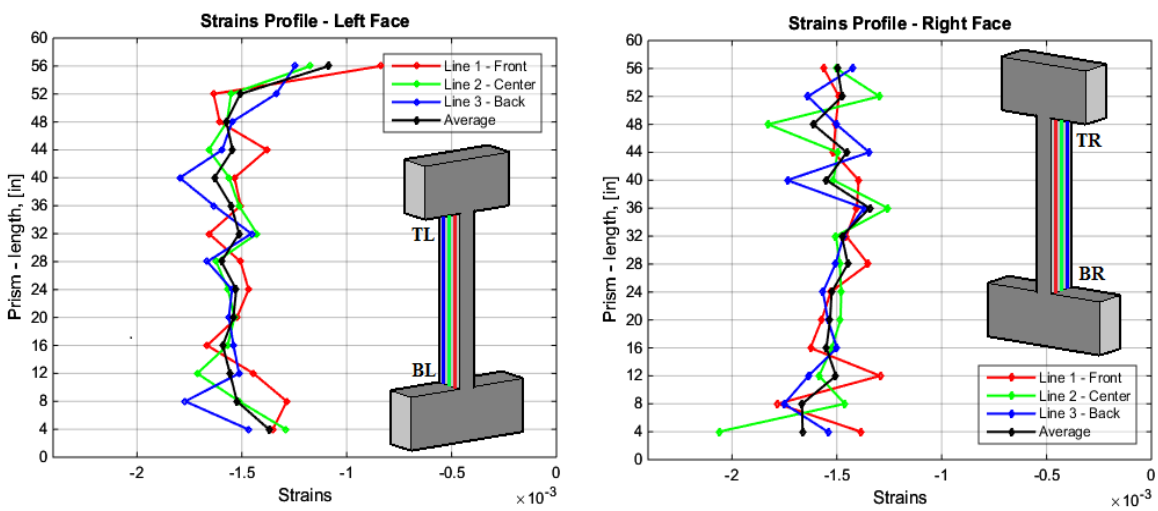

Figure A-29. Test 2: Strain profiles at maximum compressive load

4.2 Cyclic Axial Loading

A quasi-static displacement/load controlled procedure was established for the second part of the test. Unsymmetrical cycles were used to evaluate the seismic performance of prism P1-P2. The axial displacement history started with elastic single cycles analytically predicted. The targets in tension were chosen as fractions of the yielding displacement referred as: $0.25\varepsilon_y$, $0.50\varepsilon_y$, $0.75\varepsilon_y$, and ε_y. After yielding, three identical cycles at different axial tensile displacement ductility levels continued until buckling was captured upon compressive loading. The unique compressive target was established from the first part of the experiment, corresponding to Po = -358 kips, which was applied on each cycle during the whole test, Figure A-30.

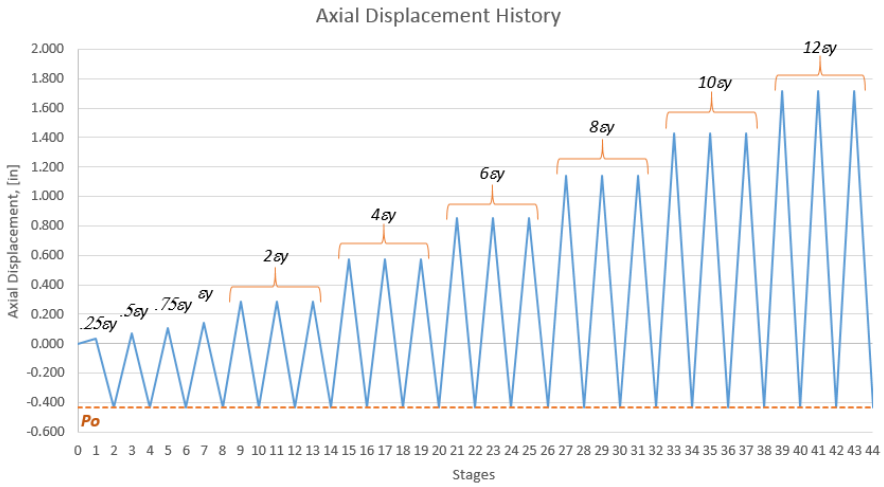

Figure A-30. Test 2: Displacement History applied during the second part of the test

First cracks developed at the footing-prism interface on the right face and along the height of the prism during 0.50ε_y, Figure A-31. The crack propagation at 1ε_y, 2ε_y, and 4ε_y appears in Figure A-32, Figure A-33, and Figure A-34, respectively. Upon loading to 2ε_y, more small cracks formed and extended to the beam-column connections. Crack widths close to 1/16 in. were captured at 4ε_y. During the following cycle the cracks became wider and the number of new cracks decreased as depicted in Figure A-35. In addition, it was observed that the spacing of the horizontal cracks were originated by the spacing of the transverse reinforcement since they fairly corresponded to each other.

Signs of concrete flaking on the footing-prism interface were observed in the first cycle at 6ε_y. At the end of the third cycle when a compression load of -336 Kips was being applied, concrete cover fell down on the back face of the prism. The transverse reinforcement was exposed within a length of 34 in. Before resuming the test, debris was removed to protect the instrumentation and subsequently the target compressive load was reached, Figure A-36. In the cycles associated with an 8ε_y tensile demand, cracks became wider as observed in Figure A-37 and the concrete cover continued falling apart in the same region described before. At the end of the third cycle, the transverse reinforcement was uncovered within a height of 54 in. All through these cycles, the specimen remained visibly straight. As tensile demands increased during the cycles related to 10ε_y, the out-of-plane buckling mechanism was visually captured upon compressive loading. In this scenario, where the out-of-plane deformation is relatively small, the compression force developed to resist the overturning moment, can be fully reached as cracks close and consequently, the prism returns to a fairly straight and stable position as shown in Figure A-38.

Cracks widths close to 2.5mm (3/32 in.) were measured during the first cycle at 12ε_y, Figure A-39. The distribution of the cracks was uniform along the height of the prism. The local buckling mechanism described above was similarly observed during the first two cycles corresponding to a

tensile demand of $12\varepsilon_y$, Figure A-40 and Figure A-41. In the third cycle upon compressive loading, a different scenario was captured where instability occurred as illustrated in Figure A-42.

Figure A-31. Test 2: First cracks at 0.5 εy

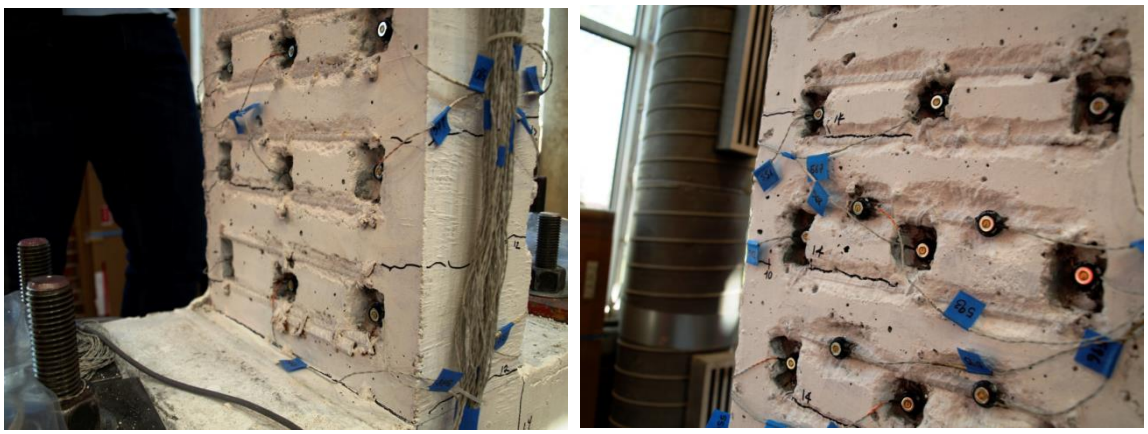

Figure A-32. Test 2: Propagation of cracks at 1.0 εy

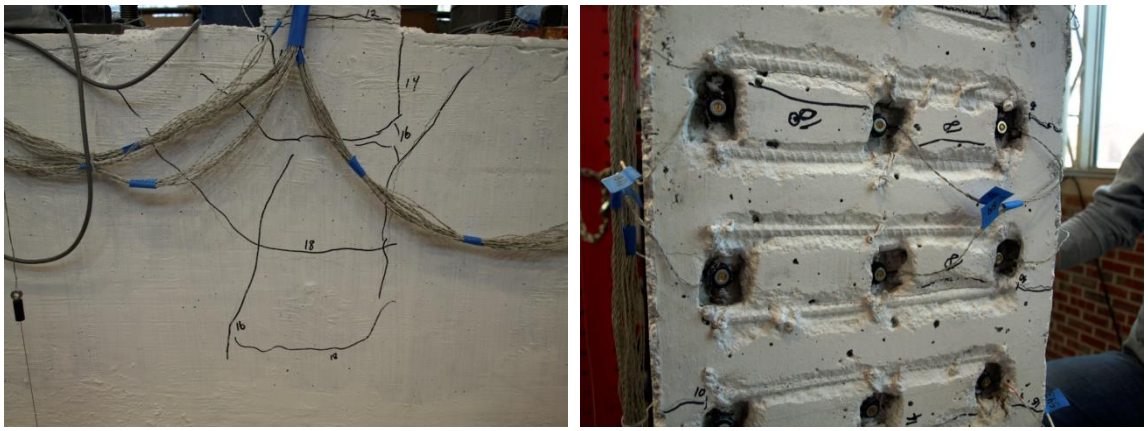

Figure A-33. Test 2: Propagation of cracks at 2.0 εy - First cycle

Figure A-34. Test 2: Propagation of cracks at 4.0 εy - First cycle

Figure A-35. Test 2: Propagation of cracks at 6.0 εy - First cycle

Figure A-36. Test 2: Concrete cover fell down at -368 kips - Third cycle of 6.0 εy

Figure A-37. Test 2: Propagation of cracks at 8.0 εy - First cycle

Figure A-38. Test 2: Evolution of the deformed shape during compression loading. Second cycle of 10εy

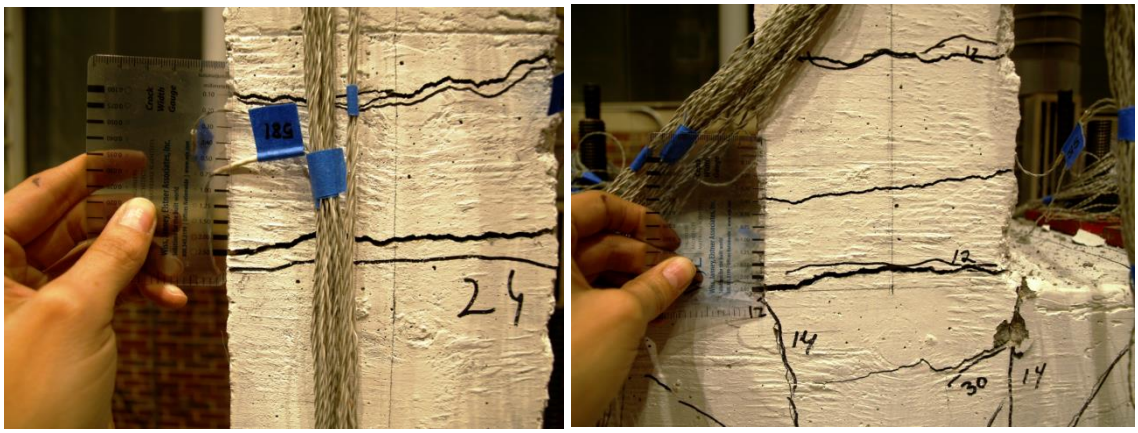

Figure A-39. Test 2: Observed cracks at 12εy

Figure A-40. Test 2: Evolution of the deformed shape during compression loading. First cycle of 12εy

Figure A-41. Test 2: Evolution of the deformed shape during compression loading. Second cycle of 12εy

Figure A-42. Test 2: Evolution of instable out-of-plane buckling developed under compression loading. Third cycle for 12εy

Figure A-43. Test 2: Final state at midheight, bottom and top regions

The end of the test showing local concrete crushing at midheight, bottom right (BR) and top right (TR) regions of the prism is presented in Figure A-43. Notice a well confined concrete core at this phase. A plumb line was used in order to identify the transverse curvature distribution along the height of the prism, Figure A-44. It was observed that the maximum normalized out-of-plane deformation, δ/b = 3in./5in., exceeded 0.5.

Figure A-44. Test 2: Buckled shape of prism P1-P2

Figure A-45 depicts the entire structural response of P1-P2 as a function of axial forces and displacements. In the last six cycles an axial stiffness reduction is evident by the time the axial compressive load approaches -100 kips. At this phase, the specimen is still extended a length close to 0.7 in. These points where associated with the onset of out-of-plane buckling. Due to the intrinsic eccentricity in the developed compressive force, one side of the wall end region closes first resulting in out-of-plane deformations. Once the cracks close, the prism gains stiffness and is able to carry the same axial load as in previous cycles. In the last cycle, instability was captured since the prism was not able to recover its strength. The maximum applied load at this stage was -232 kips, equivalent to 65% of the axial design compressive force, *Po*.

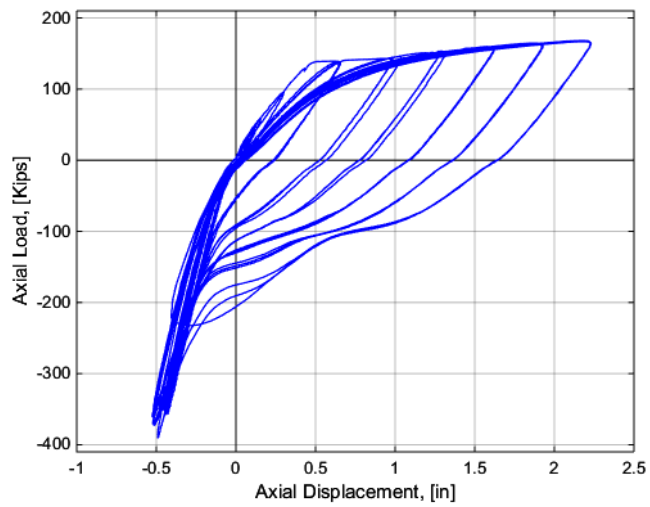

Figure A-45. Test 2: Axial structural response of prism P1-P2

Strain profiles captured during the last tensile cycle are presented in Figure A-46. Some readings from the infrared LEDs located on the back reinforcement line (blue line) of the specimen were lost due to accumulated damage. The average of the strains in the left and right faces is close to 2.8%, value established as target equivalent to $12\varepsilon_y$. Figure A-47 shows the strain profiles of the onset of buckling during the last cycle upon compressive loads. The strains average is close to 2.2% in both faces.

Figure A-48 illustrates the evolution of the nominal axial strain captured from gage 22 at the center of the specimen on the right face versus the normalized out-of-plane deformation. Notice a stable response of the prism at low levels of axial tensile strains. The normalized out-of-plane displacements increased upon compressive loading during the first cycle associated with $8\varepsilon_y$. Throughout the first cycle of $12\varepsilon_y$, the specimen suffered from a permanent out-of-plane deformation. A sudden increment on this deformation took place at the moment it reached a normalized value of 0.35 and the compression load was -160 kips, which represents 45% of the axial design compressive force, *Po*.

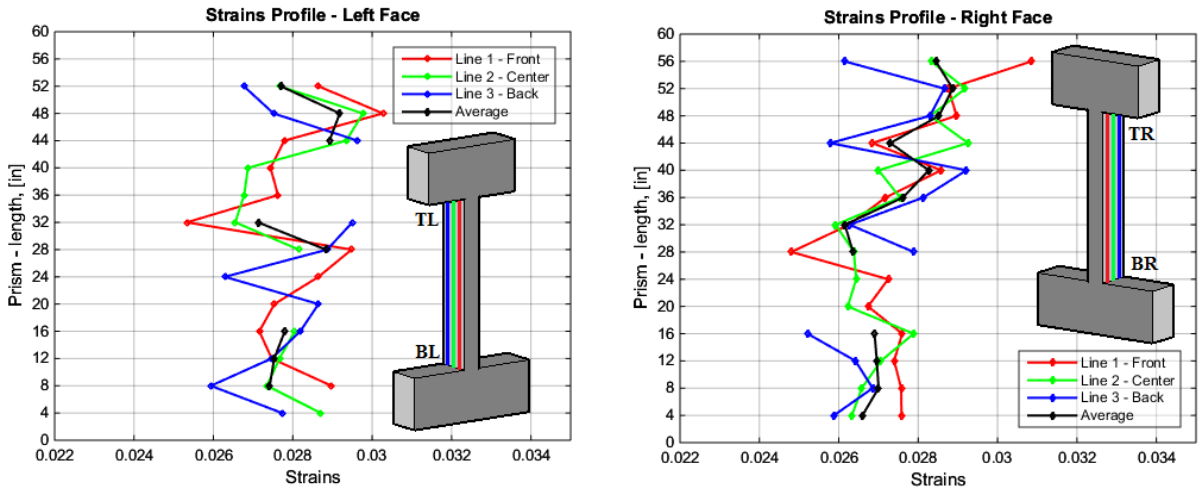

Figure A-46. Test 2: Strain profiles at 12 ε_y during the last cycle

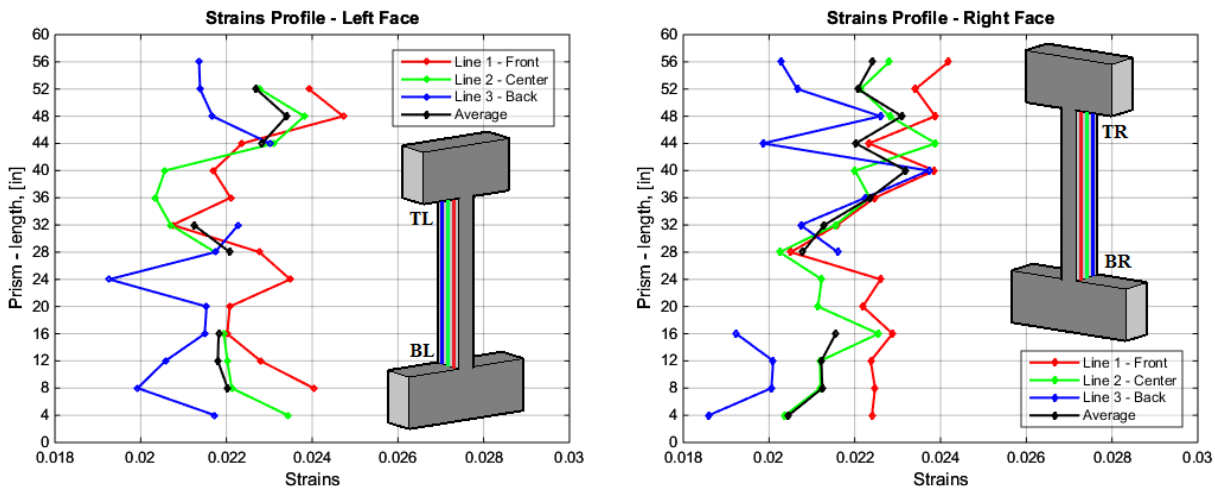

Figure A-47. Test 2: Strain profiles at onset of buckling during the last cycle

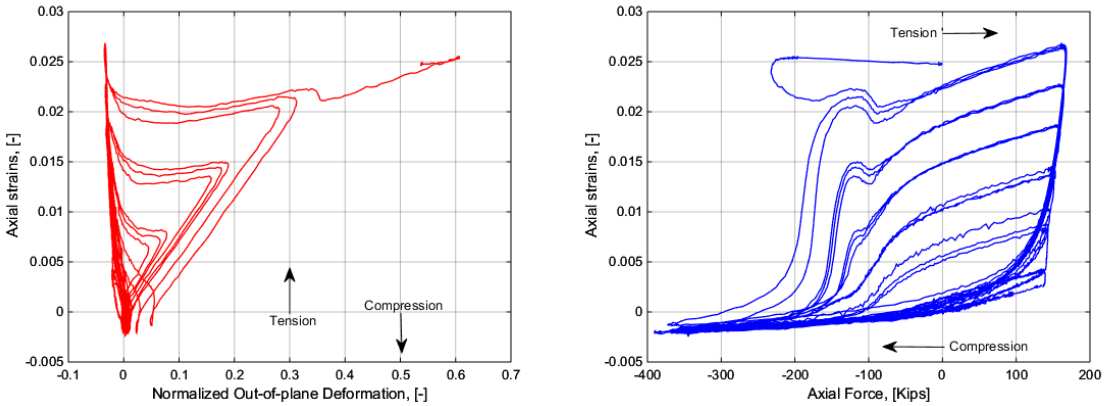

Figure A-48. Test 2: Response of specimen P1-P2 captured from a midheight gage on the right face

5. Conclusions

Specimen P1-P2 was tested during six hours where two loading patterns were applied. The first part of the test indicates the prism reached the maximum axial design compressive load with zero loss of capacity. The average compressive strain in both faces was close to -0.0015, less than the yielding strain.

In the second part of the test, progressive cyclic axial loads/strains were applied to the specimen reaching maximum values close to the axial design compressive force, Po = -358 kips and $12\varepsilon_y$, in compression and tension, respectively. The specimen presented a stable response at low levels of axial tensile demands. Out-of-plane deformations were not noticed during the cycles before $8\varepsilon_y$. Beyond the first cycle of $8\varepsilon_y$, a gradual increase in the out-of-plane deformations were captured until instability developed during the last cycle of $12\varepsilon_y$. The large buckling displacement led to concrete crushing and spalling in the central region. The axial force at this stage was 47% of the compressive force in the previous cycle.

Neither bar buckling nor bar fracture were detected during or after the test. The stirrups remained as originally constructed. Analysis of the data from this test will continue, as a consequence the material presented here should be considered preliminary. Further experiments will reveal more information about the effectiveness of the reinforcement detailing recommended in guidelines to prevent lateral instability in RC structural walls.

Stability of Ductile RC Structural Walls – Assessment of the Local Buckling Failure Mode

Test 3

29 – March – 2016

Summary Report

Prepared for:

Alaska Department of Transportation

Prepared by:

RA – Ana Gabriela Haro

PIs – Mervyn Kowalsky and Rob Chai

North Carolina State University

Raleigh – NC

1. Executive Summary

Test 3 was conducted at the Constructed Facilities Laboratory on Thursday, March 27, 2016, as part of the load path project. The specimen was designed and built simulating boundary elements from prototype walls. A monotonic and constant lateral displacement equivalent to 1% drift was applied first to the specimen followed by cyclic axial compressive loads and tensile displacements to capture its structural performance and to determine additional critical parameters associated with lateral instability of RC walls. The first part of the results are presented in this report. Further analyses will be elaborated.

2. Introduction

Recent earthquakes in New Zealand and Chile have illustrated the importance of out-of-plane stability of concrete wall elements due to in-plane loading. Pier walls are occasionally employed by Alaska DOT for their in-plane lateral stiffness. While these walls are normally thicker than the walls typically found in building applications, their clear heights are also larger, giving rise to height-to-thickness ratios which may be larger than that of buildings. Some analyses have demonstrated that walls as thick as 20 in. may be prone to buckling, depending on their length and height.

Noticing the concentration of damage in the boundary elements of rectangular reinforced concrete structural walls due to higher stress and strain demands, some past investigations by others have been carried out on prisms, which was found to be an economical way to study the inelastic instability of structural walls. In general, the main objective of these tests focuses on subjecting specimens to cyclic tension and compression actions to simulate vertical components of actual seismic loading.

While past tests on prisms has shown existing models to be promising, missing from the models is the interaction with out-of-plane loading. The existing models correlate tensile strain from in plane loading to out-of-plane deformation, assuming a prescribed curvature distribution. If loading occurs in the out-of-plane direction, the relationship between tensile strain and out-of-plane deformations must be adjusted to reflect this. In its simplest form, this would be an addition of an out-of-plane displacement to the existing equation. However, out-of-plane displacement may impact the distribution of curvature with height, thus requiring additional adjustments to the models.

A total of 12 prisms are being experimentally tested in the Constructed Facilities Laboratory (CFL) during this project. The support conditions for the 12 prisms are conceived as fixed-fixed. The first testing phase will involve controlled load paths where the specimens are subjected to tension/compression cycles in addition to lateral loading to mimic the effects of out-of-plane displacements. In the second phase, longitudinal reinforcement ratios will be varied – between the two phases, reinforcement ratios will span the typical values employed by Alaska DOT for pier walls. The details associated with the two phases are presented in Table A-5.

This first phase consists of testing six 1/2-scale identical specimens. The thickness of the prisms is 5 in. since the cover was excluded from the construction. The geometry used is 5x12x60 in, corresponding to an aspect ratio (*h/b = height/thickness*) of 10 (including the missing cover). The longitudinal reinforcement ratio is 2.6% (6 bars #5). Transverse reinforcement consists of #3 diameter rebar spaced at 2 in. and was placed as shown in Figure A-49.

Table A-5. Test 3: Description of the experimental phases

Phase	Tests	Geometry	Reinforcement	Loading
1	6	Thickness and Height (based on prototype wall). (6”x12” ; actual geometry = 5”x12”)	Longitudinal (6bars#5) and transverse (#3@2in) reinforcement ratios similar for the 6 specimens.	Controlled 3D load path
2	6	Same as phase 1 (Based on actual pier walls formerly used by the Alaska DOT)	Longitudinal reinforcement ratio varies. (3 specimens 6bars#3 and 3 specimens 6bars#4)	Controlled 3D load path

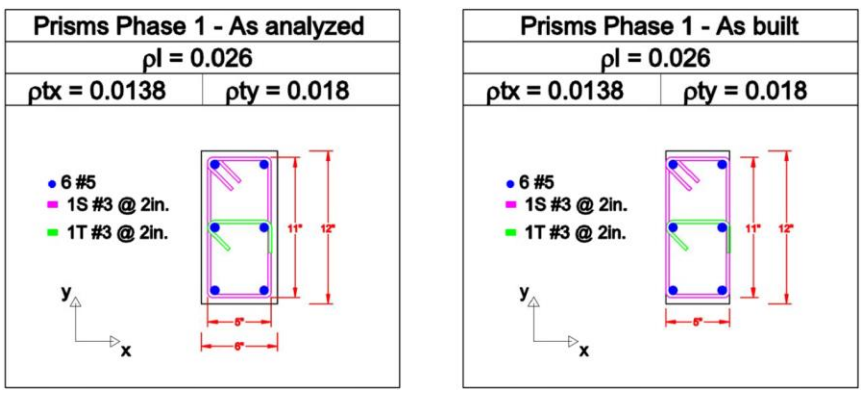

Figure A-49. Test 3: Phase 1 - Cross section of the prisms

Table A-6. Test 3: Phase 1 - Steel tensile test properties for bars #3 and #5

Sample No.	Bar #	fy (ksi)	εy = fy/Es	fu (ksi)	εu
1	3	74.7	0.0026	103.3	0.0916
2	3	74.8	0.0026	100.6	0.0750
3	3	79.6	0.0027	105.0	0.0927
4	3	76.8	0.0026	103.4	0.0770
5	3	77.0	0.0027	103.3	0.0736
6	3	77.1	0.0027	103.2	0.1040
#3 Average		**76.7**	**0.0026**	**103.1**	**0.0856**
1	5	69.4	0.0024	96.4	0.1100
2	5	68.2	0.0024	95.6	0.1124
3	5	68.7	0.0024	97.7	0.0981
4	5	70.1	0.0024	97.4	0.1128
5	5	70.0	0.0024	98.0	0.1326
#5 Average		**69.3**	**0.0024**	**97.0**	**0.1132**

Regarding the material properties, an unconfined concrete strength of 5 ksi and reinforcement yielding strength of 60 ksi were considered as design values to define the load/displacement history for the test. Table A-6 shows the actual steel tensile test properties for the #3 and #5 bars. The reinforcement detailing was established according to the ACI 318 and NEHERP guidelines for ductile columns and boundary elements.

3. Test Setup

The test setup consisted of a 14 ft long steel loading beam placed on the top of the specimen and connected to three actuators: two vertically inclined 440 kips actuators which induce axial loads and one horizontal 55 kips actuator to apply out-of-plane displacements. Two steel frames are used to restrain torsion in the loading beam. Two concrete blocks attached to the strong floor support the specimen to reach the required height associated with the effective length of the 440 kips actuators. Figure A-50 depicts the test setup drawings and Figure A-51 shows pictures of the area where the components of the project are placed.

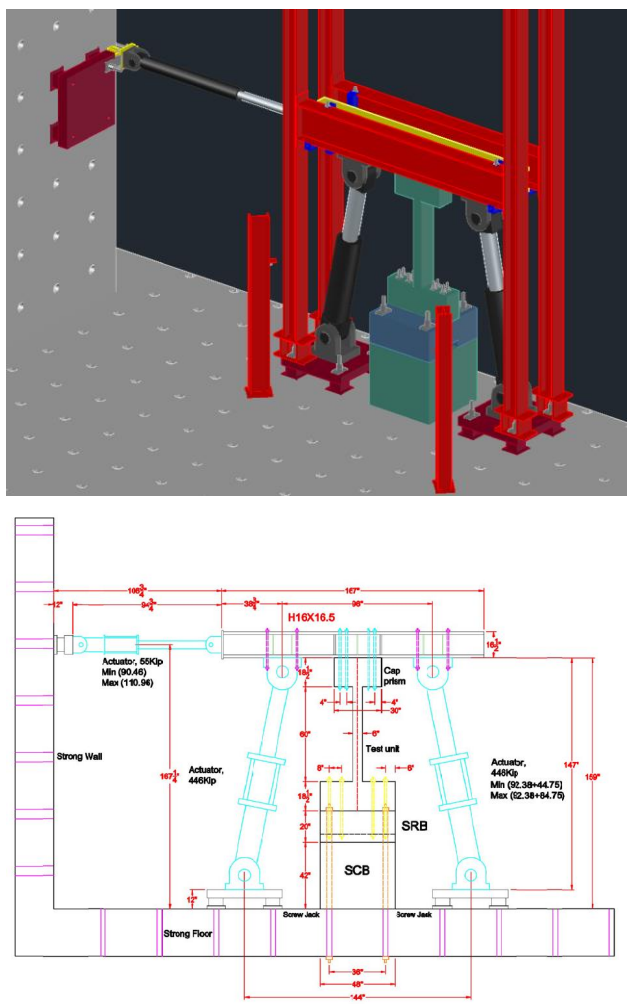

Figure A-50. Test 3: Test setup drawings

Figure A-51. Test 3: Test setup in the CFL at NC State

The horizontal actuator is controlled by displacements. The vertically inclined actuator located at the left hand side of the specimen, Figure A-50, is controlled by rotations captured throughout an inclinometer attached to the loading beam. The actuator placed at the right hand of the specimen is controlled by a combination of forces and displacements. Loads and strokes in the actuators are measured through integrated LVDTs and loads cells.

Relative displacements resulting from the interaction between the loading beam, the specimen, and the support concrete block were obtained through 4 linear potentiometers. In addition, axial deformations of the prism were registered through 4 string potentiometers. Another string potentiometer was used to capture the lateral displacement of the loading beam.

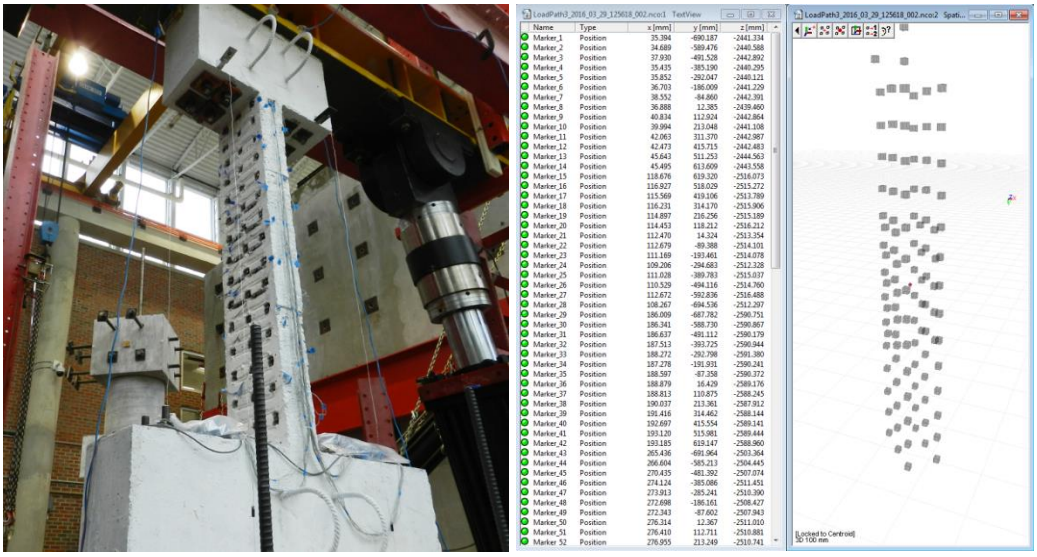

Figure A-52. Test 3: Instrumentation – Optotrak LEDs distribution on right face of the specimen and Spatial coordinate output

A total of 104 infrared LEDs from the optical tracking system Optotrak Certus developed by Northern Digital Inc. were placed directly on the steel reinforcement of the prism. The objective was to establish longitudinal and transverse strains in real time throughout a MATLAB code recently developed for this purpose at the CFL. Four additional infrared LEDs were positioned on the front face of the prism cap as a plane of reference. Figure A-52 shows the distribution of the LEDs on the right face of the prism and the overall allocation of the markers obtained from the Optotrak spatial coordinate output.

4. Test Summary

First, an out-of-plane displacement of 0.6 in., equivalent to 1% drift, was induced to specimen P1-P3 (Phase 1 – Prism 3). The purpose was to keep this displacement constant during the entire test, which in addition, included unsymmetrical cyclic axial compressive loads and tensile displacements. The axial displacement history started with elastic single cycles analytically predicted. The targets in tension were chosen as fractions of the yielding displacement referred as: $0.25\varepsilon_y$, $0.50\varepsilon_y$, and $0.75\varepsilon_y$. Including the axial yielding point, ε_y, three identical cycles at different axial tensile displacement ductility levels continued until buckling was captured upon compressive loading. The unique compressive target load, $P_{1\%}$ = -319 kips, was established considering P-Δ effects, representing 89% of the maximum axial design compressive load, Po = -358 kips, Figure A-53.

During the 0.6 in. lateral displacement, first cracks appeared on the bottom left (BL) and top right (TR) regions of the prism, Figure A-54. Strain profiles captured at this stage for each reinforcement line and for each face are displayed in Figure A-55, where the corresponding average has also been included. A total of 13 gages were established for each longitudinal bar along the 60 in. height, Y axis. As expected, maximum values close to 0.15% are observed in the BL and TR regions.

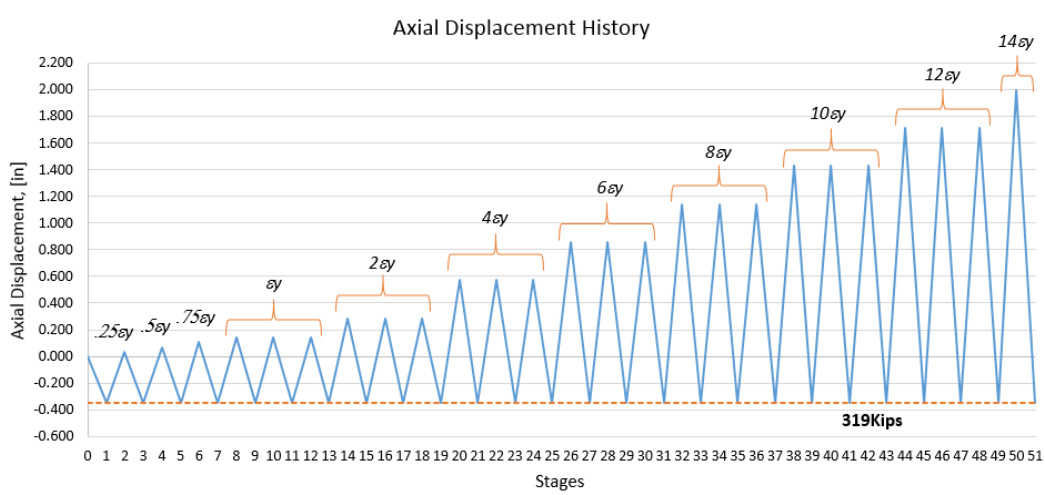

Figure A-53. Test 3: Axial Displacement History applied to specimen P1-P3

Figure A-54. Test 3: First cracks at 0.6 in. out-of-plane displacement

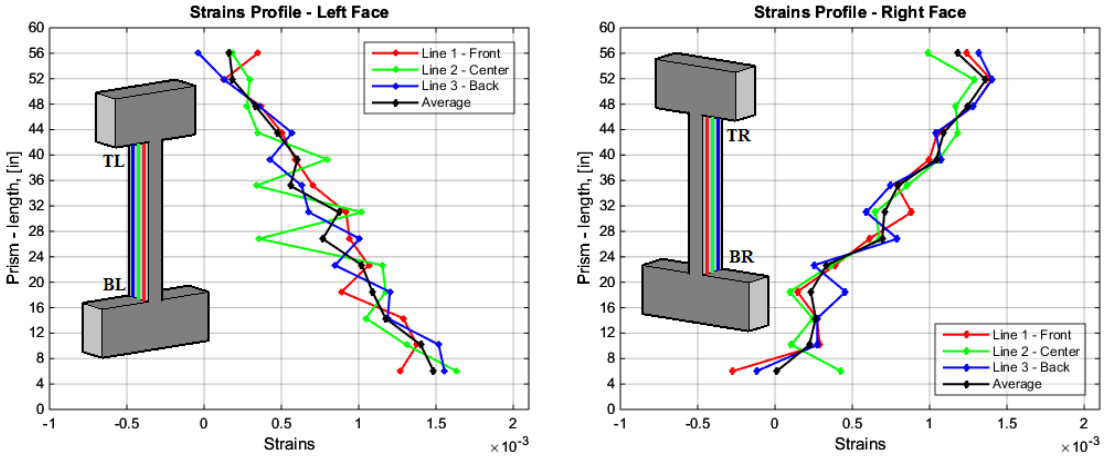

Figure A-55. Test 3: Strain profiles at 0.6 in. out-of-plane displacement

Subsequently, the first compressive load was induced to the specimen. A small vertical crack appeared in the concrete cover from the back face of the prism. Horizontal cracks became more numerous upon yielding tensile demands. Small cracks formed and extended to the beam-column connections. During the application of compressive loads, the cracks tended to close as expected. Crack propagations at cycles related to $1\varepsilon_y$ through $12\varepsilon_y$ appear in Figure A-56 through Figure A-62. Upon loading to $2\varepsilon_y$, more small cracks formed and extended to the beam-column connections. Crack widths close to 1/32 in. were captured at $2\varepsilon_y$. During the following cycles the cracks became wider and the number of new cracks decreased. It was noticed that the spacing of the horizontal cracks are induced by the spacing of the transverse reinforcement. Signs of concrete spalling on the back face of the prism were observed in the first cycle at $4\varepsilon_y$. Crack widths close to 0.05 in. and 0.075 in. were captured at $6\varepsilon_y$ and $8\varepsilon_y$, respectively. Cracks became wider than 0.10 in. for the $10\varepsilon_y$ and $12\varepsilon_y$ cycles. During tensile demands

at 14ε_y, concrete cover fell down on the back face of the prism and transverse reinforcement was exposed in different regions. At this time, debris was removed to protect the instrumentation, Figure A-63. The cracks became visibly wider than previous cycles.

Figure A-56. Test 3: Propagation of cracks at 1.0 εy

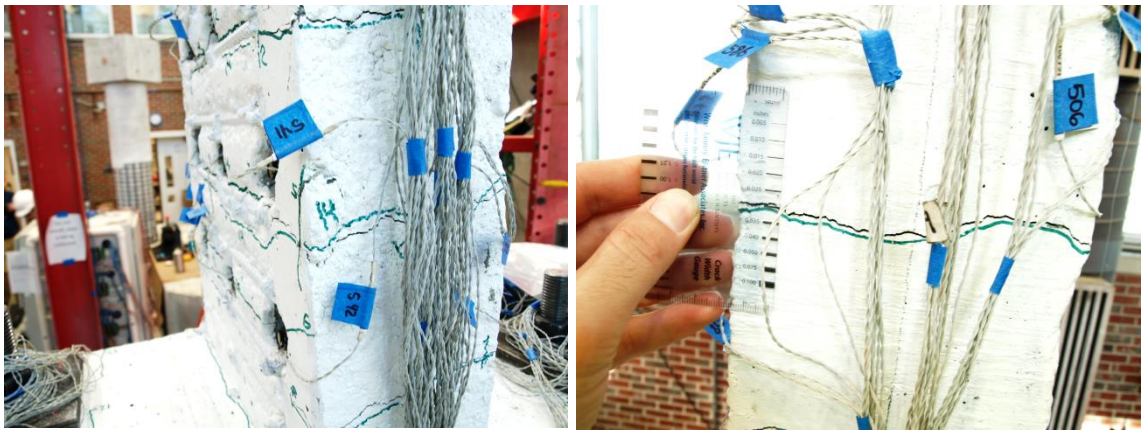

Figure A-57. Test 3: Propagation of cracks at 2.0 εy – First cycle

Figure A-58. Test 3: Propagation of cracks at 4.0 εy – First cycle

Figure A-59. Test 3: Propagation of cracks at 6.0 εy – First cycle

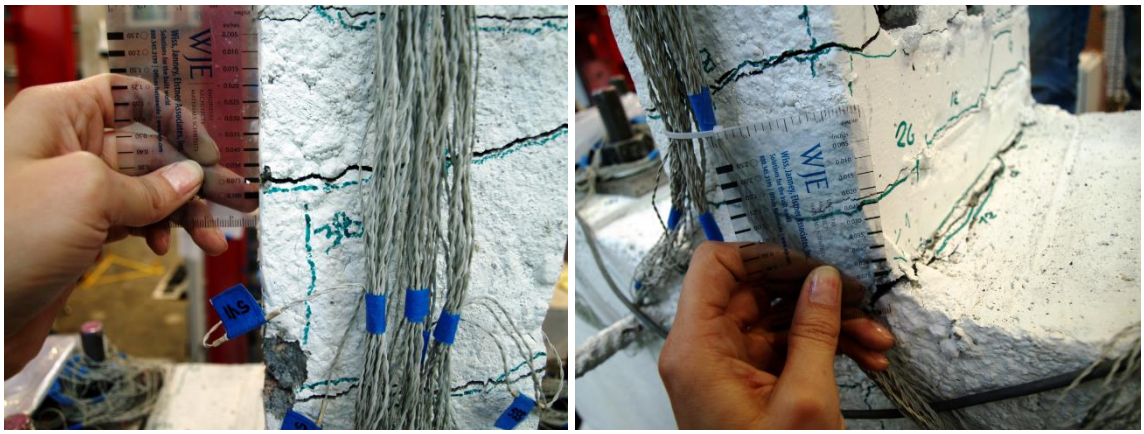

Figure A-60. Test 3: Propagation of cracks at 8.0 εy – First cycle

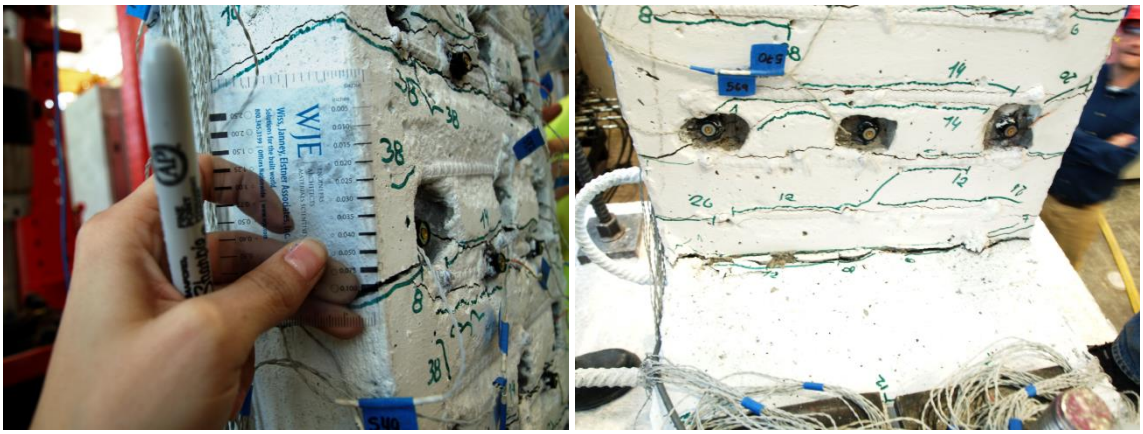

Figure A-61. Test 3: Propagation of cracks at 10.0 εy – First cycle

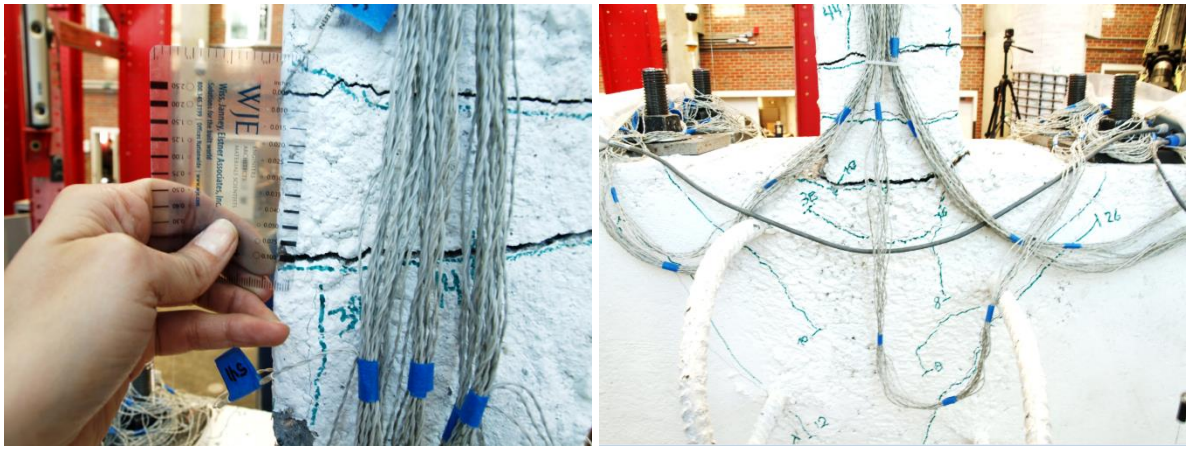

Figure A-62. Test 3: Propagation of cracks at 12.0 εy – First cycle

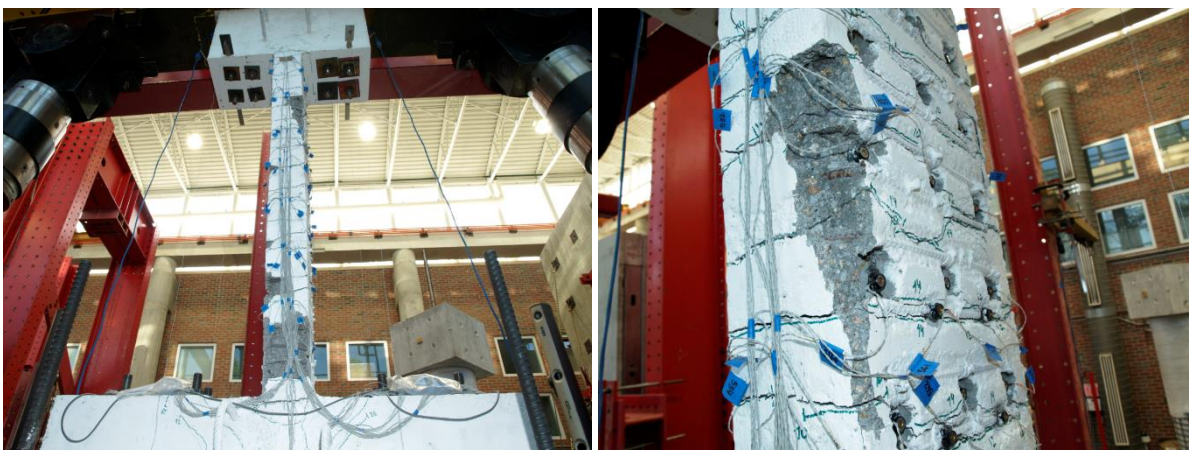

Figure A-63. Test 3: Propagation of cracks at 14.0 εy – First cycle

Throughout the first cycle related to $8\varepsilon_y$, out-of-plane buckling was visually captured upon compressive loading. This scenario, where the out-of-plane deformations were relatively small, was observed during the three cycles corresponding to $8\varepsilon_y$, $10\varepsilon_y$, and $12\varepsilon_y$. After experimenting these out-of-plane deformations, the prism returned to a fairly straight position when the cracks closed and consequently it was able to resist the intrinsic forces associated with compressive forces developed to sustain overturning moments.

However, in the first cycle associated with $14\varepsilon_y$ upon compressive loading, a different scenario was captured where instability occurred as illustrated in Figure A-64. The final state of the prism showing local concrete crushing at midheight, bottom right (BR) and top right (TR) regions is presented in Figure A-65. Notice a well confined concrete core at this phase. A plumb line was used in order to

identify the transverse curvature distribution along the height of the prism, Figure A-66. It was observed that the maximum normalized out-of-plane deformation, δ/b = 3.6in./5in., exceeded 0.5.

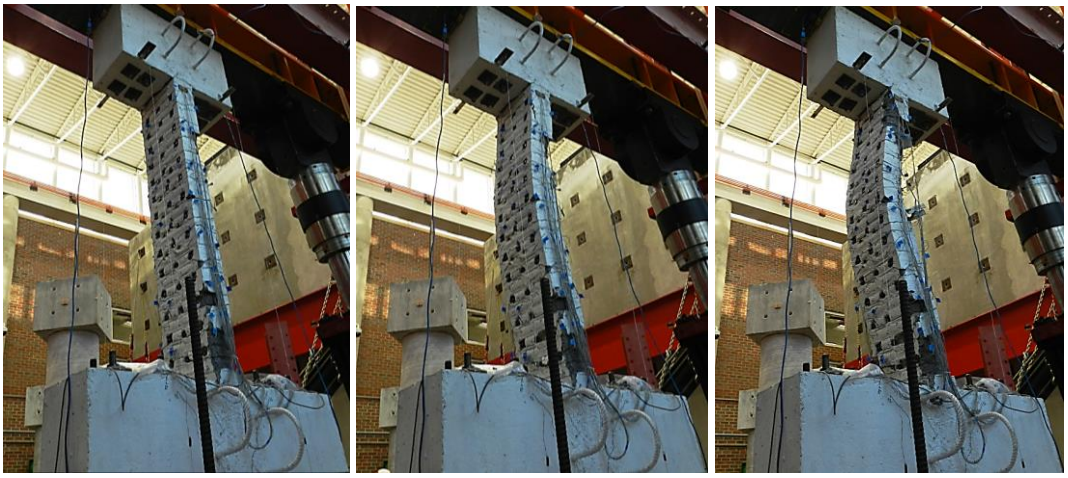

Figure A-64. Test 3: Evolution of instability developed under compression loading. First cycle for 14εy

Figure A-65. Test 3: Final state of prism P1-P3. Concrete crushing at midheight, bottom and top regions

Figure A-66. Test 3: Buckled shape of prism P1-P3

Figure A-67 depicts the entire structural response of P1-P3 as a function of axial forces and displacements. In the cycles where buckling started to be captured, the axial stiffness reduced significantly by the time the axial compressive load approaches 30% of the axial design compressive force, *Po* = -358 kips. These points were associated with the onset of out-of-plane buckling. Notice that the specimen is still extended. Due to the intrinsic eccentricity in the developed compressive force, one side of the wall end region closes first resulting in out-of-plane deformations. Once the cracks close, the prism gains stiffness and is able to carry the same axial load as in previous cycles. In the last cycle, instability was captured since the prism was not able to recover its strength. The maximum applied load at this stage was -210 kips, equivalent to 60% of *Po*, and 66% of the load applied in a previous cycle.

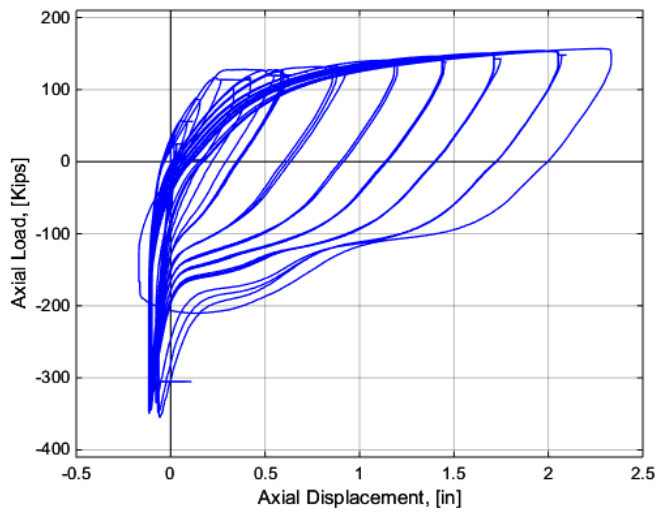

Figure A-67. Test 3: Axial structural response of prism P1-P3

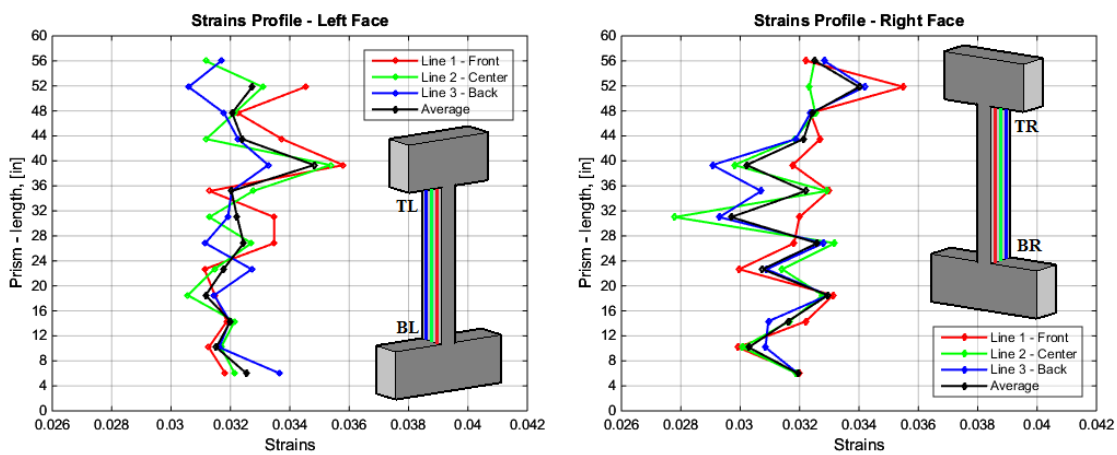

Figure A-68. Test 3: Strain profiles at 14 εy during the first cycle

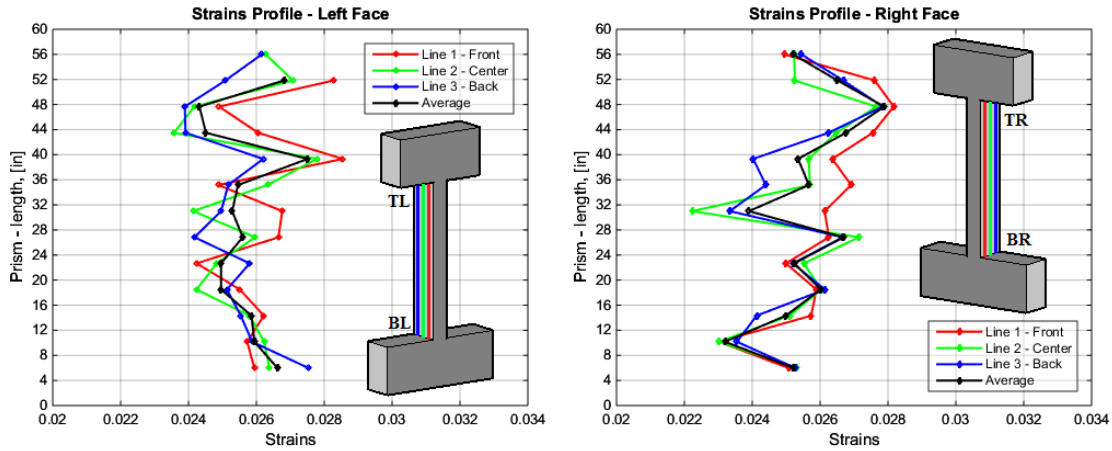

Figure A-69. Test 3: Strain profiles at onset of buckling during the last cycle

Strain profiles captured during the last tensile cycle are presented in Figure A-68. The average of the strains in both faces of the prism is approximately 3.2%, value close to the target at 14ε_y. Figure A-69 shows strain profiles of the onset of buckling during the last cycle upon compressive loads. The strains average is close to 2.6% in both faces.

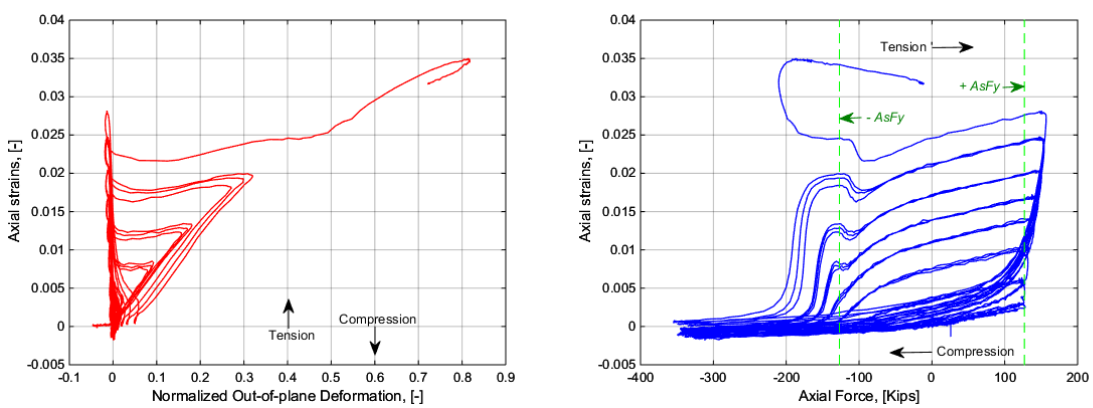

Figure A-70. Test 3: Response of specimen P1-P3 captured from a midheight gage on the right face

Figure A-70 illustrates the evolution of the nominal axial strain captured from gage 21 at the center of the specimen on the right face versus the normalized out-of-plane deformation. Notice a stable response of the prism at low levels of axial tensile strains. The normalized out-of-plane displacements increased upon compressive loading during the first cycle associated with 8ε_y. Throughout the first cycle of 12ε_y, the specimen suffered from a permanent out-of-plane deformation. A sudden increment on this deformation took place at the moment it reached a normalized value of 0.45 and the compression load was -144 kips, which represents 40% of the axial design compressive force, *Po*, and 45% of $P_{1\%}$ = -319 kips. Yielding forces, *AsFy*, in tension and compression are also plotted in Figure A-70, where *As* is the area of the longitudinal reinforcement.

5. Conclusions

Specimen P1-P3 was successfully tested during five hours where combined load patterns were applied. A lateral out-of-plane displacement equivalent to 1% drift was sustained during the entire test to analyze its influence on the stability of RC walls. The maximum tensile strain in BL and TR regions of the prism during the first stage, where axial loads were not induced, was close to 0.0015.

Subsequently, progressive cyclic axial loads/strains were applied to the specimen reaching maximum values fairly close to the targets $P_{1\%}$ = -319 kips and $14\varepsilon_y$, in compression and tension, respectively. The specimen presented a stable response at low levels of axial tensile demands. Out-of-plane deformations were not noticed during the cycles before $8\varepsilon_y$. Beyond the first cycle of $8\varepsilon_y$, a gradual increment in the out-of-plane deformations were captured until instability developed during the first cycle of $14\varepsilon_y$. The large buckling displacement led to concrete crushing and spalling in the central region. The axial force at this stage was 66% of the target compressive force.

Neither bar buckling nor bar fracture were detected during or after the test. The stirrups remained as originally constructed. Analysis of the data from this test will continue, as a consequence the material presented here should be considered preliminary. Further experiments will reveal more information about the effectiveness of the reinforcement detailing recommended in guidelines to prevent lateral instability in RC structural walls.

Stability of Ductile RC Structural Walls – Assessment of the Local Buckling Failure Mode

Test 4

April - 12 - 2016

Summary Report

Prepared for:

Alaska Department of Transportation

Prepared by:

RA – Ana Gabriela Haro

PIs – Mervyn Kowalsky and Rob Chai

North Carolina State University

Raleigh – NC

1. Executive Summary

Test 4 was conducted at the Constructed Facilities Laboratory on Thursday, April 12, 2016, as part of the load path project. The specimen was designed and built simulating boundary elements from prototype walls. A monotonic and constant lateral displacement equivalent to 4% drift was applied first to the specimen followed by cyclic axial compressive loads and tensile displacements to capture its structural performance and to determine additional critical parameters associated with lateral instability of RC walls. The first part of the results are presented in this report. Further analyses will be elaborated.

2. Introduction

Recent earthquakes in New Zealand and Chile have illustrated the importance of out-of-plane stability of concrete wall elements due to in-plane loading. Pier walls are occasionally employed by Alaska DOT for their in-plane lateral stiffness. While these walls are normally thicker than the walls typically found in building applications, their clear heights are also larger, giving rise to height-to-thickness ratios which may be larger than that of buildings. Some analyses have demonstrated that walls as thick as 20 in. may be prone to buckling, depending on their length and height.

Noticing the concentration of damage in the boundary elements of rectangular reinforced concrete structural walls due to higher stress and strain demands, some past investigations by others have been carried out on prisms, which was found to be an economical way to study the inelastic instability of structural walls. In general, the main objective of these tests focuses on subjecting specimens to cyclic tension and compression actions to simulate vertical components of actual seismic loading.

While past tests on prisms has shown existing models to be promising, missing from the models is the interaction with out-of-plane loading. The existing models correlate tensile strain from in plane loading to out-of-plane deformation, assuming a prescribed curvature distribution. If loading occurs in the out-of-plane direction, the relationship between tensile strain and out-of-plane deformations must be adjusted to reflect this. In its simplest form, this would be an addition of an out-of-plane displacement to the existing equation. However, out-of-plane displacement may impact the distribution of curvature with height, thus requiring additional adjustments to the models.

A total of 12 prisms are being experimentally tested in the Constructed Facilities Laboratory (CFL) during this project. The support conditions for the 12 prisms are conceived as fixed-fixed. The first testing phase will involve controlled load paths where the specimens are subjected to tension/compression cycles in addition to lateral loading to mimic the effects of out-of-plane displacements. In the second phase, longitudinal reinforcement ratios will be varied – between the two phases, reinforcement ratios will span the typical values employed by Alaska DOT for pier walls. The details associated with the two phases are presented in Table A-7.

This first phase consists of testing six 1/2-scale identical specimens. The thickness of the prisms is 5 in. since the cover was excluded from the construction. The geometry used is 5x12x60 in, corresponding to an aspect ratio (*h/b = height/thickness*) of 10 (including the missing cover). The longitudinal reinforcement ratio is 2.6% (6 bars #5). Transverse reinforcement consists of #3 diameter rebar spaced at 2 in. and was placed as shown in Figure A-71.

Table A-7. Test 4: Description of the experimental phases

Phase	Tests	Geometry	Reinforcement	Loading
1	6	Thickness and Height (based on prototype wall). (6”x12” ; actual geometry = 5”x12”)	Longitudinal (6bars#5) and transverse (#3@2in) reinforcement ratios similar for the 6 specimens.	Controlled 3D load path
2	6	Same as phase 1 (Based on actual pier walls formerly used by the Alaska DOT)	Longitudinal reinforcement ratio varies. (3 specimens 6bars#3 and 3 specimens 6bars#4)	Controlled 3D load path

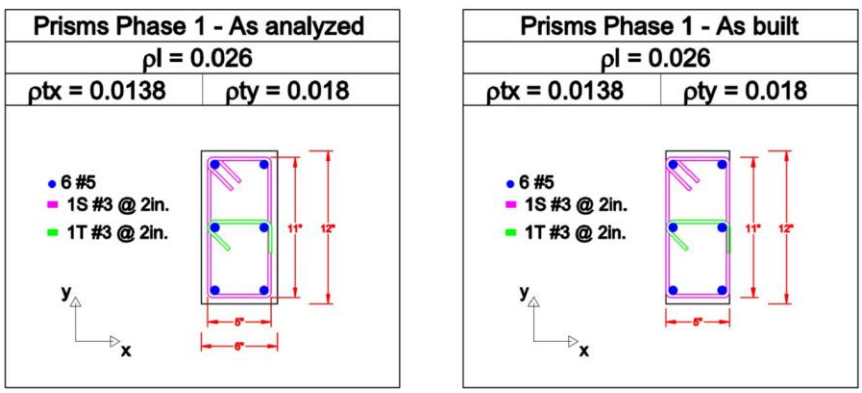

Figure A-71. Phase 1 - Cross section of the prisms

Table A-8. Test 4: Phase 1 - Steel tensile test properties for bars #3 and #5

Sample No.	Bar #	fy (ksi)	εy = fy/Es	fu (ksi)	εu
1	3	74.7	0.0026	103.3	0.0916
2	3	74.8	0.0026	100.6	0.0750
3	3	79.6	0.0027	105.0	0.0927
4	3	76.8	0.0026	103.4	0.0770
5	3	77.0	0.0027	103.3	0.0736
6	3	77.1	0.0027	103.2	0.1040
#3 Average		**76.7**	**0.0026**	**103.1**	**0.0856**
1	5	69.4	0.0024	96.4	0.1100
2	5	68.2	0.0024	95.6	0.1124
3	5	68.7	0.0024	97.7	0.0981
4	5	70.1	0.0024	97.4	0.1128
5	5	70.0	0.0024	98.0	0.1326
#5 Average		**69.3**	**0.0024**	**97.0**	**0.1132**

Regarding the material properties, an unconfined concrete strength of 5 ksi and reinforcement yielding strength of 60 ksi were considered as design values to define the experimental load history in compression. Actual values were used to calculate tensile demands. Table A-8 shows the actual steel tensile test properties for the #3 and #5 bars. The reinforcement detailing was established according to the ACI 318 and NEHERP guidelines for ductile columns and boundary elements.

3. Test Setup

The test setup consisted of a 14 ft long steel loading beam placed on the top of the specimen and connected to three actuators: two vertically inclined 440 kips actuators which induce axial loads and one horizontal 55 kips actuator to apply out-of-plane displacements. Two steel frames are used to restrain torsion in the loading beam. Two concrete blocks attached to the strong floor support the specimen to reach the required height associated with the effective length of the 440 kips actuators. Figure A-72 depicts the test setup drawings and Figure A-73 shows a picture of the area where the components of the project are placed.

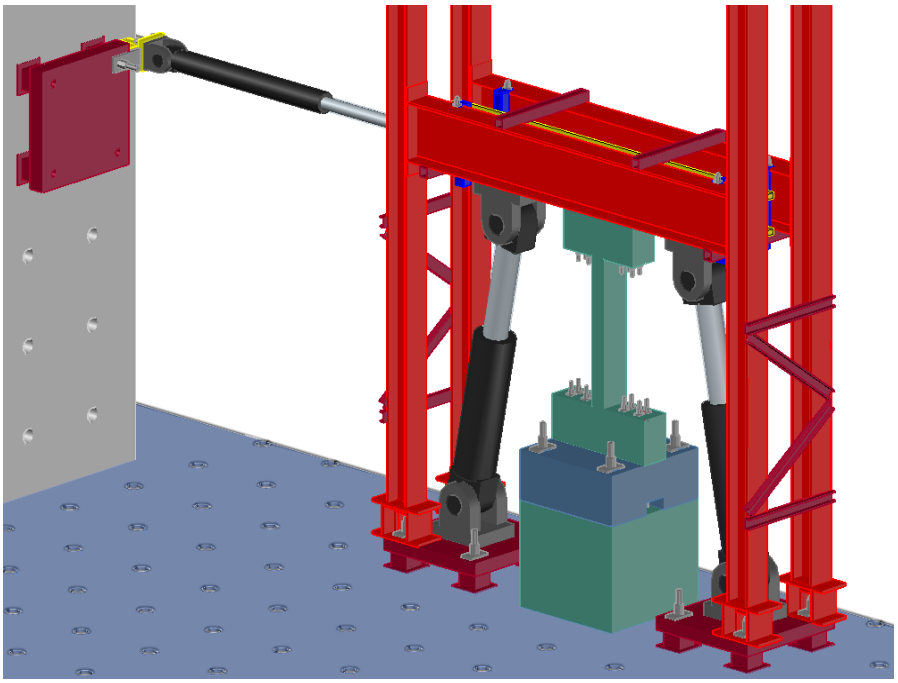

Figure A-72. Test 4: Test setup drawings

The horizontal actuator is controlled by displacements. The vertically inclined actuator located at the left hand side of the specimen, Figure A-72, is controlled by rotations captured throughout an inclinometer attached to the loading beam. The actuator placed at the right hand of the specimen is controlled by a combination of forces and displacements. Loads and strokes in the actuators are measured through integrated LVDTs and loads cells.

Figure A-73. Test 4: Test setup in the CFL at NC State

Relative displacements resulting from the interaction between the loading beam, the specimen, and the support concrete block were obtained through 4 linear potentiometers. In addition, axial deformations of the prism were registered through 4 string potentiometers. Another string potentiometer was used to capture the lateral displacement of the loading beam.

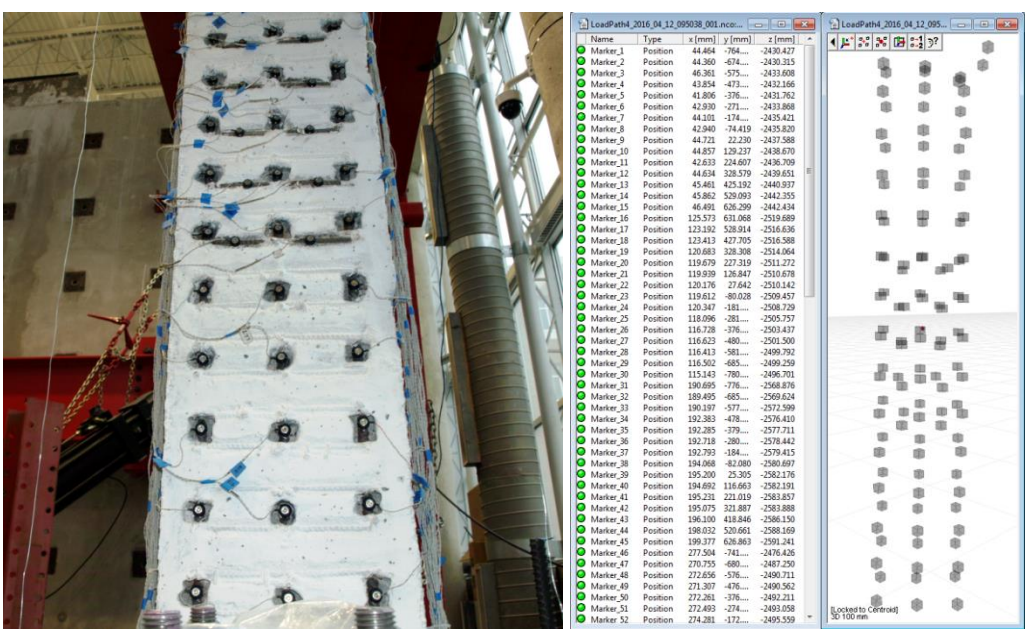

Figure A-74. Test 4: Instrumentation – Optotrak LEDs distribution on right face of the specimen and Spatial coordinate output

A total of 110 infrared LEDs from the optical tracking system Optotrak Certus developed by Northern Digital Inc. were placed directly on the steel reinforcement of the prism. The objective was to establish longitudinal and transverse strains in real time throughout a MATLAB code recently developed for this purpose at the CFL. Four additional infrared LEDs were positioned on the front face of the prism cap as a plane of reference. Figure A-74 shows the distribution of the LEDs on the right face of the prism and the overall allocation of the markers obtained from the Optotrak spatial coordinate output.

4. Test Summary

First, an out-of-plane displacement of 2.4 in., equivalent to 4% drift, was induced to specimen P1-P4 (Phase 1 – Prism 4). The purpose was to keep this displacement constant during the entire test, which in addition, included unsymmetrical cyclic axial compressive loads and tensile displacements. The axial displacement history started with elastic single cycles analytically predicted. The targets in tension were chosen as fractions of the yielding displacement referred as: $0.25\varepsilon_y$, $0.50\varepsilon_y$, and $0.75\varepsilon_y$ and $1.0\varepsilon_y$. Subsequently, three identical cycles at different axial tensile displacement ductility levels continued until buckling was captured upon compressive loading. The unique compressive target load, $P_{4\%}$ = -241 kips, was established considering P-Δ effects, representing 67% of the maximum axial design compressive load, Po = -358 kips, Figure A-75. The load $P_{4\%}$ was calculated following the linear interaction from Eq. (1).

$$P_{\%} = P_o - (P_O - P_b)\frac{M_{\%}}{M_b} \qquad (1)$$

where, P_b = 164 kips and M_b = 475 kip.in are the axial force and bending moment at balanced failure, respectively. The flexural moment at 4% out-of-plane drift ratio is $M_{4\%} = P_{4\%}(0.04*60in.)/2$. Substituting this expression in Eq. (1) and solving for $P_{4\%}$, the target value is obtained.

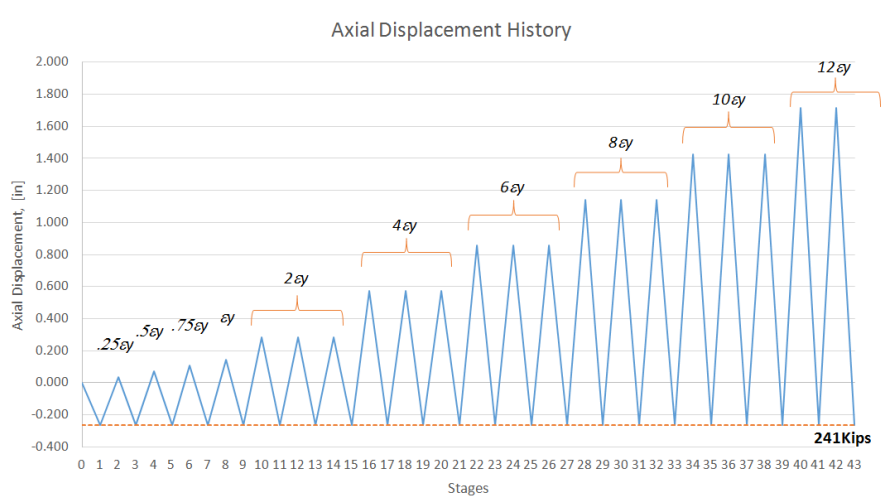

Figure A-75. Test 4: Axial Displacement History applied to specimen P1-P4

During the 2.4 in. lateral displacement, cracks appeared on the bottom left (BL) and top right (TR) regions of the prism, Figure A-76. Concrete spalling was also observed on the same regions. Strain profiles captured at this stage for each reinforcement line and for each face are displayed in Figure A-77, where the corresponding average has also been included. A total of 14 gages were established for each longitudinal bar along the 60 in. height, Y axis. Maximum values close to 0.4% and 1.5% are observed in the BL and TR regions, respectively.

Figure A-76. Test 4: Cracks at BL and TR regions at 2.4 in. out-of-plane displacement

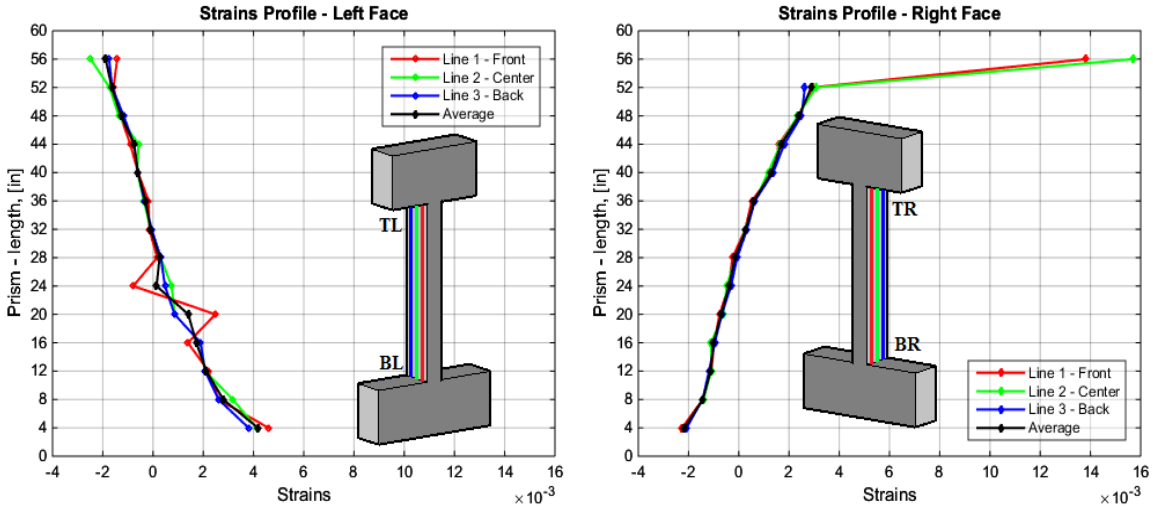

Figure A-77. Test 4: Strain profiles at 2.4 in. out-of-plane displacement

Subsequently, the first compressive load was induced to the specimen. Vertical cracks appeared in the concrete cover at TL and BR regions accompanied by concrete spalling. In general, upon yielding tensile demands, horizontal cracks became more numerous and small cracks formed and extended to the beam-column connections. During the application of compressive loads, the cracks tended to close

only in the central region of the prism. Once again, it was noticed that the spacing of the horizontal cracks are induced by the spacing of the transverse reinforcement.

Crack propagations at cycles related to $1\varepsilon_y$ through $12\varepsilon_y$ appear in Figure A-78 through Figure A-85. Crack widths between 1/32 in. and 3/64 in. were captured close to the joints at $1\varepsilon_y$. Concrete spalling became more severe at TL and BR regions where the damage was concentrated. On the central region, crack widths close to 1/32 in. were captured at $2\varepsilon_y$. During the first cycle associated with $4\varepsilon_y$ cracks widths close to 1/16 in. were observed on the BL and TR regions, and new cracks formed on the central region. In the following cycles the number of new cracks decreased. Through tensile demands at $6\varepsilon_y$, crack widths close to 0.075 in. were measured on the central region. Concrete flacking and concrete spalling propagated approximately 8 in. on TL and BR regions, which became more severe during the following cycles.

Figure A-78. Test 4: Propagation of damage at first compression

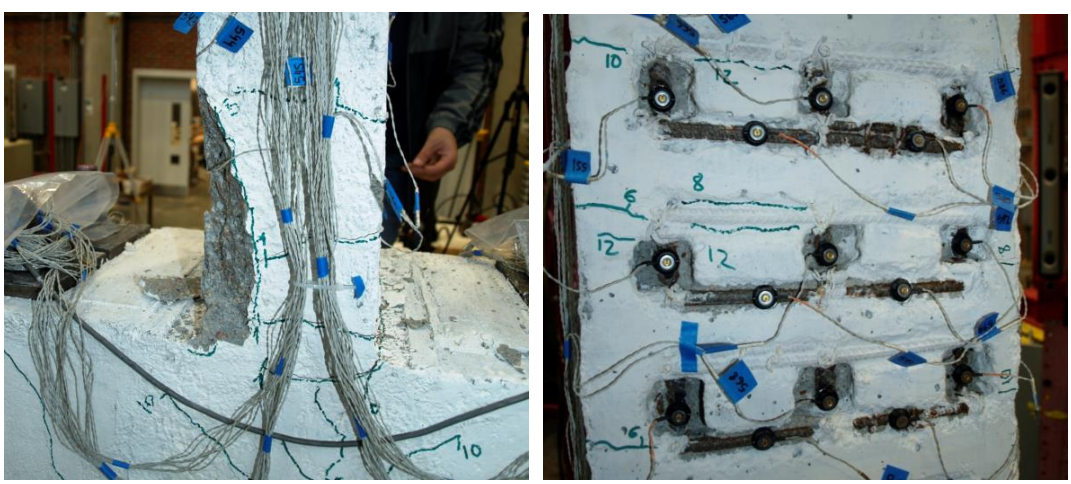

Figure A-79. Test 4: Propagation of damage at 1.0 εy – First cycle

Figure A-80. Test 4: Propagation of cracks at 2.0 εy – First cycle

Figure A-81. Test 4: Propagation of cracks at 4.0 εy – First cycle

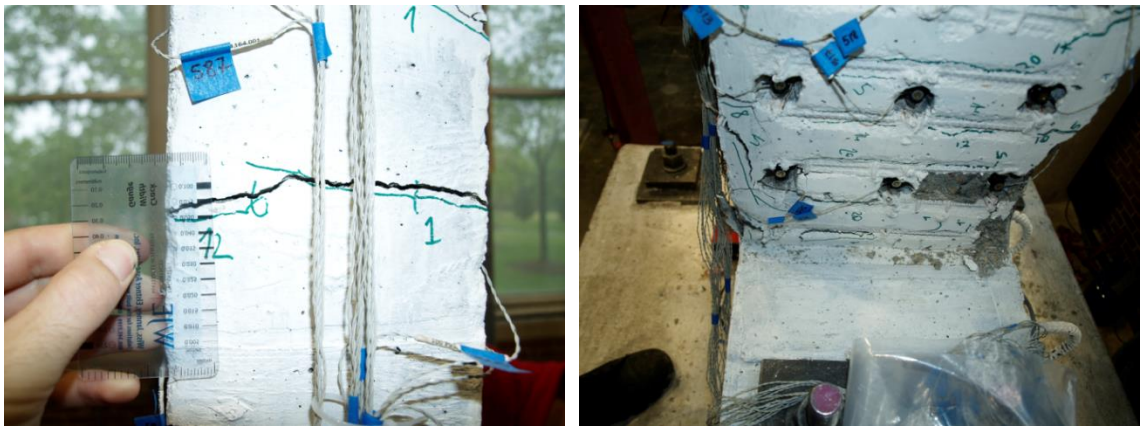

Figure A-82. Test 4: Propagation of damage at 6.0 εy – First cycle

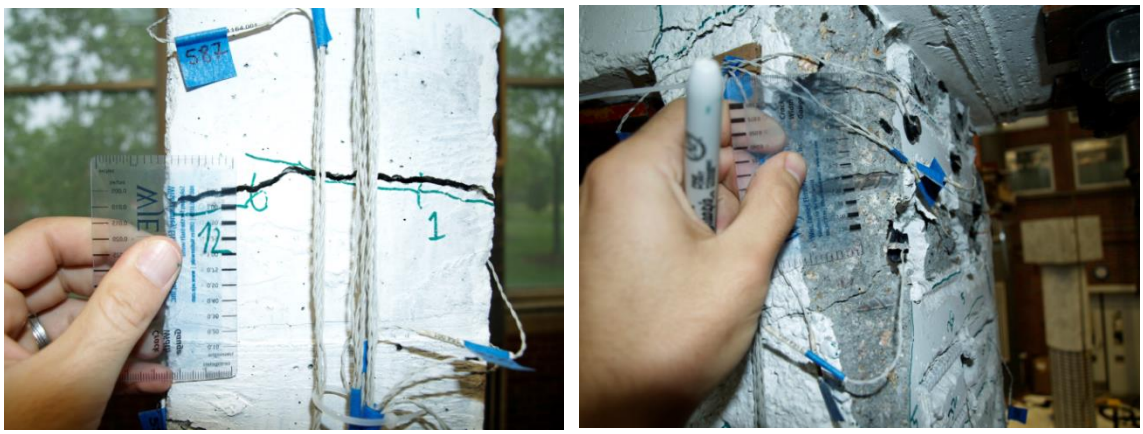

Figure A-83. Test 4: Propagation of damage at 8.0 εy – First cycle

Figure A-84. Test 4: Propagation of cracks at 10.0 εy – First cycle

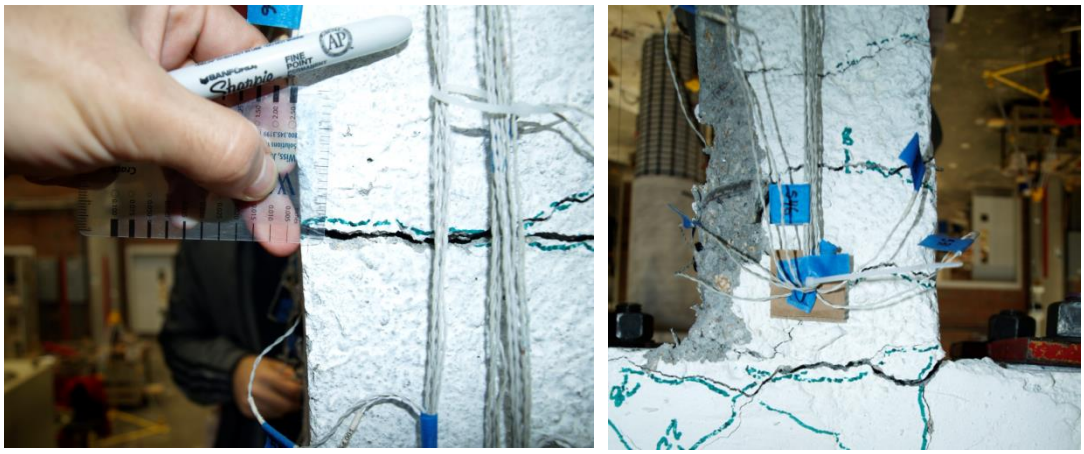

Figure A-85. Test 4: Propagation of cracks at 12.0 εy – First cycle

Upon the $8\varepsilon_y$ first cycle, crack widths close to 0.10 in. were measured in the central region. Concrete cover continued to fall down on the TL and BR regions and consequently transverse reinforcement was exposed on the corners. The cracks became visibly wider than previous cycles and close to 1/8 in. beyond the $10\varepsilon_y$ cycles.

During the first cycle related to $10\varepsilon_y$, out-of-plane buckling was visually captured upon compressive loading. This scenario, where the out-of-plane deformations were relatively small, was observed during the three cycles corresponding to $10\varepsilon_y$. After experimenting these out-of-plane deformations, the prism returned to a fairly straight position when the cracks closed and consequently it was able to resist the intrinsic forces associated with compressive forces developed to sustain overturning moments.

However, in the first cycle associated with $12\varepsilon_y$ upon compressive loading, a different scenario was captured. Even though the prism was able to carry the same level of compressive loads achieved in previous cycles, it preserved a deformed but stable shape. It was in the second cycle where instability occurred as illustrated in Figure A-86. The final state of the prism showing local concrete crushing at midheight, bottom right (BR) and top right (TR) regions is presented in Figure A-87. Notice a well confined concrete core at this phase.

Figure A-86. Test 4: Instability developed under compression loading. Second cycle for 12εy

Figure A-87. Test 4: Final state of prism P1-P4. Concrete crushing at midheight, bottom and top regions

Figure A-88 depicts the entire structural response of P1-P4 as a function of axial forces and displacements. In the cycles where buckling started to be captured, the axial stiffness reduced significantly by the time the axial compressive load approaches 30% of the axial design compressive force, *Po* = -358 kips, phenomenon also captured for P1-P2 and P1-P3. These points are associated with the onset of out-of-plane buckling. Notice that the specimen is still extended. Due to the intrinsic eccentricity in the developed compressive force, one side of the wall end region closes first resulting in out-of-plane deformations. Once the cracks close, the prism gains stiffness and is able to carry the same axial load as in previous cycles. In the last cycle, instability was captured since the prism was not able to recover its strength. The maximum applied load at this stage was -208 kips, equivalent to 58% of *Po*, and 86% of the load applied in a previous cycle.

Strain profiles captured during the last tensile cycle are presented in Figure A-89. The average of the strains in both faces of the prism is approximately 2.5%, value close to the target at $12\varepsilon_y$. Figure A-90 shows strain profiles of the onset of buckling during the last cycle upon compressive loads. The strains average is close to 2.3% in both faces. However, notice higher values on BL and TR regions due to the influence of the constant out-of-plane displacement applied to the specimen.

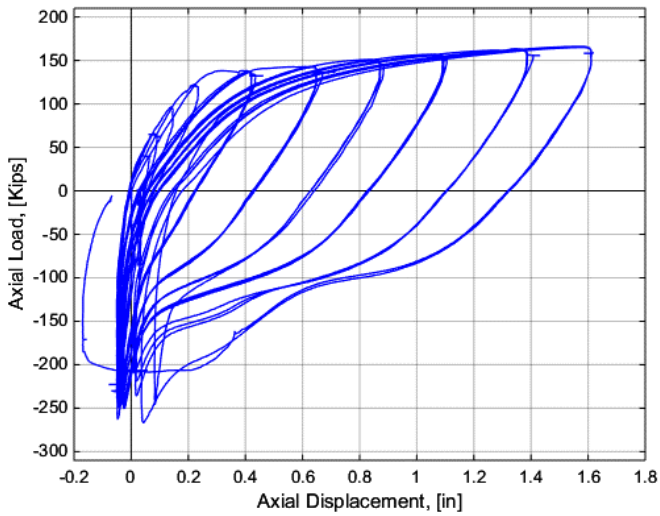

Figure A-88. Test 4: Axial structural response of prism P1-P4

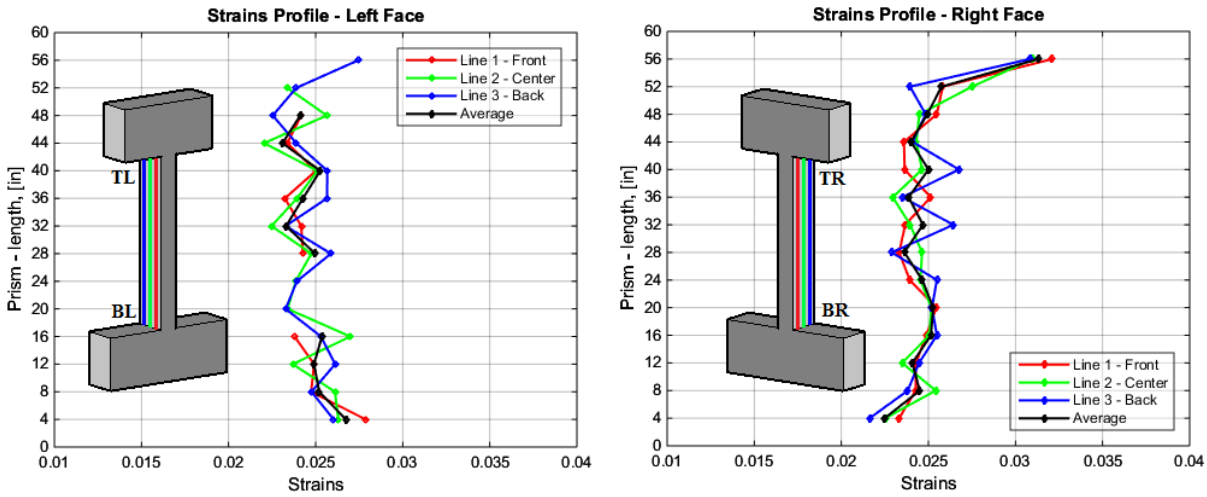

Figure A-89. Test 4: Strain profiles at 12 εy during the second cycle

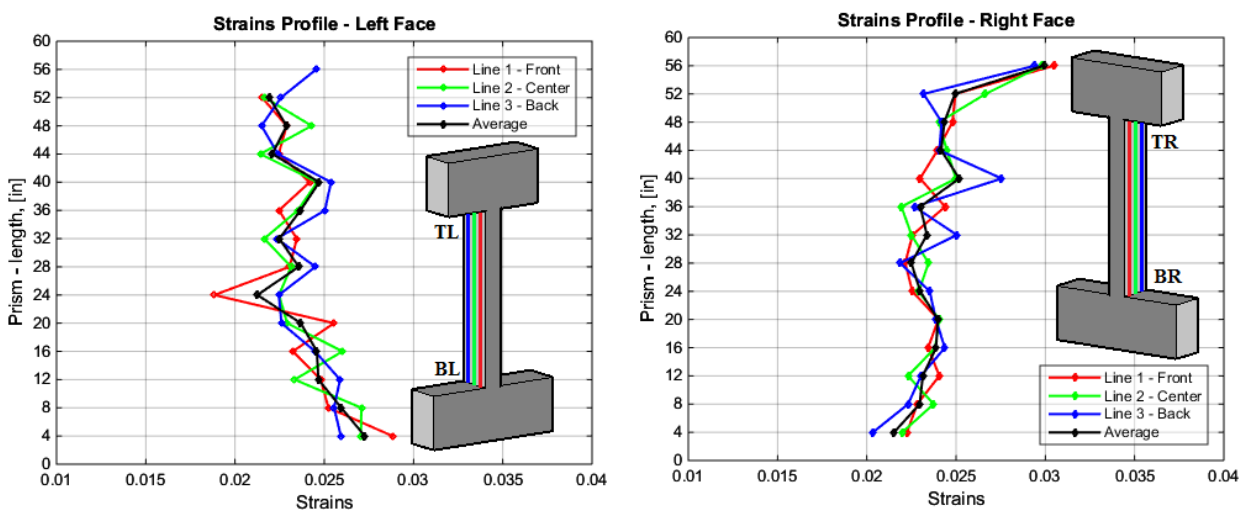

Figure A-90. Test 4: Strain profiles at onset of instability

Figure A-91 illustrates the evolution of the nominal axial strain captured from gage 22 at the center of the specimen on the right face versus the normalized out-of-plane deformation and the axial force. The maximum compression strain reached a value of -4.3%.

Figure A-92 shows the variation of strains computed from gage 67 located on the center of the prism on the left face. The maximum tensile strain is 2.9%.The onset of instability is captured at the time the normalized out-of-plane displacement exceeds negative 0.14. Notice a stable response of the prism at low levels of axial tensile strains.

The normalized out-of-plane displacements increased upon compressive loading during the first cycle associated with $10\varepsilon_y$. Throughout the first cycle of $12\varepsilon_y$, the specimen suffered from a slight permanent out-of-plane deformation. A sudden increment on this deformation took place during the second cycle at the moment the compression load was -162 kips, which represents 45% of the axial design

compressive force, *Po*, and 67% of $P_{4\%}$ = -241 kips. Yielding forces, *AsFy*, in tension and compression are also plotted in Figure A-91 and Figure A-92, where *As* is the area of the longitudinal reinforcement.

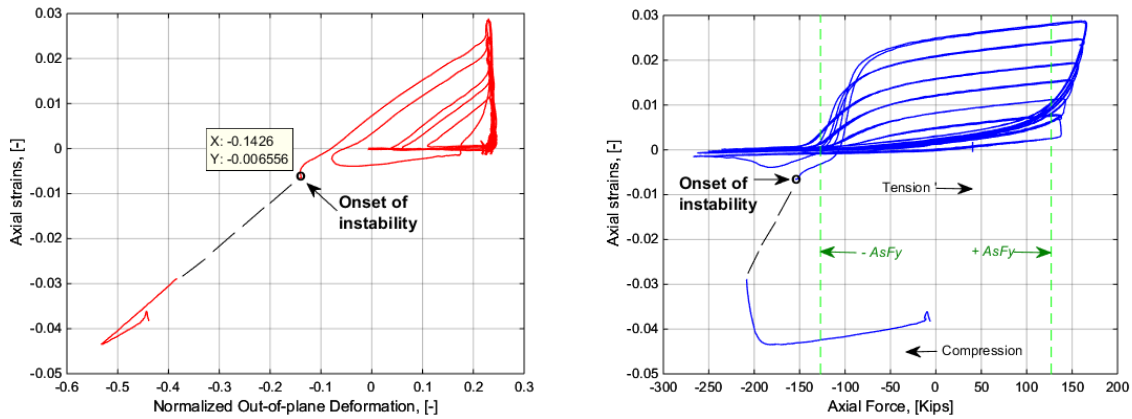

Figure A-91. Test 4: Response of specimen P1-P4 captured from a midheight gage on the right face

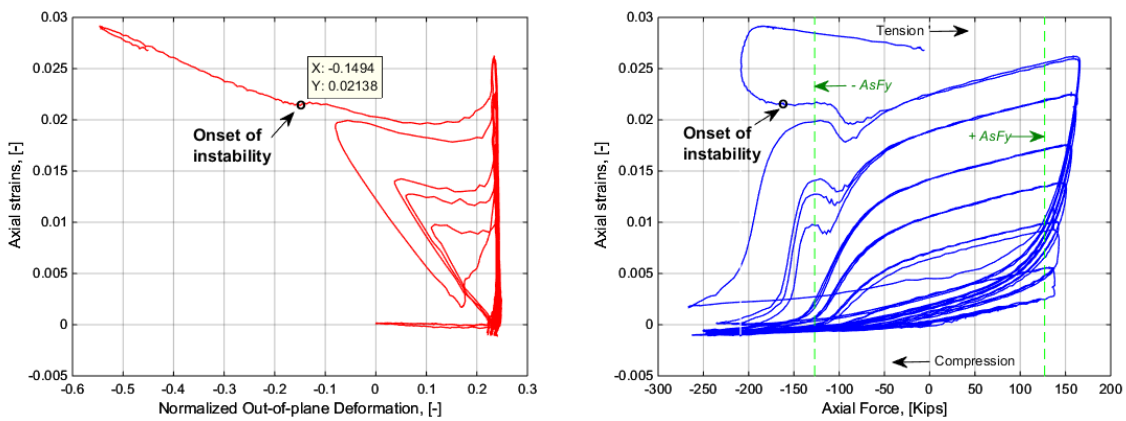

Figure A-92. Test 4: Response of specimen P1-P4 captured from a midheight gage on the left face

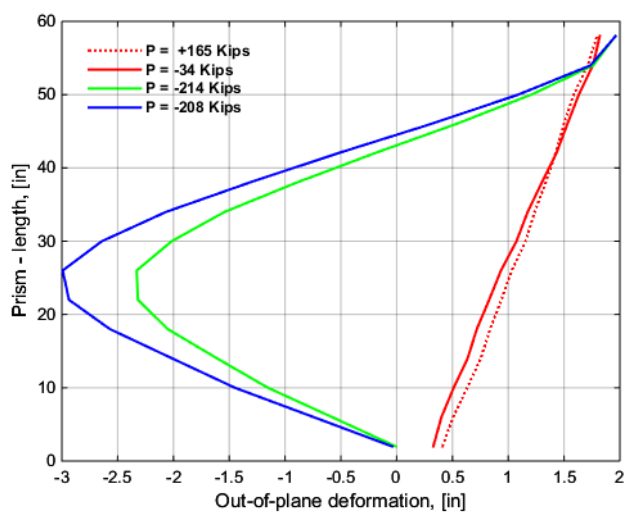

Figure A-93. Test 4: Evolution of the buckling shape during the last cycle under compressive loads

The evolution of the buckling shape during the last cycle of the test when the prism was subjected to compressive forces is plotted in Figure A-93. Four stages were considered: maximum tensile demand, onset of buckling, zero axial displacement, and maximum compressive load. It can be observed that the maximum out-of-plane deformation is 3.0 in. located 4 in. below midheight.

5. Conclusions

Specimen P1-P4 was successfully tested during five hours where combined load patterns were applied. A lateral out-of-plane displacement equivalent to 4% drift was sustained during the entire test to analyze its influence on the stability of RC walls. The maximum tensile strain in BL and TR regions of the prism during the first stage, where axial loads were not induced, was close to 0.004 and 0.015, respectively.

Subsequently, progressive cyclic axial loads/strains were applied to the specimen reaching maximum values fairly close to the targets $P_{4\%}$ = -241 kips and $12\varepsilon_y$, in compression and tension, respectively. The specimen presented a stable response at low levels of axial tensile demands. Out-of-plane deformations were not noticed during the cycles before $10\varepsilon_y$. Beyond the first cycle of $10\varepsilon_y$, a gradual increment in the out-of-plane deformations were captured until instability developed during the second cycle of $12\varepsilon_y$. The large buckling displacement led to concrete crushing and spalling in the central, TR, and BL regions. The axial force at this stage was 86% of the compressive force in the previous cycle.

Neither bar buckling nor bar fracture were detected during or after the test. The stirrups remained as originally constructed. Analysis of the data from this test will continue, as a consequence the material presented here should be considered preliminary. Further experiments will reveal more information about the effectiveness of the reinforcement detailing recommended in guidelines to prevent lateral instability in RC structural walls.

Stability of Ductile RC Structural Walls – Assessment of the Local Buckling Failure Mode

Test 5

June - 07 - 2016

Summary Report

Prepared for:

Alaska Department of Transportation

Prepared by:

RA – Ana Gabriela Haro

PIs – Mervyn Kowalsky and Rob Chai

North Carolina State University

Raleigh – NC

1. Executive Summary

Test 5 was conducted at the Constructed Facilities Laboratory on Thursday, June 7, 2016, as part of the load path project. The specimen was designed and built simulating boundary elements from prototype walls. A combination of cyclic lateral displacements and cyclic axial compressive loads and tensile displacements were applied to the specimen to capture its structural performance and to determine additional critical parameters associated with lateral instability of RC walls. The first part of the results are presented in this report. Further analyses will be elaborated.

2. Introduction

Recent earthquakes in New Zealand and Chile have illustrated the importance of out-of-plane stability of concrete wall elements due to in-plane loading. Alaska DOT occasionally employs pier walls because of their in-plane lateral stiffness. While these walls are normally thicker than the walls typically found in building applications, their clear heights are also larger, giving rise to height-to-thickness ratios which may be larger than that of buildings. Some analyses have demonstrated that walls as thick as 20 in. may be prone to buckling, depending on their length and height.

Noticing the concentration of damage in the boundary elements of rectangular reinforced concrete structural walls due to higher stress and strain demands, some past investigations by others have been carried out on prisms, which was found to be an economical way to study the inelastic instability of structural walls. In general, the main objective of these tests focuses on subjecting specimens to cyclic tension and compression actions to simulate vertical components of actual seismic loading.

While past tests on prisms has shown existing models to be promising, missing from the models is the interaction with out-of-plane loading. The existing models correlate tensile strain from in plane loading to out-of-plane deformation, assuming a prescribed curvature distribution. If loading occurs in the out-of-plane direction, the relationship between tensile strain and out-of-plane deformations must be adjusted to reflect this. In its simplest form, this would be an addition of an out-of-plane displacement to the existing equation. However, out-of-plane displacement may impact the distribution of curvature with height, thus requiring additional adjustments to the models.

A total of 12 prisms are being experimentally tested in the Constructed Facilities Laboratory (CFL) during this project. The support conditions for the 12 prisms are conceived as fixed-fixed. The first testing phase will involve controlled load paths where the specimens are subjected to tension/compression cycles in addition to lateral loading to mimic the effects of out-of-plane displacements. In the second phase, longitudinal reinforcement ratios will be varied – between the two phases, reinforcement ratios will span the typical values employed by Alaska DOT for pier walls. The details associated with the two phases are presented in Table A-9.

This first phase consists of testing six 1/2-scale identical specimens. The thickness of the prisms is 5 in. since the cover was excluded from the construction. The geometry used is 5x12x60 in, corresponding to an aspect ratio (*h/b = height/thickness*) of 10 (including the missing cover). The longitudinal reinforcement ratio is 2.6% (6 bars #5). Transverse reinforcement consists of #3 diameter rebar spaced at 2 in. and was placed as shown in Figure A-94.

Table A-9. Test 5: Description of the experimental phases

Phase	Tests	Geometry	Reinforcement	Loading
1	6	Thickness and Height (based on prototype wall). (6”x12” ; actual geometry = 5”x12”)	Longitudinal (6bars#5) and transverse (#3@2in) reinforcement ratios similar for the 6 specimens.	Controlled 3D load path
2	6	Same as phase 1 (Based on actual pier walls formerly used by the Alaska DOT)	Longitudinal reinforcement ratio varies. (3 specimens 6bars#3 and 3 specimens 6bars#4)	Controlled 3D load path

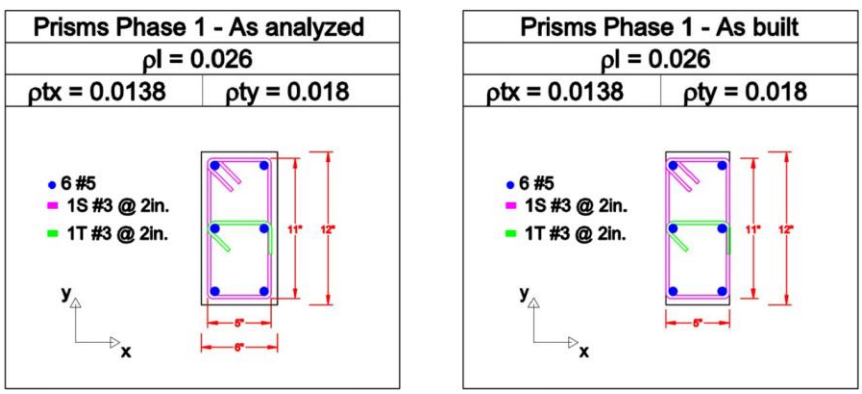

Figure A-94. Test 5: Phase 1 - Cross section of the prisms

Table A-10. Test 5: Phase 1 - Steel tensile test properties for bars #3 and #5

Sample No.	Bar #	fy (ksi)	εy = fy/Es	fu (ksi)	εu
1	3	74.7	0.00258	103.3	0.0916
2	3	74.8	0.00258	100.6	0.0750
3	3	79.6	0.00274	105.0	0.0927
4	3	76.8	0.00265	103.4	0.0770
5	3	77.0	0.00265	103.3	0.0736
6	3	77.1	0.00266	103.2	0.1040
#3 Average		**76.7**	**0.00264**	**103.1**	**0.0856**
1	5	69.4	0.00239	96.4	0.1100
2	5	68.2	0.00235	95.6	0.1124
3	5	68.7	0.00237	97.7	0.0981
4	5	70.1	0.00242	97.4	0.1128
5	5	70.0	0.00242	98.0	0.1326
#5 Average		**69.3**	**0.00239**	**97.0**	**0.1132**

Regarding the material properties, an unconfined concrete strength of 5 ksi and reinforcement yielding strength of 60 ksi were considered as design values to define the experimental load history in compression. Actual values were used to calculate tensile demands. Table A-10 shows the actual steel tensile test properties for the #3 and #5 bars. The reinforcement detailing was established according to the ACI 318 and NEHERP guidelines for ductile columns and boundary elements.

3. Test Setup

The test setup consisted of a 14 ft long steel loading beam placed on the top of the specimen and connected to three actuators: two vertically inclined 440 kips actuators which induce axial loads and one horizontal 55 kips actuator to apply out-of-plane displacements. Two steel frames are used to restrain torsion in the loading beam. Two concrete blocks attached to the strong floor support the specimen to reach the required height associated with the effective length of the 440 kips actuators. Figure A-95 depicts the test setup drawings and Figure A-96 shows a picture of the area where the components of the project were placed.

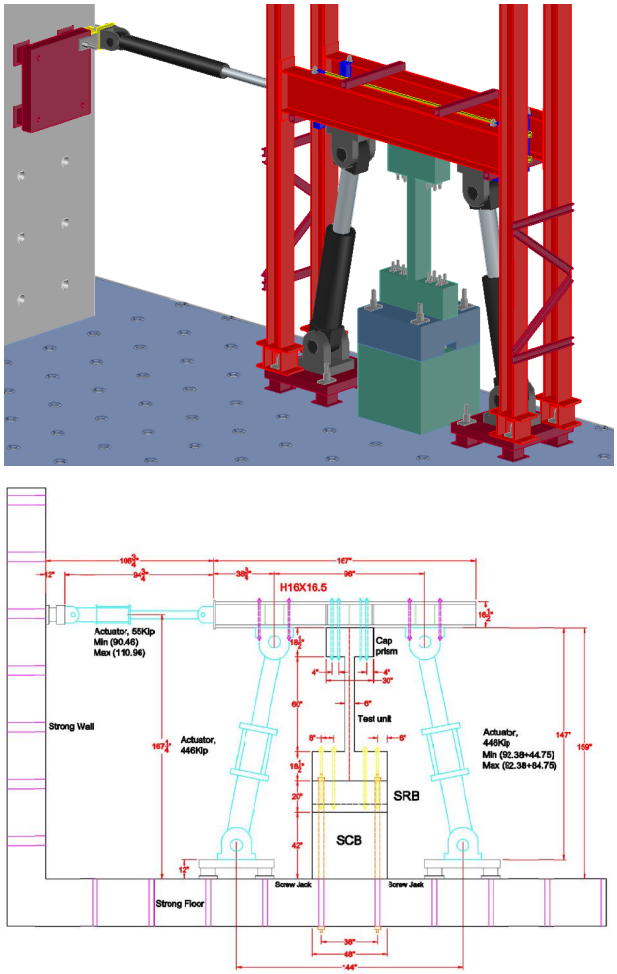

Figure A-95. Test 5: Test setup drawings

Figure A-96. Test 5: Test setup in CFL at NC State

The horizontal actuator is controlled by displacements. The vertically inclined actuator located at the left hand side of the specimen, Figure A-95, is controlled by rotations captured throughout an inclinometer attached to the loading beam. The actuator placed at the right hand of the specimen is controlled by a combination of forces and displacements. Loads and strokes in the actuators are measured through integrated LVDTs and loads cells.

Relative displacements resulting from the interaction between the loading beam, the specimen, and the support concrete block were obtained through 4 linear potentiometers. In addition, axial deformations of the prism were registered through 4 string potentiometers. Another string potentiometer was used to capture the lateral displacement of the loading beam.

A total of 110 infrared LEDs from the optical tracking system Optotrak Certus developed by Northern Digital Inc. were placed directly on the steel reinforcement of the prism. The objective was to establish longitudinal and transverse strains in real time throughout a MATLAB code recently developed for this purpose at the CFL, named “REALSTRAIN”. Four additional infrared LEDs were positioned on the front face of the prism cap as a plane of reference. Figure A-97 shows the distribution of the LEDs on the right face of the prism and the overall allocation of the markers obtained from the Optotrak spatial coordinate output.

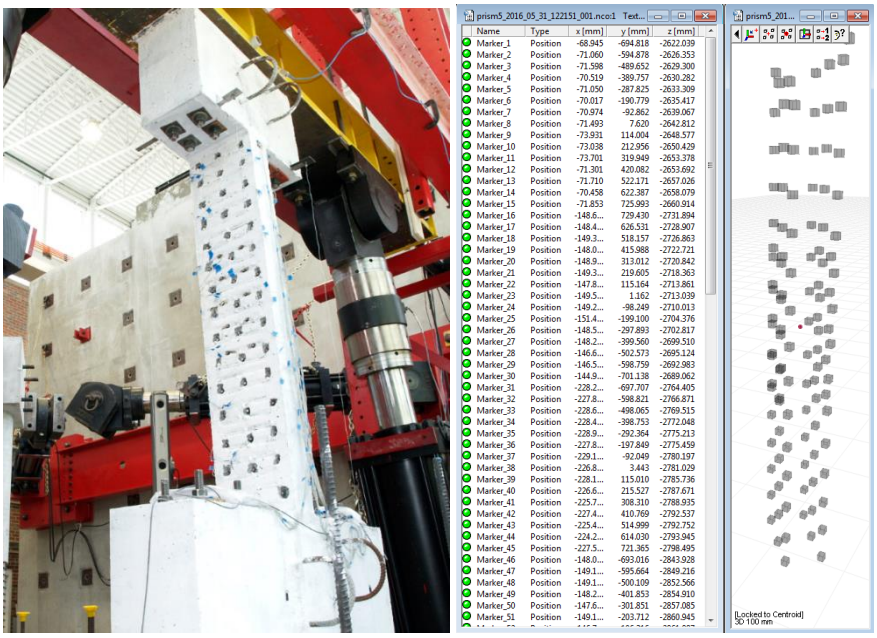

Figure A-97. Test 5: Instrumentation – Optotrak LEDs distribution on right face of the specimen and Spatial coordinate output

4. Test Summary

Specimen P1-P5 (Phase 1 – Prism 5) was subjected to cyclic out-of-plane displacements combined with cyclic axial tensile displacements and compressive loads. The axial displacement history started with elastic single cycles analytically predicted. The targets regarding the out-of-plane displacements were established as ratios of a maximum 4% drift, Figure A-98. In relation to the axial demands, the peak values in tension were chosen as fractions of the yielding strain referred as: $0.25\varepsilon_y$, $0.50\varepsilon_y$, and $0.75\varepsilon_y$ and $1.0\varepsilon_y$. Subsequently, three identical cycles at different axial tensile displacement ductility levels continued until buckling was captured upon compressive loading. The compressive target loads, $P_{\%}$, were established considering P-Δ effects, representing different percentages of the maximum axial design compressive load, Po = -358 kips. The load $P_{\%}$ was calculated following the linear interaction from Eq. (1).

$$P_{\%} = P_o - (P_O - P_b)\frac{M_{\%}}{M_b} \qquad (1)$$

where, P_b = 164 kips and M_b = 475 kip.in are the axial force and bending moment at balanced failure, respectively. The flexural moment at different out-of-plane drift values is $M_{\%} = P_{\%}(Drift_{\%}*60in.)/2$. Substituting this expression in Eq. (1) and solving for $P_{\%}$, the target values are obtained. Figure A-99 displays the intended axial history considered for specimen P1-P5. Notice the different values reached in compression due to the analysis mentioned above.

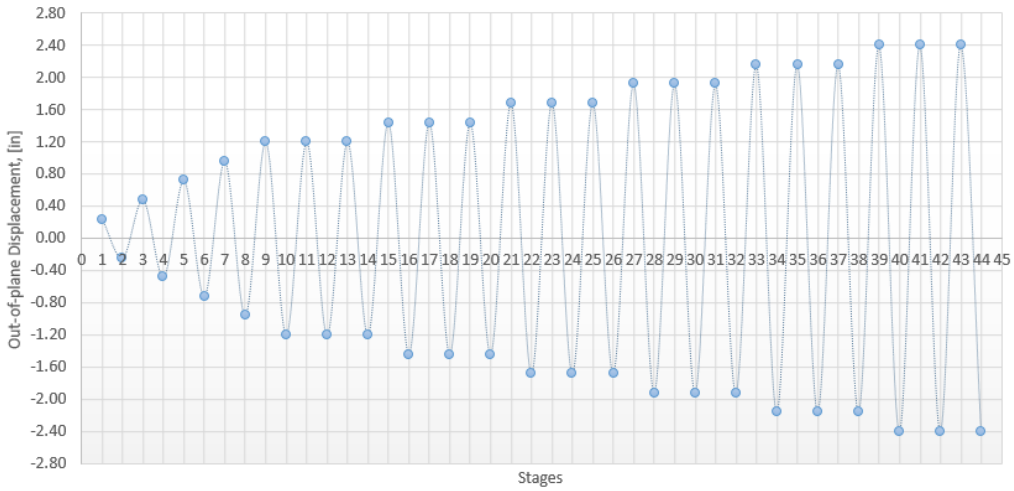

Figure A-98. Test 5: Intended Out-of-Plane Displacement History considered for specimen P1-P5

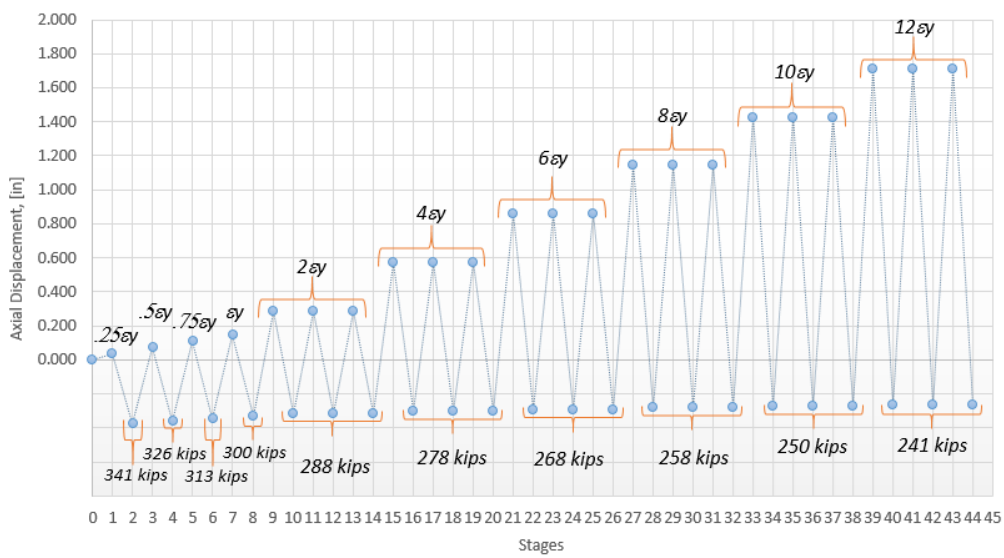

Figure A-99. Test 5: Intended Axial Displacement and Load History considered for specimen P1-P5

During the elastic cycles regarding the tensile demands and up to +0.96 in. in the out-of-plane direction, cracks propagated along the height of the prism and the joints. Figure A-100 shows part of the damage captured at this stage. Concrete flacking was also observed on the interface between the prism and the joints. Crack widths close to 1/16 in. were measured at TR (top right) and BL (bottom left) regions. Strain profiles captured at this stage for each reinforcement line and for each face are displayed in Figure A-101, where the corresponding average has also been included. A total of 14 gages were established for each longitudinal bar along the 60 in. height, Y axis. Tensile strains close to 0.3% are observed in the BL and TR regions. Figure A-102 shows the strain profiles captured during stage 8 where the axial compressive load applied to the specimen reached a value of 300 kips and the out-of-plane displacement was -0.96 in. Horizontal cracks formed in the previous cycle closed at this stage.

Figure A-100. Test 5: Propagation of damage at 1.0 εy (axial) and +0.96 in. (out-of-plane)

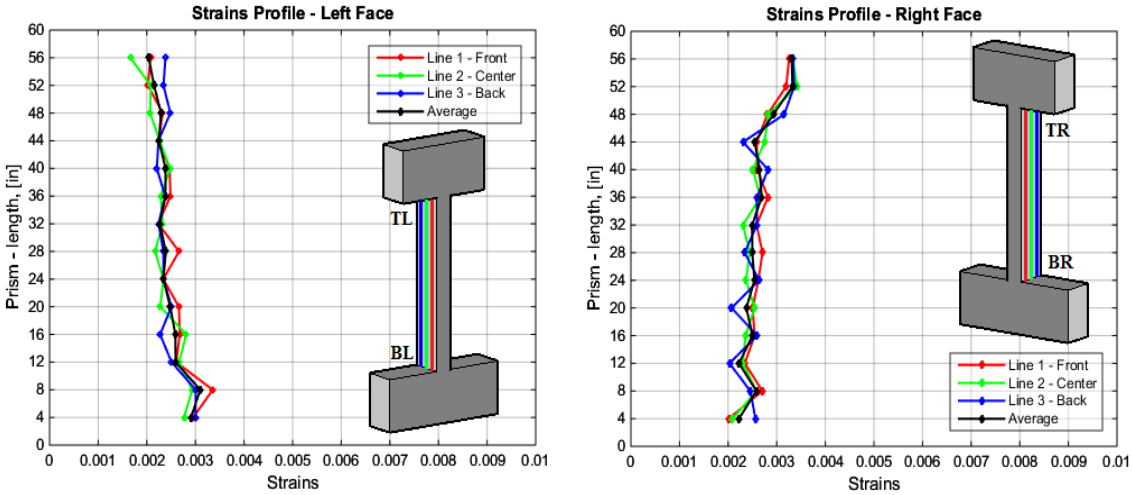

Figure A-101. Test 5: Strain profiles at 1.0 εy and +0.96 in. out-of-plane displacement demands

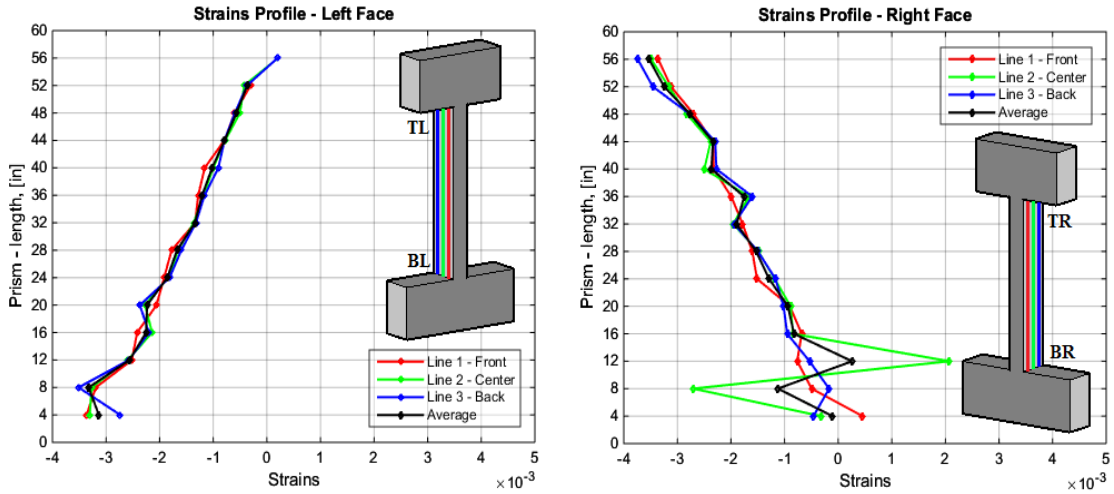

Figure A-102. Test 5: Strain profiles at P=-300 kips and -0.96 in. out-of-plane displacement demands

In general, upon yielding tensile demands, horizontal cracks became more numerous and wider. Small cracks formed and extended to the beam-column connections. During the application of compressive loads, the cracks tended to close specially in the central region of the prism. As mentioned in previous reports, it was noticed that the spacing of the transverse reinforcement induces the spacing of the horizontal cracks.

The damage at $2\varepsilon_y$ and +1.2 in. out-of-plane displacement appears on Figure A-103, where crack widths bigger than 5/64 in. were captured at the footing-prism interface. During stage 10 when the specimen was subjected to an axial compressive force of 288 kips and the out-of-plane displacement was -1.2 in., vertical cracks appeared in the concrete cover at TR and BL regions accompanied by concrete flacking, Figure A-104. Throughout the following two cycles at stages 12 and 14, concrete cover fell down on the BL region and consequently transverse reinforcement was exposed on the corners, Figure A-105.

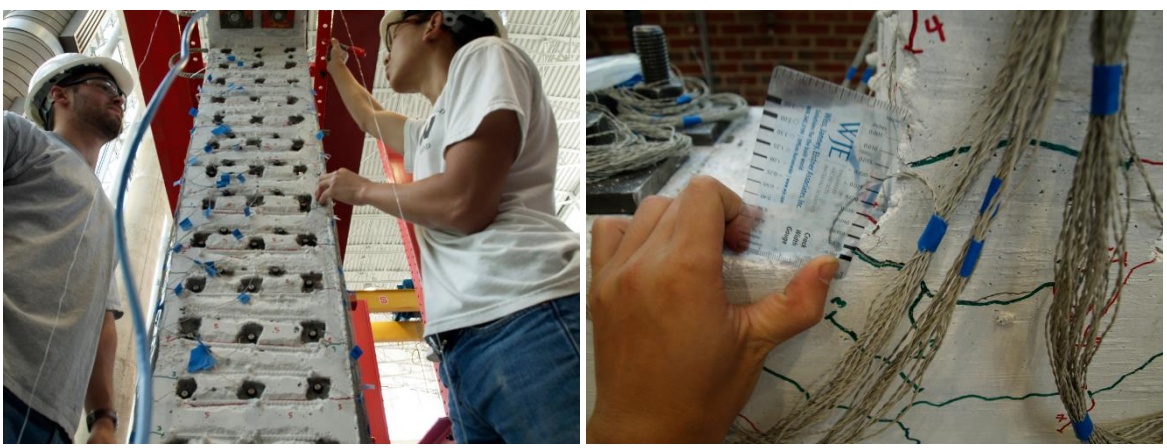

Figure A-103. Test 5: Propagation of cracks at 2.0 εy (axial) and +1.2 in. (out-of-plane) – First cycle

Damage propagation at different stages are presented from Figure A-106 to Figure A-112. During the first cycle associated with $4\varepsilon_y$, cracks widths close to 3/32 in. were observed on the BL and TR regions. Few new cracks formed in the prism. Concrete flacking and concrete spalling propagated upon a 278 kips compressive load and a -1.44in. out-of-plane displacement corresponding to stage 16. This damage was observed along 10 in. height approximately in the TR and BL regions, which extended during the following cycles.

Through tensile demands at $6\varepsilon_y$, and an out-of-plane displacement equal to 1.68 in., crack widths close to 5/64 in. were measured on the central region of the prism. Concrete spalling propagated at TR and BL regions during a compressive load of 268 kips and an out-of-plane displacement of -1.68in. at stage 22.

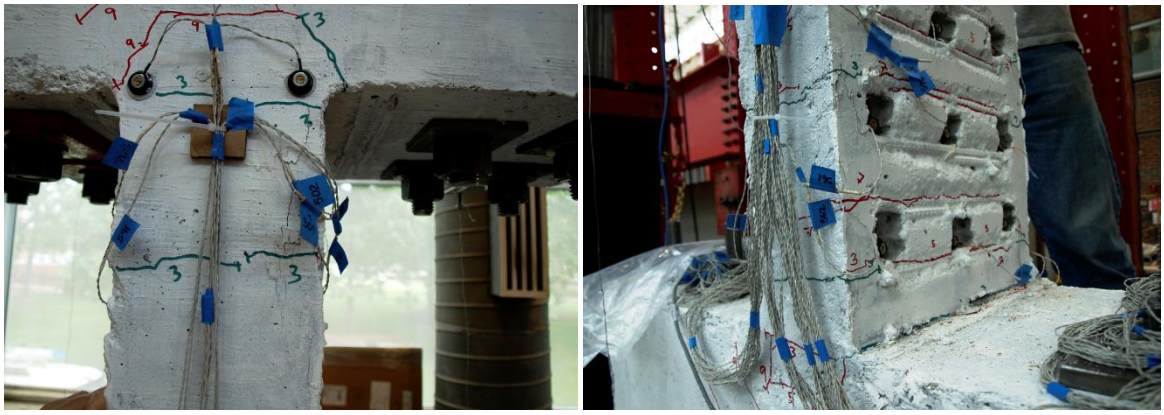

Figure A-104. Test 5: Propagation of damage at P=-288 kips and -1.2 in. out-of-plane displacement – First cycle

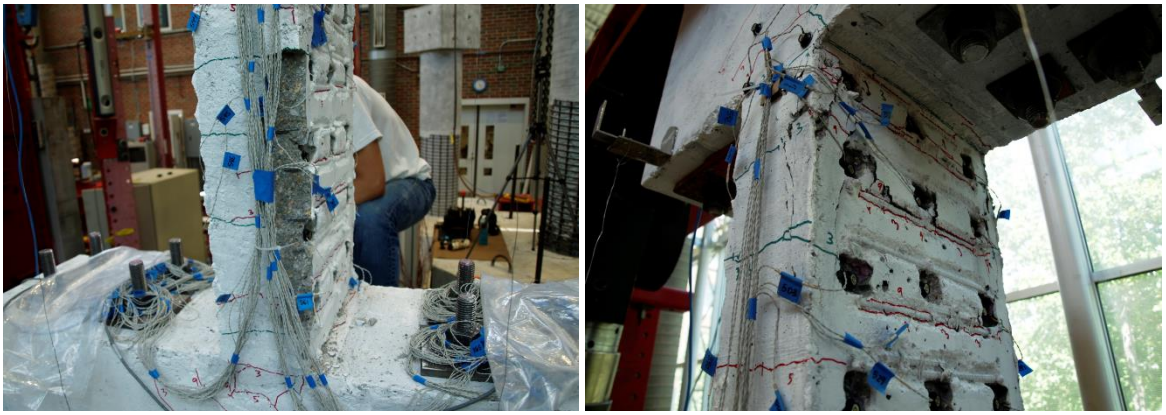

Figure A-105. Test 5: Propagation of damage during stages 12 and 14

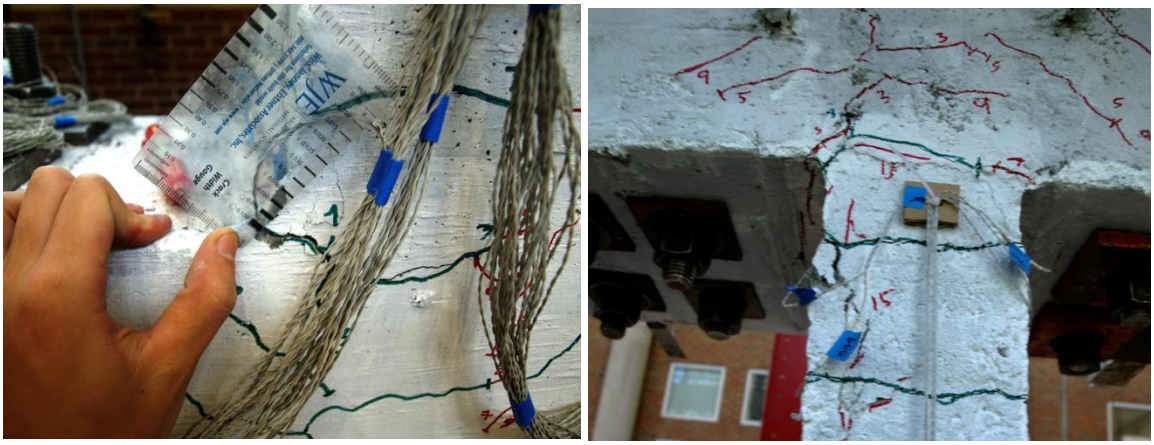

Figure A-106. Test 5: Propagation of damage at 4εy (axial) and +1.44 in. (out-of-plane) – First cycle

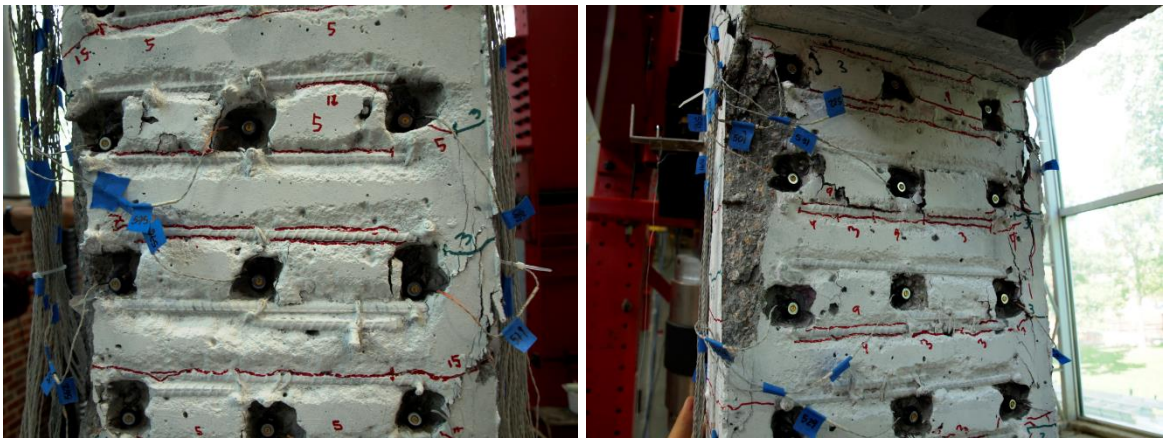

Figure A-107. Test 5: Propagation of damage at P=-278 kips and -1.44 in. out-of-plane displacement – First cycle

Figure A-108. Test 5: Propagation of damage at 6εy (axial) and +1.68 in. (out-of-plane) – First cycle

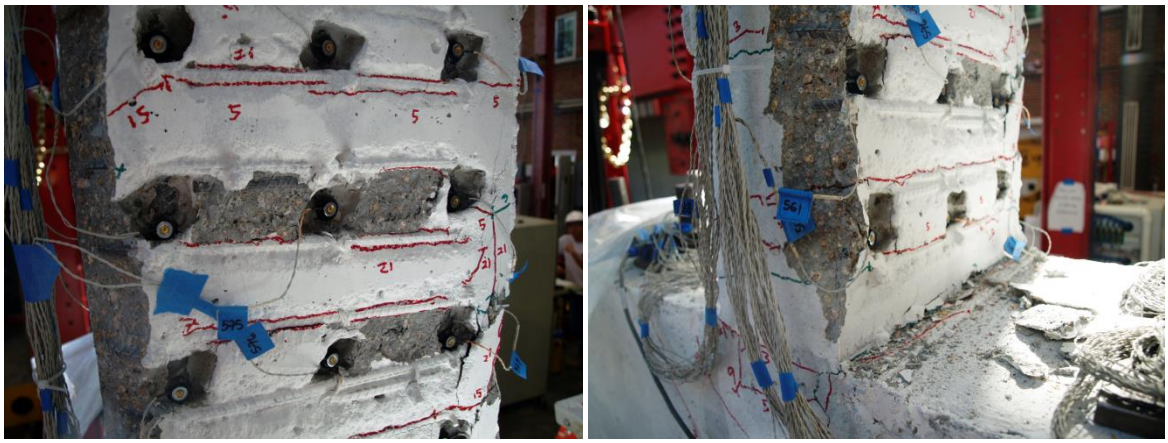

Figure A-109. Test 5: Propagation of damage at P=-268 kips and -1.68 in. out-of-plane displacement – First cycle

Figure A-110. Test 5: Propagation of damage at 8εy (axial) and +1.92 in. (out-of-plane) – First cycle

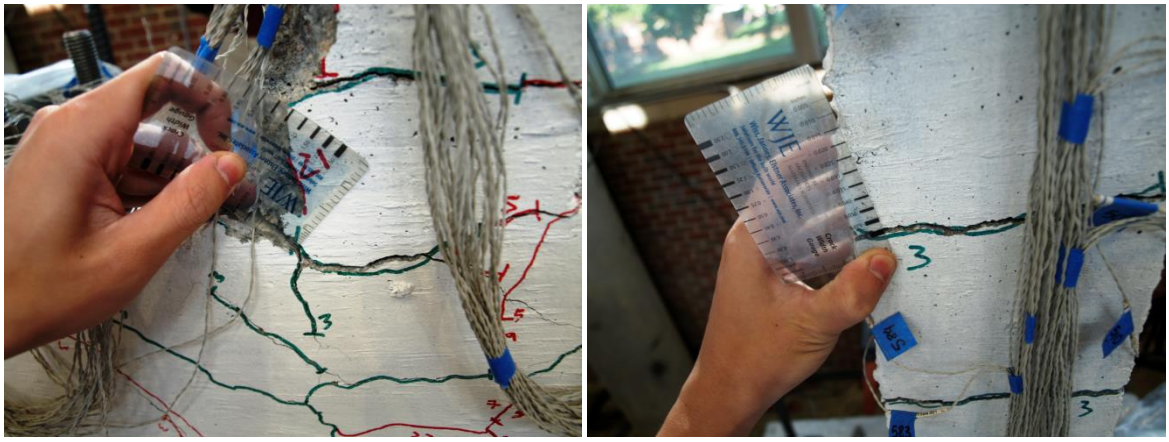

Figure A-111. Test 5: Propagation of damage at 10εy (axial) and +2.16 in. (out-of-plane) – First cycle

Figure A-112. Test 5: Propagation of damage at 12εy (axial) and +2.16 in. (out-of-plane) – First cycle

In the following cycles the number of new cracks decreased. Upon $8\varepsilon_y$ and +1.92 in. out-of-plane displacement during the first cycle at stage 33, crack widths greater than 5/64 in. were measured in the central region of the prism. Concrete cover continued to fall down on the TL and BR regions and more stirrups were exposed on the corners. In the interface between the prism and the foundation, the cracks became visibly wider than previous cycles and close to 1/4 in. beyond the $10\varepsilon_y$ cycles.

Throughout the first cycle related to $10\varepsilon_y$, out-of-plane buckling was visually captured upon compressive loading. This scenario, where the out-of-plane deformations were relatively small, was observed during the three cycles corresponding to $10\varepsilon_y$. After experimenting these out-of-plane deformations, the prism returned to a fairly straight position when the cracks closed and consequently it was able to resist the intrinsic forces associated with compressive forces developed to withstand overturning moments.

In the first cycle associated with 12εy and upon compressive loading, a different scenario was captured when instability occurred as illustrated in Figure A-113. The final state of the prism showing local damage is presented in Figure A-114. The stirrups remained as originally constructed.

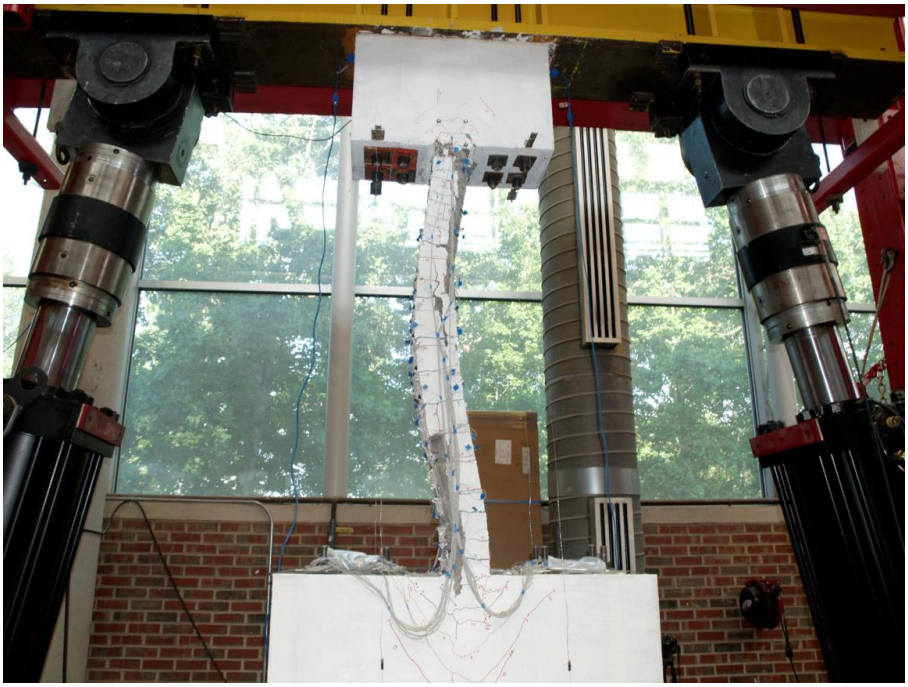

Figure A-113. Test 5: Instability developed under compression loading. First cycle for 12εy

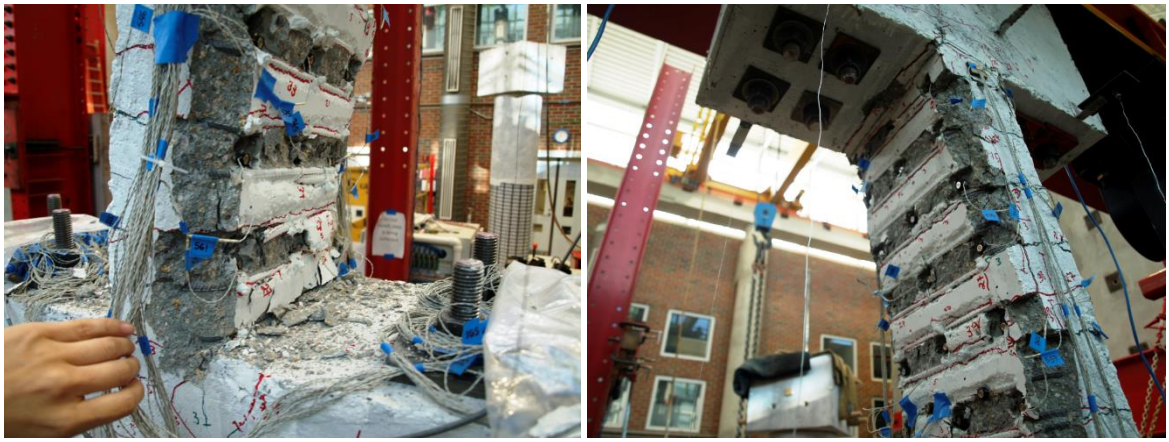

Figure A-114. Test 5: Final state of prism P1-P5. Local damage

Figure A-115 depicts the axial and out-of-plane actions captured for P1-P5 as a function of forces and displacements. In the cycles where buckling started to be captured, the axial stiffness reduced significantly by the time the axial compressive load approaches 30% of the axial design compressive force, *Po* = -358 kips, phenomenon also captured for P1-P2, P1-P3, and P1-P4. These points are associated with the onset of out-of-plane buckling. Notice that the specimen is still extended. Due to the intrinsic eccentricity in the developed compressive force, one side of the wall end region closes first resulting in out-of-plane deformations. Once the cracks close, the prism gains stiffness and is able to carry the same axial load as in previous cycles. In the last cycle, instability was captured since the prism was not able to recover its strength. The maximum applied load at this stage was -210 kips, equivalent to 59% of *Po*, and 71% of the load applied in a previous cycle.

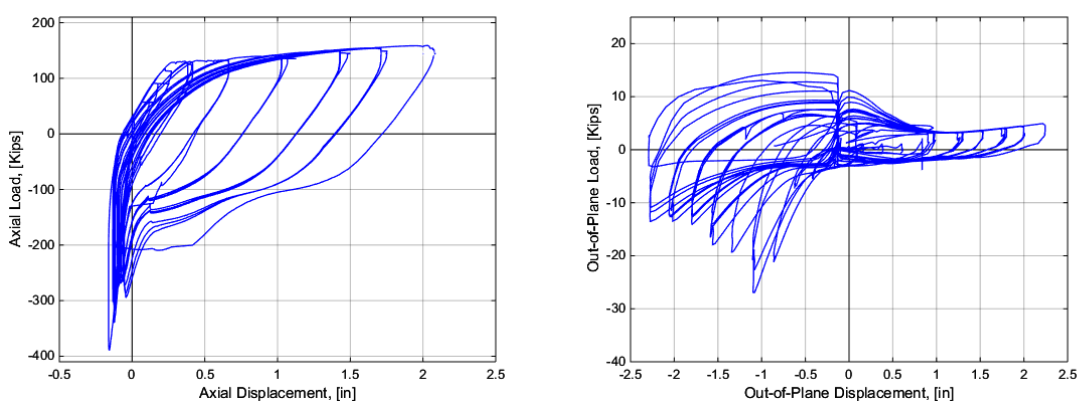

Figure A-115. Test 5: Axial Load vs. Axial displacement and Out-of-Plane Load vs. Out-of-Plane Displacement applied to prism P1-P5

Strain profiles captured during the last tensile cycle are presented in Figure A-116. The average of the strains calculated in both faces at midheight of the prism is approximately 2.7%, value close to the target at $12\varepsilon_y$. Figure A-117 shows strain profiles at the onset of buckling during the last cycle upon

compressive loads. The strains average at midheight of the prism is close to 2.0% on the left face and 1.7% on the right face. Notice a lower value on the side where the concave shape is later developed.

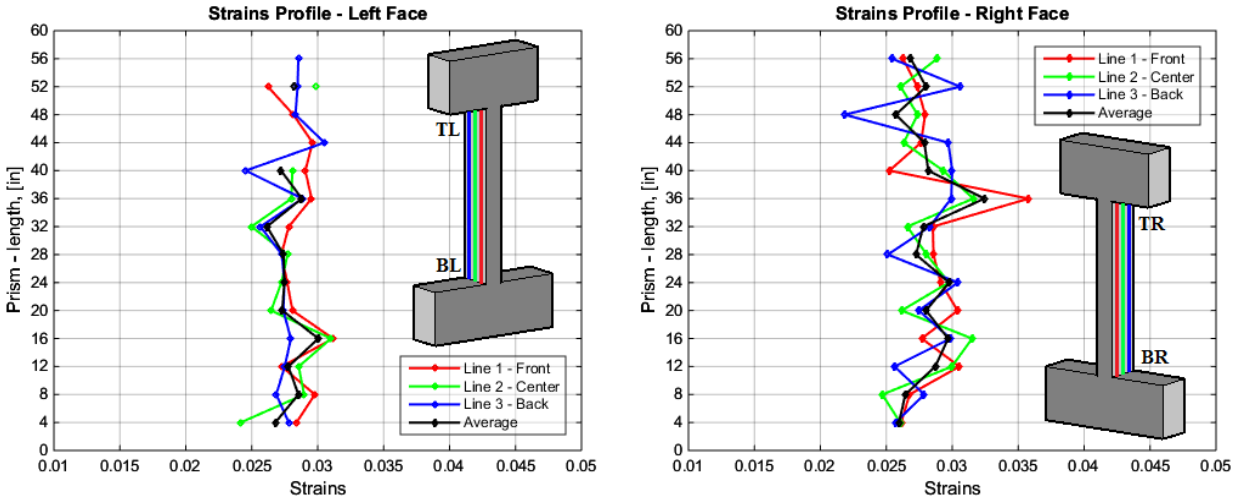

Figure A-116. Test 5: Strain profiles at 12 εy and +2.4 in. out-of-plane displacement demands during the first cycle

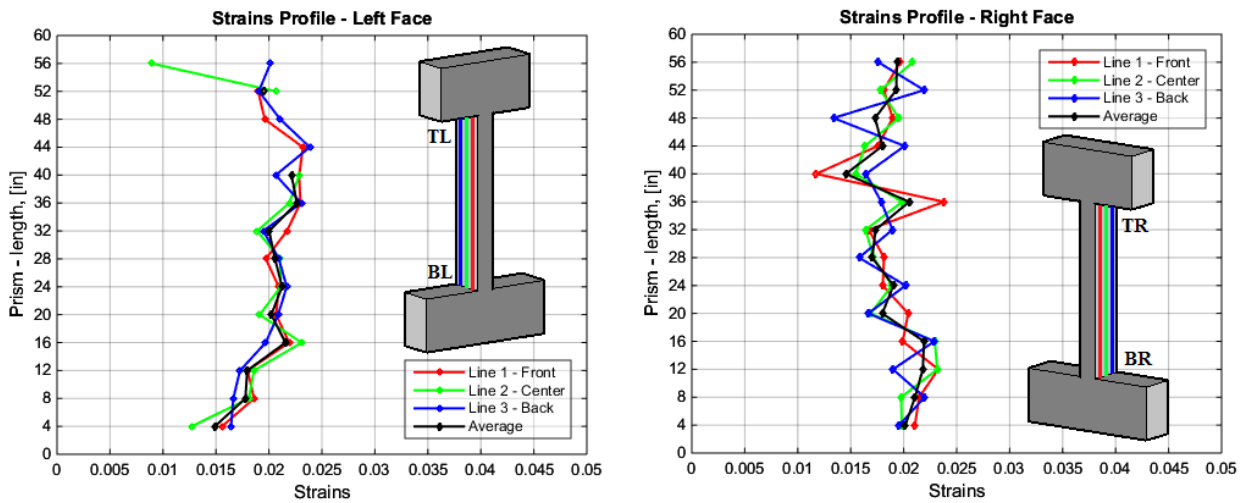

Figure A-117. Test 5: Strain profiles at onset of instability

Figure A-118 illustrates the evolution of the nominal axial strain captured from gage 22 at the center of the specimen on the right face versus the normalized out-of-plane deformation and the axial force. The maximum compression strain reached a value of -1.9%. Figure A-119 shows the variation of strains computed from gage 67 located at the center of the prism on the left face, where the maximum tensile strain is 3.0%. The onset of instability is captured at the time the normalized out-of-plane displacement exceeds negative 0.37. Notice a stable response of the prism at low levels of axial tensile strains.

The normalized out-of-plane deformations increased upon compressive loading during and after the first cycle associated with $8\varepsilon_y$. A sudden increment on this deformation took place during the first cycle associated with $12\varepsilon_y$ at the moment the compression load was -142 kips, which represents 40% of the axial design compressive force, *Po*, and 57% of the load reached in a previous cycle. Yielding forces, *AsFy*, in tension and compression are also plotted in Figure A-118 and Figure A-119, where *As* is the area of the longitudinal reinforcement.

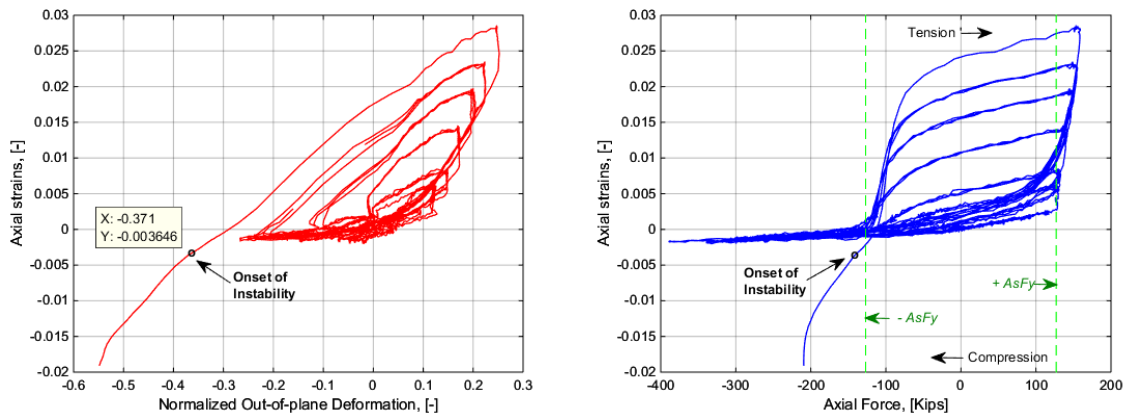

Figure A-118. Test 5: Response of specimen P1-P5 captured from a midheight gage on the right face

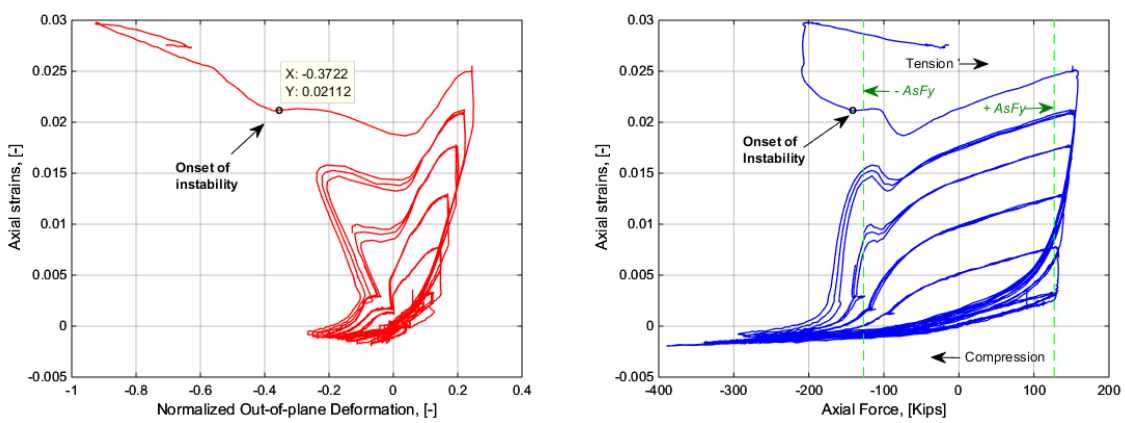

Figure A-119. Test 5: Response of specimen P1-P5 captured from a midheight gage on the left face

The evolution of the buckling shape during the last cycle of the test when the prism was subjected to compressive forces is plotted in Figure A-120. Four stages were considered: maximum tensile demand, onset of buckling, zero axial displacement, and maximum compressive load. It can be established that the maximum out-of-plane deformation is around 4.2 in. located at midheight.

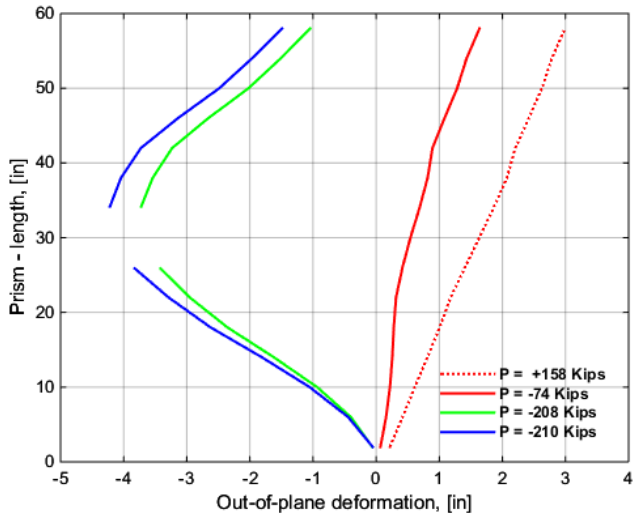

Figure A-120. Test 5: Evolution of the buckling shape during the last cycle under compressive loads

5. Conclusions

Specimen P1-P5 was successfully tested during six hours where combined and progressive cyclic out-of-plane lateral displacements and cyclic axial loads were applied. P-Δ effects were included to establish the different target loads in compression which were associated with their corresponding lateral displacement. The tensile strain demands beyond yielding were controlled and adjusted in real time according to the readings reported by the MATLAB code "REALSTRAIN".

Regarding the stability of the specimen, it presented a stable response at early cycles. Indeed, out-of-plane deformations were not visibly noticed during the cycles before $10\varepsilon_y$. Beyond the first cycle of $10\varepsilon_y$, a gradual increment in the out-of-plane deformations were captured until instability developed during the first cycle of $12\varepsilon_y$. The large buckling displacement led to concrete crushing and spalling in the central, TR, and BL regions. The axial force at this stage was 71% of the compressive force in the previous cycle.

Neither bar buckling nor bar fracture were detected during or after the test. The stirrups remained as originally constructed. Analysis of the data from this test will continue, as a consequence the material presented here should be considered preliminary. Further experiments will reveal more information about the effectiveness of the reinforcement detailing recommended in guidelines to prevent lateral instability in RC structural walls.

Stability of Ductile RC Structural Walls – Assessment of the Local Buckling Failure Mode

Test 6

June - 14 - 2016

Summary Report

Prepared for:

Alaska Department of Transportation

Prepared by:

RA – Ana Gabriela Haro

PIs – Mervyn Kowalsky and Rob Chai

North Carolina State University

Raleigh – NC

1. Executive Summary

Test 6 was conducted at the Constructed Facilities Laboratory on Thursday, June 14, 2016, as part of the load path project. The specimen was designed and built simulating boundary elements from prototype walls. A monotonic and constant lateral displacement equivalent to 8% drift was applied first to the specimen followed by cyclic axial compressive loads and tensile displacements to capture its structural performance and to determine additional critical parameters associated with lateral instability of RC walls. The first part of the results are presented in this report. Further analyses will be elaborated.

2. Introduction

Recent earthquakes in New Zealand and Chile have illustrated the importance of out-of-plane stability of concrete wall elements due to in-plane loading. Pier walls are occasionally employed by Alaska DOT for their in-plane lateral stiffness. While these walls are normally thicker than the walls typically found in building applications, their clear heights are also larger, giving rise to height-to-thickness ratios which may be larger than that of buildings. Some analyses have demonstrated that walls as thick as 20 in. may be prone to buckling, depending on their length and height.

Noticing the concentration of damage in the boundary elements of rectangular reinforced concrete structural walls due to higher stress and strain demands, some past investigations by others have been carried out on prisms, which was found to be an economical way to study the inelastic instability of structural walls. In general, the main objective of these tests focuses on subjecting specimens to cyclic tension and compression actions to simulate vertical components of actual seismic loading.

While past tests on prisms has shown existing models to be promising, missing from the models is the interaction with out-of-plane loading. The existing models correlate tensile strain from in plane loading to out-of-plane deformation, assuming a prescribed curvature distribution. If loading occurs in the out-of-plane direction, the relationship between tensile strain and out-of-plane deformations must be adjusted to reflect this. In its simplest form, this would be an addition of an out-of-plane displacement to the existing equation. However, out-of-plane displacement may impact the distribution of curvature with height, thus requiring additional adjustments to the models.

A total of 12 prisms are being experimentally tested in the Constructed Facilities Laboratory (CFL) during this project. The support conditions for the 12 prisms are conceived as fixed-fixed. The first testing phase will involve controlled load paths where the specimens are subjected to tension/compression cycles in addition to lateral loading to mimic the effects of out-of-plane displacements. In the second phase, longitudinal reinforcement ratios will be varied – between the two phases, reinforcement ratios will span the typical values employed by Alaska DOT for pier walls. The details associated with the two phases are presented in Table A-11.

This first phase consists of testing six 1/2-scale identical specimens. The thickness of the prisms is 5 in. since the cover was excluded from the construction. The geometry used is 5x12x60 in, corresponding to an aspect ratio (*h/b = height/thickness*) of 10 (including the missing cover). The longitudinal reinforcement ratio is 2.6% (6 bars #5). Transverse reinforcement consists of #3 diameter rebar spaced at 2 in. and was placed as shown in Figure A-121.

Table A-11. Test 6: Description of the experimental phases

Phase	Tests	Geometry	Reinforcement	Loading
1	6	Thickness and Height (based on prototype wall). (6”x12” ; actual geometry = 5”x12”)	Longitudinal (6bars#5) and transverse (#3@2in) reinforcement ratios similar for the 6 specimens.	Controlled 3D load path
2	6	Same as phase 1 (Based on actual pier walls formerly used by the Alaska DOT)	Longitudinal reinforcement ratio varies. (3 specimens 6bars#3 and 3 specimens 6bars#4)	Controlled 3D load path

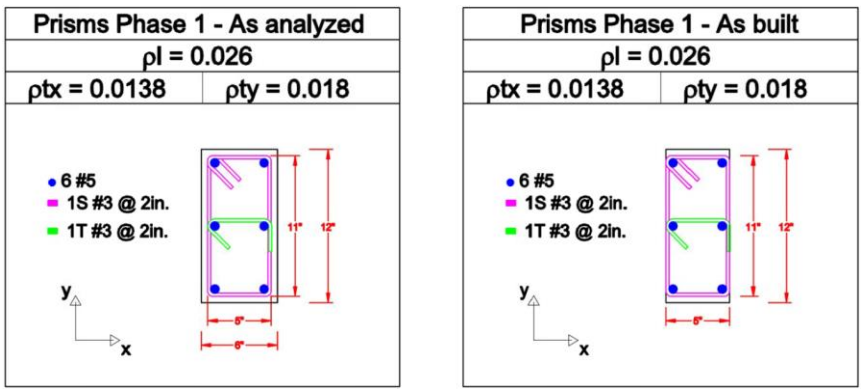

Figure A-121. Test 6: Phase 1 - Cross section of the prisms

Table A-12. Test 6: Phase 1 - Steel tensile test properties for bars #3 and #5

Sample No.	Bar #	fy (ksi)	εy = fy/Es	fu (ksi)	εu
1	3	74.7	0.0026	103.3	0.0916
2	3	74.8	0.0026	100.6	0.0750
3	3	79.6	0.0027	105.0	0.0927
4	3	76.8	0.0026	103.4	0.0770
5	3	77.0	0.0027	103.3	0.0736
6	3	77.1	0.0027	103.2	0.1040
#3 Average		**76.7**	**0.0026**	**103.1**	**0.0856**
1	5	69.4	0.0024	96.4	0.1100
2	5	68.2	0.0024	95.6	0.1124
3	5	68.7	0.0024	97.7	0.0981
4	5	70.1	0.0024	97.4	0.1128
5	5	70.0	0.0024	98.0	0.1326
#5 Average		**69.3**	**0.0024**	**97.0**	**0.1132**

Regarding the material properties, an unconfined concrete strength of 5 ksi and reinforcement yielding strength of 60 ksi were considered as design values to define the experimental load history in compression. Actual values were used to calculate tensile demands. Table A-12 shows the actual steel tensile test properties for the #3 and #5 bars. The reinforcement detailing was established according to the ACI 318 and NEHERP guidelines for ductile columns and boundary elements.

3. Test Setup

The test setup consisted of a 14 ft long steel loading beam placed on the top of the specimen and connected to three actuators: two vertically inclined 440 kips actuators which induce axial loads and one horizontal 55 kips actuator to apply out-of-plane displacements. Two steel frames are used to restrain torsion in the loading beam. Two concrete blocks attached to the strong floor support the specimen to reach the required height associated with the effective length of the 440 kips actuators. Figure A-122 depicts the test setup drawings and Figure A-123 shows a picture of the area where the components of the project are placed.

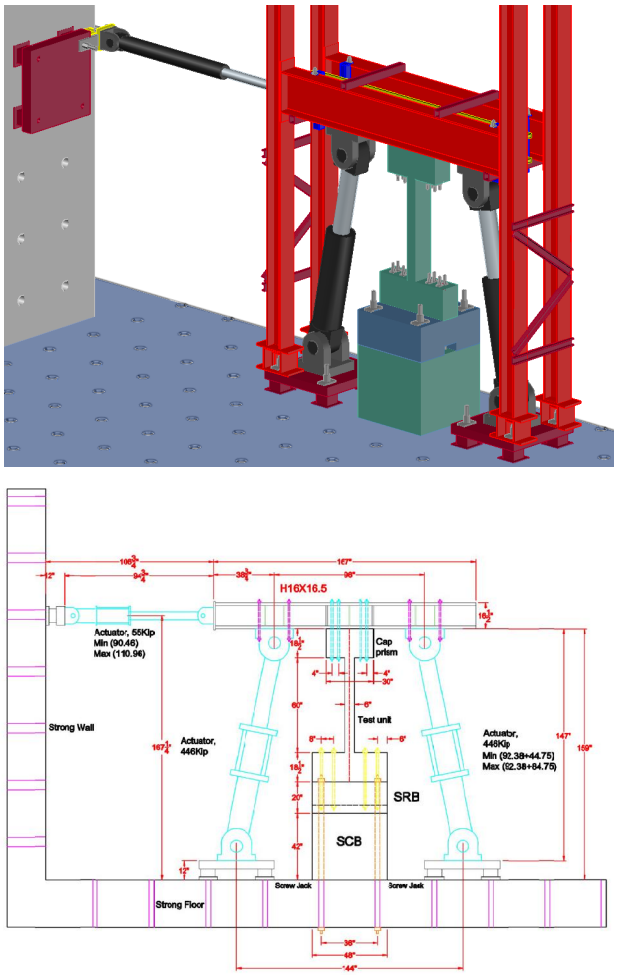

Figure A-122. Test 6: Test setup drawings

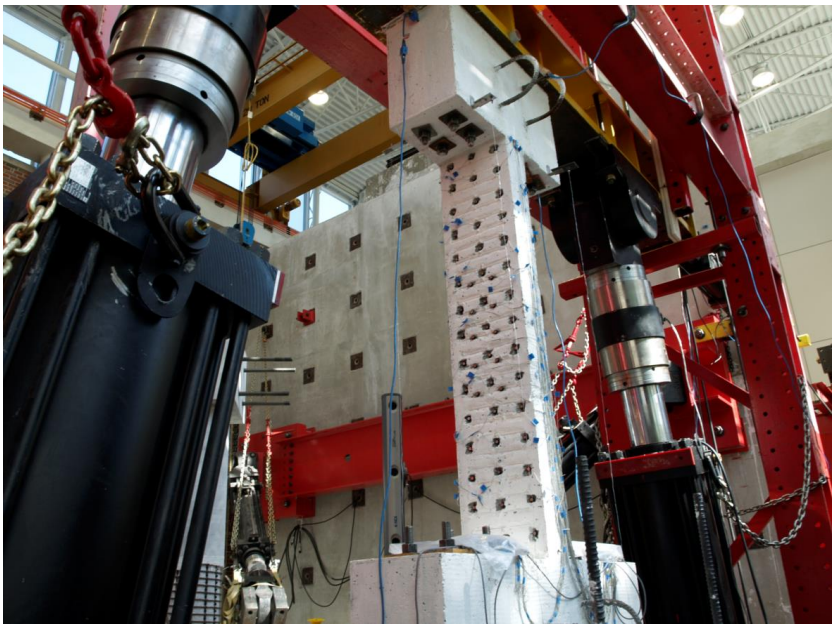

Figure A-123. Test 6: Test setup in CFL at NC State

The horizontal actuator is controlled by displacements. The vertically inclined actuator located at the left hand side of the specimen, Figure A-122, is controlled by rotations captured throughout an inclinometer attached to the loading beam. The actuator placed at the right hand of the specimen is controlled by a combination of forces and displacements. Loads and strokes in the actuators are measured through integrated LVDTs and loads cells.

Relative displacements resulting from the interaction between the loading beam, the specimen, and the support concrete block were obtained through 3 linear potentiometers. In addition, axial deformations of the prism were registered through 4 string potentiometers. Another string potentiometer was used to capture the lateral displacement of the loading beam.

A total of 107 infrared LEDs from the optical tracking system Optotrak Certus developed by Northern Digital Inc. were placed directly on the steel reinforcement of the prism. The objective was to establish longitudinal and transverse strains in real time throughout a MATLAB code, named “REALSTRAIN”, developed for this purpose at CFL. Four additional infrared LEDs were positioned on the front face of the prism cap as a plane of reference. Due to a camera range limitation in the left side of the prism, 3 LEDs were attached directly on concrete instead of the steel reinforcement. A total of 114 infrared LEDs were used during this experiment. Figure A-124 shows the distribution of the LEDs on the right face of the prism and the overall allocation of the markers obtained from the Optotrak spatial coordinate output.

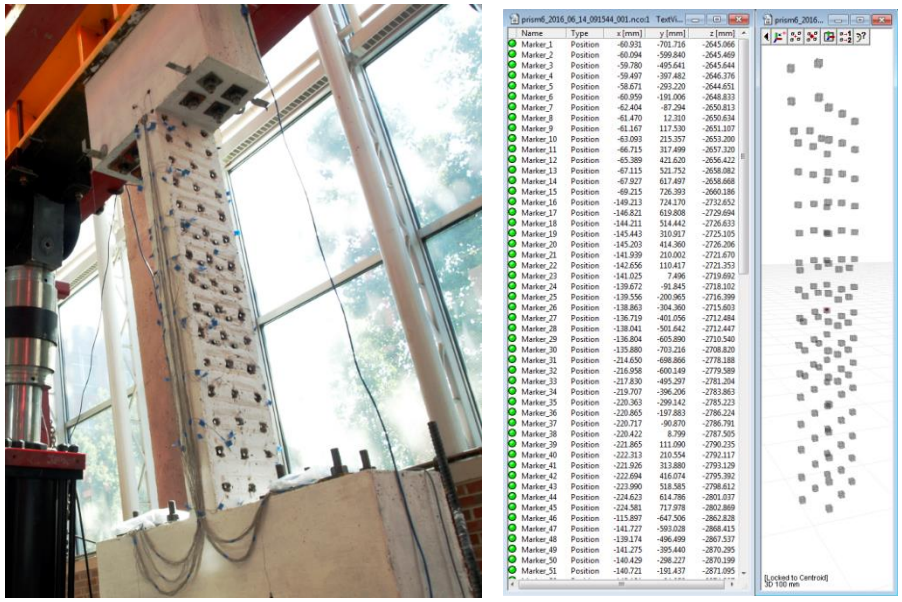

Figure A-124. Test 6: Instrumentation – Optotrak LEDs distribution on right face of the specimen and Spatial coordinate output

4. Test Summary

First, an out-of-plane displacement of 4.8 in., equivalent to 8% drift, was induced to specimen P1-P6 (Phase 1 – Prism 6). The purpose was to keep this displacement constant during the entire test, which in addition, included unsymmetrical cyclic axial compressive loads and tensile displacements. The axial displacement history started with elastic single cycles analytically predicted. The targets in tension were chosen as fractions of the yielding displacement referred as: $0.25\varepsilon_y$, $0.50\varepsilon_y$, and $0.75\varepsilon_y$ and $1.0\varepsilon_y$. Subsequently, three identical cycles at different axial tensile displacement ductility levels continued until buckling was captured upon compressive loading. The unique compressive target load, $P_{8\%}$ = -182 kips, was established considering P-Δ effects, representing 51% of the maximum axial design compressive load, Po = -358 kips, Figure A-125. The load $P_{8\%}$ was calculated following the linear interaction from Eq. (1).

$$P_{\%} = P_o - (P_O - P_b)\frac{M_{\%}}{M_b} \qquad (1)$$

where, P_b = 164 kips and M_b = 475 kip.in are the axial force and bending moment at balanced failure, respectively. The flexural moment at 8% out-of-plane drift ratio is $M_{4\%} = P_{8\%}(0.08*60in.)/2$. Substituting this expression in Eq. (1) and solving for $P_{8\%}$, the target value is obtained.

Throughout the 4.8 in. lateral displacement, big cracks appeared on the bottom left (BL) and top right (TR) regions of the prism, Figure A-126. Flexural crack widths close to 0.10 in. were measured in the mentioned regions. Concrete spalling was also observed on top left TL and bottom right (BR) regions. Strain profiles captured at this stage for each reinforcement line and for each face are displayed in Figure A-127, where the corresponding average has also been included. A total of 14 gages were

established for each longitudinal bar along the 60 in. height, Y axis. Maximum values close to 2.0% and 3.0% are observed in the BL and TR regions, respectively.

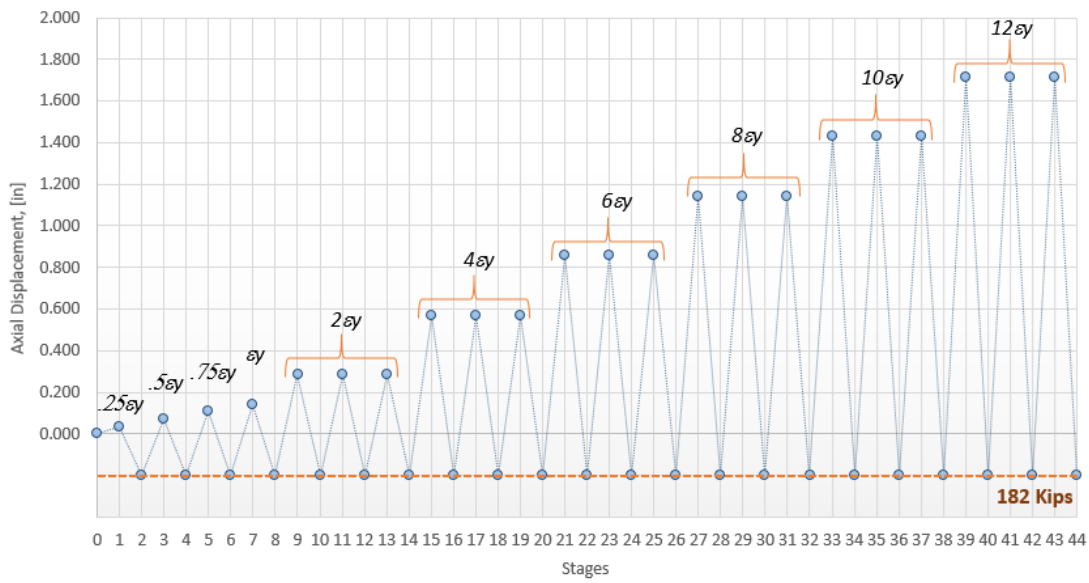

Figure A-125. Test 6: Intended Axial Displacement History for specimen P1-P6

Subsequently, the first tensile load related to 0.25εy was induced to the specimen. In general, upon yielding tensile demands, horizontal cracks became more numerous and small cracks formed and extended to the beam-column connections. During the application of compressive loads, the horizontal cracks tended to close only in the central region of the prism. Vertical cracks that appeared in the concrete cover at TL and BR regions after the first compressive load, generated concrete spalling in the subsequent cycles. Once again, it was noticed that the spacing of the horizontal cracks are induced by the spacing of the transverse reinforcement.

Crack propagations at cycles related to $1\varepsilon_y$ through $12\varepsilon_y$ appear in Figure A-128 through Figure A-133. Crack widths close to 3/16 in. were captured close to the joints at $2\varepsilon_y$. Concrete spalling became more severe at TL and BR regions where the damage was concentrated. On the central region, crack widths close to 1/64in. were captured at $2\varepsilon_y$. The cycles for $4\varepsilon_y$ were not induced to the specimen. During the first cycle associated with $6\varepsilon_y$ cracks widths close to 3/32 in. were observed on the BL and TR regions, and new cracks formed on the central region. In the following cycles the number of new cracks decreased. Through tensile demands at $8\varepsilon_y$, crack widths close to 0.075 in. were measured on the central region. Concrete spalling propagated approximately 8 in. and 10 in. on TL and BR regions, respectively, and consequently transverse reinforcement was exposed on the corners.

Figure A-126. Test 6: Cracks at BL and TR regions at 4.8 in. out-of-plane displacement

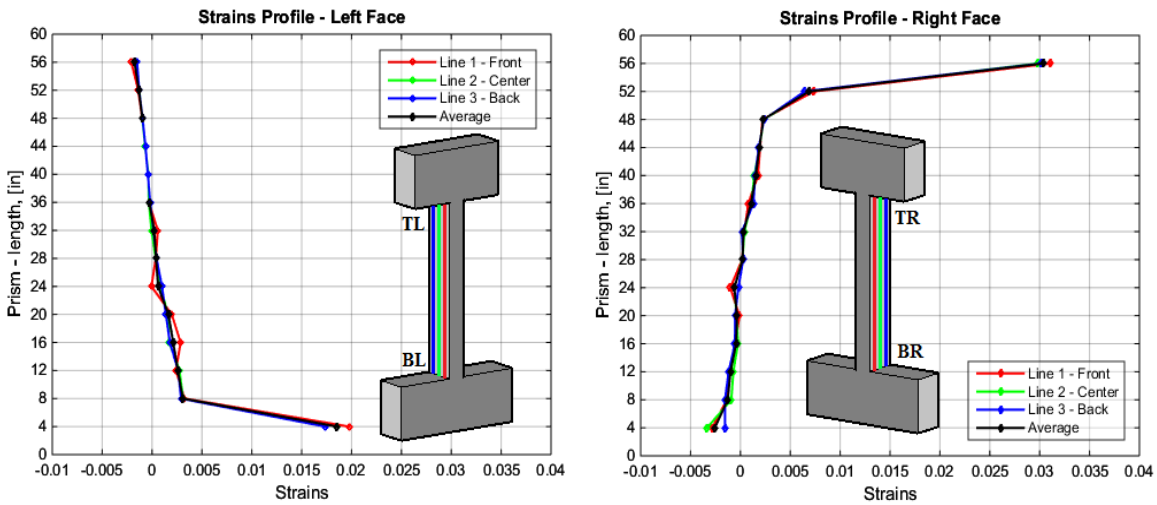

Figure A-127. Test 6: Strain profiles at 4.8 in. out-of-plane displacement

Figure A-128. Test 6: Propagation of damage at 1.0 εy – First cycle

Figure A-129. Test 6: Propagation of damage at 2.0 εy – First cycle

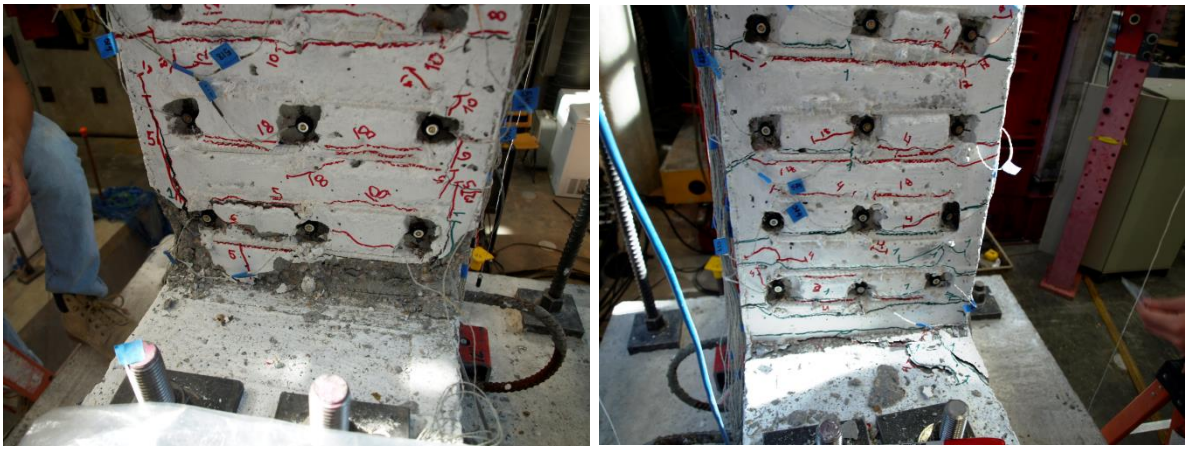

Figure A-130. Test 6: Propagation of cracks at 6.0 εy – First cycle

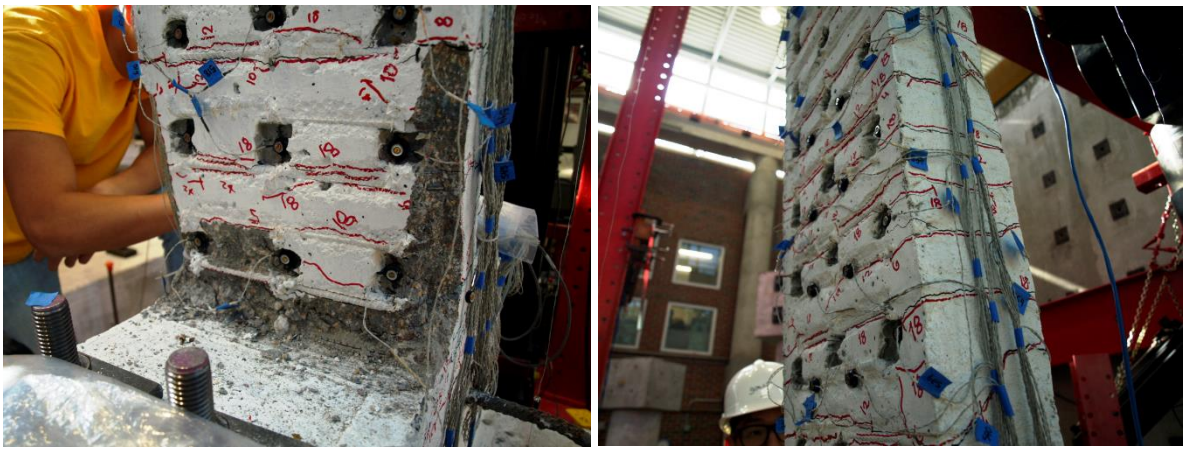

Figure A-131. Test 6: Propagation of damage at 8.0 εy – First cycle

Figure A-132. Test 6: Propagation of damage at 10.0 εy – First cycle

Figure A-133. Test 6: Propagation of damage at 12.0 εy – First cycle

Upon the $10\varepsilon_y$ first cycle, crack widths close to 3/16 in. were measured in the BR region. Concrete cover continued to fall down on the TL and BR regions. During the cycles associated with $12\varepsilon_y$ the cracks became visibly wider than previous cycles and severe damage was observed in the interface between the prism and the footing.

Throughout the first cycle related to $10\varepsilon_y$, out-of-plane buckling was visually captured upon compressive loading. This scenario, where the out-of-plane deformations were relatively small, was observed during the three cycles corresponding to $10\varepsilon_y$ and the first cycle for $12\varepsilon_y$. After experimenting these out-of-plane deformations, the prism returned to a fairly straight position when the cracks closed and consequently it was able to resist the intrinsic forces associated with compressive forces developed to sustain overturning moments.

In the second cycle related to $12\varepsilon_y$, when compressive loads were applied, a stable buckled shape was captured at the end of this stage. At this point the prism resisted a compressive load similar to previous cycles. The same phenomenon occurred during the third cycle for $12\varepsilon_y$ even though slight concrete crushing was observed in the middle region on the right face of the prism, Figure A-134. Since the prism was able to withstand the same level of compressive loads, an additional $14\varepsilon_y$ cycle was induced to the prism. More damage propagated along the specimen. The prism did not recover a straight configuration under $14\varepsilon_y$ tensile demands as may be noticed in Figure A-135, which implied that the prism already experienced inelastic instability in a previous cycle. Upon compressive loads, instability was more evident as illustrated in Figure A-136. The final state of the prism showing local concrete crushing at midheight, bottom right (BR) and top right (TR) regions is presented in Figure A-137. The type of failure at this stage resulted as a combination of out-of-plane buckling and shear stresses.

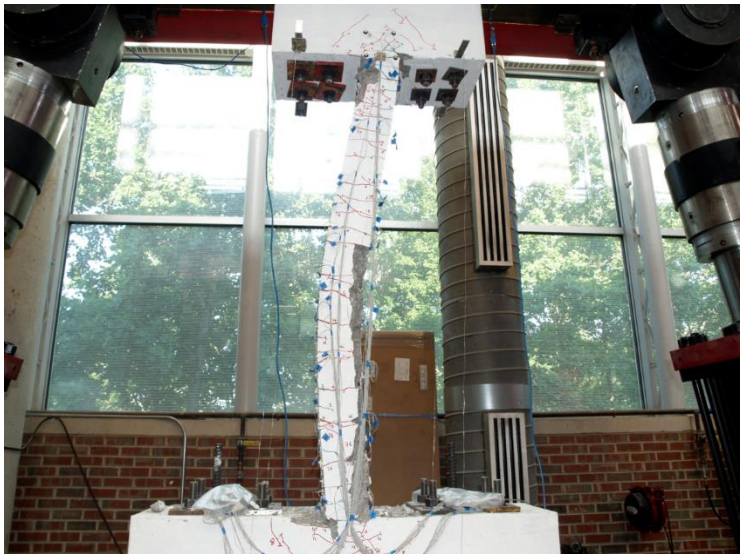

Figure A-134. Test 6: Stable buckled shape of the prism upon compressive loads – Third cycle for 12.0 εy

Figure A-135. Test 6: Propagation of damage at 14.0 εy – First cycle

Figure A-136. Test 6: Instability developed under compression loading. Second cycle for 12εy

Figure A-137. Test 6: Final state of prism P1-P6. Concrete crushing at midheight, bottom and top regions

Figure A-138 depicts the entire structural response of P1-P6 as a function of axial forces and displacements. In the cycles where buckling started to be captured, the axial stiffness reduced significantly by the time the axial compressive load approaches 30% of the axial design compressive force, *Po* = -358 kips, phenomenon also captured for the last 4 tests. These points are associated with the onset of out-of-plane buckling. Notice that the specimen is still extended. Due to the intrinsic eccentricity in the developed compressive force, one side of the wall end region closes first resulting in out-of-plane deformations. Once the cracks close, the prism gains stiffness and is able to carry the same axial load as in previous cycles. In the last cycle, instability was more evident since the prism was not able to recover its strength. The maximum applied load at this stage was -100 kips, equivalent to 28% of Po, and 55% of the load applied in a previous cycle.

Strain profiles captured during $1\varepsilon_y$ is presented in Figure A-139. The average of the strains in both faces at midheight of the prism is approximately 0.24%, value close to the target at $1\varepsilon_y$. Figure A-140

shows the strain profiles computed at 14ε_y, where the strain values at midheight are 3.5% and 3.0% on the left face and right face, respectively, close to the target value, 3.3%. The difference between the values captured on both faces could be attributed to the performance of the specimen during a previous cycle, where the prism already experienced inelastic buckling.

Figure A-141 shows strain profiles at the onset of inelastic buckling during the last cycle upon compressive loads. Notice higher values on BL and TR regions due to the influence of the constant out-of-plane displacement applied to the specimen.

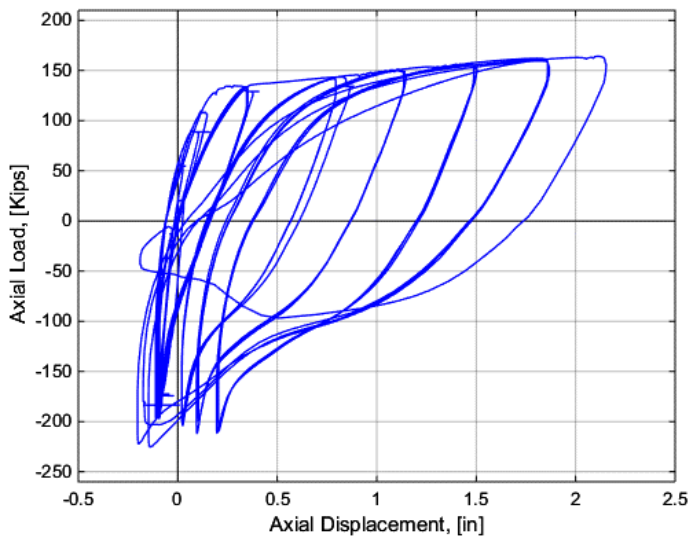

Figure A-138. Test 6: Axial structural response of prism P1-P6

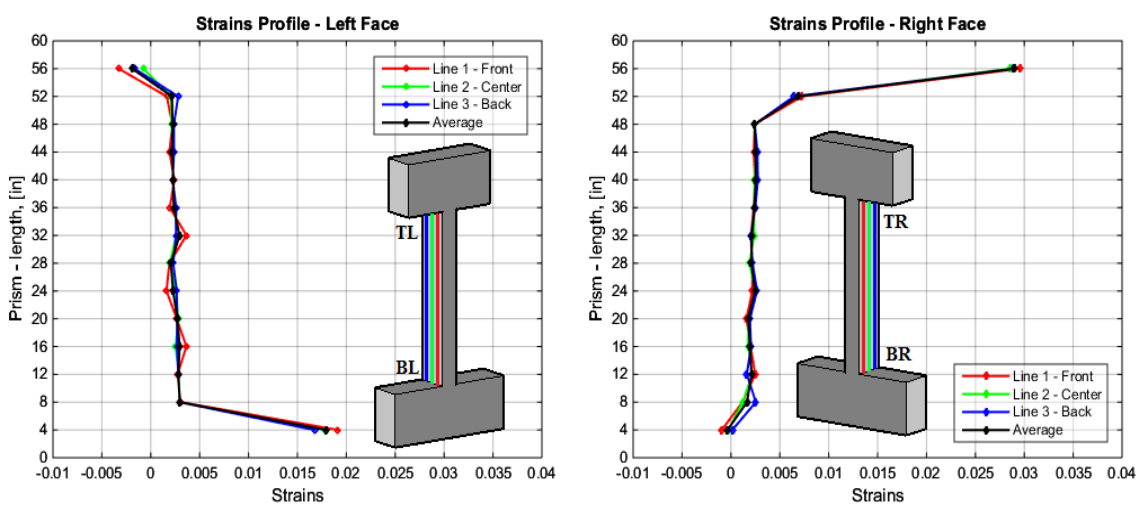

Figure A-139. Test 6: Strain profiles at 1.0 εy during the first cycle

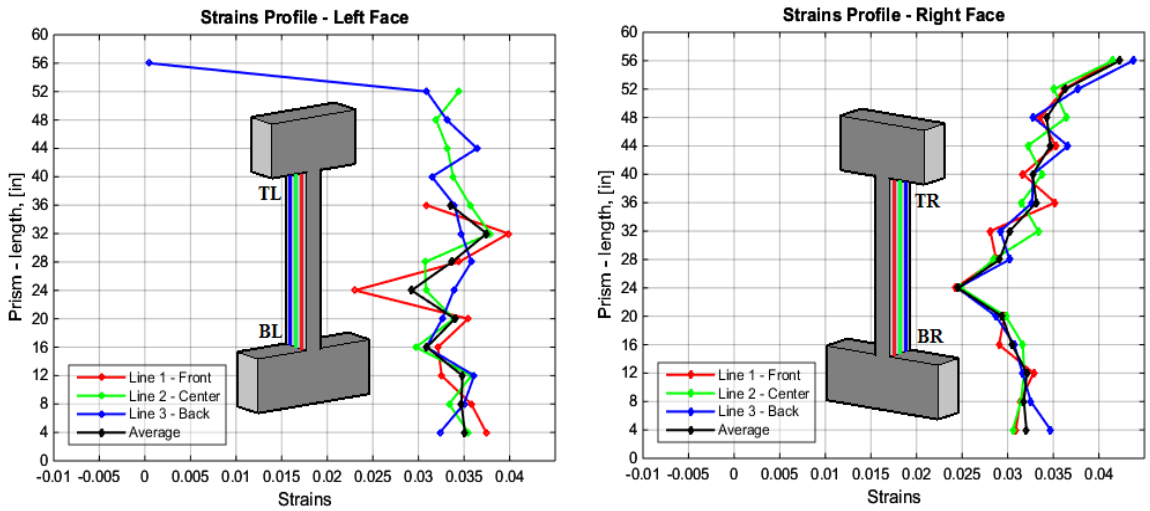

Figure A-140. Test 6: Strain profiles at 14 εy during the first cycle

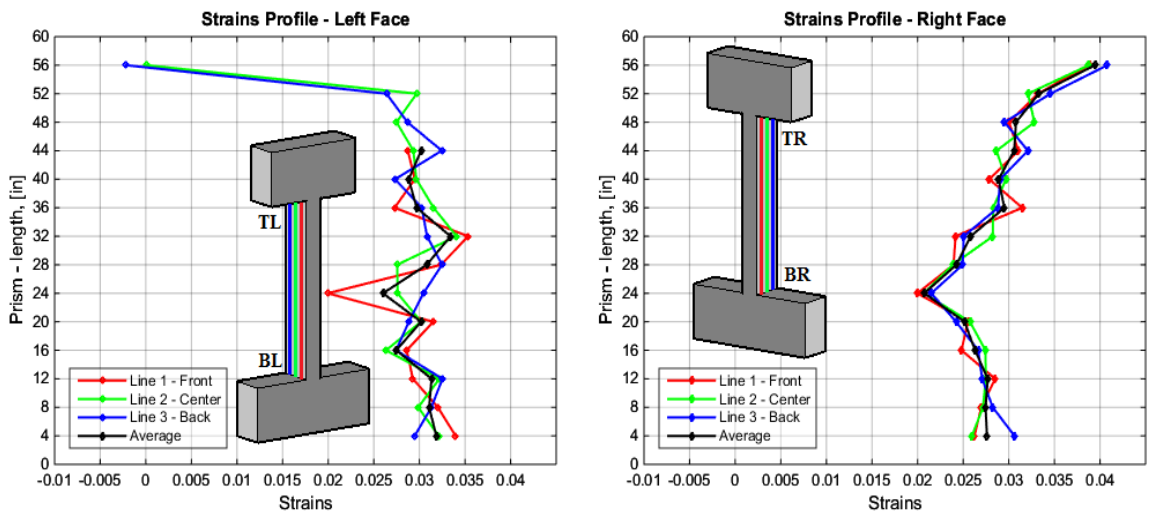

Figure A-141. Test 6: Strain profiles at onset of instability

Figure A-142 illustrates the evolution of the nominal axial strain captured from gage 22 at the center of the specimen on the right face versus the normalized out-of-plane deformation and the axial force. The maximum compression strain reached a value of -1.6%. Figure A-143 shows the variation of strains computed from gage 67 located at the center of the prism on the left face. The maximum tensile strains captured during the last cycle for 12 ε_y and the first cycle for 14 ε_y are 2.9% and 3.7%, respectively. The actual onset of instability is captured at the time the normalized out-of-plane displacement reaches 0.09. Notice a stable response of the prism at low levels of axial tensile strains. The normalized out-of-plane displacements increased upon compressive loading during the first cycle associated with 10ε_y. Throughout the first cycle of 12ε_y, the specimen suffered from a slight permanent

out-of-plane deformation. A sudden increment on this deformation took place during the third cycle at the moment the compression load was -158 kips, which represents 44% of the axial design compressive force, *Po*, and 87% of $P_{8\%}$ = -182 kips. Yielding forces, *AsFy*, in tension and compression are also plotted in Figure A-142 and Figure A-143, where *As* is the area of the longitudinal reinforcement.

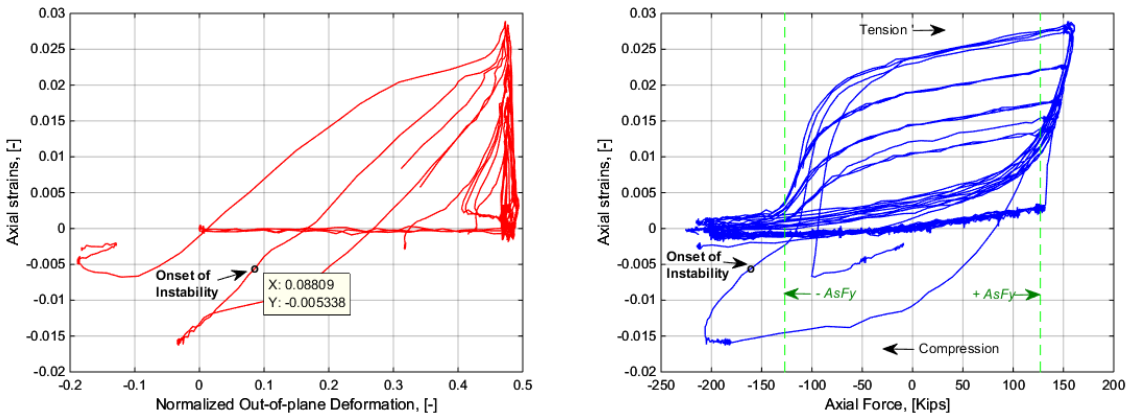

Figure A-142. Test 6: Response of specimen P1-P6 captured from a midheight gage on the right face

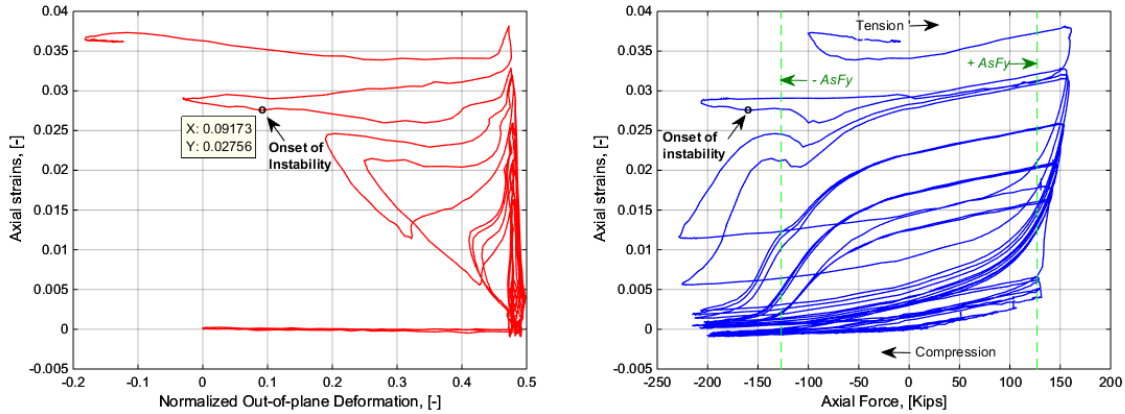

Figure A-143. Test 6: Response of specimen P1-P6 captured from a midheight gage on the left face

The evolution of the buckling shape during the last cycle of the test when the prism was subjected to compressive forces is plotted in Figure A-144. Four stages were considered: maximum tensile demand, onset of buckling, zero axial displacement, and maximum compressive load. It is observed that the maximum out-of-plane deformation is in total 4.0 in. located 16 in. below midheight. The shapes originated throughout this analysis coincide with the shape captured in Figure A-136.

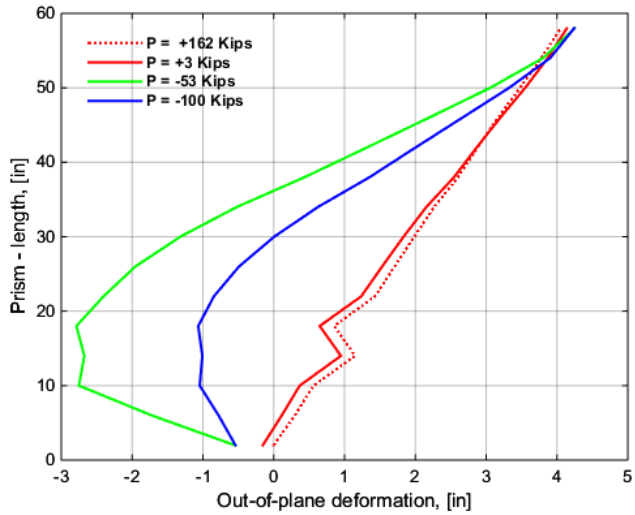

Figure A-144. Test 6: Evolution of the buckling shape during the last cycle under compressive loads

5. Conclusions

Specimen P1-P6 was successfully tested during six hours where combined load patterns were applied. A lateral out-of-plane displacement equivalent to 8% drift was sustained during the entire test to analyze its influence on the stability of RC walls. The maximum tensile strain in BL and TR regions of the prism during the first stage, where axial loads were not induced, was close to 2% and 3%, respectively.

Subsequently, progressive cyclic axial loads/strains were applied to the specimen reaching maximum values fairly close to the targets $P_{8\%}$ = -182 kips and 14ε_y, in compression and tension, respectively. The specimen presented a stable response at low levels of axial tensile demands. Out-of-plane deformations were not noticed during the cycles before 10ε_y. Beyond the first cycle of 10ε_y, a gradual increment in the out-of-plane deformations were captured until the test ended. The actual onset of instability occurred during the third cycle for 12ε_y. The large out-of-plane buckling displacement in the last cycle corresponding to 12ε_y, led to concrete cover crushing and spalling in the bottom region. The failure mode captured in the last cycle was a combination of buckling instability and shear failure. The axial force at this stage was 55% of the target compressive force.

Bar fracture was not detected during or after the test. The stirrups remained as originally constructed, however, the 90 degree hook of the ties opened where the severe damage was concentrated. Analysis of the data from this test will continue, as a consequence the material presented here should be considered preliminary. Further experiments will reveal more information about the effectiveness of the reinforcement detailing recommended in guidelines to prevent lateral instability in RC structural walls.

Stability of Ductile RC Structural Walls – Assessment of the Local Buckling Failure Mode

Test 7

July – 21 – 2016

Summary Report

Prepared for:

Alaska Department of Transportation

Prepared by:

RA – Ana Gabriela Haro

PIs – Mervyn Kowalsky and Rob Chai

North Carolina State University

Raleigh – NC

1. Executive Summary

Test 7 was conducted at the Constructed Facilities Laboratory on Thursday, July 21, 2016, as part of the second phase related to the load path project. The specimen was designed and built simulating boundary elements from prototype walls. An axial compression load followed by cyclic axial tensile displacements and compressive loads were applied to the specimen to capture its structural performance and to determine additional critical parameters associated with lateral instability of RC walls. The first part of the results are presented in this report. Further analyses will be elaborated.

2. Introduction

Recent earthquakes in New Zealand and Chile have illustrated the importance of out-of-plane stability of concrete wall elements due to in-plane loading. Pier walls are occasionally employed by Alaska DOT for their in-plane lateral stiffness. While these walls are normally thicker than the walls typically found in building applications, their clear heights are also larger, giving rise to height-to-thickness ratios which may be larger than that of buildings. Some analyses have demonstrated that walls as thick as 20 in. may be prone to buckling, depending on their length and height.

Noticing the concentration of damage in the boundary elements of rectangular reinforced concrete structural walls due to higher stress and strain demands, some past investigations by others have been carried out on prisms, which was found to be an economical way to study the inelastic instability of structural walls. In general, the main objective of these tests focuses on subjecting specimens to cyclic tension and compression actions to simulate vertical components of actual seismic loading.

While past tests on prisms has shown existing models to be promising, missing from the models is the interaction with out-of-plane loading. The existing models correlate tensile strain from in plane loading to out-of-plane deformation, assuming a prescribed curvature distribution. If loading occurs in the out-of-plane direction, the relationship between tensile strain and out-of-plane deformations must be adjusted to reflect this. In its simplest form, this would be an addition of an out-of-plane displacement to the existing equation. However, out-of-plane displacement may impact the distribution of curvature with height, thus requiring additional adjustments to the models.

A total of 12 prisms are being experimentally tested in the Constructed Facilities Laboratory (CFL) during this project. The support conditions for the 12 prisms are conceived as fixed-fixed. The first testing phase involved controlled load paths where the specimens were subjected to tension/compression cycles in addition to lateral loading to mimic the effects of out-of-plane displacements. In the second phase, longitudinal reinforcement ratios varied to consider the typical values employed by Alaska DOT for pier walls. The details associated with the two phases are presented in Table A-13.

Table A-13. Test 7: Description of the experimental phases

Phase	Tests	Geometry	Reinforcement	Loading
1	6	Thickness and Height (based on prototype wall). (6”x12” ; actual geometry = 5”x12”)	Longitudinal (6bars#5) and transverse (#3@2in) reinforcement ratios similar for the 6 specimens.	Controlled 3D load path
2	6	Same as phase 1 (Based on actual pier walls formerly used by the Alaska DOT)	Longitudinal reinforcement ratio varies. (3 specimens 6bars#4 and 3 specimens 6bars#3)	Controlled 3D load path

This first phase consisted of testing six 1/2-scale identical specimens. The thickness of the prisms was 5 in. since the cover was excluded from the construction. The geometry used was 5x12x60 in., corresponding to an aspect ratio (*h/b = height/thickness*) of 10 (including the missing cover). The longitudinal reinforcement ratio was 2.6% (6 bars #5). Transverse reinforcement consisted of #3 diameter rebar spaced at 2 in. and was placed as shown in Figure A-145.

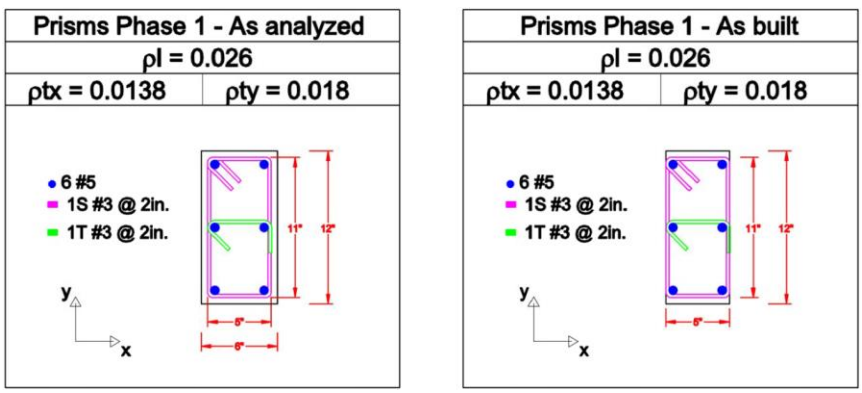

Figure A-145. Test 7: Phase 1 - Cross section of the prisms

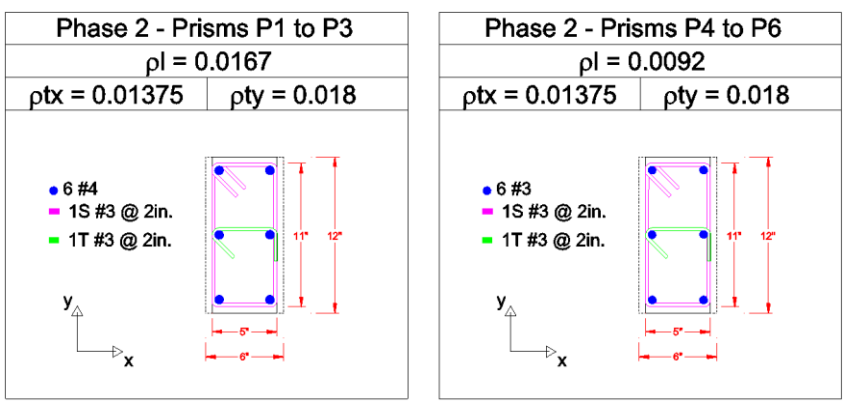

Figure A-146. Test 7: Phase 2 - Cross section of the prisms

The first phase concluded in June 2016. During the second phase, six more specimens are being tested following similar load protocols. The geometry of the six specimens is the same as the one adopted during the first phase, 5x12x60 in. Two different longitudinal ratios are used. The first three specimens consist of 6 #4 longitudinal bars and the other three specimens consist of 6 bars #3, corresponding to reinforcement ratios of 1.7% and 0.9%, respectively. The distribution of transverse reinforcement is similar to the one used for the first phase, Figure A-146.

Regarding the material properties, an unconfined concrete strength of 5 ksi and reinforcement yielding strength of 60 ksi were considered as design values to define the load/displacement history for the test. Table A-14 shows the actual steel tensile test properties for the #3 and #4 bars associated with the first three specimens of the second phase. The reinforcement detailing was established according to the ACI 318 and NEHERP guidelines for ductile columns and boundary elements.

Table A-14. Test 7: Phase 2 - Steel tensile test properties for bars #3 and #4

Sample No.	Bar #	fy (ksi)	εy = fy/Es	fu (ksi)	εu
1	3	68.7	0.0024	100.1	0.0909
2	3	69.3	0.0024	101.2	0.0796
3	3	71.4	0.0025	100.9	0.0764
4	3	68.1	0.0023	100.6	0.1035
5	3	69.8	0.0024	100.5	0.1119
6	3	71.6	0.0025	100.9	0.1021
#3 Average		**69.8**	**0.00241**	**100.7**	**0.0941**
1	4	71.0	0.0024	93.6	0.1261
2	4	68.1	0.0023	90.7	0.1109
3	4	69.0	0.0024	90.9	0.0955
4	4	67.9	0.0023	91.0	0.1192
5	4	67.3	0.0023	90.3	0.0867
6	4	71.0	0.0024	94.3	0.1031
#4 Average		**69.1**	**0.00238**	**91.8**	**0.1069**

3. Test Setup

The test setup consisted of a 14 ft long steel loading beam placed on the top of the specimen and connected to three actuators: two vertically inclined 440 kips actuators which induce axial loads and one horizontal 55 kips actuator to apply out-of-plane displacements. Two steel frames are used to restrain torsion in the loading beam. Two concrete blocks attached to the strong floor support the specimen to reach the required height associated with the effective length of the 440 kips actuators. Figure A-147 displays the test setup drawings and Figure A-148 shows a picture of the area where the components of the project are placed.

The horizontal actuator is controlled by displacements. The vertically inclined actuator located at the left hand side of the specimen, Figure A-147, is controlled by rotations captured throughout an inclinometer attached to the loading beam. The actuator placed at the right hand of the specimen is controlled by a combination of forces and displacements. Loads and strokes in the actuators are measured through integrated LVDTs and loads cells.

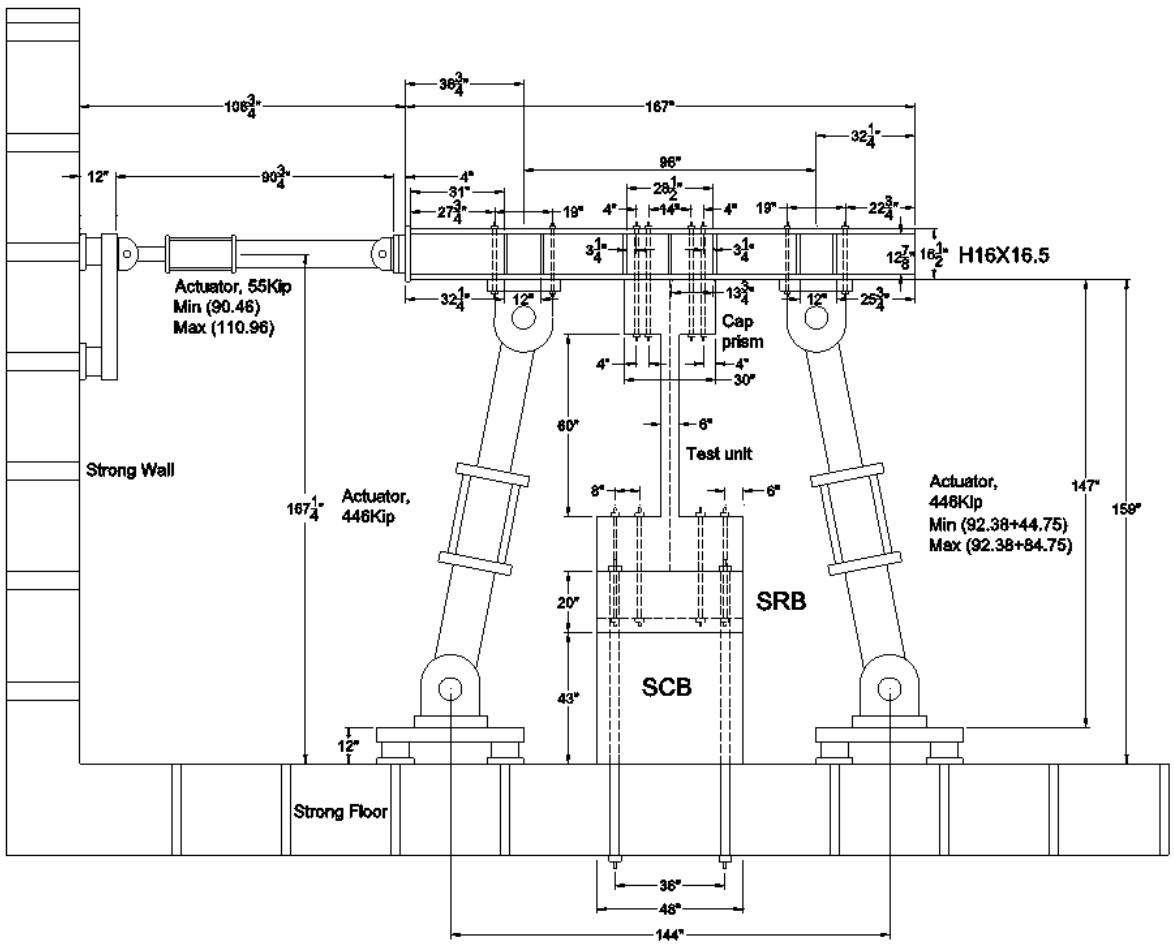

Figure A-147. Test 7: Test setup drawings

Relative displacements resulting from the interaction between the specimen and the connecting concrete block were obtained through 2 linear potentiometers. In addition, axial deformations of the prism were registered through 4 string potentiometers. Another string potentiometer was used to capture the lateral displacement of the loading beam.

Figure A-148. Test 7: Test setup in the CFL at NC State

A total of 110 infrared LEDs from the optical tracking system Optotrak Certus developed by Northern Digital Inc. were placed directly on the steel reinforcement of the prism. The objective is to establish longitudinal and transverse strains in real time throughout the MATLAB code "REALSTRAIN", created during the first phase of the project. Four additional infrared LEDs were positioned on the front face of the prism cap as a plane of reference. For the second phase, REALSTRAIN has been modified to capture, in addition, real time displacements of the prism cap. Figure A-149 shows the distribution of the LEDs on the right face of the prism and the overall allocation of the markers obtained from the Optotrak spatial coordinate output.

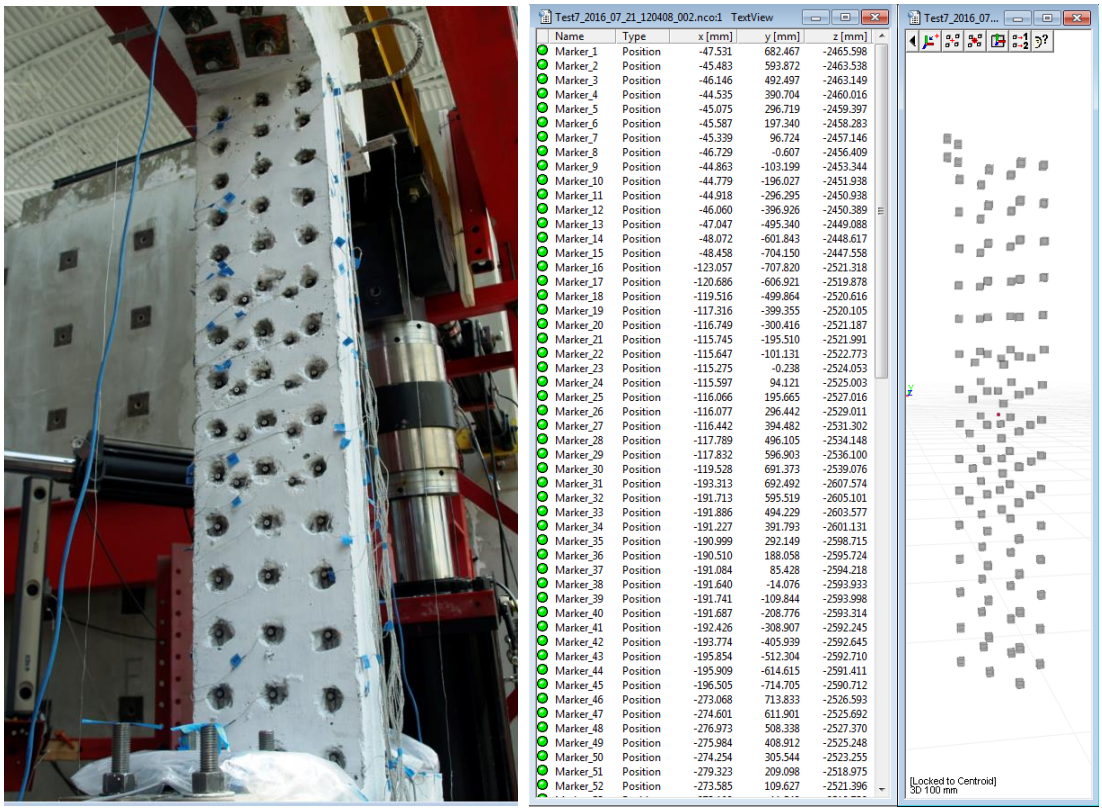

Name	Type	x [mm]	y [mm]	z [mm]
Marker_1	Position	-47.531	682.467	-2465.598
Marker_2	Position	-45.483	593.872	-2463.538
Marker_3	Position	-46.146	492.497	-2463.149
Marker_4	Position	-44.535	390.704	-2460.016
Marker_5	Position	-45.075	296.719	-2459.397
Marker_6	Position	-45.587	197.340	-2458.283
Marker_7	Position	-45.339	96.724	-2457.146
Marker_8	Position	-46.729	-0.607	-2456.409
Marker_9	Position	-44.863	-103.199	-2453.344
Marker_10	Position	-44.779	-196.027	-2451.938
Marker_11	Position	-44.918	-296.295	-2450.938
Marker_12	Position	-46.060	-396.926	-2450.389
Marker_13	Position	-47.047	-495.340	-2449.088
Marker_14	Position	-48.072	-601.843	-2448.617
Marker_15	Position	-48.458	-704.150	-2447.558
Marker_16	Position	-123.057	-707.820	-2521.318
Marker_17	Position	-120.686	-606.921	-2519.878
Marker_18	Position	-119.516	-499.864	-2520.616
Marker_19	Position	-117.316	-399.355	-2520.105
Marker_20	Position	-116.749	-300.416	-2521.187
Marker_21	Position	-115.745	-195.510	-2521.991
Marker_22	Position	-115.647	-101.131	-2522.773
Marker_23	Position	-115.275	-0.238	-2524.053
Marker_24	Position	-115.597	94.121	-2525.003
Marker_25	Position	-116.066	195.665	-2527.016
Marker_26	Position	-116.077	296.442	-2529.011
Marker_27	Position	-116.442	394.482	-2531.302
Marker_28	Position	-117.789	496.105	-2534.148
Marker_29	Position	-117.832	596.903	-2536.100
Marker_30	Position	-119.528	691.373	-2539.076
Marker_31	Position	-193.313	692.492	-2607.574
Marker_32	Position	-191.713	595.519	-2605.101
Marker_33	Position	-191.886	494.229	-2603.577
Marker_34	Position	-191.227	391.793	-2601.131
Marker_35	Position	-190.999	292.149	-2598.715
Marker_36	Position	-190.510	188.058	-2595.724
Marker_37	Position	-191.084	85.428	-2594.218
Marker_38	Position	-191.640	-14.076	-2593.933
Marker_39	Position	-191.741	-109.844	-2593.998
Marker_40	Position	-191.687	-208.776	-2593.314
Marker_41	Position	-192.426	-308.907	-2592.245
Marker_42	Position	-193.774	-405.939	-2592.645
Marker_43	Position	-195.854	-512.304	-2592.710
Marker_44	Position	-195.909	-614.615	-2591.411
Marker_45	Position	-196.505	-714.705	-2590.712
Marker_46	Position	-273.068	713.833	-2526.593
Marker_47	Position	-274.601	611.901	-2525.692
Marker_48	Position	-276.973	508.338	-2527.370
Marker_49	Position	-275.984	408.912	-2525.248
Marker_50	Position	-274.254	305.544	-2523.255
Marker_51	Position	-279.323	209.098	-2518.975
Marker_52	Position	-273.585	109.627	-2521.396

Figure A-149. Test 7: Instrumentation – Optotrak LEDs distribution on right face of the specimen and Spatial coordinate output

4. Test Summary

The first part of the test consisted of applying an axial compressive load followed by a second part where cyclic axial tensile displacements and compressive loads were induced to the specimen, identified as P2-P7 (Phase 2 – Prism 7), after it returned to the initial position.

4.1 Monotonic Compressive Loading

Specimen P2-P7, first was subjected to an axial load equivalent to the design axial compression capacity of the prism, *Po* = -322 kips. The purpose of this part of the test was to confirm that the boundary element of the wall could sustain this level of compressive load in the absence of lateral displacements.

The test was successfully conducted with no signs of damage. Strain profiles captured at this stage for each reinforcement line and for each face are displayed in Figure A-150. A total of 14 gages were established for each longitudinal bar along the 60 in. height, Y axis. The average compressive strain in both faces is close to -0.17%, which is less than the yielding compressive strain, -0.238%.

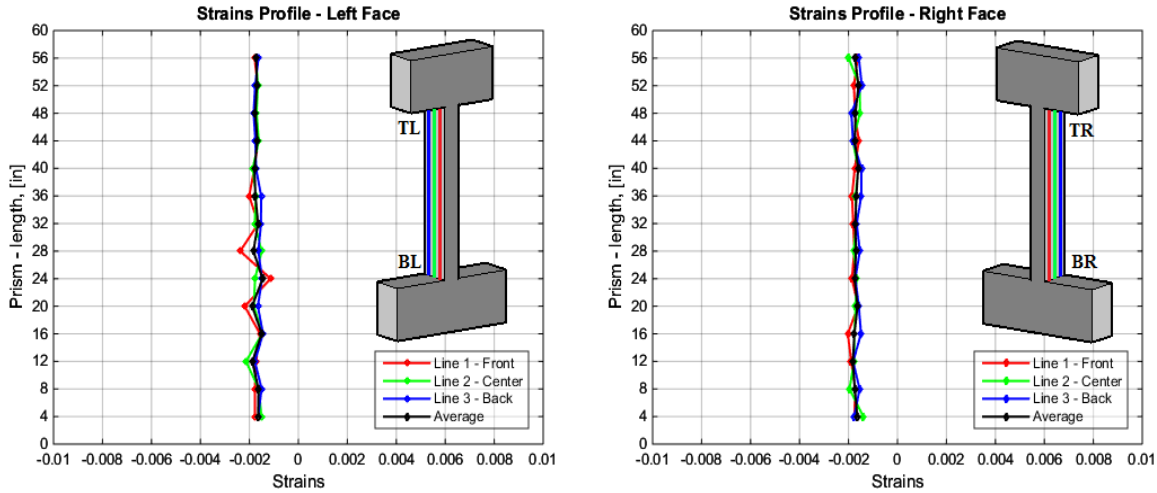

Figure A-150. Test 7: Strain profiles at maximum compressive load during stage # 1

4.2 Cyclic Axial Loading

A quasi-static displacement/load controlled procedure was established for the second part of the test. Unsymmetrical cycles were used to evaluate the seismic performance of prism P2-P7. The axial displacement history started with an elastic single cycle analytically predicted. After yielding, three identical cycles at different axial tensile displacement ductility levels continued until buckling was captured upon compressive loading. The unique compressive target was established from the first part of the experiment, corresponding to *Po* = -322 kips, which was applied on each cycle during the whole test, Figure A-151.

Damage propagation at $1\varepsilon_y$, $2\varepsilon_y$, $4\varepsilon_y$, and $6\varepsilon_y$ is presented in Figure A-152 through Figure A-155, respectively. Upon loading to $1\varepsilon_y$ small horizontal cracks appeared all along the prism and slightly extended to the moment connections. Crack widths of about 0.03in. were captured at the interface between the prism and the foundation. Upon compressive loads cracks uniformly closed as expected. This phenomenon was observed during the following cycles until instability was captured. In the course of the cycles corresponding to $2\varepsilon_y$, more small cracks formed and the old ones propagated. Crack widths close to 0.035 in. and 0.05 in. were captured at midheight during the $4\varepsilon_y$ and $6\varepsilon_y$ cycles, respectively. Throughout the following cycles the cracks became wider and the number of new cracks decreased. In addition, it was observed that the spacing of the horizontal cracks were generated by the cavities created to include the infrared LEDs.

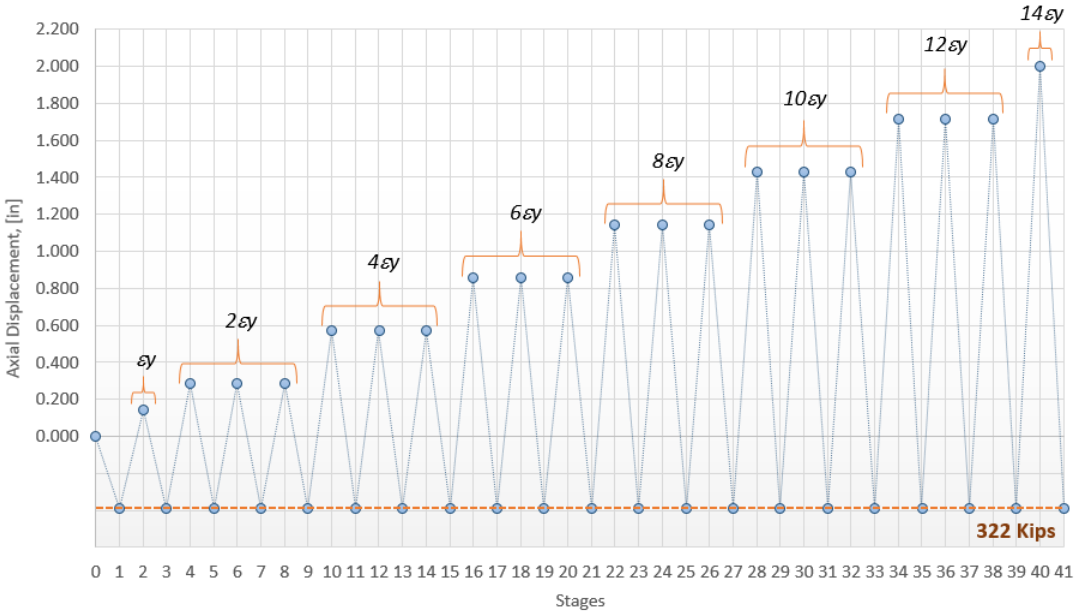

Figure A-151. Test 7: Displacement / Force History applied during the test

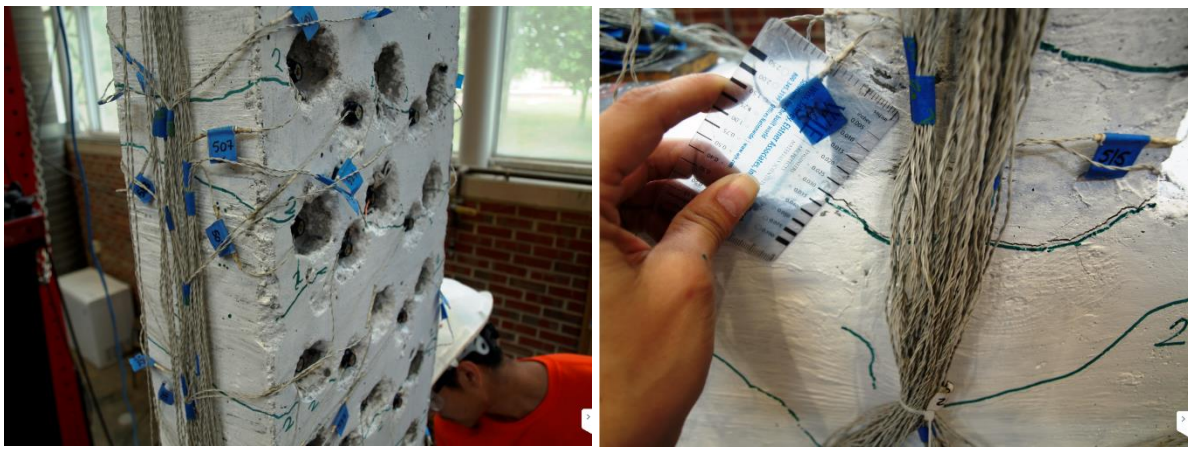

Figure A-152. Test 7: Propagation of damage at 1.0 εy

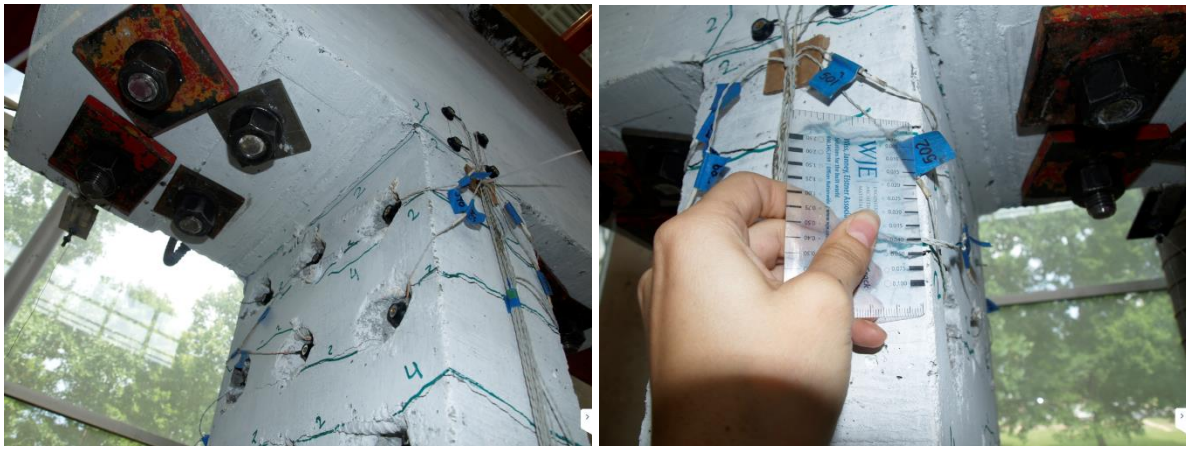

Figure A-153. Test 7: Propagation of damage at 2.0 εy - First cycle

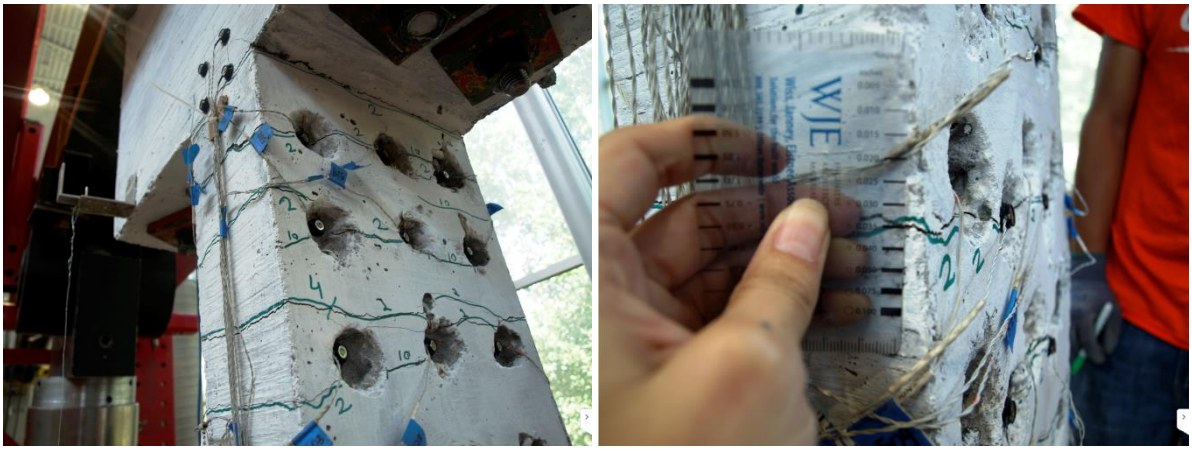

Figure A-154. Propagation of damage at 4.0 εy - First cycle

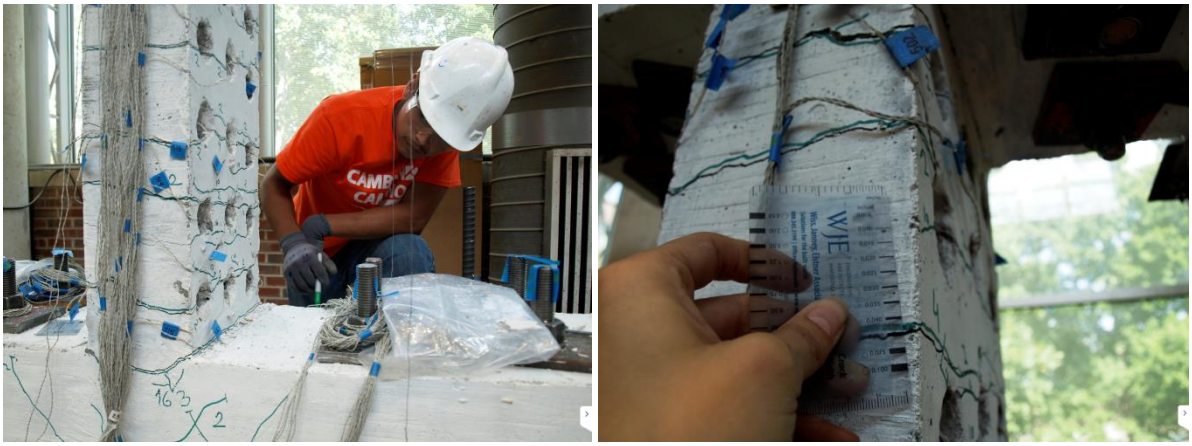

Figure A-155. Test 7: Propagation of damage at 6.0 εy - First cycle

Figure A-156 shows the propagation of damage for the cycles associated with $8\varepsilon_y$, where crack widths close to 0.075 in. were observed at midheight. Signs of concrete flaking on the footing-prism interface were observed in the first cycle at $10\varepsilon_y$. Vertical and diagonal cracks were also observed during this cycle and horizontal crack widths of about 0.10 in. were measured, Figure A-157. During the first cycle at $12\varepsilon_y$, cracks widths reached 1/8 in., Figure A-158. Upon tensile loads during the last cycle related to $12\varepsilon_y$, concrete cover fell down on the back face of the prism. The transverse reinforcement was exposed within a length of 14 in. Before resuming the test, debris was removed to protect the instrumentation and subsequently the target compressive load was reached. At this stage more concrete cover fell down in the same region exposing the transverse reinforcement within a length of 26 in., approximately, Figure A-159.

As tensile demands increased during the cycles related to $10\varepsilon_y$ and $12\varepsilon_y$ the out-of-plane buckling mechanism was visually captured upon compressive loading. In this scenario, where the out-of-plane

deformation is relatively small, the compression force developed to resist the overturning moment, can be fully reached as cracks close and consequently, the prism returns to a fairly straight and stable position.

Figure A-156. Test 7: Propagation of damage at 8.0 εy - First cycle

Figure A-157. Test 7: Propagation of damage at 10.0 εy - First cycle

Figure A-158. Test 7: Propagation of damage at 12.0 εy - First cycle

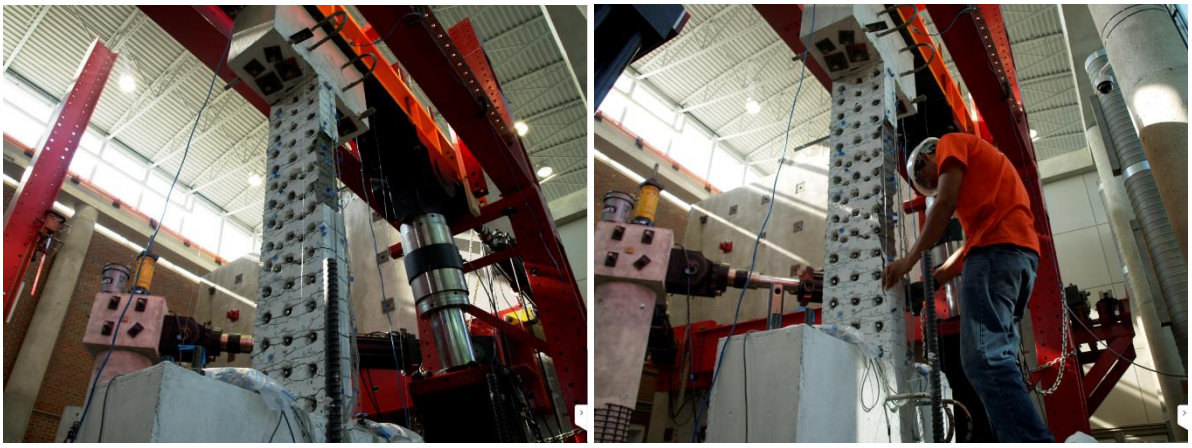

Figure A-159. Test 7: Concrete spalling upon tensile and compressive loads - Third cycle for 12.0 εy

Figure A-160. Test 7: Propagation of damage at 14.0 εy - First cycle

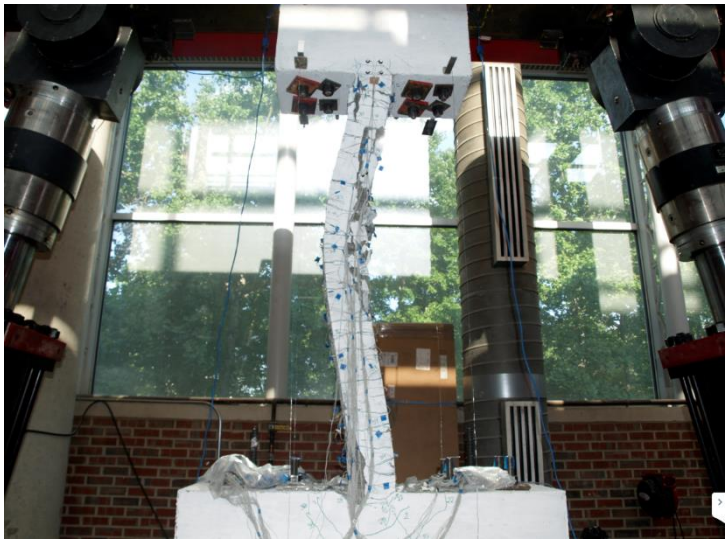

Figure A-161. Test 7: Instability captured upon compressive loads for 14εy – First cycle

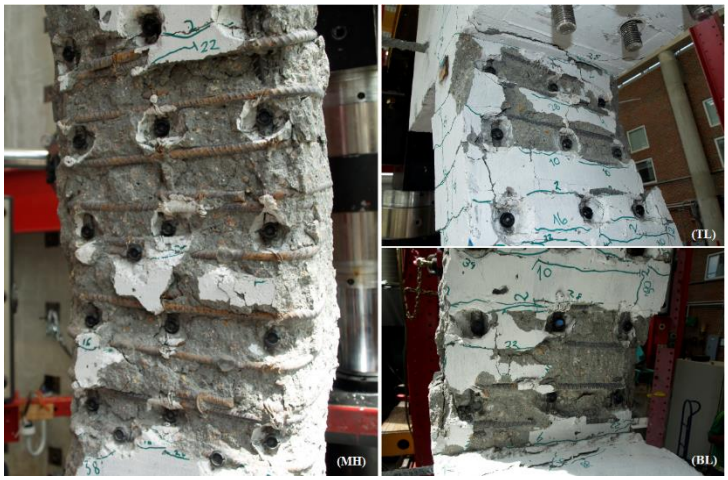

Figure A-162. Test 7: Final state at midheight, bottom and top regions

Cracks widths close to 3/16 in. were measured during the first cycle at $14\varepsilon_y$, Figure A-160. The distribution of cracks was uniform along the height of the prism. Upon compressive loading, instability occurred as illustrated in Figure A-161.

The end of the test showing local concrete crushing at midheight, Top left (TL) and Bottom left (BL) regions of the prism is presented in Figure A-162. Notice a well confined concrete core at this phase. A plumb line was used in order to identify manually out-of-plane deformations along the height of the prism, Figure A-163. It was observed that the maximum normalized out-of-plane deformation, δ/b = 4in./5in., exceeded 0.5. This measurement was taken once the prism was not subjected to any kind of loads.

Figure A-163. Test 7: Buckled shape of prism P2-P7

Figure A-164 depicts the entire structural response of P2-P7 as a function of axial forces captured from the vertical components of the actuators and axial displacements calculated from the optotrak system.

In the last 4 cycles an axial stiffness reduction is evident by the time the axial compressive load approaches -70 kips. At this phase, the specimen is still extended a length close to 1.0 in. These points where associated with the onset of out-of-plane buckling. Due to the intrinsic eccentricity in the developed compressive force, one side of the wall end region closes first resulting in out-of-plane deformations. Once the cracks close, the prism gains stiffness and is able to carry the same axial load as in previous cycles. In the last cycle, instability was captured since the prism was not able to recover its strength. The maximum applied load at this stage was -154 kips, equivalent to 47% of the axial design compressive force, *Po*.

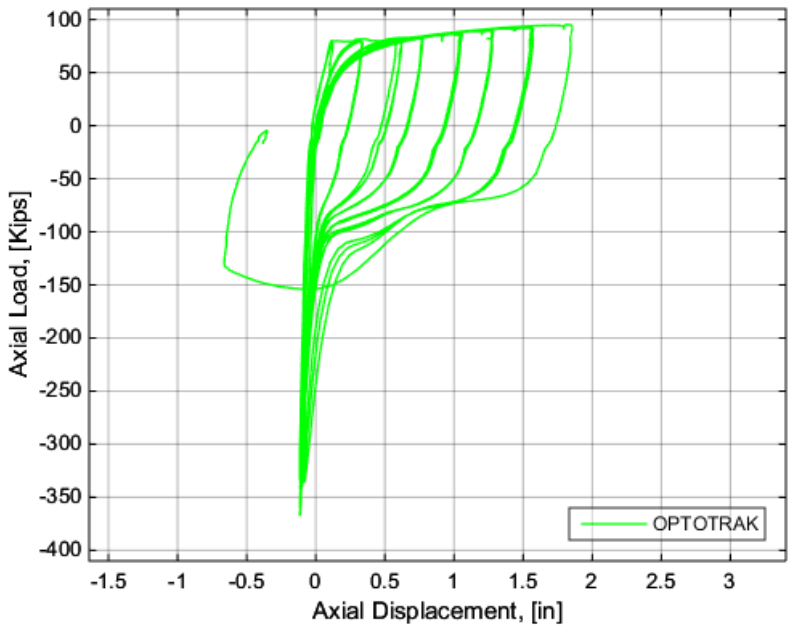

Figure A-164. Test 7: Axial structural response of prism P2-P7

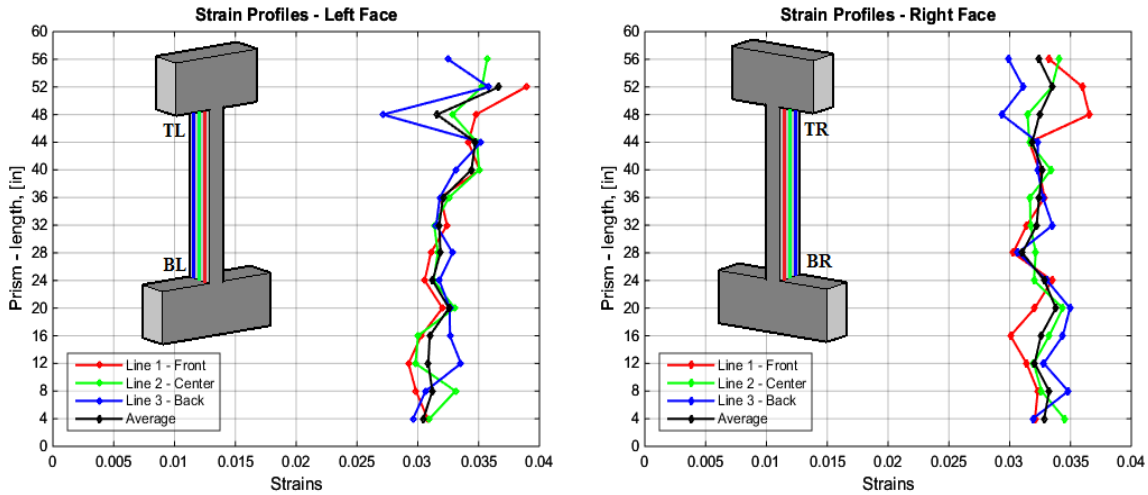

Figure A-165. Test 7: Strain profiles at 14 εy during the last cycle

Strain profiles captured during the last tensile cycle are presented in Figure A-165. The average of the strains in the left and right faces is 3.2%, close to the value established as target equivalent to 14ε_y. Figure A-166 illustrates the evolution of the nominal axial strain captured from gage 22 at the center of the specimen on the right face versus the normalized out-of-plane deformation and the axial force. The maximum compression strain reached a value of -2.3%. Figure A-167 shows the variation of strains computed from gage 67 located at the center of the prism on the left face. The maximum tensile strains captured during the last cycle upon compressive loads is 4.7%. The actual onset of instability is captured at the time the normalized out-of-plane displacement reaches -0.46. Notice a stable response of the prism at low levels of axial tensile strains.

The normalized out-of-plane displacements increased upon compressive loading during the first cycle associated with 8ε_y. A sudden increment on this deformation took place during the first cycle of 14ε_y at the time the compression load was -97 kips, which represents 30% of the axial design compressive force, *Po*. Yielding forces, *AsFy*, in tension and compression are also plotted in Figure A-166 and Figure A-167, where *As* is the area of the longitudinal reinforcement.

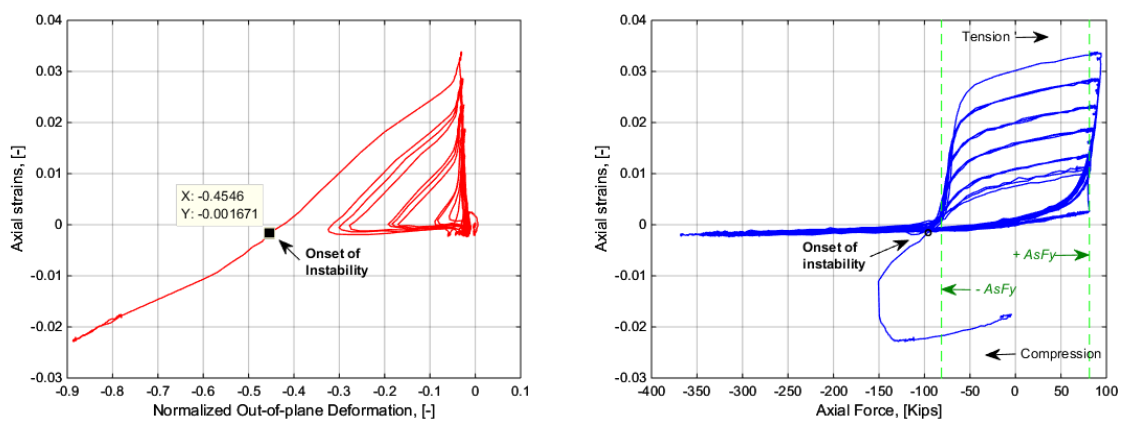

Figure A-166. Test 7: Response of specimen P2-P7 captured from a midheight gage on the right face

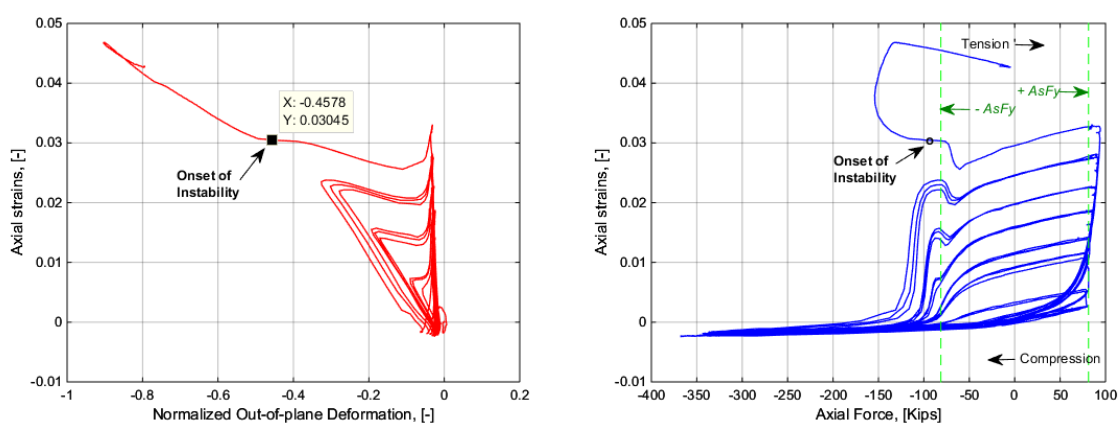

Figure A-167. Test 7: Response of specimen P2-P7 captured from a midheight gage on the left face

The evolution of the buckling shape during the last cycle of the test when the prism was subjected to compressive forces is plotted in Figure A-168. Four stages were considered: maximum tensile demand, onset of buckling, zero axial displacement, and maximum out-of-plane deformation, which is in total 4.35 in. located 4 in. above midheight.

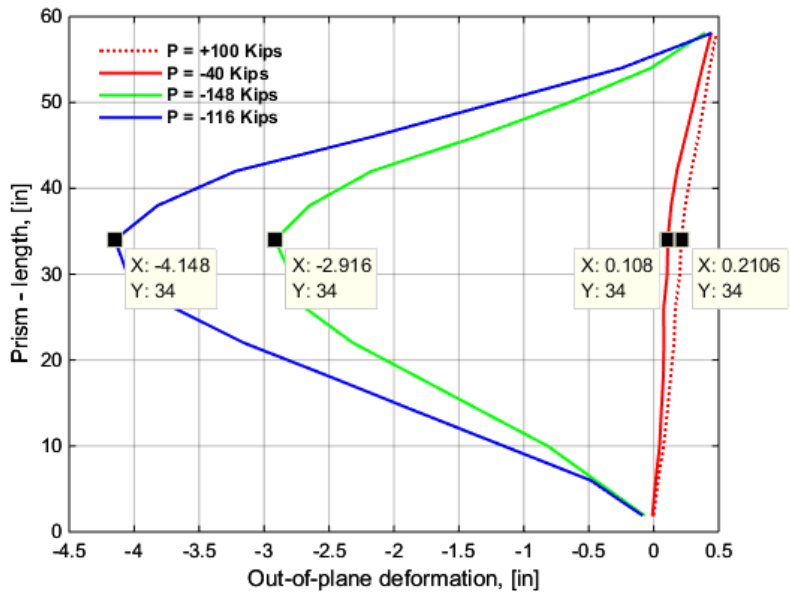

Figure A-168. Test 7: Evolution of the buckling shape during the last cycle under compressive loads

5. Conclusions

Specimen P2-P7 was tested during four hours where two loading patterns were applied. The first part of the test indicates the prism reached the maximum axial design compressive load with zero loss of capacity. The average compressive strain in both faces was close to -0.0017, less than the yielding strain.

In the second part of the test, progressive cyclic axial loads/strains were applied to the specimen reaching maximum values close to the axial design compressive force, *Po* = -322 kips and 14ε_y, in compression and tension, respectively. The specimen presented a stable response at low levels of axial tensile demands. Out-of-plane deformations were not noticed during the cycles before 8ε_y. Beyond the first cycle of 8ε_y, a gradual increase in the out-of-plane deformations were captured until instability developed during the first cycle of 14ε_y. The large buckling displacement led to concrete crushing and spalling in the central region. The axial force at this stage was 30% of the compressive force applied in a previous cycle.

Neither bar buckling nor bar fracture were detected during or after the test. The stirrups remained as originally constructed. Analysis of the data from this test will continue, as a consequence the material presented here should be considered preliminary. Further experiments will reveal more information

about the effectiveness of the reinforcement detailing recommended in guidelines to prevent lateral instability in RC structural walls.

Stability of Ductile RC Structural Walls – Assessment of the Local Buckling Failure Mode

Test 8

August – 17 – 2016

Summary Report

Prepared for:

Alaska Department of Transportation

Prepared by:

RA – Ana Gabriela Haro

PIs – Mervyn Kowalsky and Rob Chai

North Carolina State University

Raleigh – NC

1. Executive Summary

Test 8 was conducted at the Constructed Facilities Laboratory on Wednesday, August 17, 2016, as part of the second phase related to the load path project. The specimen was designed and built simulating boundary elements from prototype walls. A monotonic and constant lateral displacement equivalent to 4% drift was applied first to the specimen followed by cyclic axial tensile displacements and compressive loads. The purpose of this test was to capture the structural performance of the specimen #8 and to determine additional critical parameters associated with lateral instability of RC walls. The first part of the results are presented in this report. Further analyses will be elaborated.

2. Introduction

Recent earthquakes in New Zealand and Chile have illustrated the importance of out-of-plane stability of concrete wall elements due to in-plane loading. Pier walls are occasionally employed by Alaska DOT for their in-plane lateral stiffness. While these walls are normally thicker than the walls typically found in building applications, their clear heights are also larger, giving rise to height-to-thickness ratios which may be larger than that of buildings. Some analyses have demonstrated that walls as thick as 20 in. may be prone to buckling, depending on their length and height.

Noticing the concentration of damage in the boundary elements of rectangular reinforced concrete structural walls due to higher stress and strain demands, some past investigations by others have been carried out on prisms, which was found to be an economical way to study the inelastic instability of structural walls. In general, the main objective of these tests focuses on subjecting specimens to cyclic tension and compression actions to simulate vertical components of actual seismic loading.

While past tests on prisms has shown existing models to be promising, missing from the models is the interaction with out-of-plane loading. The existing models correlate tensile strain from in plane loading to out-of-plane deformation, assuming a prescribed curvature distribution. If loading occurs in the out-of-plane direction, the relationship between tensile strain and out-of-plane deformations must be adjusted to reflect this. In its simplest form, this would be an addition of an out-of-plane displacement to the existing equation. However, out-of-plane displacement may impact the distribution of curvature with height, thus requiring additional adjustments to the models.

A total of 12 prisms are being experimentally tested in the Constructed Facilities Laboratory (CFL) during this project. The support conditions for the 12 prisms are conceived as fixed-fixed. The first testing phase involved controlled load paths where the specimens were subjected to tension/compression cycles in addition to lateral loading to mimic the effects of out-of-plane displacements. In the second phase, longitudinal reinforcement ratios varied to consider the typical values employed by Alaska DOT for pier walls. The details associated with the two phases are presented in Table A-15.

This first phase consisted of testing six 1/2-scale identical specimens. The thickness of the prisms was 5 in. since the cover was excluded from the construction. The geometry used was 5x12x60 in., corresponding to an aspect ratio (*h/b = height/thickness*) of 10 (including the missing cover). The longitudinal reinforcement ratio was 2.6% (6 bars #5). Transverse reinforcement consisted of #3 diameter rebar spaced at 2 in. and was placed as shown in Figure A-169.

Table A-15. Test 8: Description of the experimental phases

Phase	Tests	Geometry	Reinforcement	Loading
1	6	Thickness and Height (based on prototype wall). (6”x12” ; actual geometry = 5”x12”)	Longitudinal (6bars#5) and transverse (#3@2in) reinforcement ratios similar for the 6 specimens.	Controlled 3D load path
2	6	Same as phase 1 (Based on actual pier walls formerly used by the Alaska DOT)	Longitudinal reinforcement ratio varies. (3 specimens 6bars#4 and 3 specimens 6bars#3)	Controlled 3D load path

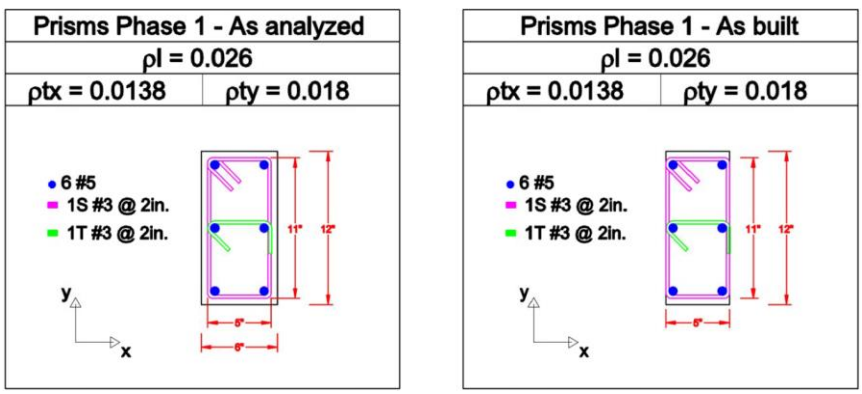

Figure A-169. Test 8: Phase 1 - Cross section of the prisms

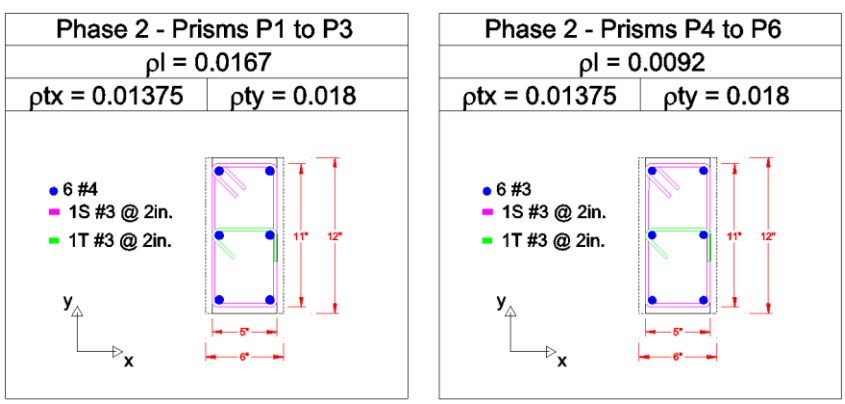

Figure A-170. Test 8: Phase 2 - Cross section of the prisms

The first phase concluded in June 2016. During the second phase, six more specimens are being tested following similar load protocols. The geometry of the six specimens is the same as the one adopted

during the first phase, 5x12x60 in. Two different longitudinal ratios are used. The first three specimens consist of 6 #4 longitudinal bars and the other three specimens consist of 6 bars #3, corresponding to reinforcement ratios of 1.7% and 0.9%, respectively. The distribution of transverse reinforcement is similar to the one used for the first phase, Figure A-170.

Regarding the material properties, an unconfined concrete strength of 5 ksi and reinforcement yielding strength of 60 ksi were considered as design values to define the load/displacement history for the test. Table A-16 shows the actual steel tensile test properties for the #3 and #4 bars associated with the first three specimens of the second phase. The reinforcement detailing was established according to the ACI 318 and NEHERP guidelines for ductile columns and boundary elements.

Table A-16. Test 8: Phase 2 - Steel tensile test properties for bars #3 and #4

Sample No.	Bar #	fy (ksi)	εy = fy/Es	fu (ksi)	εu
1	3	68.7	0.0024	100.1	0.0909
2	3	69.3	0.0024	101.2	0.0796
3	3	71.4	0.0025	100.9	0.0764
4	3	68.1	0.0023	100.6	0.1035
5	3	69.8	0.0024	100.5	0.1119
6	3	71.6	0.0025	100.9	0.1021
#3 Average		**69.8**	**0.00241**	**100.7**	**0.0941**
1	4	71.0	0.0024	93.6	0.1261
2	4	68.1	0.0023	90.7	0.1109
3	4	69.0	0.0024	90.9	0.0955
4	4	67.9	0.0023	91.0	0.1192
5	4	67.3	0.0023	90.3	0.0867
6	4	71.0	0.0024	94.3	0.1031
#4 Average		**69.1**	**0.00238**	**91.8**	**0.1069**

3. Test Setup

The test setup consisted of a 14 ft long steel loading beam placed on the top of the specimen and connected to three actuators: two vertically inclined 440 kips actuators which induce axial loads and one horizontal 55 kips actuator to apply out-of-plane displacements. Two steel frames are used to restrain torsion in the loading beam. Two concrete blocks attached to the strong floor support the specimen to reach the required height associated with the effective length of the 440 kips actuators. Figure A-171 displays the test setup drawings and Figure A-172 shows a picture of the area where the components of the project are placed.

The horizontal actuator is controlled by displacements. The vertically inclined actuator located at the left hand side of the specimen, Figure A-171, is controlled by rotations captured throughout an

inclinometer attached to the loading beam. The actuator placed at the right hand of the specimen is controlled by a combination of forces and displacements. Loads and strokes in the actuators are measured through integrated LVDTs and loads cells.

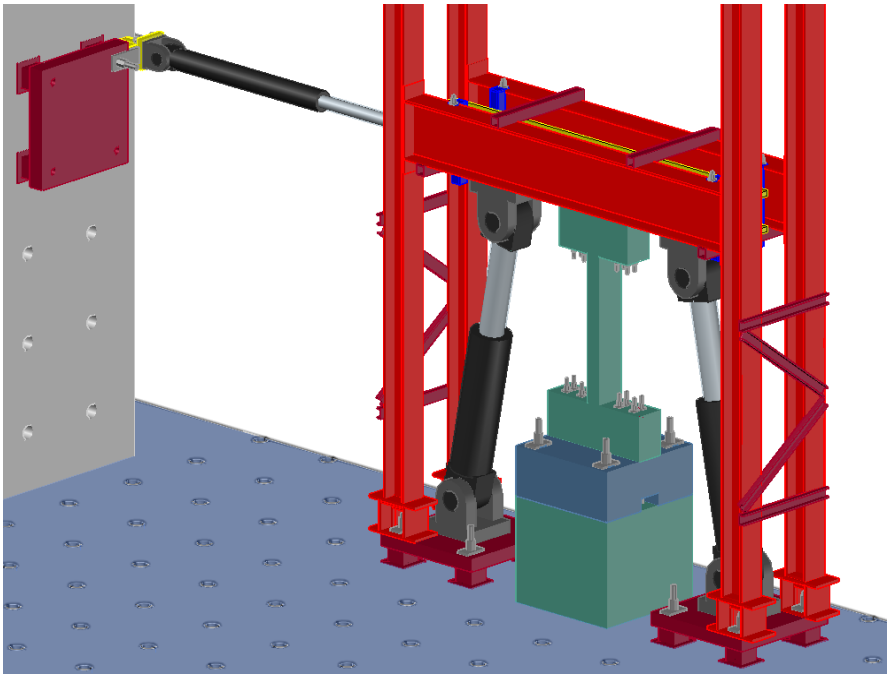

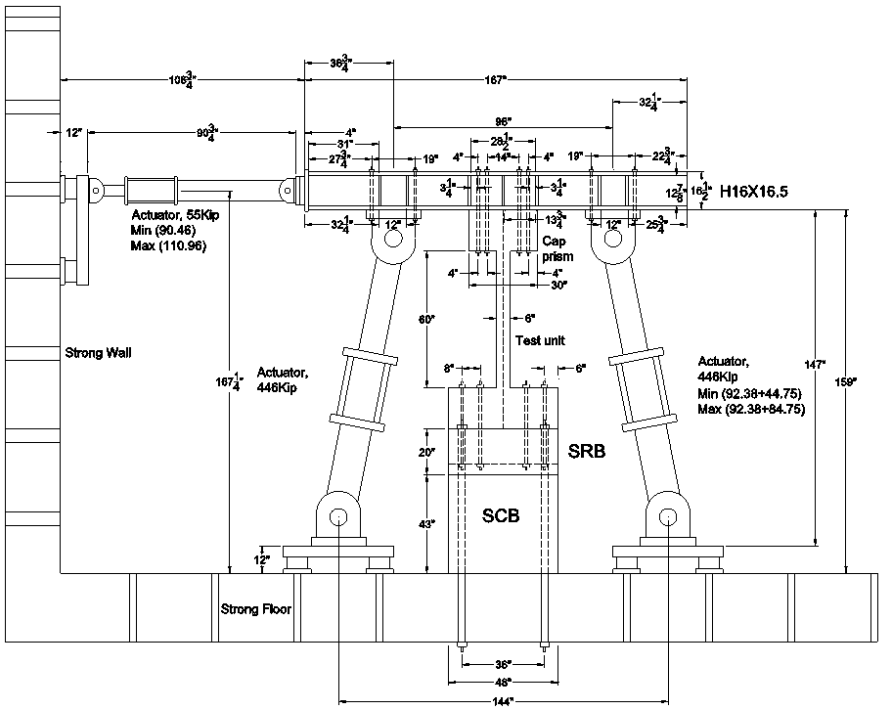

Figure A-171. Test 8: Test setup drawings

Figure A-172. Test 8: Test setup in the CFL at NC State

Relative displacements resulting from the interaction between the specimen and the connecting concrete block were obtained through 2 linear potentiometers. In addition, axial deformations of the prism were registered through 4 string potentiometers. Another string potentiometer was used to capture the lateral displacement of the loading beam.

A total of 110 infrared LEDs from the optical tracking system Optotrak Certus developed by Northern Digital Inc. were placed directly on the steel reinforcement of the prism. The objective is to establish longitudinal and transverse strains in real time throughout the MATLAB code "REALSTRAIN", created during the first phase of the project. Four additional infrared LEDs were positioned on the front face of the prism cap as a plane of reference. For the second phase, REALSTRAIN has been modified to capture, in addition, real time displacements of the prism cap. Figure A-173 shows the distribution of the LEDs on the right face of the prism and the overall allocation of the markers obtained from the Optotrak spatial coordinate output.

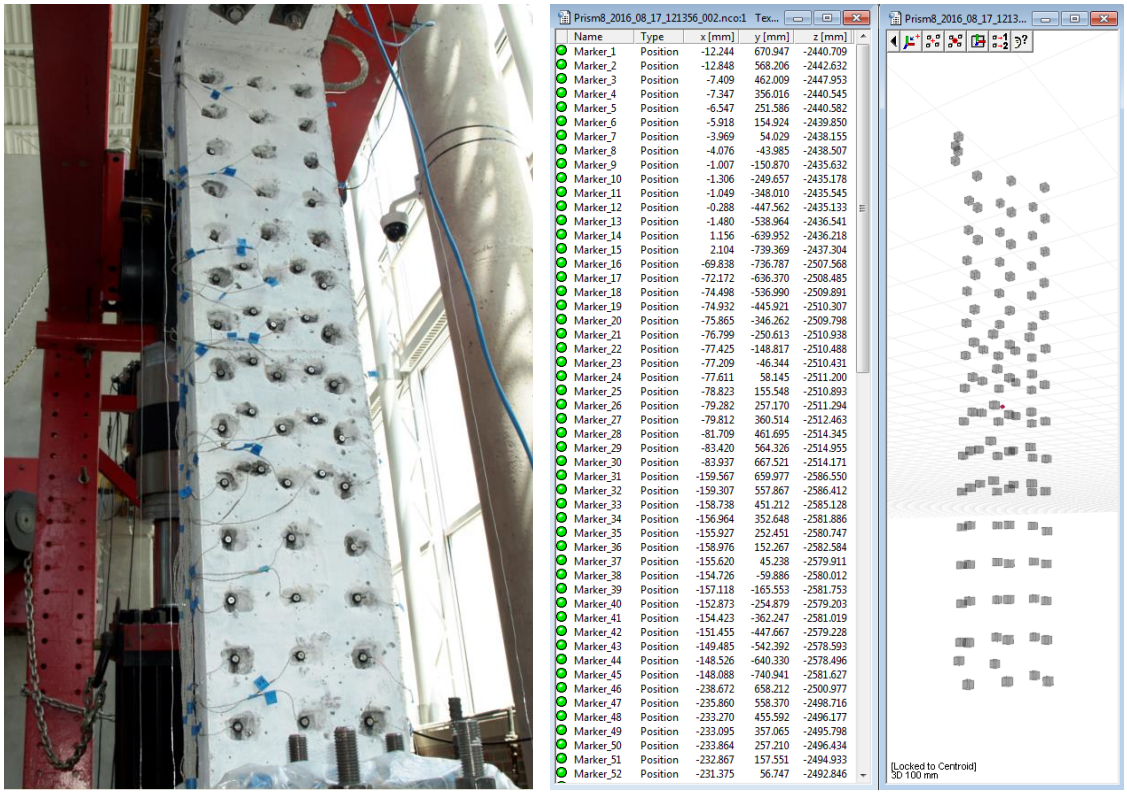

Figure A-173. Test 8: Instrumentation – Optotrak LEDs distribution on right face of the specimen and Spatial coordinate output

4. Test Summary

First, an out-of-plane displacement of 2.4 in., equivalent to 4% drift, was induced to specimen P2-P8 (Phase 2 – Prism 8). The purpose was to keep this displacement constant during the entire test, which in addition, included unsymmetrical cyclic axial compressive loads and tensile displacements. The axial displacement history started with two elastic single cycles analytically predicted. The targets in tension were chosen as fractions of the yielding displacement referred as: $0.75\varepsilon_y$ and $1.0\varepsilon_y$. Subsequently, three identical cycles at different axial tensile displacement ductility levels continued until buckling was captured upon compressive loading. The unique compressive target load, $P_{4\%}$ = -222 kips, was established considering P-Δ effects, representing 69% of the maximum axial design compressive load, Po = -322 kips, Figure A-174. The load $P_{4\%}$ was calculated following the linear interaction from Eq. (1).

$$P_{\%} = P_o - (P_O - P_b)\frac{M_{\%}}{M_b} \qquad (1)$$

where, P_b = 165 kips and M_b = 418 kip.in are the axial force and bending moment at balanced failure, respectively. The flexural moment at 4% out-of-plane drift ratio is $M_{4\%} = P_{4\%}(0.04*60in.)/2$. Substituting this expression in Eq. (1) and solving for $P_{4\%}$, the target value is obtained.

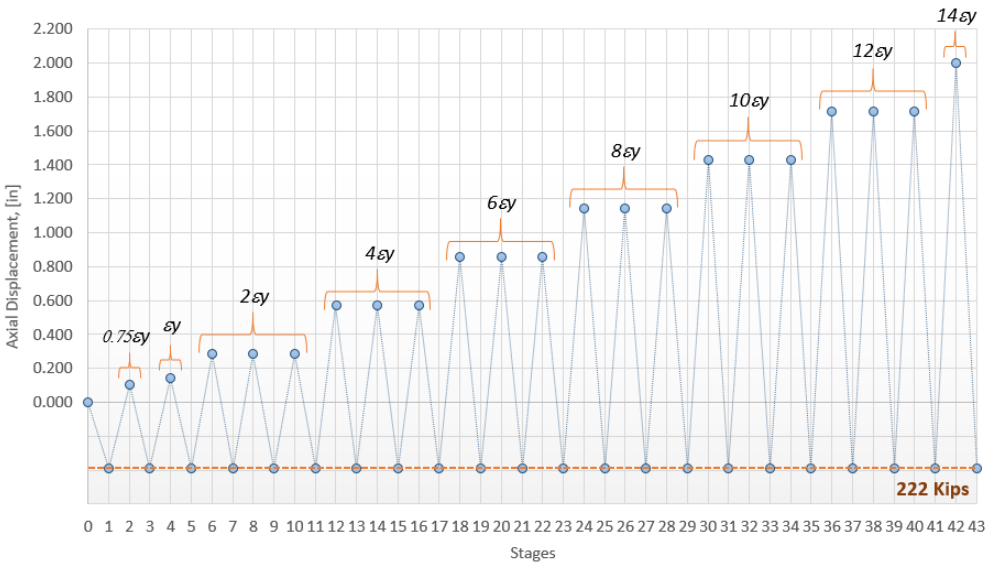

Figure A-174. Test 8: Axial Displacement / Force History applied during test #8

During the 2.4 in. lateral displacement, cracks appeared on the bottom left (BL) and top right (TR) regions of the prism, Figure A-175. Concrete flacking was observed on the bottom right (BR) and the top left (TL) regions. Strain profiles captured at this stage for each reinforcement line and for each face are displayed in Figure A-176, where the corresponding average has also been included. A total of 14 gages were established for each longitudinal bar along the 60 in. height, Y axis. Maximum tensile values close to 0.5% were calculated in the BL and TR regions, respectively.

Figure A-175. Test 8: Cracks at BL and TR regions at 2.4 in. out-of-plane displacement

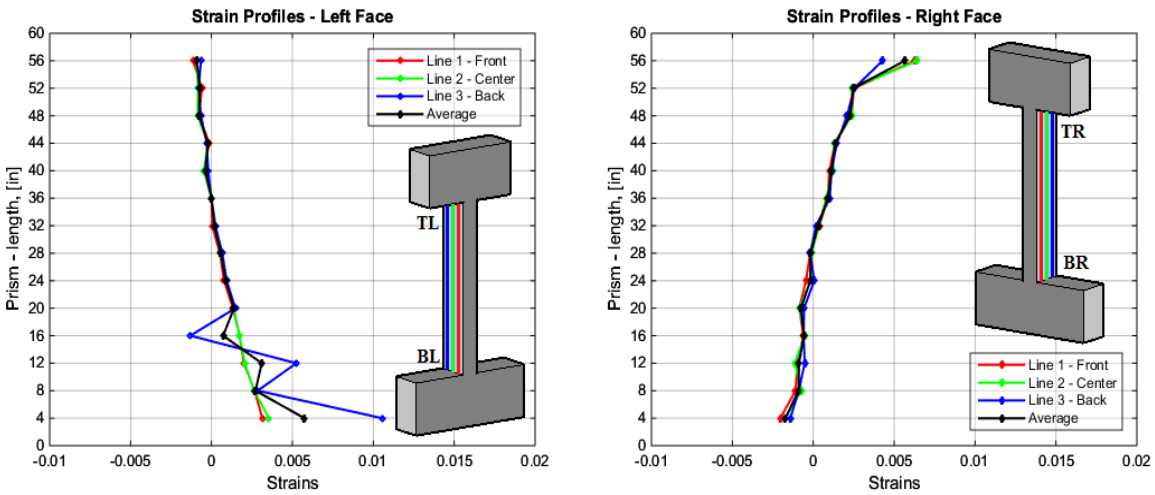

Figure A-176. Test 8: Strain profiles at 2.4 in. out-of-plane displacement

Subsequently, the first compressive load was induced to the specimen. Vertical cracks appeared in the concrete cover at TL and BR regions accompanied by concrete spalling, Figure A-177. In general, upon yielding tensile demands, horizontal cracks became more numerous and small cracks formed and extended to the beam-column connections.

Figure A-177. Test 8: Propagation of damage upon compressive loads during the first axial cycle

Damage propagation at $1\varepsilon_y$, $2\varepsilon_y$, $4\varepsilon_y$, and $6\varepsilon_y$ is presented in Figure A-178 through Figure A-181, respectively. Upon loading to $1\varepsilon_y$ small horizontal cracks appeared all along the prism and slightly extended to the moment connections. Crack widths of about 1/4 in. were captured at the interface between the prism and the footing. Upon compressive loads cracks uniformly closed as expected. This phenomenon was observed during the following cycles until instability was captured. In the course of the cycles corresponding to $2\varepsilon_y$, new cracks formed and the old ones propagated. Crack widths close to 0.075 in. were captured at midheight. Throughout the following cycles the cracks became wider and

the number of new cracks decreased. In addition, it was observed that the horizontal cracks developed where the stirrups are located. Concrete spalling became more severe during the $4\varepsilon_y$ and $6\varepsilon_y$ cycles.

Figure A-178. Test 8: Propagation of damage at 1.0 εy

Figure A-179. Test 8: Propagation of damage at 2.0 εy - First cycle

Figure A-180. Test 8: Propagation of damage at 4.0 εy - First cycle

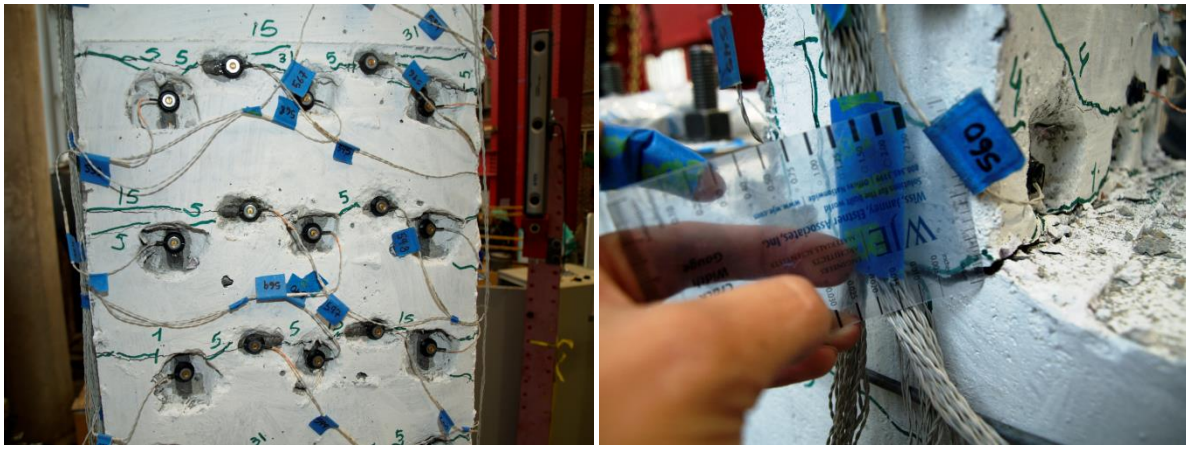

Figure A-181. Test 8: Propagation of damage at 6.0 εy - First cycle

Figure A-182 shows the propagation of damage for the cycles associated with $8\varepsilon_y$, where crack widths close to 3/16 in. and 0.075 in. were observed at the prism-footing interface and midheight, respectively. Propagation of concrete spalling on the TL region were observed in the first cycle at $10\varepsilon_y$. Diagonal cracks were also observed during this cycle and horizontal crack widths of about 1/8 in. were measured at midheight, Figure A-183. During the first cycle at $12\varepsilon_y$, cracks widths reached 1/4 in. at the prism-footing, Figure A-184. After the cycles associated with $12\varepsilon_y$, the transverse reinforcement was exposed within a length of 12 in. on the TL and BR regions.

Figure A-182. Test 8: Propagation of damage at 8.0 εy - First cycle

Figure A-183. Test 8: Propagation of damage at 10.0 εy - First cycle

Figure A-184. Test 8: Propagation of damage at 12.0 εy - First cycle

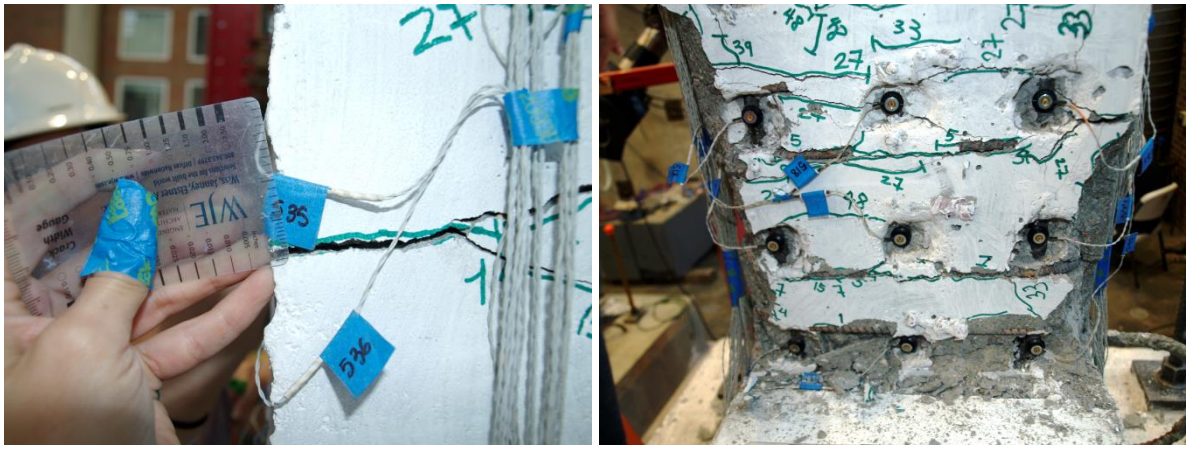

Figure A-185. Test 8: Propagation of damage at 14.0 εy - First cycle

As tensile demands increased during the cycles related to $10\varepsilon_y$ and $12\varepsilon_y$ the out-of-plane buckling mechanism was visually captured upon compressive loading. In this scenario, where the out-of-plane deformation is relatively small, the compression force developed to resist the overturning moment, can be fully reached as cracks close and consequently, the prism returns to a fairly straight and stable position. Cracks widths close to 5/32 in. were measured at midheight during the first cycle at $14\varepsilon_y$, Figure A-185. The distribution of cracks was nearly uniform along the height of the prism. Upon compressive loading, instability occurred as illustrated in Figure A-186. The end of the test showing local concrete crushing at midheight, Top left (TL) and Bottom left (BL) regions of the prism is presented in Figure A-187. Notice a well confined concrete core at this phase.

Figure A-186. Test 8: Instability captured upon compressive loads for 14εy – First cycle

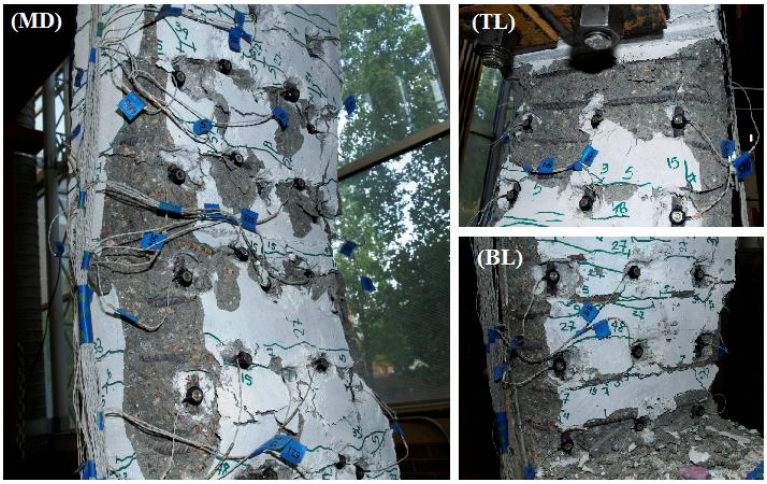

Figure A-187. Test 8: Final state at midheight (MD), bottom left (BL) and top left (TL) regions

Figure A-188 depicts the entire structural response of P2-P8 as a function of axial forces captured from the vertical components of the actuators and axial displacements calculated from the Optotrak system. In the last 4 cycles an axial stiffness reduction is evident by the time the axial compressive load approaches -60 kips. At this phase, the specimen is still extended a length close to 1.0 in. These points are associated with the onset of out-of-plane buckling. Due to the intrinsic eccentricity in the developed compressive force, one side of the wall end region closes first resulting in out-of-plane deformations. Once the cracks close, the prism gains stiffness and is able to carry the same axial load as in previous cycles. In the last cycle, instability was captured since the prism was not able to recover its strength. The maximum applied load at this stage was -189 kips, equivalent to 85% of the axial design compressive force considering P-Δ effects, $P_{4\%}$ = 222 kips.

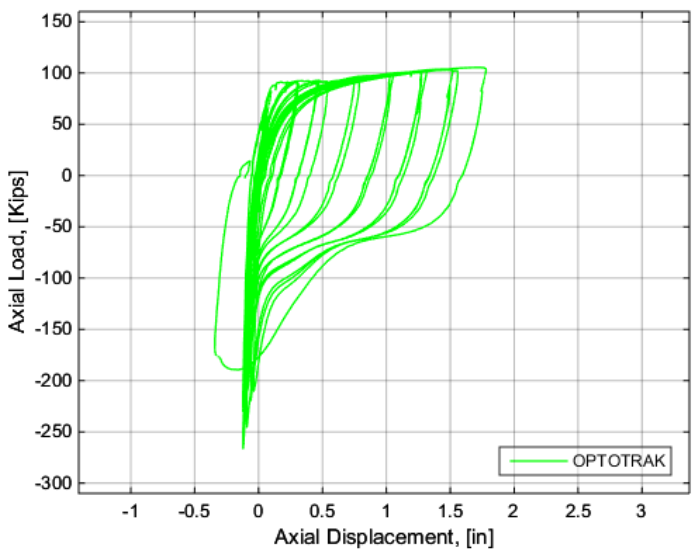

Figure A-188. Test 8: Axial structural response of prism P2-P8

Strain profiles captured during the last tensile cycle are presented in Figure A-189. The average of the strains in the left face 3.2% and the right face is 3.3%, close to the value established as target equivalent to $14\varepsilon_y$. Figure A-190 illustrates the evolution of the nominal axial strain captured from gage 22 at the center of the specimen on the right face versus the normalized out-of-plane deformation and the axial force. The maximum compression strain reached a value of -3.7%.

Figure A-191 shows the variation of strains computed from gage 67 located at the center of the prism on the left face. The maximum tensile strains captured during the last cycle upon compressive loads is 3.6%. The actual onset of instability is captured at the time the relative normalized out-of-plane displacement reaches -0.15. Notice a stable response of the prism at low levels of axial tensile strains. The normalized out-of-plane displacements increased upon compressive loading during the first cycle associated with $8\varepsilon_y$. A sudden increment on this deformation took place during the first cycle of $14\varepsilon_y$

at the time the compression load was -97 kips, which represents 30% of the axial design compressive force, *Po*. Yielding forces, *AsFy*, in tension and compression are also plotted in Figure A-190 and Figure A-191, where *As* is the area of the longitudinal reinforcement.

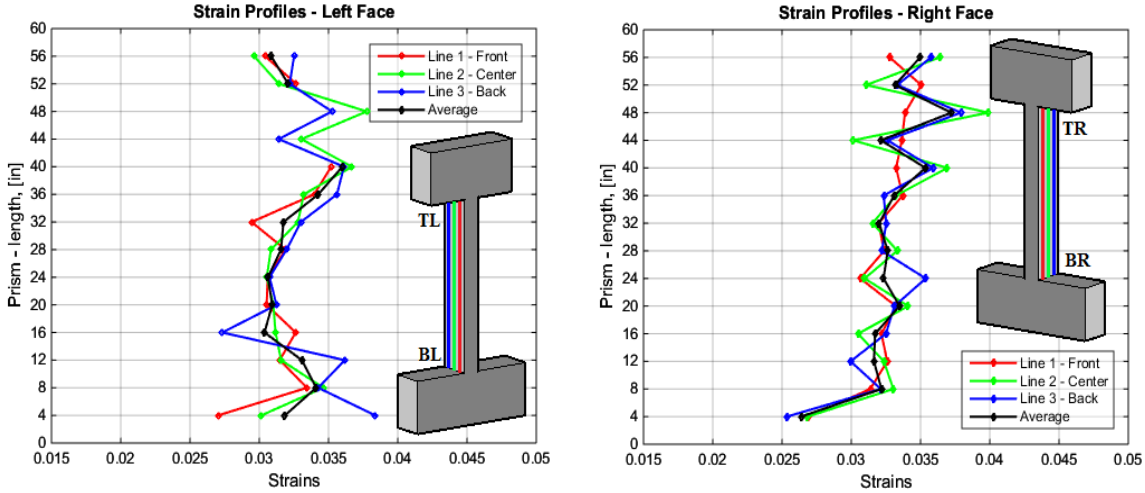

Figure A-189. Test 8: Strain profiles at 14 εy during the last cycle

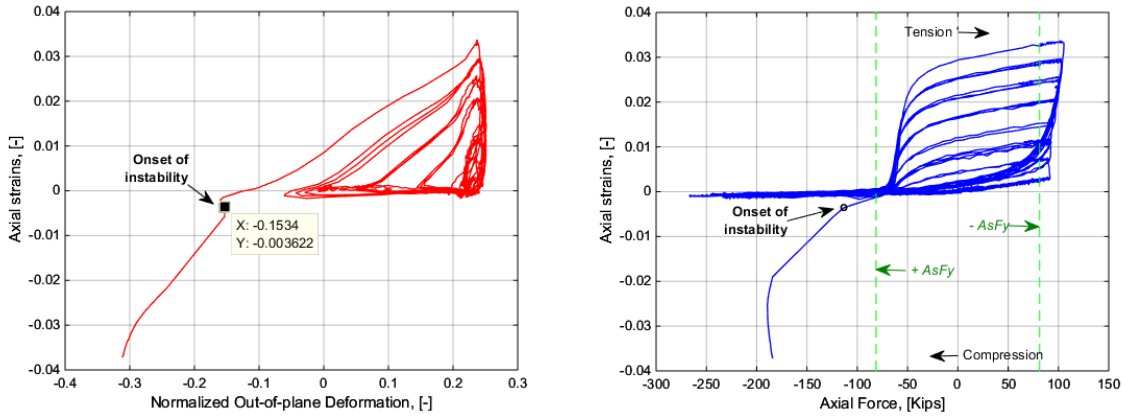

Figure A-190. Test 8: Response of specimen P2-P8 captured from a midheight gage on the right face

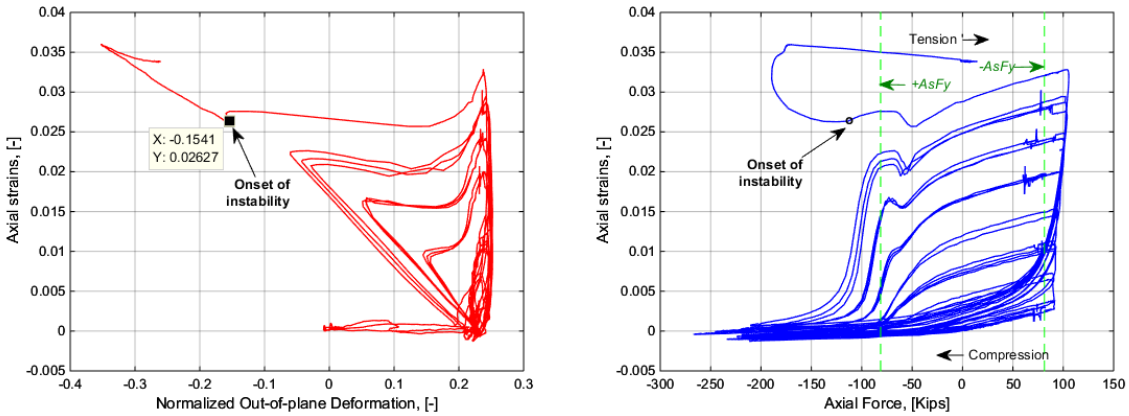

Figure A-191. Test 8: Response of specimen P2-P8 captured from a midheight gage on the left face

The evolution of the buckling shape during the last cycle of the test when the prism was subjected to compressive forces is plotted in Figure A-192. Four stages were considered: maximum tensile demand, onset of buckling, zero axial displacement, and maximum out-of-plane deformation, which is in total 1.856 + 0.887 = 2.74 in. located at midheight.

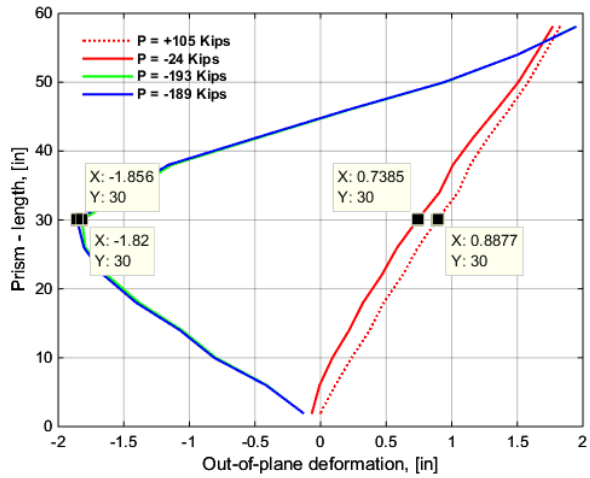

Figure A-192. Test 8: Evolution of the buckling shape during the last cycle under compressive loads

5. Conclusions

Specimen P2-P8 was tested during five hours where two loading patterns were applied. During the first part, a monotonic out-of-plane displacement was induced until reaching a target of 2.4 in. equivalent to 4% drift. Maximum tensile values close to 0.5% were determined in the bottom left (BL) and top right (TR) regions, beyond the yielding strain.

In the second part of the test, progressive cyclic axial loads/strains were applied to the specimen reaching maximum values close to the axial compressive force including P-Δ effects, $P_{4\%}$ = -222 kips and 14ε_y, in compression and tension, respectively. The specimen presented a stable response at low levels of axial tensile demands. Out-of-plane deformations were not noticed during the cycles before 8ε_y. Beyond the first cycle of 8ε_y, a gradual increase in the out-of-plane deformations were captured until instability occurred during the first cycle of 14ε_y. The large buckling displacement led to concrete crushing and spalling in the central region of the prism. The axial force at this stage was 85% of the compressive force applied in a previous cycle.

Neither bar buckling nor bar fracture were detected during or after the test. The stirrups remained as originally constructed. Analysis of the data from this test will continue, as a consequence the material presented here should be considered preliminary. Further experiments will reveal more information about the effectiveness of the reinforcement detailing recommended in guidelines to prevent lateral instability in RC structural walls.

Stability of Ductile RC Structural Walls – Assessment of the Local Buckling Failure Mode

Test 9

August – 31 – 2016

Summary Report

Prepared for:

Alaska Department of Transportation

Prepared by:

RA – Ana Gabriela Haro

PIs – Mervyn Kowalsky and Rob Chai

North Carolina State University

Raleigh – NC

1. Executive Summary

Test 9 was conducted at the Constructed Facilities Laboratory on Wednesday, August 31, 2016, as part of the second phase related to the load path project. The specimen was designed and built simulating boundary elements from prototype bridge pier walls. A monotonic and constant lateral displacement equivalent to 2.5% drift was applied first to the specimen followed by an axial seismic historic record from 1994 Northridge earthquake (Sylmar station). The purpose of this test was to capture the structural performance of the specimen #9 and to determine additional critical parameters associated with lateral instability of RC walls. The first part of the results are presented in this report. Further analyses will be elaborated.

2. Introduction

Recent earthquakes in New Zealand and Chile have illustrated the importance of out-of-plane stability of concrete wall elements due to in-plane loading. Pier walls are occasionally employed by Alaska DOT for their in-plane lateral stiffness. While these walls are normally thicker than the walls typically found in building applications, their clear heights are also larger, giving rise to height-to-thickness ratios which may be larger than that of buildings. Some analyses have demonstrated that walls as thick as 20 in. may be prone to buckling, depending on their length and height.

Noticing the concentration of damage in the boundary elements of rectangular reinforced concrete structural walls due to higher stress and strain demands, some past investigations by others have been carried out on prisms, which was found to be an economical way to study the inelastic instability of structural walls. In general, the main objective of these tests focuses on subjecting specimens to cyclic tension and compression actions to simulate vertical components of actual seismic loading.

While past tests on prisms has shown existing models to be promising, missing from the models is the interaction with out-of-plane loading. The existing models correlate tensile strain from in plane loading to out-of-plane deformation, assuming a prescribed curvature distribution. If loading occurs in the out-of-plane direction, the relationship between tensile strain and out-of-plane deformations must be adjusted to reflect this. In its simplest form, this would be an addition of an out-of-plane displacement to the existing equation. However, out-of-plane displacement may impact the distribution of curvature with height, thus requiring additional adjustments to the models.

A total of 12 prisms are being experimentally tested in the Constructed Facilities Laboratory (CFL) during this project. The support conditions for the 12 prisms are conceived as fixed-fixed. The first testing phase involved controlled load paths where the specimens were subjected to tension/compression cycles in addition to lateral loading to mimic the effects of out-of-plane displacements. In the second phase, longitudinal reinforcement ratios varied to consider the typical

values employed by Alaska DOT for pier walls. The details associated with the two phases are presented in Table A-17.

Table A-17. Test 9: Description of the experimental phases

Phase	Tests	Geometry	Reinforcement	Loading
1	6	Thickness and Height (based on prototype wall). (6”x12” ; actual geometry = 5”x12”)	Longitudinal (6bars#5) and transverse (#3@2in) reinforcement ratios similar for the 6 specimens.	Controlled 3D load path
2	6	Same as phase 1 (Based on actual pier walls formerly used by the Alaska DOT)	Longitudinal reinforcement ratio varies. (3 specimens 6bars#4 and 3 specimens 6bars#3)	Controlled 3D load path

This first phase consisted of testing six 1/2-scale identical specimens. The thickness of the prisms was 5 in. since the cover was excluded from the construction. The geometry used was 5x12x60 in., corresponding to an aspect ratio (*h/b = height/thickness*) of 10 (including the missing cover). The longitudinal reinforcement ratio was 2.6% (6 bars #5). Transverse reinforcement consisted of #3 diameter rebar spaced at 2 in. and was placed as shown in Figure A-193.

The first phase concluded in June 2016. During the second phase, six more specimens are being tested following similar load protocols. The geometry of the six specimens is the same as the one adopted during the first phase, 5x12x60 in. Two different longitudinal ratios are used. The first three specimens consist of 6 #4 longitudinal bars and the other three specimens consist of 6 bars #3, corresponding to reinforcement ratios of 1.7% and 0.9%, respectively. The distribution of transverse reinforcement is similar to the one used for the first phase, Figure A-194.

Regarding the material properties, an unconfined concrete strength of 5 ksi and reinforcement yielding strength of 60 ksi were considered as design values to define the load/displacement history for the test. Table A-18 shows the actual steel tensile test properties for the #3 and #4 bars associated with the first three specimens of the second phase. The reinforcement detailing was established according to the ACI 318 and NEHERP guidelines for ductile columns and boundary elements.

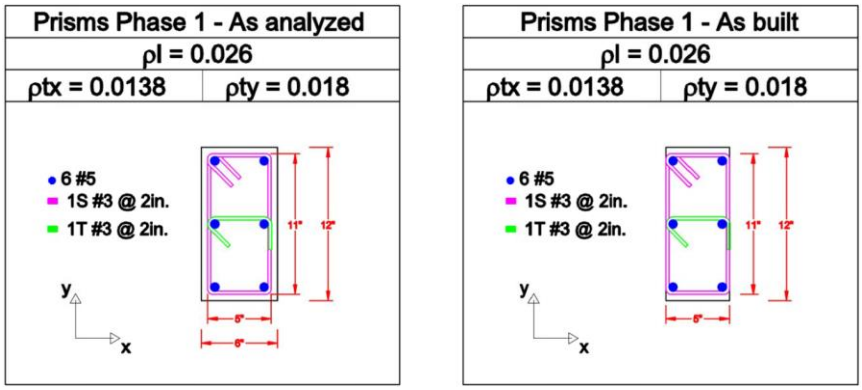

Figure A-193. Test 9: Phase 1 - Cross section of the prisms

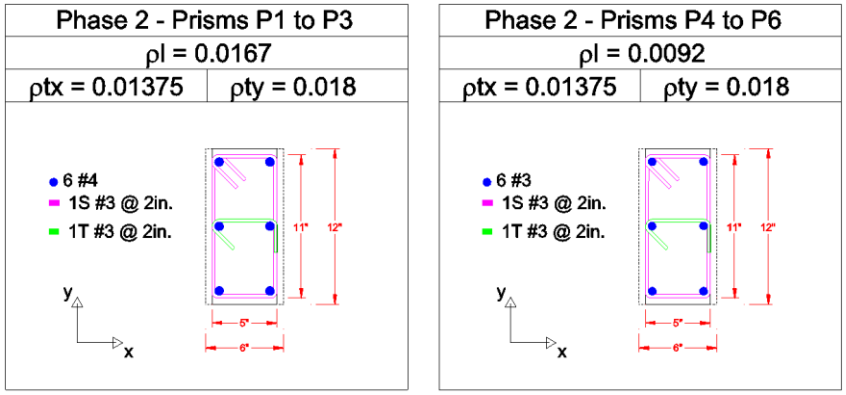

Figure A-194. Test 9: Phase 2 - Cross section of the prisms

Table A-18. Test 9: Phase 2 - Steel tensile test properties for bars #3 and #4

Sample No.	Bar #	fy (ksi)	εy = fy/Es	fu (ksi)	εu
1	3	68.7	0.0024	100.1	0.0909
2	3	69.3	0.0024	101.2	0.0796
3	3	71.4	0.0025	100.9	0.0764
4	3	68.1	0.0023	100.6	0.1035
5	3	69.8	0.0024	100.5	0.1119
6	3	71.6	0.0025	100.9	0.1021
#3 Average		**69.8**	**0.00241**	**100.7**	**0.0941**
1	4	71.0	0.0024	93.6	0.1261
2	4	68.1	0.0023	90.7	0.1109
3	4	69.0	0.0024	90.9	0.0955
4	4	67.9	0.0023	91.0	0.1192
5	4	67.3	0.0023	90.3	0.0867
6	4	71.0	0.0024	94.3	0.1031
#4 Average		**69.1**	**0.00238**	**91.8**	**0.1069**

3. Test Setup

The test setup consisted of a 14 ft long steel loading beam placed on the top of the specimen and connected to three actuators: two vertically inclined 440 kips actuators which induce axial loads and one horizontal 55 kips actuator to apply out-of-plane displacements. Two steel frames are used to restrain torsion in the loading beam. Two concrete blocks attached to the strong floor support the specimen to reach the required height associated with the effective length of the 440 kips actuators. Figure A-195 displays the test setup drawings and Figure A-196 shows a picture of the area where the components of the project are placed.

The horizontal actuator is controlled by displacements. The vertically inclined actuator located at the left hand side of the specimen, Figure A-195, is controlled by rotations captured throughout an inclinometer attached to the loading beam. The actuator placed at the right hand of the specimen is controlled by a combination of forces and displacements. Loads and strokes in the actuators are measured through integrated LVDTs and loads cells.

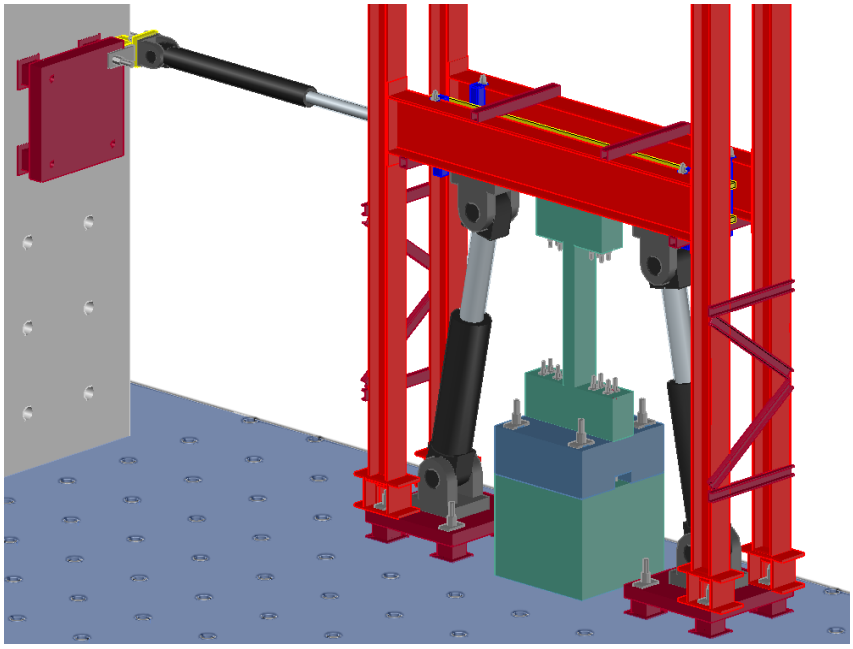

Figure A-195. Test 9: Test setup drawings

Figure A-196. Test 9: Test setup in the CFL at NC State

Relative displacements resulting from the interaction between the specimen and the connecting concrete block were obtained through 2 linear potentiometers. In addition, axial deformations of the prism were registered through 4 string potentiometers. Another string potentiometer was used to capture the lateral displacement of the loading beam.

A total of 110 infrared LEDs from the optical tracking system Optotrak Certus developed by Northern Digital Inc. were placed directly on the steel reinforcement of the prism. The objective is to establish longitudinal and transverse strains in real time throughout the MATLAB code "REALSTRAIN", created during the first phase of the project. Four additional infrared LEDs were positioned on the front face of the prism cap as a plane of reference. For the second phase, REALSTRAIN has been modified to capture, in addition, real time displacements of the prism cap. Figure A-197 shows the distribution of the LEDs on the left face of the prism and the overall allocation of the markers obtained from the Optotrak spatial coordinate output.

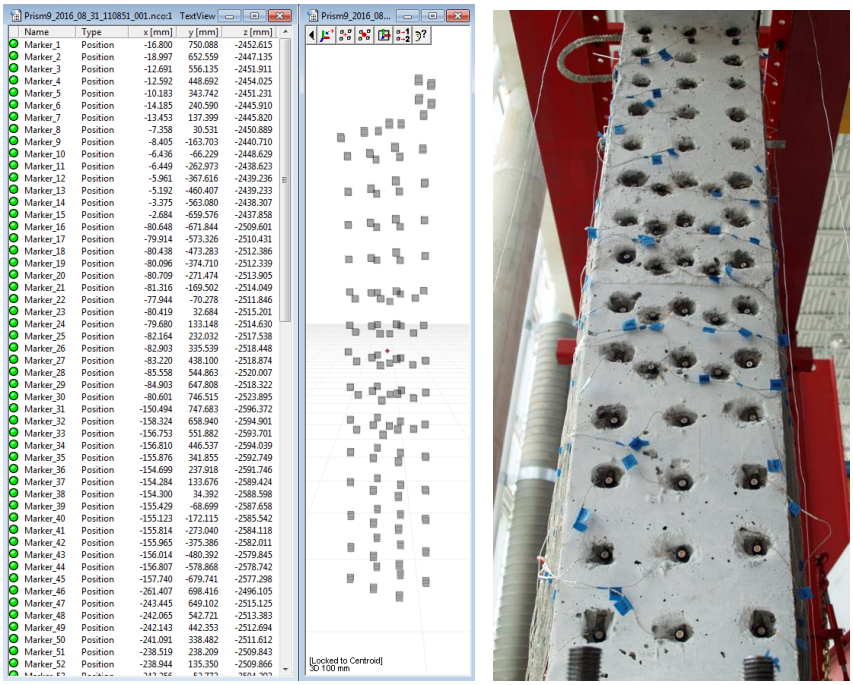

Figure A-197. Test 9: Instrumentation – Optotrak LEDs distribution on left face of the specimen and Spatial coordinate output

4. Test Summary

First, a monotonic and constant out-of-plane displacement of 1.5 in., equivalent to 2.5% drift, was induced to specimen P2-P9 (Phase 2 – Prism 9). During the entire test, this horizontal displacement was sustained. In addition, the test included a seismic axial displacement history based on the structural response of a prototype RC wall subjected to an actual in-plane horizontal earthquake record.

The earthquake would be characterized for a long duration pulse, consequently a record from the 1994 Northridge earthquake (Sylmar station) was selected. The main purpose of subjecting the specimen to this kind of demand, is to consider the effects of near-field records that contain long duration pulses. With this aim, a time history analysis was conducted using SEISMOSTRUCT. Figure A-198 shows the Sylmar earthquake horizontal accelerations applied to the prototype wall. The geometry of the wall consists of a total height of 21 meters (69 ft), a length of 4 meters (13 ft) and a thickness of 0.15 meters (6 in.). Figure A-199 presents the strain response history of a data point that corresponds to a longitudinal reinforcement 12 mm diameter steel bar located at the base of the wall in one of the boundary elements.

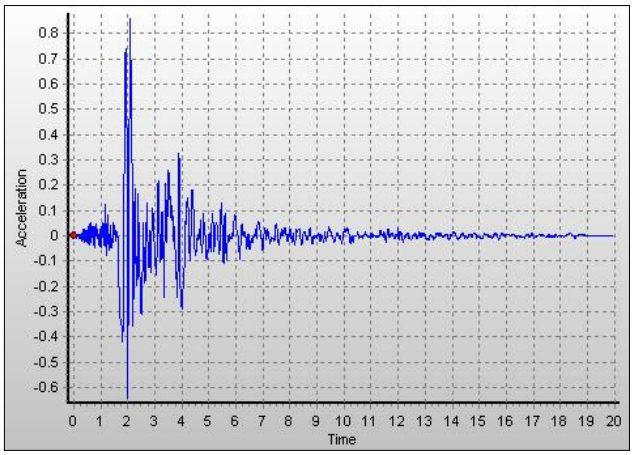

Figure A-198. Test 9: 1994 Northridge earthquake - Sylmar station accelerations record

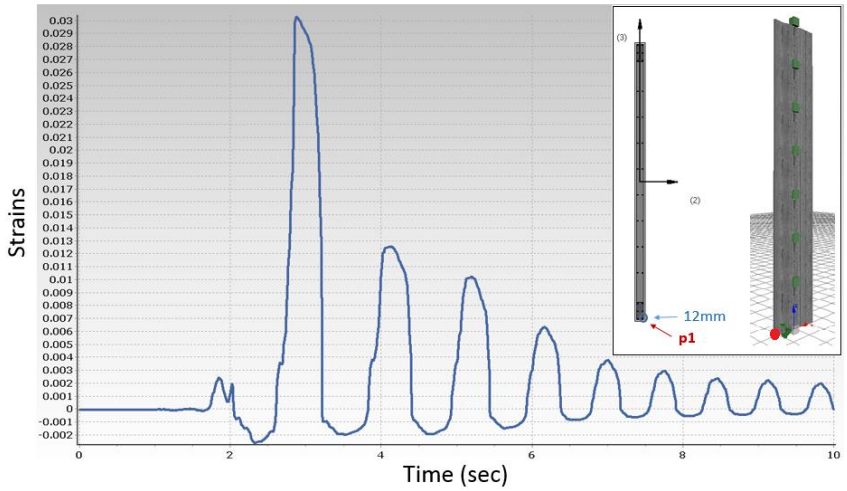

Figure A-199. Test 9: Strain time history response of a longitudinal reinforcement data point located at the base of an RC wall

Subsequently, the seismic axial displacements to be applied during test #9 were defined as stages considering the 60 in. height of the prism P2-P9 and the strains already determined in a previous step. A total of 6 stages were established for each input data. The first axial displacement history was scaled

as a function of a maximum tensile displacement associated with $14\varepsilon_y$, and the second one was scaled to $16\varepsilon_y$, see Figure A-200. The unique compressive target load, $P_{2.5\%}$ = -251 kips, was established considering P-Δ effects, representing 78% of the maximum axial design compressive load, Po = -322 kips. The load $P_{2.5\%}$ was calculated following the linear interaction from Eq. (1).

$$P_{\%} = P_o - (P_O - P_b)\frac{M_{\%}}{M_b} \qquad (1)$$

where, P_b = 165 kips and M_b = 418 kip.in are the axial force and bending moment at balanced failure, respectively. The flexural moment at 2.5% out-of-plane drift ratio is $M_{2.5\%} = P_{2.5\%}(0.025*60in.)/2$. Substituting this expression in Eq. (1) and solving for $P_{2.5\%}$, the target value is obtained.

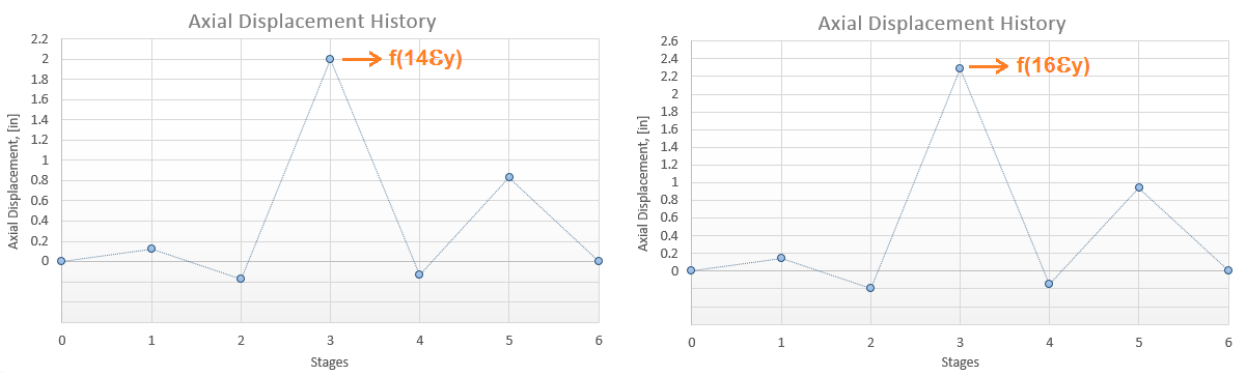

Figure A-200. Test 9: Axial displacement history inputs applied during test #9

During the 1.5 in. lateral displacement, cracks appeared on the bottom left (BL) and top right (TR) regions of the prism, Figure A-201. Strain profiles captured at this stage for each reinforcement line and for each face are displayed in Figure A-202, where the corresponding average has also been included. A total of 14 gages were established for each longitudinal bar along the 60 in. height, Y axis. Maximum tensile values close to 0.3% were determined in the BL region. In the TR region, these values were close to 1.0%. Yielding strain was exceeded in both cases.

Figure A-201. Test 9: Cracks at BL and TR regions at 1.5 in. out-of-plane displacement

Subsequently, the first axial tensile displacement, corresponding to the first stage of the 14εy seismic axial displacement history input, was induced to the specimen. New horizontal cracks appeared along the length of the prism and small cracks formed and extended to the beam-column connections. Crack widths close to 0.04 in. were measured at the footing-prism interface, Figure A-203. Upon compressive loads, cracks uniformly closed in the midheight of the prism. This phenomenon was observed during the following stages until instability was captured at the end of the test. In addition, wide vertical cracks and concrete flacking were observed in the BR and TL regions, Figure A-204. Concrete cover fell down from the Top Left (TL) region. Before resuming the test, the small pieces of concrete cover were removed to protect the instrumentation.

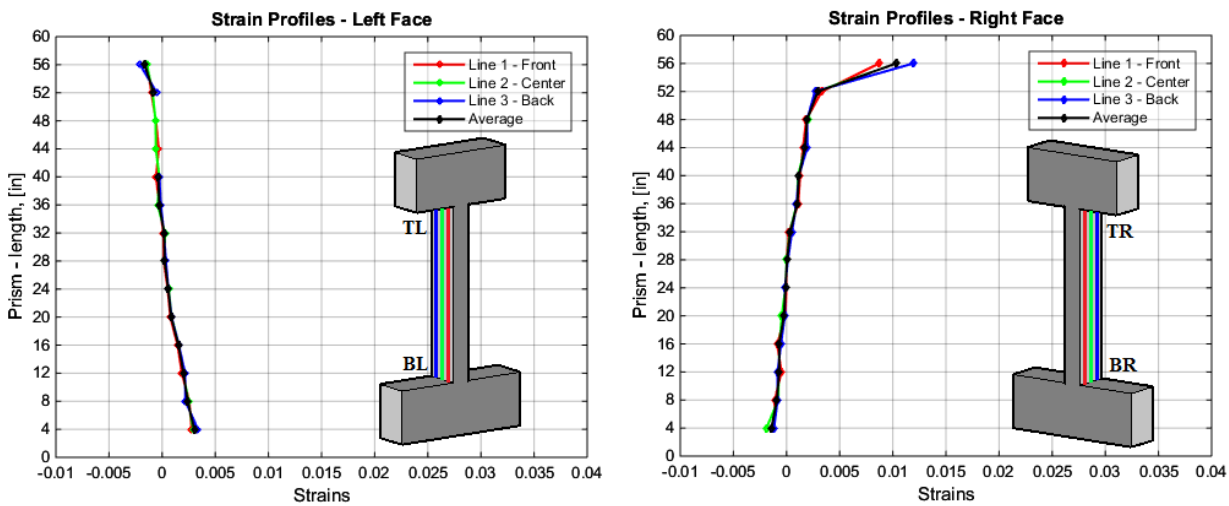

Figure A-202. Test 9: Strain profiles at 1.5 in. out-of-plane displacement

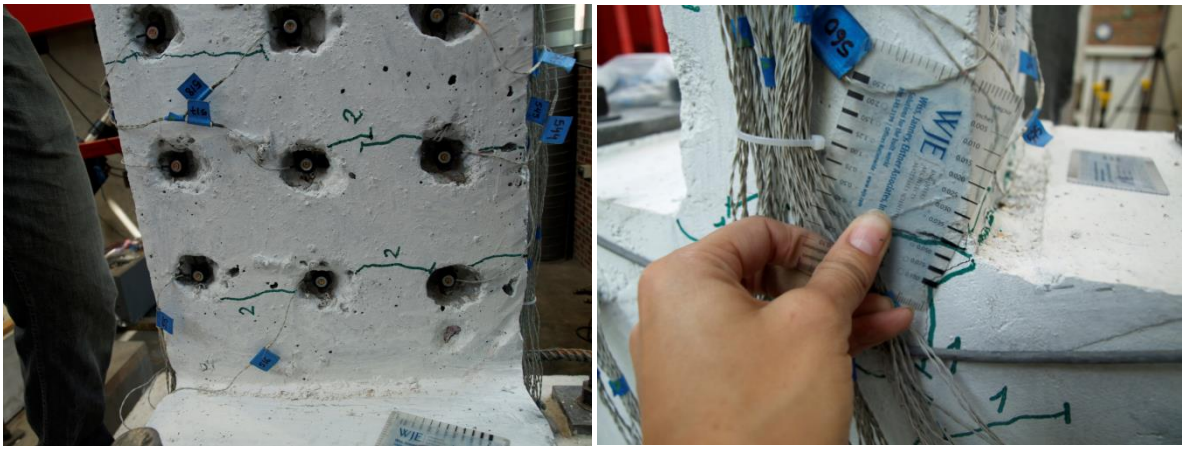

Figure A-203. Test 9: Propagation of cracks during the first axial tensile displacement.

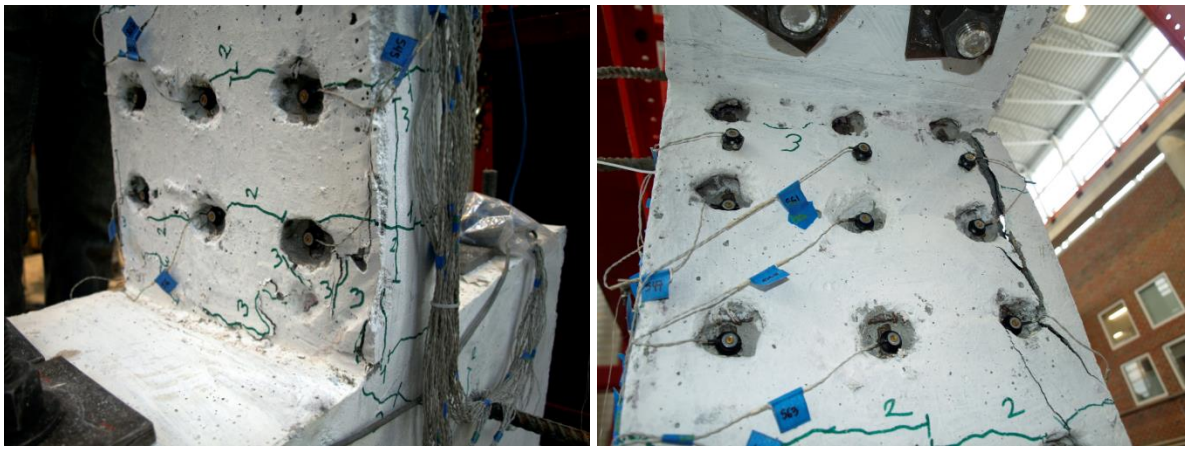

Figure A-204. Test 9: Propagation of cracks during the first axial compressive load.

Damage propagation at 14ε_y is presented in Figure A-205. Crack widths close to 1/8 in. were captured at midheight. The distribution of cracks was nearly uniform along the height of the prism. The out-of-plane buckling mechanism was visually captured upon compressive loading. In this scenario, where the out-of-plane deformation is relatively small, the compression force developed to resist the overturning moment, can be fully reached as cracks close and consequently, the prism returns to a fairly straight and stable position. Throughout the next compression stage, out-of-plane buckling deformations were not evident. During this stage, more concrete cover fell down and the transverse reinforcement was exposed as shown in Figure A-206.

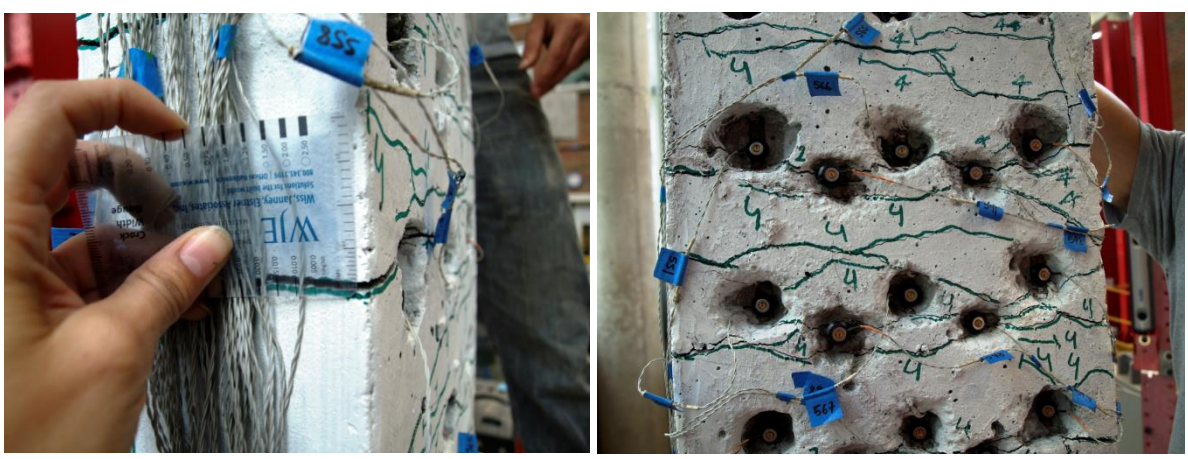

Figure A-205. Test 9: Propagation of damage at 14 εy.

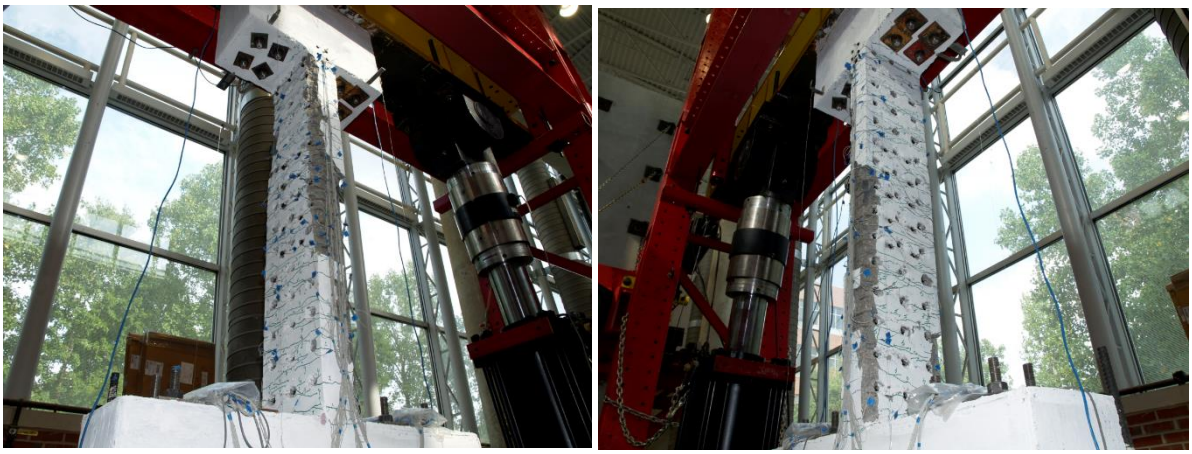

Figure A-206. Test 9: Propagation of damage upon compressive loads after 14 εy.

Since inelastic buckling was not captured during the axial displacement history associated with 14εy, then the stages related to 16εy were applied, but sustaining the same out-of-plane lateral displacement equivalent to 2.5% drift. New and wider cracks only manifested at the time the specimen was subjected to the maximum tensile demand, Figure A-207. Crack widths close to 3/16 in. were captured at midheight. Concrete spalling propagated in the BR and TL regions. The out-of-plane buckling mechanism was visually captured upon compressive loading, but the prism returned to a straight and stable position. Once the 6 stages were completed, then it was decided to apply the same displacement history related to 16εy. This time, when compressive forces were acting on the specimen after reaching the maximum tensile demand at 16εy, instability occurred as illustrated in Figure A-208. The end of the test showing local concrete crushing at midheight is displayed in the same figure. Notice a well confined concrete core at this phase.

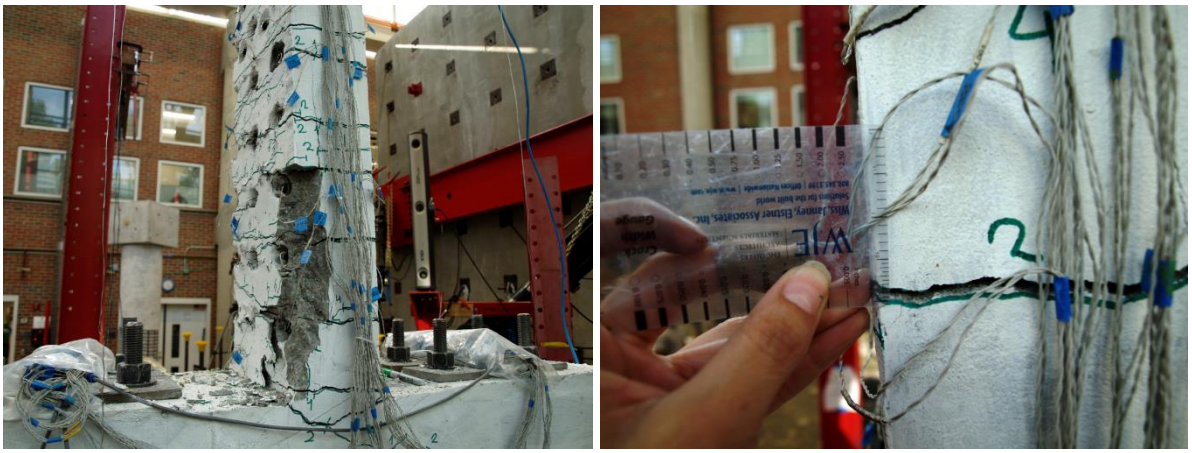

Figure A-207. Test 9: Propagation of damage at 16εy - First time

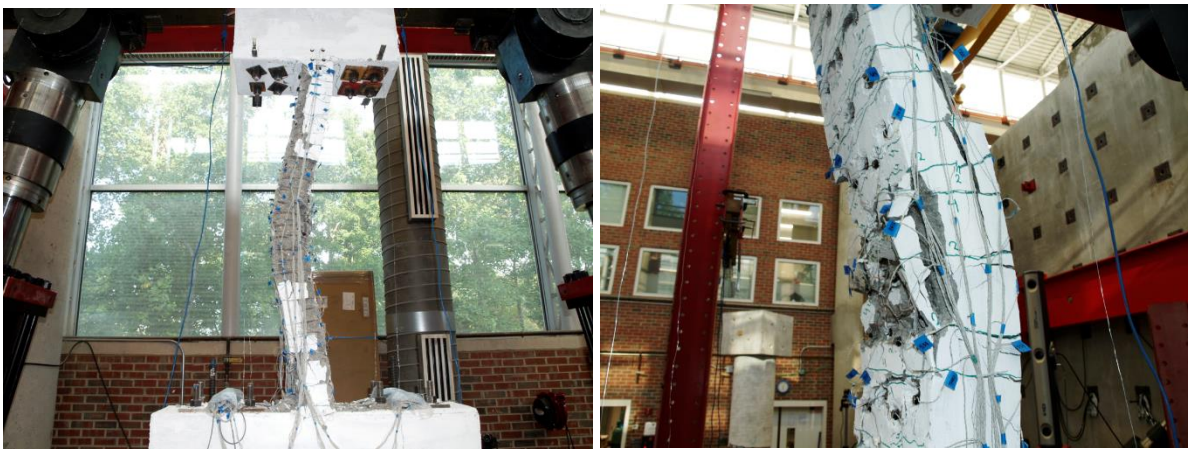

Figure A-208. Test 9: Instability captured upon compressive loads for 16εy – Second time

Figure A-209 depicts the entire structural response of P2-P9 as a function of axial forces captured from the vertical components of the actuators and axial displacements calculated from the Optotrak system. After the 14εy and 16εy stages, an axial stiffness reduction is evident by the time the axial compressive load approaches -50 kips. At these phases, the specimen is still extended a length close to 1.0 in. These points are associated with the onset of out-of-plane buckling. Due to the intrinsic eccentricity in the developed compressive force, one side of the wall end region closes first resulting in out-of-plane deformations. Once the cracks close, the prism gains stiffness and is able to carry the same axial load as in previous compressive stages. In the last stage associated with 16εy and upon compressive loads, instability was captured since the prism was not able to recover its strength. The maximum applied load at this stage was -156 kips, equivalent to 62% of the axial design compressive force considering P-Δ effects, $P_{2.5\%}$ = 251 kips.

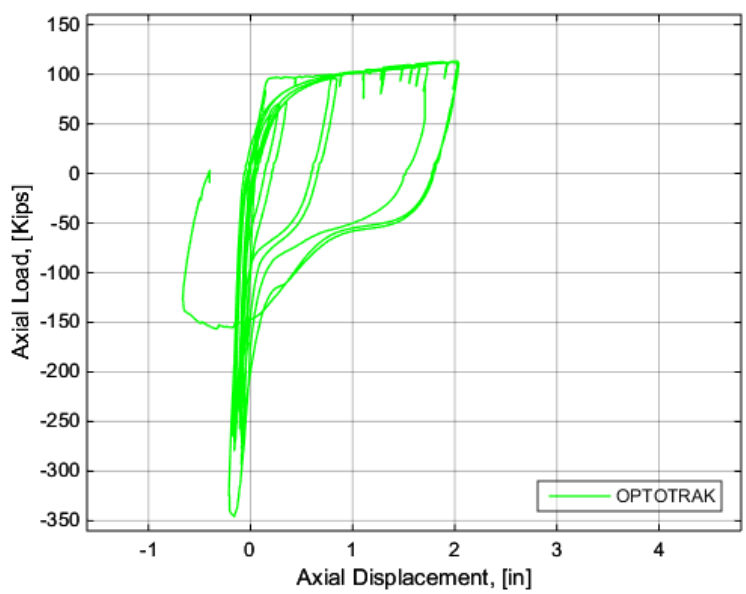

Figure A-209. Test 9: Axial structural response of prism P2-P9

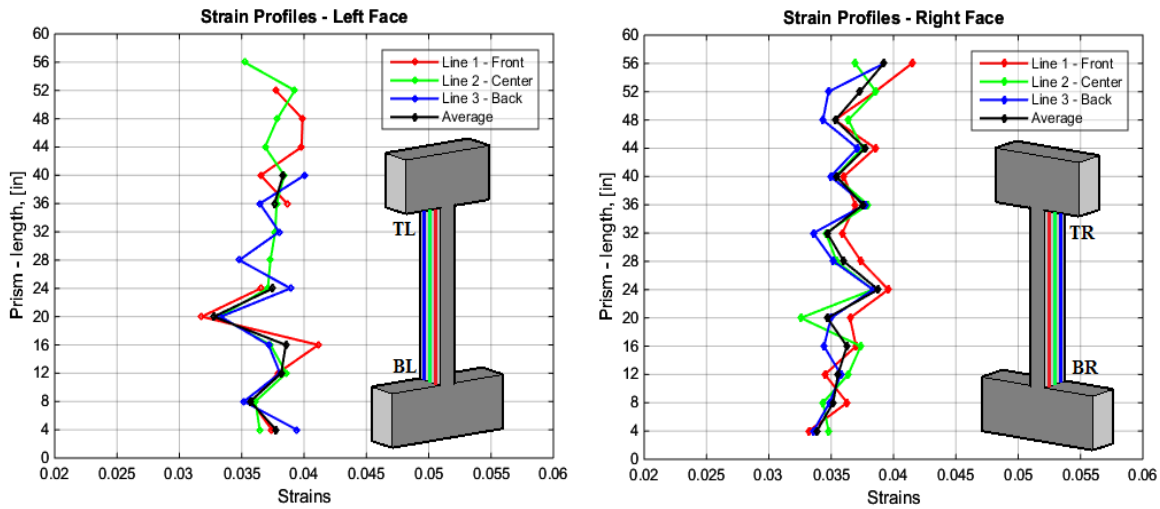

Figure A-210. Test 9: Strain profiles at 16εy during the last tensile stage

Strain profiles captured at 16εy during the last input data are presented in Figure A-210. The average of the strains in the left face is 3.8% and the right face is 3.6%, close to the value established as target equivalent to 16ε_y. Figure A-211 illustrates the evolution of the nominal axial strain captured from gage 22 at the center of the specimen on the right face versus the normalized out-of-plane deformation and the axial force. The maximum compression strain reached a value of -8.8%. Figure A-212 shows the variation of strains computed from gage 67 located at the center of the prism on the left face. The maximum tensile strain captured during the last cycle upon compressive loads is 3.9%. The actual onset of instability is captured at the time the relative normalized out-of-plane displacement reaches -0.30. Notice a stable response of the prism at low levels of axial tensile strains.

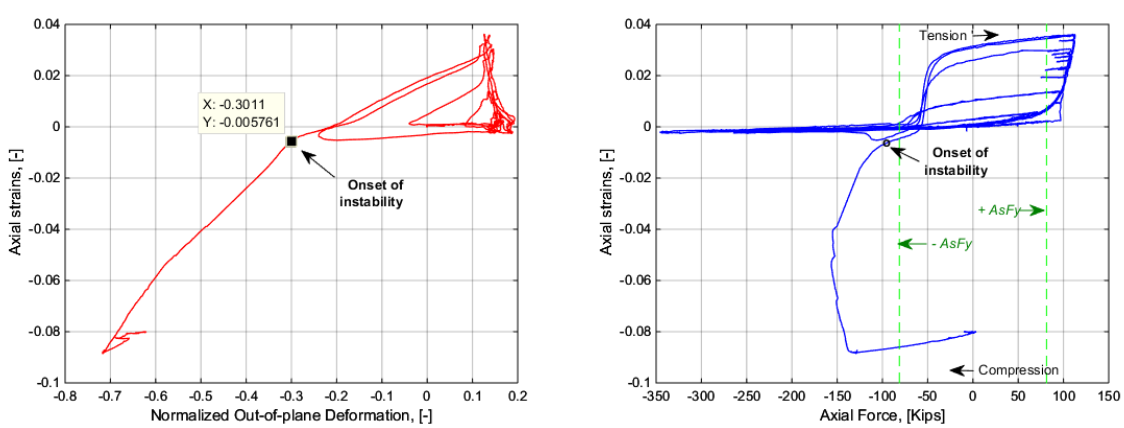

Figure A-211. Test 9: Response of specimen P2-P9 captured from a midheight gage on the right face

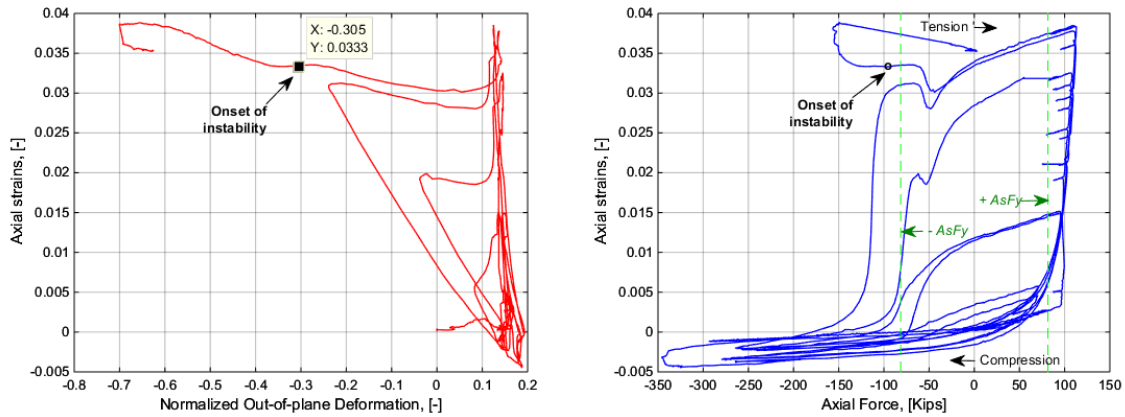

Figure A-212. Test 9: Response of specimen P2-P9 captured from a midheight gage on the left face

The normalized out-of-plane displacements increased upon compressive loading during the 14ε_y and the first 16ε_y stages. A sudden increment on this deformation took place during the second 16ε_y stage at the time the compression load was -97 kips, which represents 30% of the axial design compressive force, *Po=322 kips*. Yielding forces, *AsFy*, in tension and compression are also plotted in Figure A-211 and Figure A-212, where *As* is the area of the longitudinal reinforcement.

The evolution of the buckling shape during the last cycle of the test when the prism was subjected to compressive forces is plotted in Figure A-213. Four stages were considered: maximum tensile demand, onset of buckling, zero axial displacement, and maximum out-of-plane deformation, which is in total 3.849 + 0.459 = 4.308 in., located 4 in. below midheight.

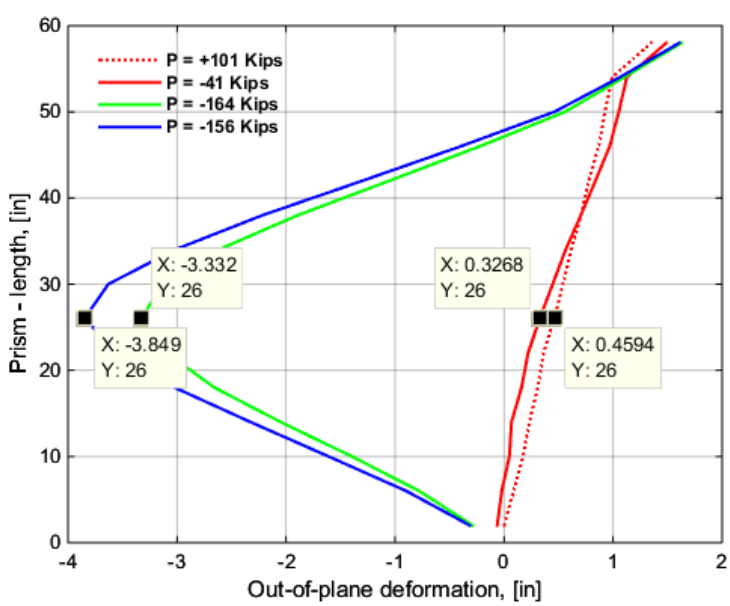

Figure A-213. Test 9: Evolution of the buckling shape during the last cycle under compressive loads

5. Conclusions

Specimen P2-P9 was tested during five hours where two loading patterns were applied. During the first part, a monotonic out-of-plane displacement was induced until reaching a target of 1.5 in. equivalent to 2.5% drift. Maximum tensile values greater than the yielding strain were determined in the bottom left (BL) and top right (TR) regions.

In the second part of the test, seismic axial displacement inputs, based on the 1994 Northridge earthquake (Sylmar station), were applied to the specimen reaching a maximum compression value close to the axial compressive force including P-Δ effects, $P_{2.5\%}$ = -251 kips. Upon tensile inputs, an axial displacement associated with $16\varepsilon_y$ was applied. The specimen presented a stable response after low levels of axial tensile demands. Out-of-plane deformations were noticed immediately after $14\varepsilon_y$ and $16\varepsilon_y$ stages when the specimen was subjected to compressive loads. Instability occurred during the last displacement history after the $16\varepsilon_y$ stage. The large buckling displacement led to concrete crushing and spalling in the central region of the prism. The axial compressive force at this stage was 62% of the compressive force applied in a previous cycle.

Neither bar buckling nor bar fracture were detected during or after the test. The stirrups remained as originally constructed. Analysis of the data from this test will continue, as a consequence the material presented here should be considered preliminary. Further experiments will reveal more information about the effectiveness of the reinforcement detailing recommended in guidelines to prevent lateral instability in RC structural walls.

Stability of Ductile RC Structural Walls – Assessment of the Local Buckling Failure Mode

Test 10

September – 16 – 2016

Summary Report

Prepared for:

Alaska Department of Transportation

Prepared by:

RA – Ana Gabriela Haro

PIs – Mervyn Kowalsky and Rob Chai

North Carolina State University

Raleigh – NC

1. Executive Summary

Test 10 was conducted at the Constructed Facilities Laboratory on Friday, September 16, 2016, as part of the third phase related to the load path project. The specimen was designed and built simulating boundary elements from prototype walls. An axial compression load followed by cyclic axial tensile displacements and compressive loads were applied to the specimen to capture its structural performance and to determine additional critical parameters associated with lateral instability of RC walls. The first part of the results are presented in this report. Further analyses will be elaborated.

2. Introduction

Recent earthquakes in New Zealand and Chile have illustrated the importance of out-of-plane stability of concrete wall elements due to in-plane loading. Pier walls are occasionally employed by Alaska DOT for their in-plane lateral stiffness. While these walls are normally thicker than the walls typically found in building applications, their clear heights are also larger, giving rise to height-to-thickness ratios which may be larger than that of buildings. Some analyses have demonstrated that walls as thick as 20 in. may be prone to buckling, depending on their length and height.

Noticing the concentration of damage in the boundary elements of rectangular reinforced concrete structural walls due to higher stress and strain demands, some past investigations by others have been carried out on prisms, which was found to be an economical way to study the inelastic instability of structural walls. In general, the main objective of these tests focuses on subjecting specimens to cyclic tension and compression actions to simulate vertical components of actual seismic loading.

While past tests on prisms has shown existing models to be promising, missing from the models is the interaction with out-of-plane loading. The existing models correlate tensile strain from in plane loading to out-of-plane deformation, assuming a prescribed curvature distribution. If loading occurs in the out-of-plane direction, the relationship between tensile strain and out-of-plane deformations must be adjusted to reflect this. In its simplest form, this would be an addition of an out-of-plane displacement to the existing equation. However, out-of-plane displacement may impact the distribution of curvature with height, thus requiring additional adjustments to the models.

A total of 12 prisms are being experimentally tested in the Constructed Facilities Laboratory (CFL) during this project. The support conditions for the 12 prisms are conceived as fixed-fixed. The first testing phase involved controlled load paths where the specimens were subjected to tension/compression cycles in addition to lateral loading to mimic the effects of out-of-plane displacements. In the second and third phases, longitudinal reinforcement ratios varied to consider the typical values employed by Alaska DOT for pier walls. The details associated with the two phases are presented in Table A-19.

This first phase consisted of testing six 1/2-scale identical specimens. The thickness of the prisms was 5 in. since the cover was excluded from the construction. The geometry used was 5x12x60 in., corresponding to an aspect ratio (*h/b = height/thickness*) of 10 (including the missing cover). The longitudinal reinforcement ratio was 2.6% (6 bars #5). Transverse reinforcement consisted of #3 diameter rebar spaced at 2 in. and was placed as shown in Figure A-214.

The first phase concluded in June 2016. For the second phase, three more specimens were tested following similar load protocols and concluded in August 2016. During the third phase, three additional specimens are being tested considering equivalent parameters than the previous phases. The geometry of the specimens built for phases 2 and 3 was the same as the one adopted during the first phase, 5x12x60 in. The three specimens related to phase 2 included 6 #4 longitudinal bars and the three specimens related to phase 3 consist of 6 bars #3, corresponding to reinforcement ratios of 1.7% and 0.9%, respectively. The distribution of transverse reinforcement is similar to the one used for the first phase, Figure A-215.

Table A-19. Test 10: Description of the experimental phases

Phase	Tests	Geometry	Reinforcement	Loading
1	6	Thickness and Height (based on prototype wall). (6”x12” ; actual geometry = 5”x12”)	Longitudinal (6 bars **#5**) and transverse (#3@2in) reinforcement ratios similar for the 6 specimens.	Controlled 3D load path
2	3	Same as phase 1 (Based on actual pier walls formerly used by the Alaska DOT)	Longitudinal reinforcement ratio varies. (3 specimens 6 bars **#4**)	Controlled 3D load path
3	3	Same as phase 2 (Based on actual pier walls formerly used by the Alaska DOT)	Longitudinal reinforcement ratio varies. (3 specimens 6 bars **#3**)	Controlled 3D load path

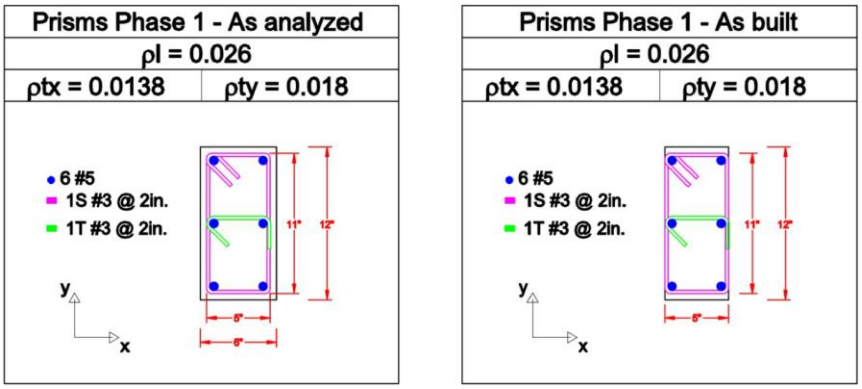

Figure A-214. Test 10: Phase 1 - Cross section of the prisms

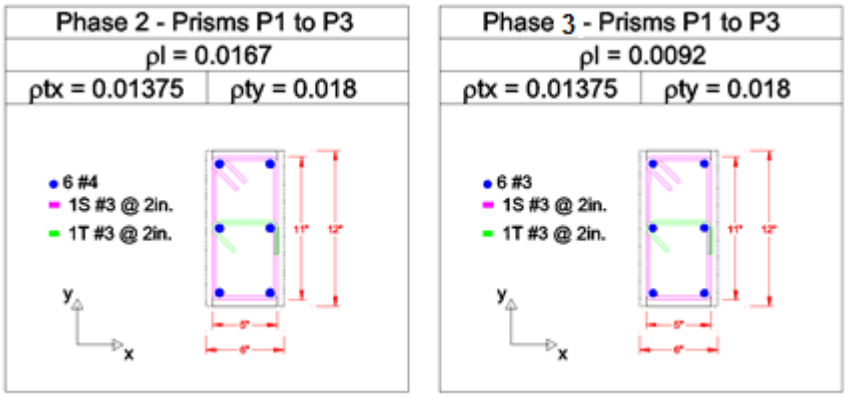

Figure A-215. Test 10: Phase 2 And Phase 3 - Cross section of the prisms

Regarding the material properties, an unconfined concrete strength of 5 ksi and reinforcement yielding strength of 62.9 ksi were considered as design values to define the load/displacement history for the test. Table A-20 shows the steel tensile test properties for the #3 bars associated with the three specimens of the third phase. The reinforcement detailing was established according to the ACI 318 and NEHERP guidelines for ductile columns and boundary elements.

Table A-20. Test 10: Phase 3 - Steel tensile test properties for bars #3 (longitudinal and transverse reinforcement)

Sample No.	Bar #	fy (ksi)	εy = fy/Es	fu (ksi)	εu
1	3	63.1	0.0022	89.0	0.1088
2	3	62.9	0.0022	89.7	0.1280
3	3	63.3	0.0022	90.3	0.1120
4	3	63.4	0.0022	90.2	0.1200
5	3	62.9	0.0022	90.1	0.1393
6	3	62.0	0.0021	89.8	0.1245
#3 Average long.		**62.9**	**0.00217**	**89.9**	**0.1221**
1	3	68.7	0.0024	100.1	0.0909
2	3	69.3	0.0024	101.2	0.0796
3	3	71.4	0.0025	100.9	0.0764
4	3	68.1	0.0023	100.6	0.1035
5	3	69.8	0.0024	100.5	0.1119
6	3	71.6	0.0025	100.9	0.1021
#3 Average transv.		**69.8**	**0.00241**	**100.7**	**0.0941**

3. Test Setup

The test setup consisted of a 14 ft long steel loading beam placed on the top of the specimen and connected to three actuators: two vertically inclined 440 kips actuators which induce axial loads and one horizontal 55 kips actuator to apply out-of-plane displacements. Two steel frames are used to

restrain torsion in the loading beam. Two concrete blocks attached to the strong floor support the specimen to reach the required height associated with the effective length of the 440 kips actuators. Figure A-216 displays the test setup drawings and Figure A-217 shows a picture of the area where the components of the project are placed.

The horizontal actuator is controlled by displacements. The vertically inclined actuator located at the left hand side of the specimen, Figure A-216, is controlled by rotations captured throughout an inclinometer attached to the loading beam. The actuator placed at the right hand of the specimen is controlled by a combination of forces and displacements. Loads and strokes in the actuators are measured through integrated LVDTs and loads cells.

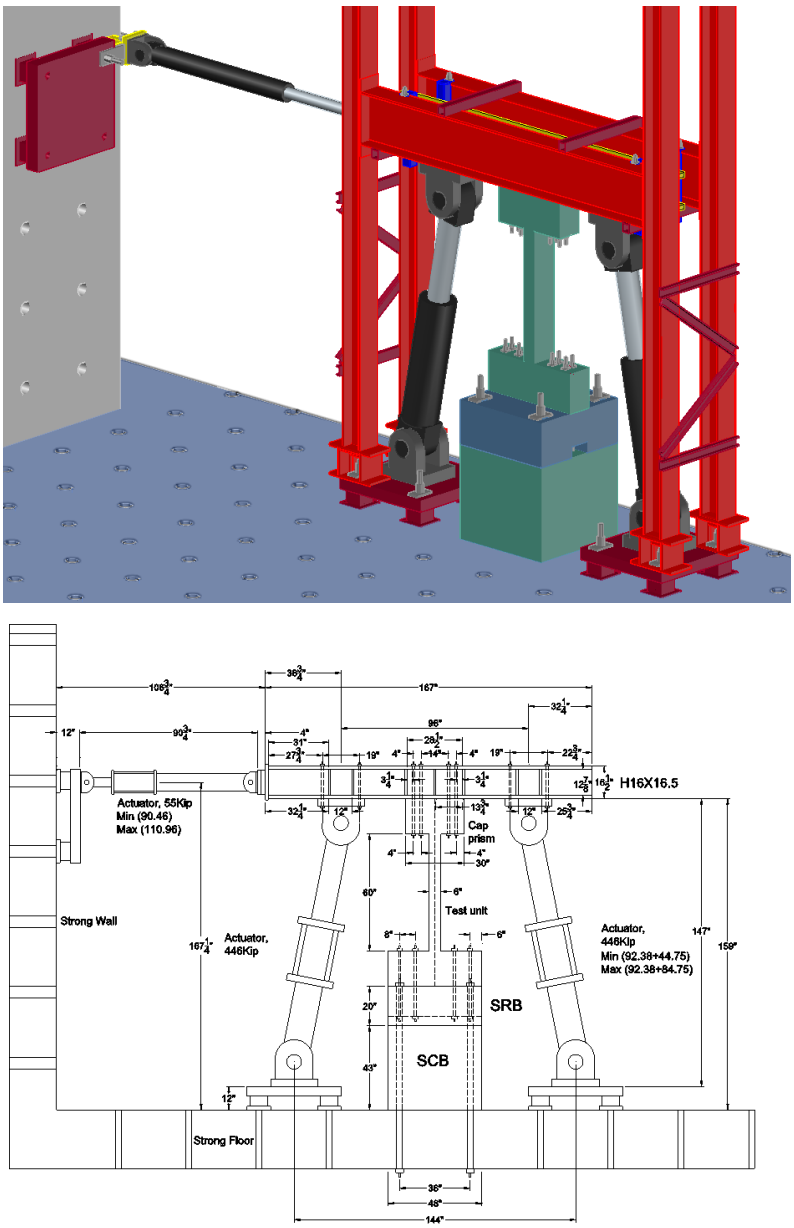

Figure A-216. Test 10: Test setup drawings

Figure A-217. Test 10: Test setup in the CFL at NC State

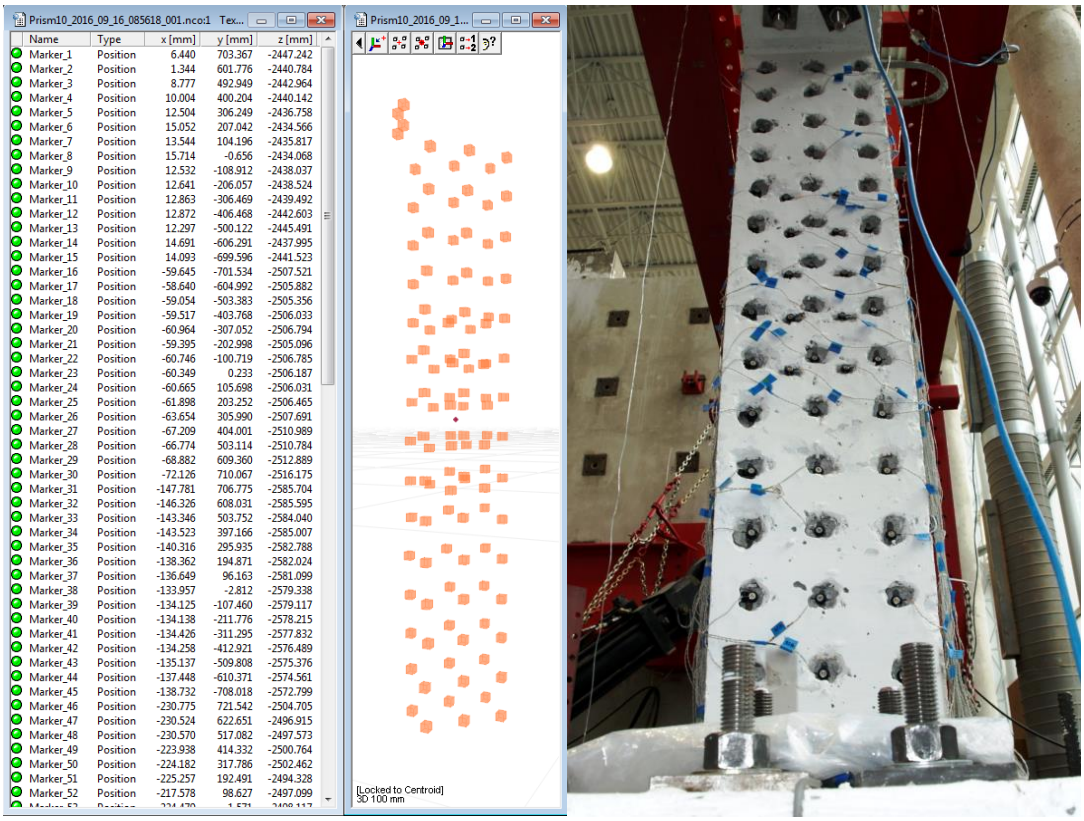

Prism10_2016_09_16_085618_001.nco:1 Tex...

Name	Type	x [mm]	y [mm]	z [mm]
Marker_1	Position	6.440	703.367	-2447.242
Marker_2	Position	1.344	601.776	-2440.784
Marker_3	Position	8.777	492.949	-2442.964
Marker_4	Position	10.004	400.204	-2440.142
Marker_5	Position	12.504	306.249	-2436.758
Marker_6	Position	15.052	207.042	-2434.566
Marker_7	Position	13.544	104.196	-2435.817
Marker_8	Position	15.714	-0.656	-2434.068
Marker_9	Position	12.532	-108.912	-2438.037
Marker_10	Position	12.641	-206.057	-2438.524
Marker_11	Position	12.863	-306.469	-2439.492
Marker_12	Position	12.872	-406.468	-2442.603
Marker_13	Position	12.297	-500.122	-2445.491
Marker_14	Position	14.691	-606.291	-2437.995
Marker_15	Position	14.093	-699.596	-2441.523
Marker_16	Position	-59.645	-701.534	-2507.521
Marker_17	Position	-58.640	-604.992	-2505.882
Marker_18	Position	-59.054	-503.383	-2505.356
Marker_19	Position	-59.517	-403.768	-2506.033
Marker_20	Position	-60.964	-307.052	-2506.794
Marker_21	Position	-59.395	-202.998	-2505.096
Marker_22	Position	-60.746	-100.719	-2506.785
Marker_23	Position	-60.349	0.233	-2506.187
Marker_24	Position	-60.665	105.698	-2506.031
Marker_25	Position	-61.898	203.252	-2506.465
Marker_26	Position	-63.654	305.990	-2507.691
Marker_27	Position	-67.209	404.001	-2510.989
Marker_28	Position	-66.774	503.114	-2510.784
Marker_29	Position	-68.882	609.360	-2512.889
Marker_30	Position	-72.126	710.067	-2516.175
Marker_31	Position	-147.781	706.775	-2585.704
Marker_32	Position	-146.326	608.031	-2585.595
Marker_33	Position	-143.346	503.752	-2584.040
Marker_34	Position	-143.523	397.166	-2585.007
Marker_35	Position	-140.316	295.935	-2582.788
Marker_36	Position	-138.362	194.871	-2582.024
Marker_37	Position	-136.649	96.163	-2581.099
Marker_38	Position	-133.957	-2.812	-2579.338
Marker_39	Position	-134.125	-107.460	-2579.117
Marker_40	Position	-134.138	-211.776	-2578.215
Marker_41	Position	-134.426	-311.295	-2577.832
Marker_42	Position	-134.258	-412.921	-2576.489
Marker_43	Position	-135.137	-509.808	-2575.376
Marker_44	Position	-137.448	-610.371	-2574.561
Marker_45	Position	-138.732	-708.018	-2572.799
Marker_46	Position	-230.775	721.542	-2504.705
Marker_47	Position	-230.524	622.651	-2496.915
Marker_48	Position	-230.570	517.082	-2497.573
Marker_49	Position	-223.938	414.332	-2500.764
Marker_50	Position	-224.182	317.786	-2502.462
Marker_51	Position	-225.257	192.491	-2494.328
Marker_52	Position	-217.578	98.627	-2497.099

Figure A-218. Test 10: Instrumentation – Optotrak LEDs distribution on right face of the specimen and Spatial coordinate output

Relative displacements resulting from the interaction between the specimen and the connecting concrete block were obtained through 2 linear potentiometers. In addition, axial deformations of the prism were registered through 4 string potentiometers. Another string potentiometer was used to capture the lateral displacement of the loading beam.

A total of 110 infrared LEDs from the optical tracking system Optotrak Certus developed by Northern Digital Inc. were placed directly on the steel reinforcement of the prism. The objective is to establish longitudinal and transverse strains in real time throughout the MATLAB code "REALSTRAIN", created during the first phase of the project. Four additional infrared LEDs were positioned on the front face of the prism cap as a plane of reference. For the second phase, REALSTRAIN was modified to capture, in addition, real time displacements of the prism cap. Figure A-218 shows the distribution of the LEDs on the right face of the prism and the overall allocation of the markers obtained from the Optotrak spatial coordinate output.

4. Test Summary

The first part of the test consisted of applying an axial compressive load followed by a second part where cyclic axial tensile displacements and compressive loads were induced to the specimen, identified as P3-P10 (Phase 3 – Prism 10).

4.1 Monotonic Compressive Loading

Specimen P3-P10, first was subjected to an axial load equivalent to the design axial compression capacity of the prism, *Po* = -294 kips. The purpose of this part of the test was to confirm that the boundary element of the wall could sustain this level of compressive load in the absence of lateral displacements. This stage correspond to "stage 1" in Figure A-220.

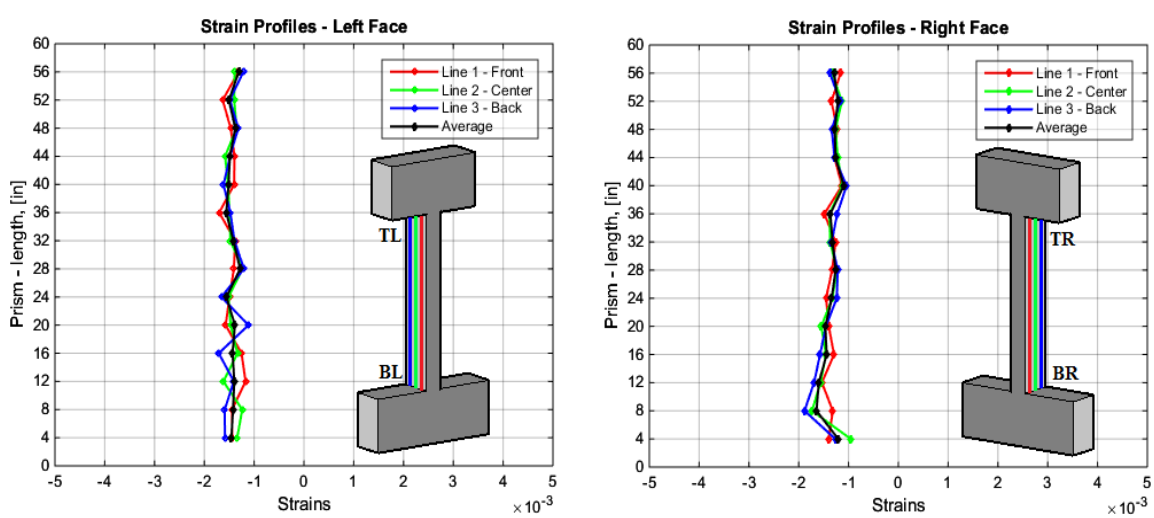

Figure A-219. Test 10: Strain profiles at maximum compressive load during stage # 1

The test was successfully conducted with no signs of damage. Strain profiles captured at this stage for each reinforcement line and for each face are displayed in Figure A-219. A total of 14 gages were established for each longitudinal bar along the 60 in. height, Y axis. The average compressive strain in both faces is close to -0.14%, which is less than the yielding compressive strain, -0.22%.

4.2 Cyclic Axial Loading

A quasi-static displacement/load controlled procedure was established for the second part of the test. Unsymmetrical cycles were used to evaluate the seismic performance of prism P3-P10. The axial displacement history started with an elastic single cycle analytically predicted. After yielding, three identical cycles at different axial tensile displacement ductility levels continued until the end of the test. The unique compressive target load was established from the first part of the experiment, corresponding to *Po* = -294 kips, which was applied on each cycle during the whole test, Figure A-220. Damage propagation at $1\varepsilon_y$, $2\varepsilon_y$, $4\varepsilon_y$, and $6\varepsilon_y$ is presented in Figure A-221 through Figure A-224, respectively. Upon loading to $1\varepsilon_y$ small horizontal cracks appeared all along the prism and slightly extended to the moment connections. Crack widths of about 0.01in. were captured at midheight. Upon compressive loads cracks uniformly closed as expected. This phenomenon was observed during the following cycles until failure was captured. In the course of the cycles corresponding to $2\varepsilon_y$, more small cracks formed and the old ones propagated. Crack widths close to 0.03 in. and 0.04 in. were measured at midheight during the $4\varepsilon_y$ and $6\varepsilon_y$ cycles, respectively. Vertical cracks were also observed during the $6\varepsilon_y$ first cycle. Throughout the following cycles the cracks became wider and the number of new cracks decreased. In addition, it was observed that the spacing of the horizontal cracks were governed by the cavities created to include the infrared LEDs.

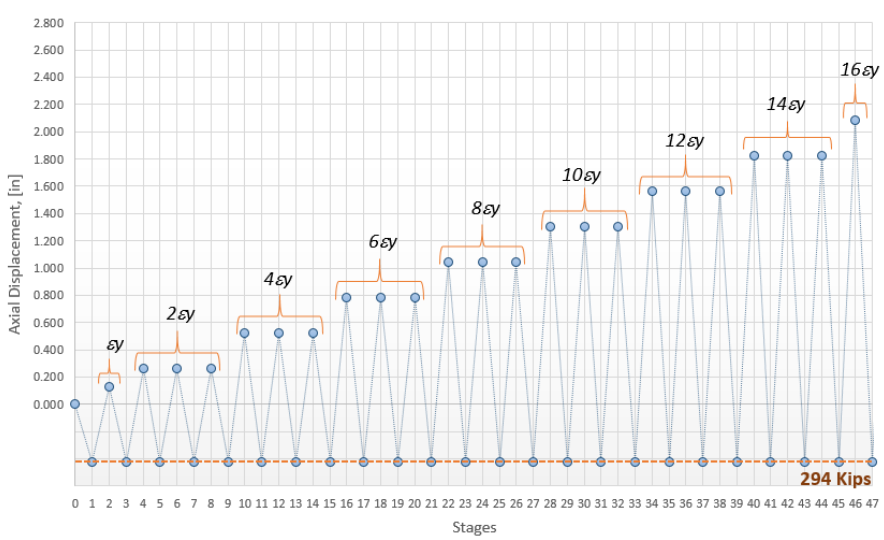

Figure A-220. Test 10: Displacement / Force History applied during the test

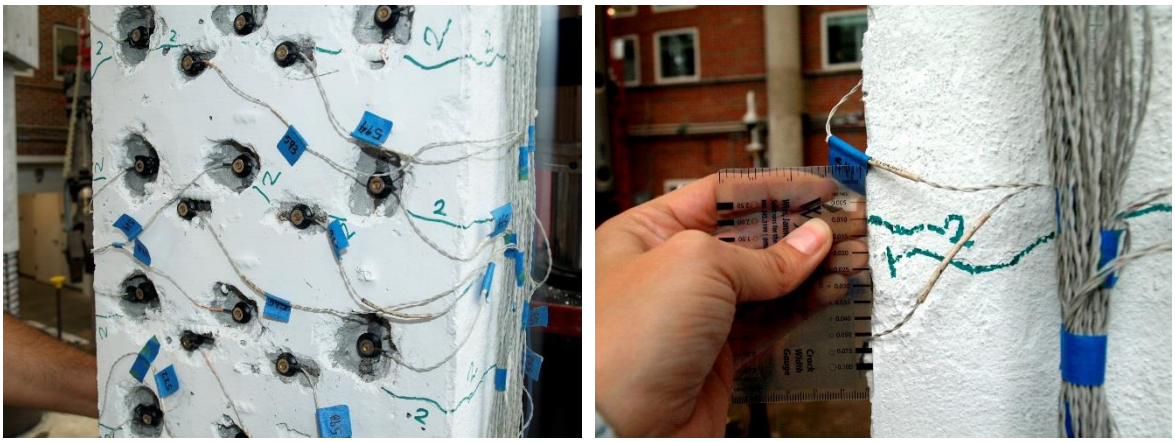

Figure A-221. Test 10: Propagation of damage at 1.0 εy

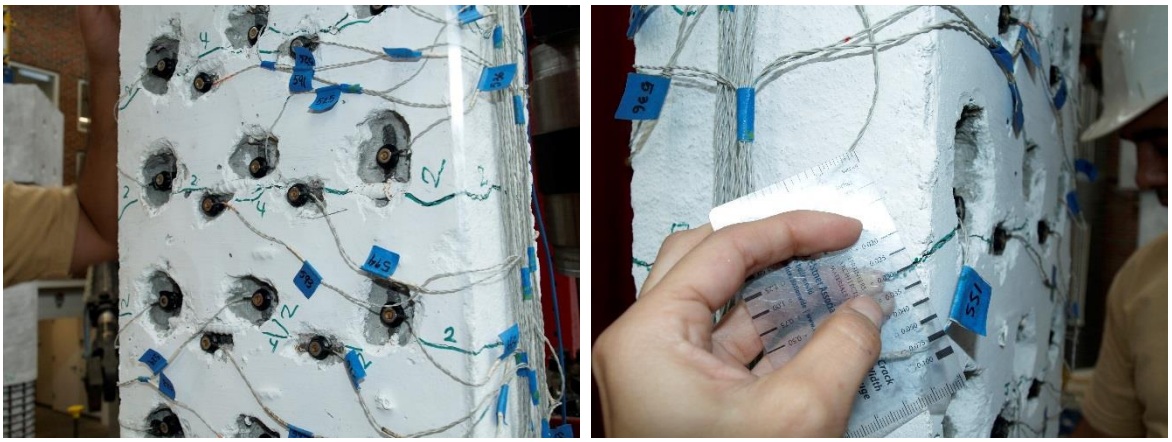

Figure A-222. Test 10: Propagation of damage at 2.0 εy - First cycle

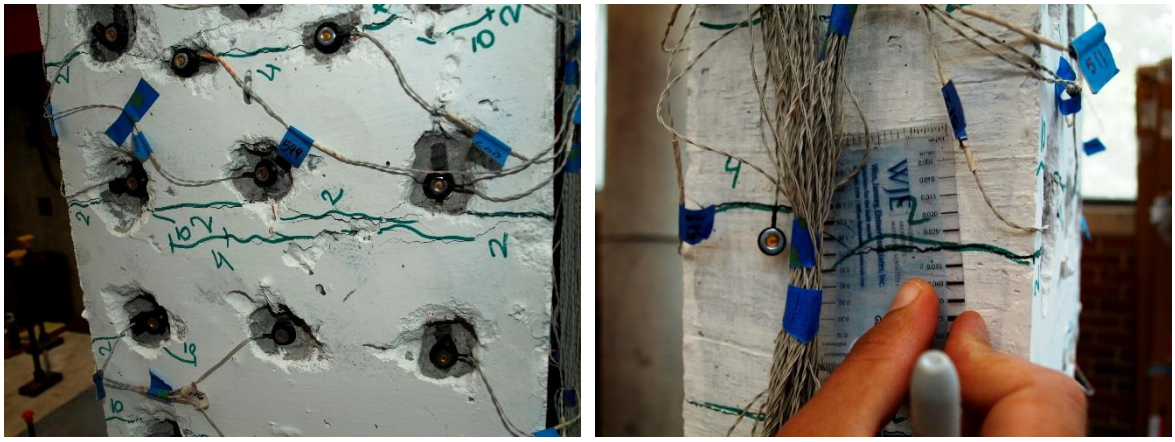

Figure A-223. Test 10: Propagation of damage at 4.0 εy - First cycle

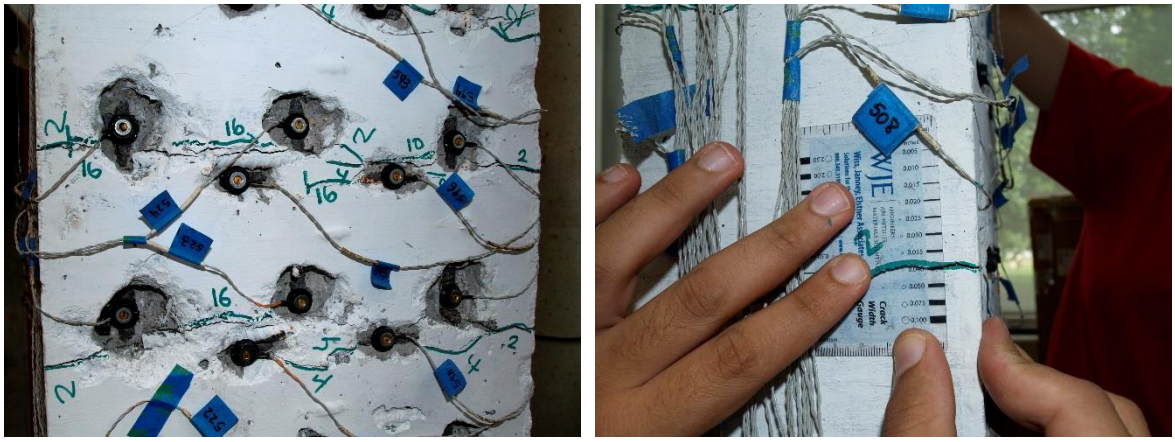

Figure A-224. Test 10: Propagation of damage at 6.0 εy - First cycle

Figure A-225 shows the propagation of damage for the cycles associated with $8\varepsilon_y$, where crack widths close to 0.075 in. were observed at midheight. Signs of concrete spalling were also observed in the first cycle associated with $8\varepsilon_y$. During the $10\varepsilon_y$ first cycle, crack widths of about 0.10 in. were measured in the interface between the prism and the footing, and close to the cap, Figure A-226. Signs of concrete spalling were also captured at this stage. During the first cycle at $12\varepsilon_y$, cracks widths reached 1/8 in., Figure A-227. Concrete cover fell down on the back face of the prism and the transverse reinforcement was exposed within a length of 18 in. Before resuming the test, debris was removed to protect the instrumentation and subsequently the target compressive load was reached. Concrete cover continued falling down in the same region during the two remaining cycles associated with $12\varepsilon_y$ exposing the transverse reinforcement within a length of 24 in., approximately. Crack widths close to 3/16 in. were measured during the first cycle at $14\varepsilon_y$, Figure A-228. The distribution of cracks was uniform along the height of the prism.

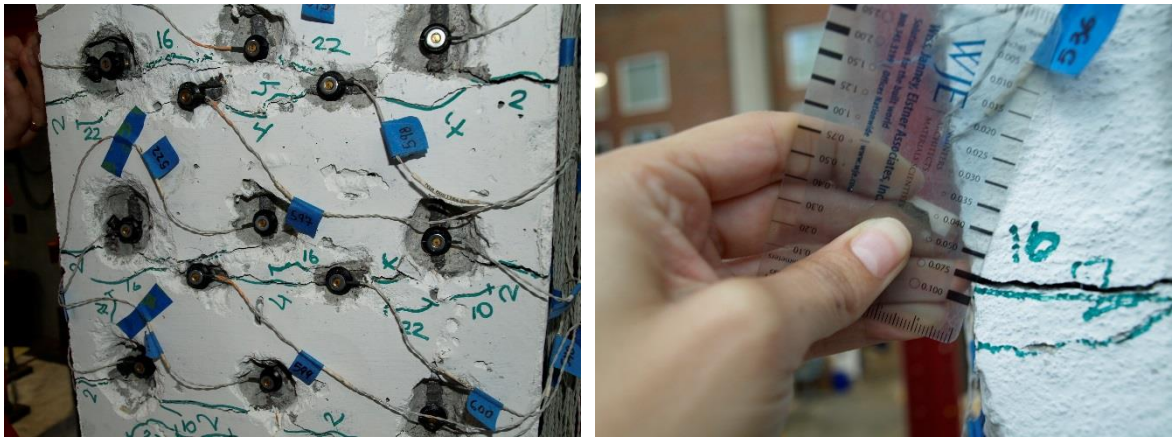

Figure A-225. Test 10: Propagation of damage at 8.0 εy - First cycle

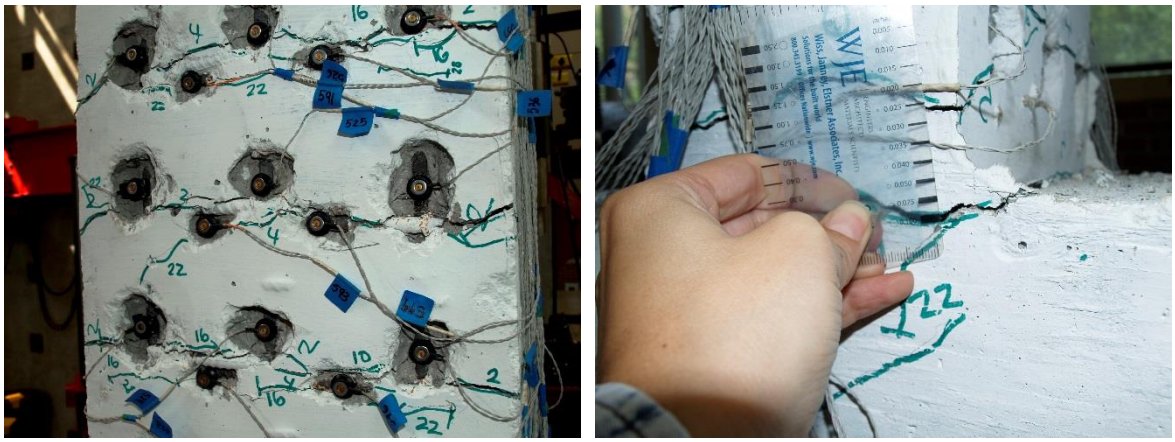

Figure A-226. Test 10: Propagation of damage at 10.0 εy - First cycle

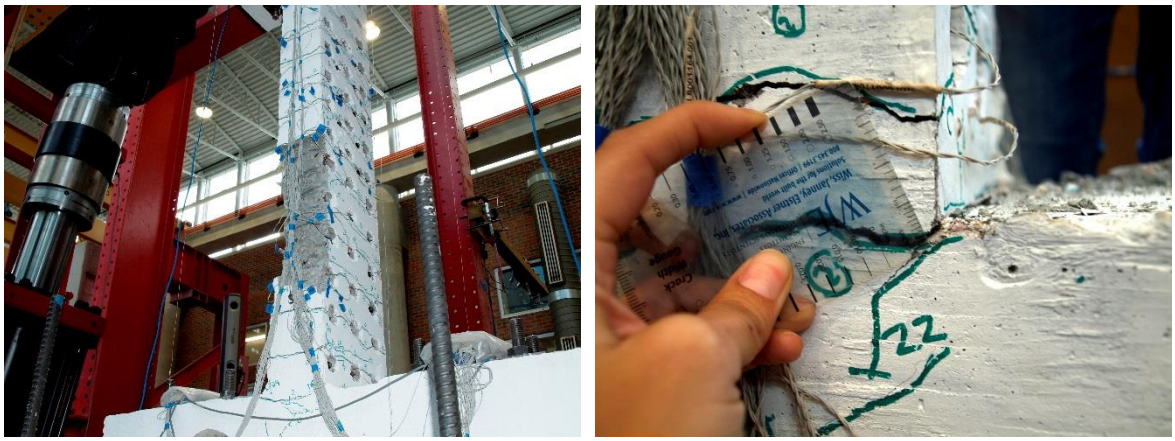

Figure A-227. Test 10: Propagation of damage at 12.0 εy - First cycle

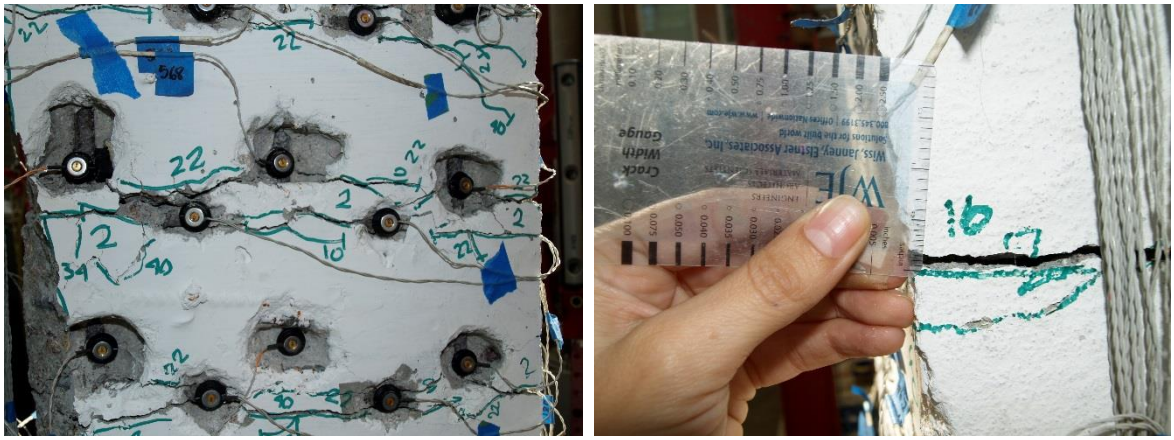

Figure A-228. Test 10: Propagation of damage at 14.0 εy - First cycle

Figure A-229. Test 10: Propagation of damage on the way to 16 εy

Figure A-230. Test 10: Specimen P3-P10 after testing

Out-of-plane buckling deformations were not observed during $10\varepsilon_y$ or $12\varepsilon_y$. As tensile demands increased during the cycles related to $14\varepsilon_y$ the out-of-plane buckling mechanism was captured upon compressive loading. In this scenario, where the out-of-plane deformation is relatively small, the compression force developed to resist the overturning moment, can be fully reached as cracks close and consequently, the prism returns to a fairly straight and stable position.

Upon tensile displacements and on the way to $16\varepsilon_y$, the bar located in the left corner on the back face fractured at midheight before reaching the target tensile target, Figure A-229. Consequently, it was decided to apply a last compressive load, and during this step bar buckling was observed in the 6 longitudinal bars all along the specimen. Figure A-230 presents the final state of the specimen.

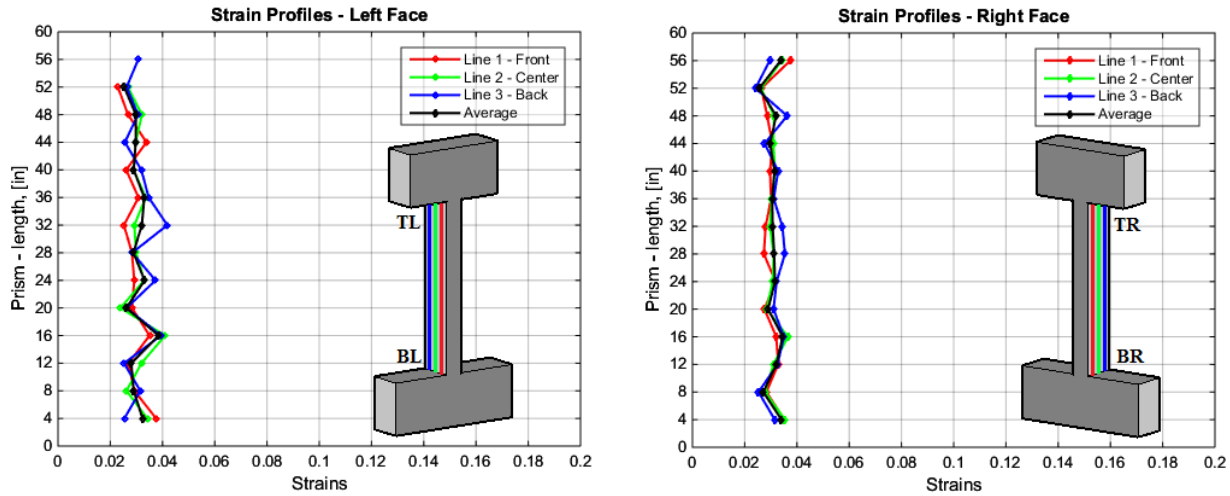

Figure A-231. Test 10: Strain profiles at 14εy during the third cycle

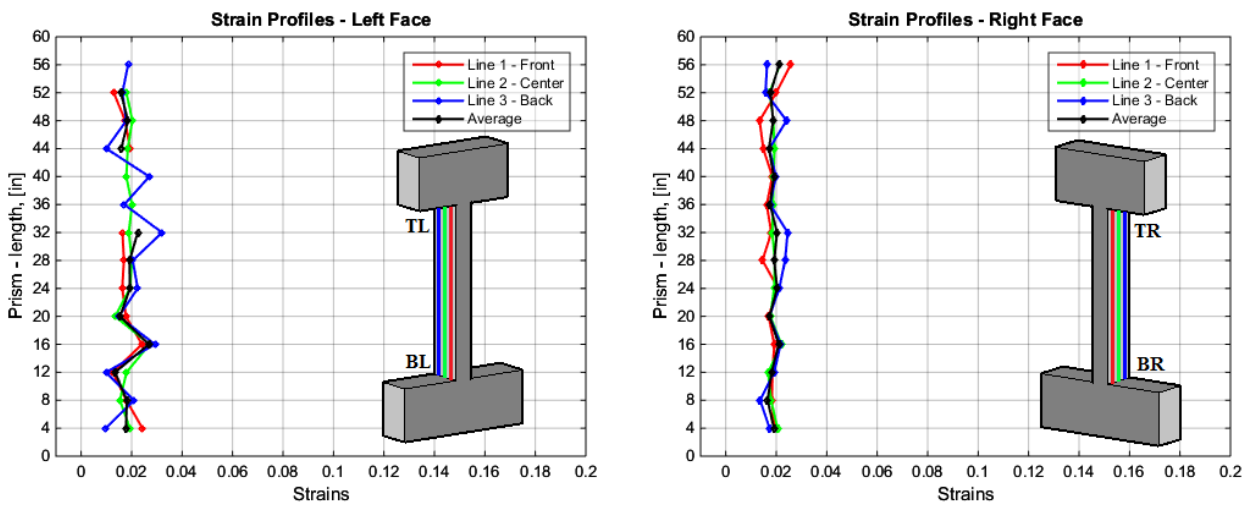

Figure A-232. Test 10: Strain profiles captured immediately before bar fracture

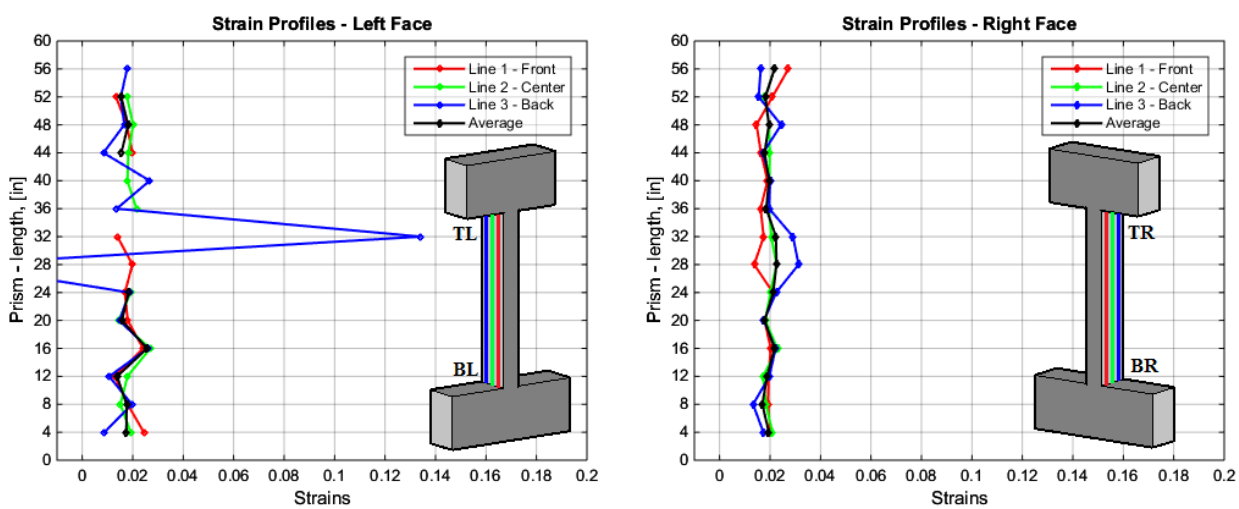

Figure A-233. Test 10: Strain profiles captured immediately after bar fracture

Figure A-231 shows strain profiles established during the last cycle for 14ε_y under tensile forces. The average of the strains in the left and right faces is 3.1%, close to the value established as target equivalent to 14ε_y=3.0%. Strain profiles captured immediately before and after bar fracture are plotted in Figure A-232 and Figure A-233, respectively. It is observed that the average of the strains immediately before fracture in both faces is close to 10ε_y; however, the strains reached in the location where the bar fractured, are close to 15ε_y. After the bar fractured, the values of the strains in that location jumped up to higher values because the infrared LED detached from the bar. The strains on the opposite face reached values slightly higher than 14ε_y.

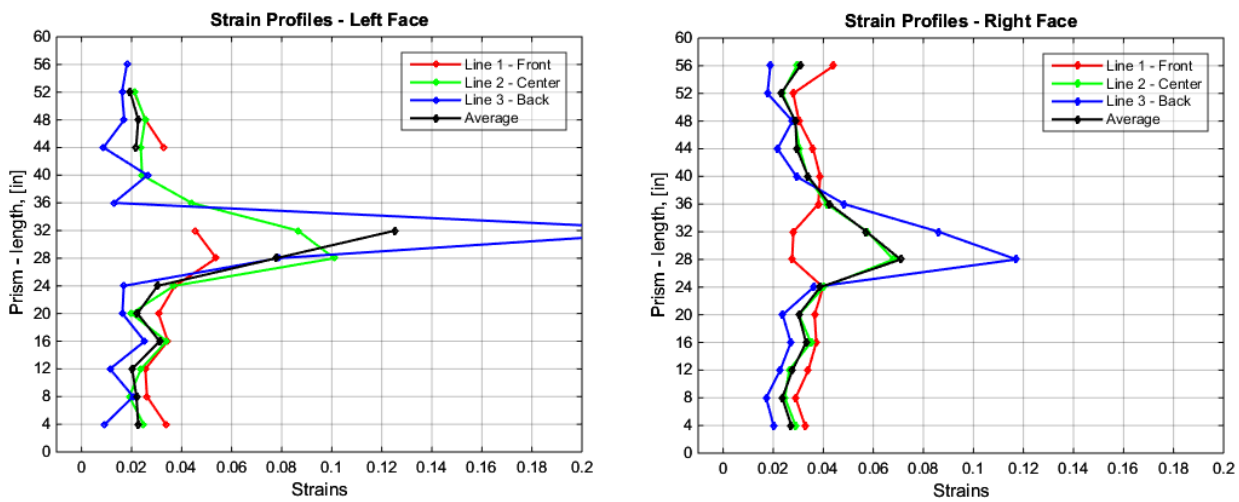

Figure A-234. Test 10: Strain profiles captured at maximum axial tensile demands after bar fracture

Figure A-234 shows the strain profiles at the time the test paused in order to observe the damage described in a previous paragraph. At this point the specimen was still subjected to tensile displacements higher than those that originated bar fracture since the test was not interrupted at that precise time. The average of the strains reached on the right face in the bottom and top regions is close to 14ε_y. Notice the higher values reached at midheight on the right face where the damage was concentrated due to bar fracture on the opposite face. The midheight values presented for the right face could be discarded because, as it was mentioned before, the infrared LED detached immediately after the bar fractured.

Figure A-235 depicts the entire structural response of P3-P10 as a function of axial forces captured from the vertical components of the actuators and axial displacements calculated from the Optotrak system. In the cycles associated with 10ε_y, 12ε_y, 14ε_y, and the last cycle, an axial stiffness reduction is evident by the time the axial compressive load approaches -34 kips. At these phases, the specimen is still extended. Once the cracks close, the prism gains stiffness and is able to carry the same axial load as in previous cycles. In the last cycle, bar fracture occurred under tensile displacements.

Consequently, upon compressive forces the prism was not able to completely recover its original strength. The maximum applied load at this stage was -272 kips, equivalent to 93% of the axial design compressive force, *Po*.

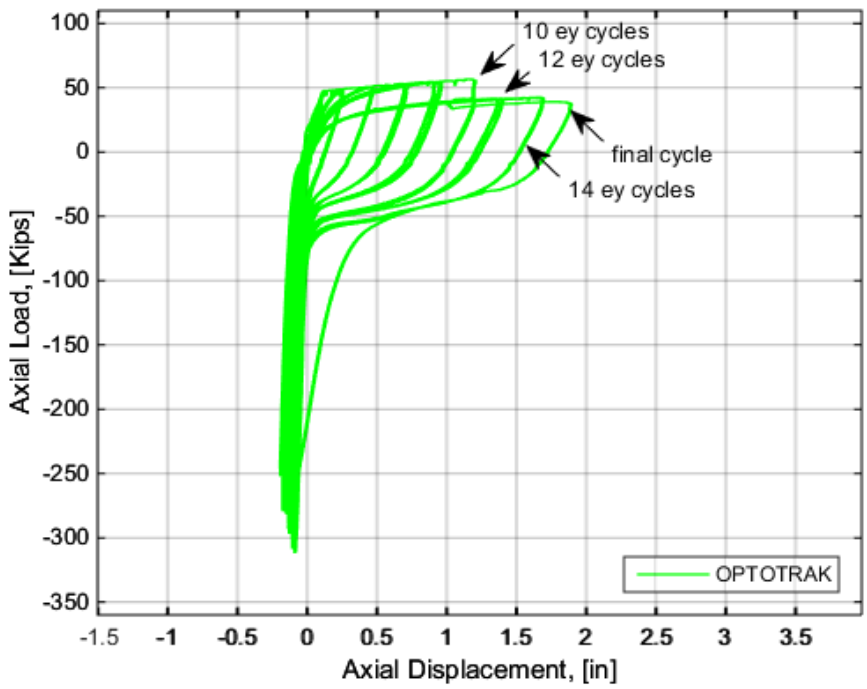

Figure A-235. Test 10: Axial structural response of prism P3-P10

Figure A-235 also shows that after the first cycle related to $10\varepsilon_y$ the axial tensile force capacity of the prism decreased from 56 kips to 41 kips, which represents a reduction of about 27%. This variation is attributed to bar buckling that probably occurred upon compressive loads before applying the second cycle related to $10\varepsilon_y$. In order to analyze this possibility, the upper and lower gages adjacent to the location where the bar fractured are considered to establish the strain responses during the test, Figure A-236. Notice that during the last 9 cycles corresponding to $10\varepsilon_y$, $12\varepsilon_y$, $14\varepsilon_y$ and under compression loads, the strains reached higher tensile values on the upper gage, and lower compressive values on the lower gage. With the aim of comparing this pattern to what happened at other location where fracture did not occurred, a second point is selected. The upper and lower adjacent strain responses are plotted in Figure A-237. It can be observed that for this case, the strain responses under compressive loads are more stable for the $10\varepsilon_y$ and $12\varepsilon_y$ cycles. However, during the $14\varepsilon_y$ cycles the analyzed point start to follow the same pattern as was described before, where tensile strains reached higher values on the upper gage, and lower compressive values on the lower gage when the specimen was being compressed. From this analysis it is concluded that the bar that fractured, certainly experienced bar buckling at earlier stages which led to a reduction in the tensile capacity of the prism and the subsequent bar rupture.

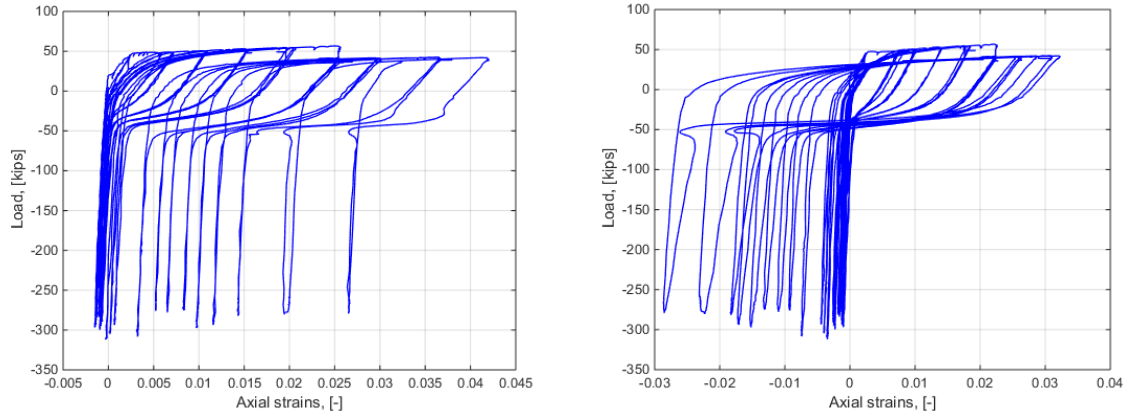

(a) (b)

Figure A-236. Test 10: Strain history response of two gages adjacent to the location where the bar fractured; (a) upper gage; (b) lower gage

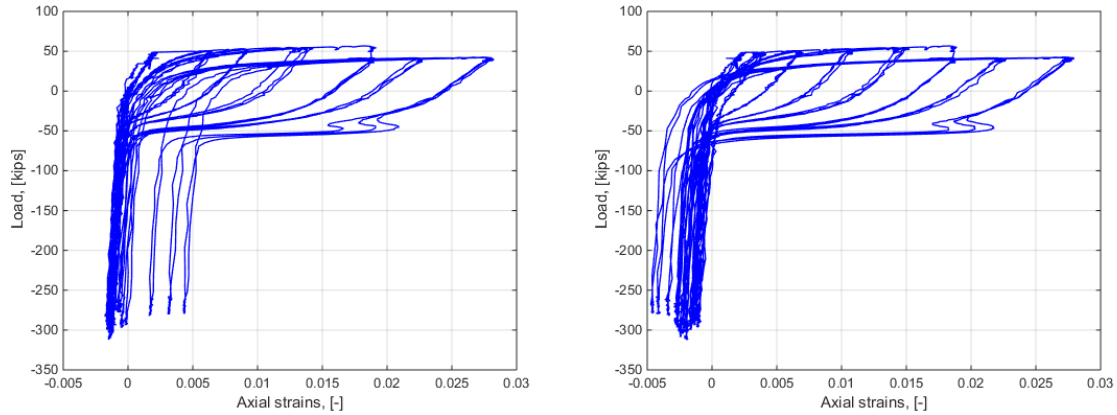

(a) (b)

Figure A-237. Test 10: Strain history response of two gages adjacent to a selected location opposite to corner place where the bar fractured; (a) upper gage; (b) lower gage

Figure A-238 illustrates the evolution of the nominal axial strain captured from gage 22 at the center of the specimen on the right face versus the normalized out-of-plane deformation and the axial force. Figure A-239 shows the variation of strains computed from gage 67 located at the center of the prism on the left face. Notice a stable response of the prism at low levels of axial tensile strains. The maximum normalized out-of-plane displacement developed upon compressive loading during the cycles associated with $14\varepsilon_y$ is 0.17. Yielding forces, *AsFy*, in tension and compression are also plotted in Figure A-238 and Figure A-239, where *As* is the area of the longitudinal reinforcement. It can be observed that during the last cycle, when the strains were close to $10\varepsilon_y$, the strain patterns changes drastically in both faces. This point has identified with the time where bar fracture occurred.

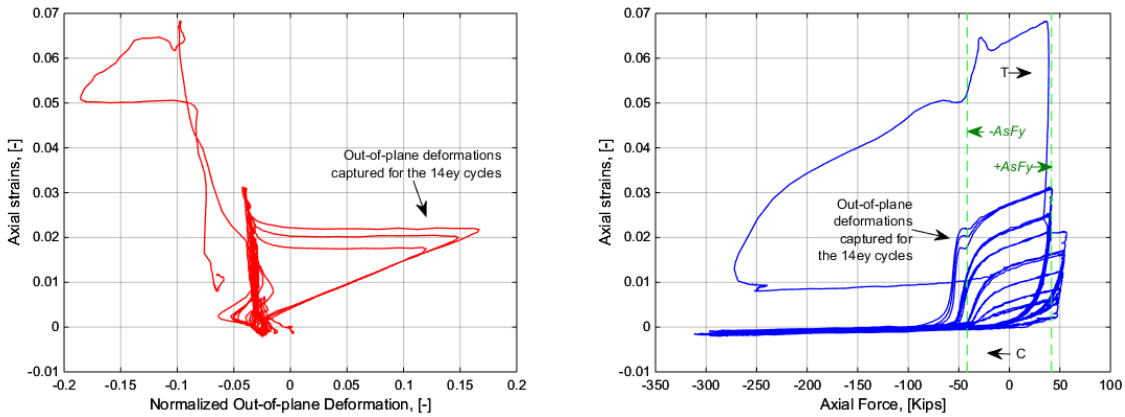

Figure A-238. Test 10: Response of specimen P3-P10 captured from a midheight gage on the right face

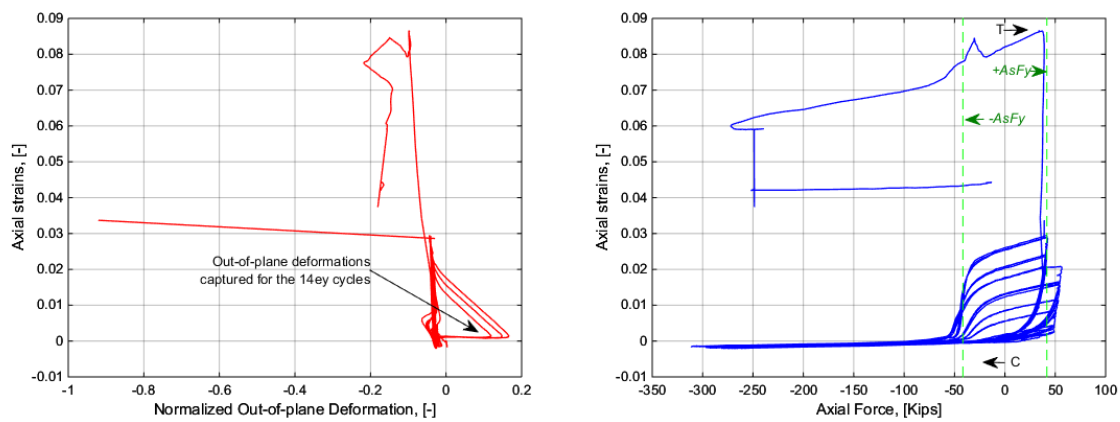

Figure A-239. Test 10: Response of specimen P3-P10 captured from a midheight gage on the left face

5. Conclusions

Specimen P3-P10 was tested during four hours where two loading patterns were applied. The first part of the test showed that the prism reached the maximum axial design compressive load with zero loss of capacity. The average compressive strain in both faces was close to -0.0014, less than the yielding strain.

In the second part of the test, progressive cyclic axial loads/strains were applied to the specimen reaching maximum values close to the axial design compressive force, *Po* = -294 kips and 16ε_y, in compression and tension, respectively. The specimen presented a stable response at low levels of axial tensile demands. Out-of-plane deformations were not noticed during the cycles before 14ε_y. Beyond the first cycle for 14ε_y, a gradual increase in the out-of-plane deformations were captured until bar fracture were observed when the specimen was subjected to tensile demands on the way to 16ε_y.

This time buckling instability did not occurred because bar buckling failure mode developed before, which led to a reduction in the tensile capacity of the specimen and a subsequent bar fracture. The stirrups remained as originally constructed. Analysis of the data from this test will continue, as a

consequence the material presented here should be considered preliminary. Further experiments will reveal more information about the effectiveness of the reinforcement detailing recommended in guidelines to prevent lateral instability in RC structural walls.

Stability of Ductile RC Structural Walls – Assessment of the Local Buckling Failure Mode

Test 11

October – 04 – 2016

Summary Report

Prepared for:

Alaska Department of Transportation

Prepared by:

RA – Ana Gabriela Haro

PIs – Mervyn Kowalsky and Rob Chai

North Carolina State University

Raleigh – NC

1. Executive Summary

Test 11 was conducted at the Constructed Facilities Laboratory on Tuesday, October 4, 2016, as part of the third phase related to the load path project. The specimen was designed and built simulating boundary elements from prototype walls. Axial cyclic tensile displacements and compressive loads generated from a cyclic loading considering subduction megathrust earthquakes were applied to the specimen to capture its structural performance and to determine additional critical parameters associated with lateral instability of RC walls. The first part of the results are presented in this report. Further analyses will be elaborated.

2. Introduction

Recent earthquakes in New Zealand and Chile have illustrated the importance of out-of-plane stability of concrete wall elements due to in-plane loading. Pier walls are occasionally employed by Alaska DOT for their in-plane lateral stiffness. While these walls are normally thicker than the walls typically found in building applications, their clear heights are also larger, giving rise to height-to-thickness ratios which may be larger than that of buildings. Some analyses have demonstrated that walls as thick as 20 in. may be prone to buckling, depending on their length and height.

Noticing the concentration of damage in the boundary elements of rectangular reinforced concrete structural walls due to higher stress and strain demands, some past investigations by others have been carried out on prisms, which was found to be an economical way to study the inelastic instability of structural walls. In general, the main objective of these tests focuses on subjecting specimens to cyclic tension and compression actions to simulate vertical components of actual seismic loading.

While past tests on prisms has shown existing models to be promising, missing from the models is the interaction with out-of-plane loading. The existing models correlate tensile strain from in plane loading to out-of-plane deformation, assuming a prescribed curvature distribution. If loading occurs in the out-of-plane direction, the relationship between tensile strain and out-of-plane deformations must be adjusted to reflect this. In its simplest form, this would be an addition of an out-of-plane displacement to the existing equation. However, out-of-plane displacement may impact the distribution of curvature with height, thus requiring additional adjustments to the models.

A total of 12 prisms are being experimentally tested in the Constructed Facilities Laboratory (CFL) during this project. The support conditions for the 12 prisms are conceived as fixed-fixed. The first testing phase involved controlled load paths where the specimens were subjected to tension/compression cycles in addition to lateral loading to mimic the effects of out-of-plane displacements. In the second and third phases, longitudinal reinforcement ratios varied to consider the typical values employed by Alaska DOT for pier walls. The details associated with the two phases are presented in Table A-21.

This first phase consisted of testing six 1/2-scale identical specimens. The thickness of the prisms was 5 in. since the cover was excluded from the construction. The geometry used was 5x12x60 in., corresponding to an aspect ratio (*h/b = height/thickness*) of 10 (including the missing cover). The longitudinal reinforcement ratio was 2.6% (6 bars #5). Transverse reinforcement consisted of #3 diameter rebar spaced at 2 in. and was placed as shown in Figure A-240.

Table A-21. Test 11: Description of the experimental phases

Phase	Tests	Geometry	Reinforcement	Loading
1	6	Thickness and Height (based on prototype wall). (6”x12” ; actual geometry = 5”x12”)	Longitudinal (6 bars **#5**) and transverse (#3@2in) reinforcement ratios similar for the 6 specimens.	Controlled 3D load path
2	3	Same as phase 1 (Based on actual pier walls formerly used by the Alaska DOT)	Longitudinal reinforcement ratio varies. (3 specimens 6 bars **#4**)	Controlled 3D load path
3	3	Same as phase 2 (Based on actual pier walls formerly used by the Alaska DOT)	Longitudinal reinforcement ratio varies. (3 specimens 6 bars **#3**)	Controlled 3D load path

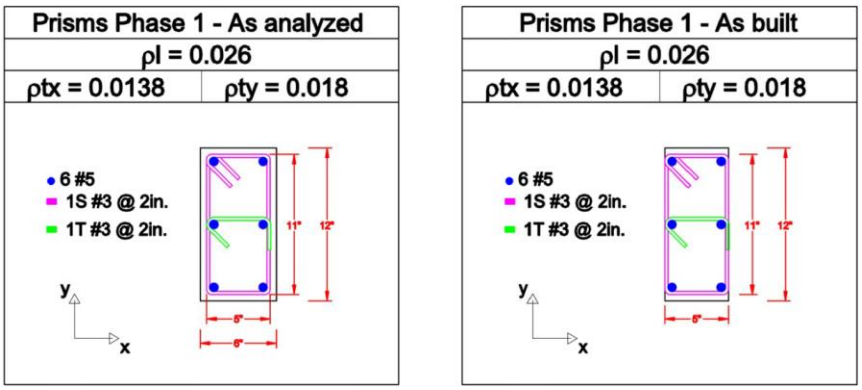

Figure A-240. Test 11: Phase 1 - Cross section of the prisms

The first phase concluded in June 2016. For the second phase, three more specimens were tested following similar load protocols and concluded in August 2016. During the third phase, three additional specimens are being tested considering equivalent parameters than the previous phases. The geometry of the specimens built for phases 2 and 3 was the same as the one adopted during the first phase, 5x12x60 in. The three specimens related to phase 2 included 6 #4 longitudinal bars and the three specimens related to phase 3 consist of 6 bars #3, corresponding to reinforcement ratios of 1.7% and 0.9%, respectively. The distribution of transverse reinforcement is similar to the one used for the first phase, Figure A-241.

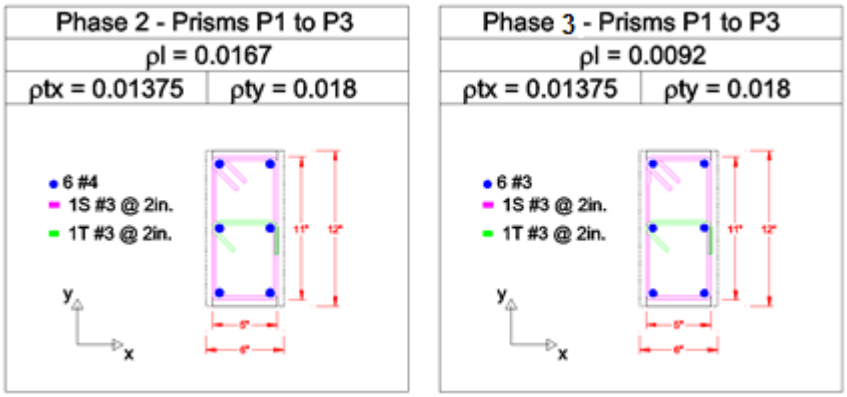

Figure A-241. Test 11: Phase 2 And Phase 3 - Cross section of the prisms

Regarding the material properties, an unconfined concrete strength of 5 ksi and reinforcement yielding strength of 62.9 ksi were considered as design values to define the load/displacement history for the test. Table A-22 shows the steel tensile test properties for the #3 bars associated with the three specimens of the third phase. The reinforcement detailing was established according to the ACI 318 and NEHERP guidelines for ductile columns and boundary elements.

Table A-22. Test 11: Phase 3 - Steel tensile test properties for bars #3 (longitudinal and transverse reinforcement)

Sample No.	Bar #	fy (ksi)	εy = fy/Es	fu (ksi)	εu
1	3	63.1	0.0022	89.0	0.1088
2	3	62.9	0.0022	89.7	0.1280
3	3	63.3	0.0022	90.3	0.1120
4	3	63.4	0.0022	90.2	0.1200
5	3	62.9	0.0022	90.1	0.1393
6	3	62.0	0.0021	89.8	0.1245
#3 Average long.		**62.9**	**0.00217**	**89.9**	**0.1221**
1	3	68.7	0.0024	100.1	0.0909
2	3	69.3	0.0024	101.2	0.0796
3	3	71.4	0.0025	100.9	0.0764
4	3	68.1	0.0023	100.6	0.1035
5	3	69.8	0.0024	100.5	0.1119
6	3	71.6	0.0025	100.9	0.1021
#3 Average transv.		**69.8**	**0.00241**	**100.7**	**0.0941**

3. Test Setup

The test setup consisted of a 14 ft long steel loading beam placed on the top of the specimen and connected to three actuators: two vertically inclined 440 kips actuators which induce axial loads and one horizontal 55 kips actuator to apply out-of-plane displacements. Two steel frames are used to

restrain torsion in the loading beam. Two concrete blocks attached to the strong floor support the specimen to reach the required height associated with the effective length of the 440 kips actuators. Figure A-242 displays the test setup drawings and Figure A-243 shows a picture of the area where the components of the project are placed.

The horizontal actuator is controlled by displacements. The vertically inclined actuator located at the left hand side of the specimen, Figure A-242, is controlled by rotations captured throughout an inclinometer attached to the loading beam. The actuator placed at the right hand of the specimen is controlled by a combination of forces and displacements. Loads and strokes in the actuators are measured through integrated LVDTs and loads cells.

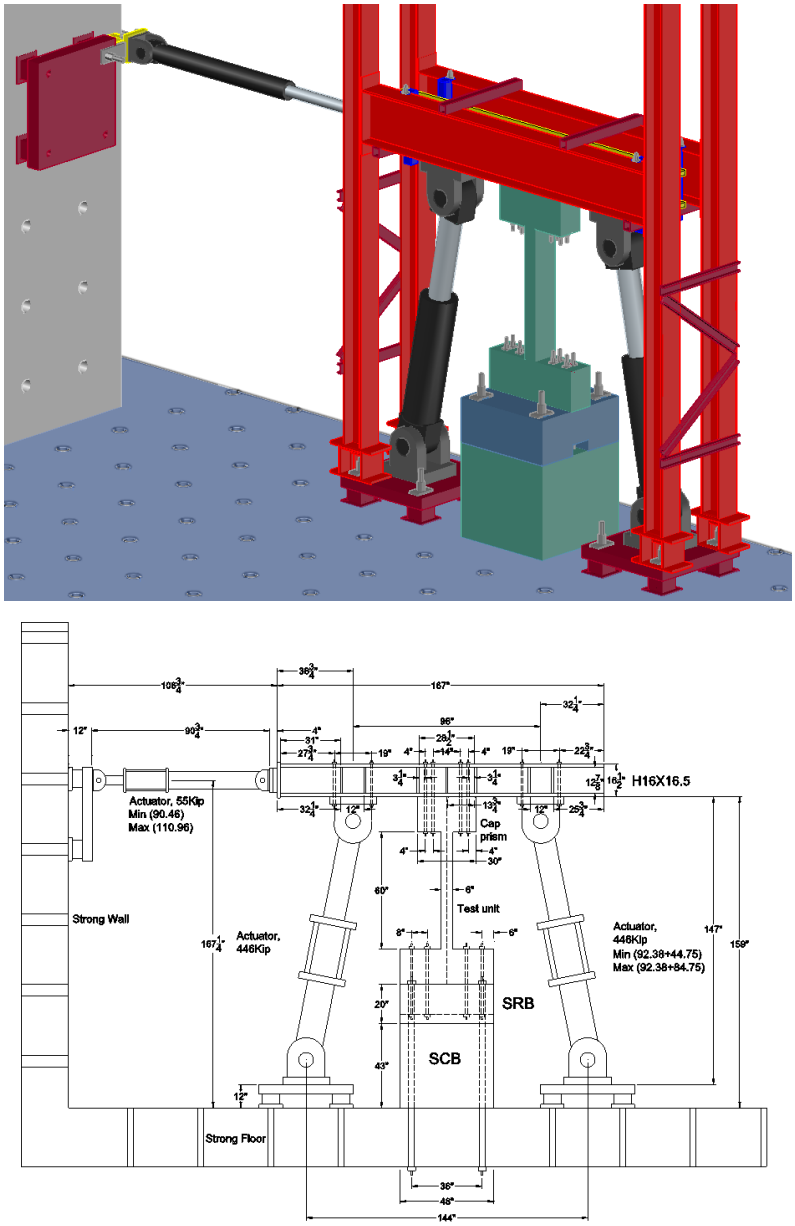

Figure A-242. Test 11: Test setup drawings

Figure A-243. Test 11: Test setup in the CFL at NC State

Relative displacements resulting from the interaction between the specimen and the connecting concrete block were obtained through 2 linear potentiometers. In addition, axial deformations of the prism were registered through 4 string potentiometers. Another string potentiometer was used to capture the lateral displacement of the loading beam.

A total of 110 infrared LEDs from the optical tracking system Optotrak Certus developed by Northern Digital Inc. were placed directly on the steel reinforcement of the prism. The objective is to establish longitudinal and transverse strains in real time throughout the MATLAB code "REALSTRAIN", created during the first phase of the project. Four additional infrared LEDs were positioned on the front face of the prism cap as a plane of reference. For the second phase, REALSTRAIN was modified to capture, in addition, real time displacements of the prism cap. Figure A-244 shows the distribution of the LEDs on the right face of the prism and the overall allocation of the markers obtained from the Optotrak spatial coordinate output.

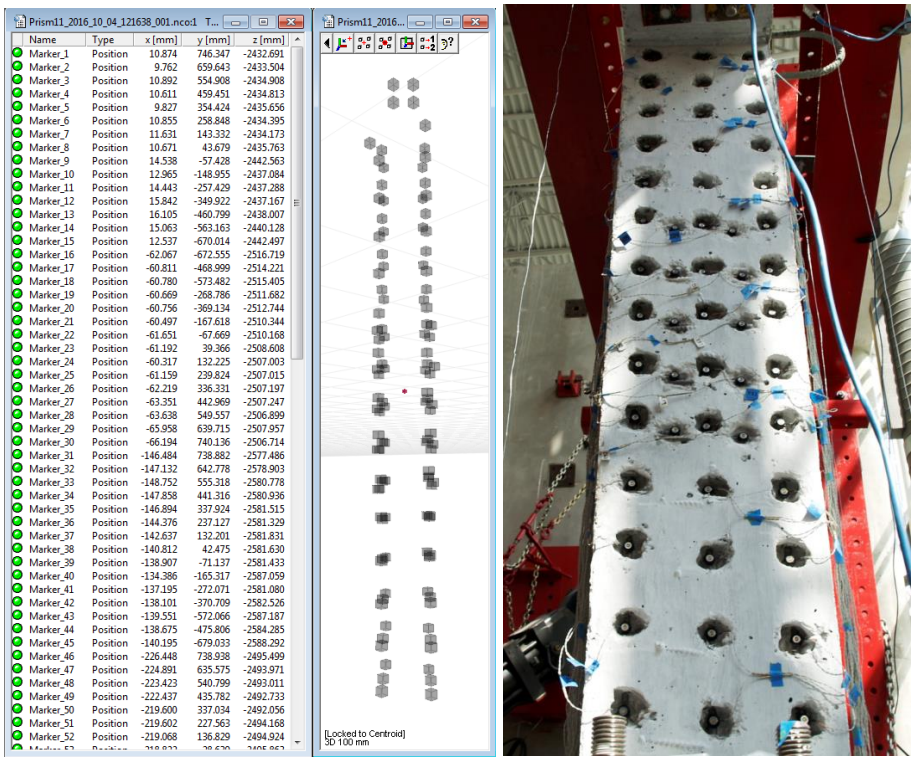

Figure A-244. Test 11: Instrumentation – Optotrak LEDs distribution on right face of the specimen and Spatial coordinate output

4. Test Summary

Specimen P3-P11 (Phase 3 – Prism 11) was subjected to axial tensile displacements and compressive loads generated from a cyclic protocol created according to (Bazaez & Dusicka, 2016), where inelastic cycles and cumulative damage demands of subduction megathrust earthquakes were considered to develop more realistic testing protocols to improve seismic assessment of RC bridge columns. Moment-Curvature analyses for 4 prototype structural walls were conducted and equivalent yield displacements (δy) were established to determine different inelastic protocols, according with the following equation:

$$f(N) = (a \cdot e^{bN} + c \cdot e^{dN})\delta_y \tag{1}$$

Where a, b, c, and d, are coefficients associated with different ductility levels and fundamental periods of predefined structural systems established in the mentioned study; and N, is the number of the inelastic cycle.

Once the cyclic displacement responses of the walls were obtained, strains developed at each stage were calculated. Strain ratios were determined as a function of ε_y. Finally, these ratios were scaled to $16\varepsilon_y$ (according to the inelastic out-of-plane buckling prediction model studied in this project, instability would occur beyond $16\varepsilon_y$ tensile demands), chosen as target value for the cycle before the

maximum peak is achieved, Figure A-245. The unique compressive target load was *Po* = -294 kips, which represents the maximum compressive capacity of the prism.

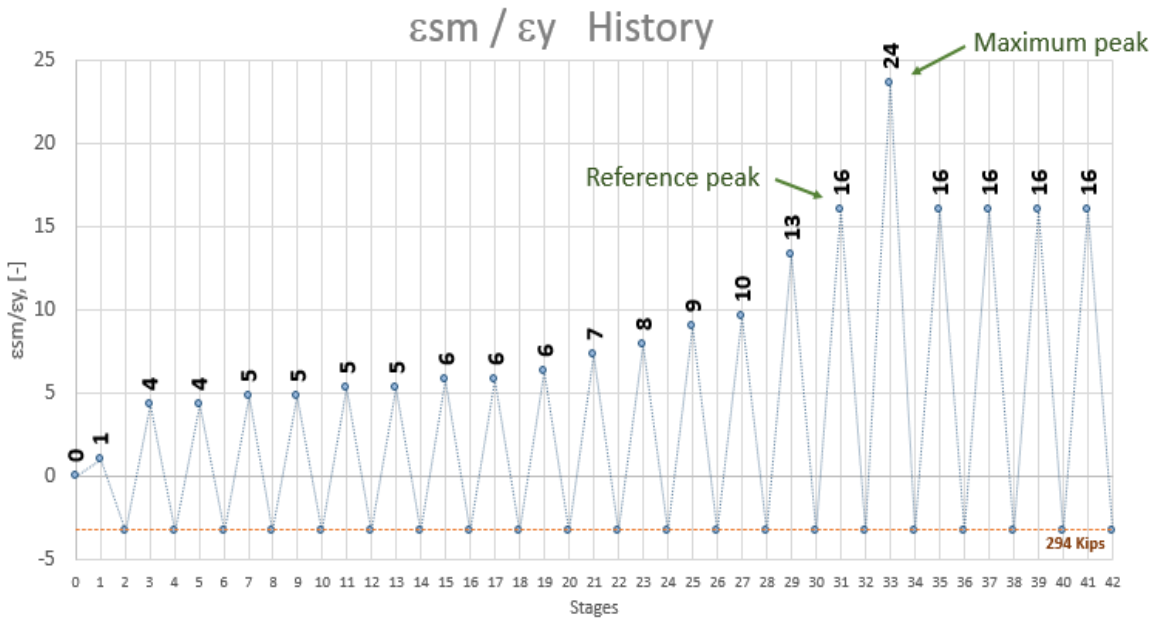

Figure A-245. Test 11: Strain / Force History intended to be applied during the test

Damage propagation at $1\varepsilon_y$, $4\varepsilon_y$, $5\varepsilon_y$, $6\varepsilon_y$, and $7\varepsilon_y$ is presented in Figure A-246 through Figure A-250, respectively. Upon $1\varepsilon_y$ strain demand, small horizontal cracks appeared all along the prism. Crack widths of about 0.005in. were captured at midheight. Upon compressive loads cracks uniformly closed as expected. This phenomenon was observed during the following cycles until failure was captured. In the course of the cycles corresponding to $4\varepsilon_y$, more cracks formed and the old ones extended. Crack widths between 0.05in. and 0.075in. were measured at midheight during the $4\varepsilon_y$, $5\varepsilon_y$, and $6\varepsilon_y$ cycles. Concrete flacking was captured upon compressive loads during the second cycle associated with $5\varepsilon_y$. Concrete spalling was observed during the $7\varepsilon_y$ cycle. Crack widths close to 0.10in. were measured at this stage on the midheight region and small vertical cracks propagated to the foundation. Throughout the following cycles the cracks became wider and the number of new cracks decreased. In addition, it was observed that the spacing of the horizontal cracks were governed by the cavities created to include the infrared LEDs.

Figure A-246. Test 11: Propagation of damage at 1 εy

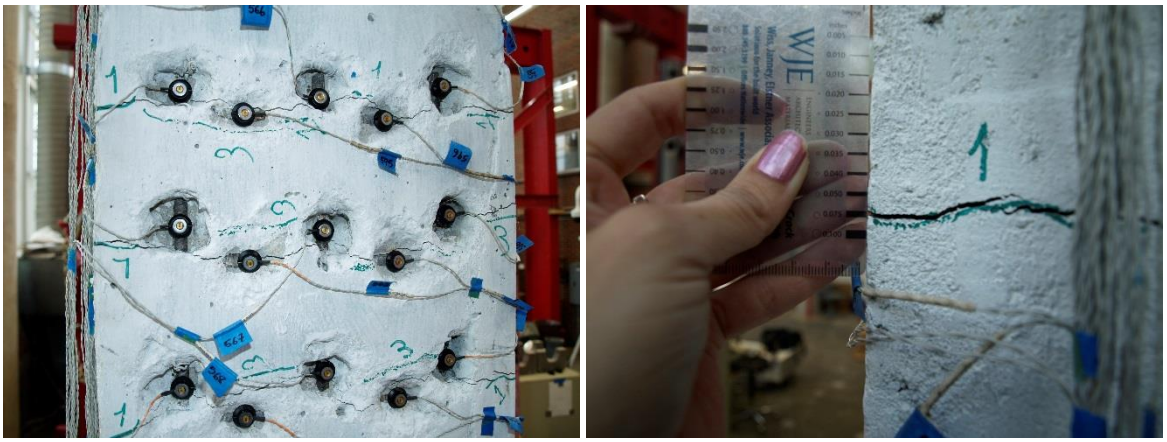

Figure A-247. Test 11: Propagation of damage at 4 εy - First cycle

Figure A-248. Test 11: Propagation of damage at 5 εy - First cycle

Figure A-249. Test 11: Propagation of damage at 6 εy - First cycle

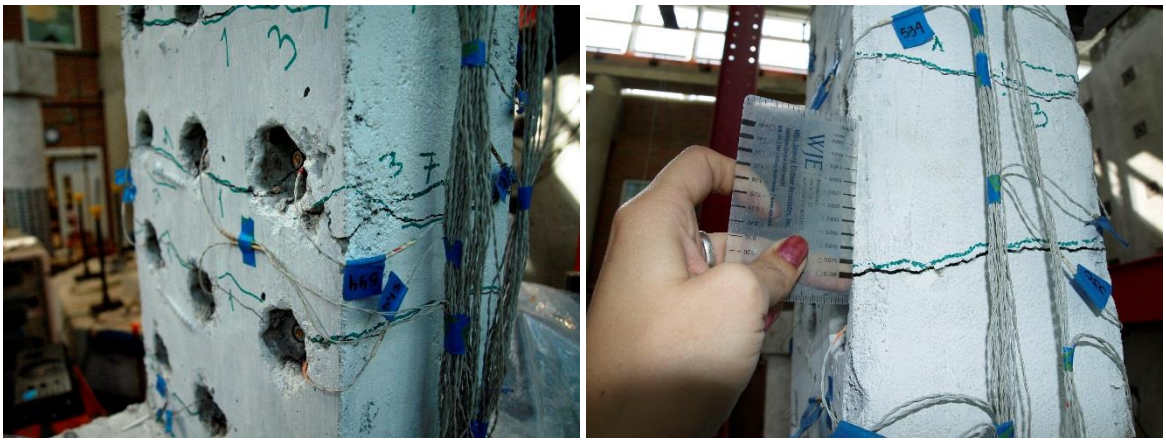

Figure A-250. Test 11: Propagation of damage at 7 εy

Figure A-251 shows the propagation of damage for the 8ε_y cycle, where crack widths close to 0.10 in. were observed at midheight. Figure A-252 and Figure A-253 show crack widths close to 1/8in. that were measured during the 9ε_y and 10ε_y cycles. Signs of concrete spalling were observed at 10ε_y; and, upon compressive loads, bar buckling was captured on the right face at midheight, Figure A-254. During the 13ε_y cycle, new cracks formed and older cracks became wider than 1/8in., Figure A-255. Upon compressive demands, the same bar that slightly buckled in a previous cycle, continued bending in the direction perpendicular to the right face where it was free to deform. Throughout the 16ε_y tensile demand, cracks widths reached 3/8in., Figure A-256. At the time the target load was achieved in compression, more bars slightly buckled all along the prism, showing a similar behavior than the one described before. Concrete spalling was also observed. Crack widths close to 1/4in. were measured when the axial tensile strain reached 24ε_y, Figure A-257. The distribution of cracks was mostly uniform along the height of the prism.

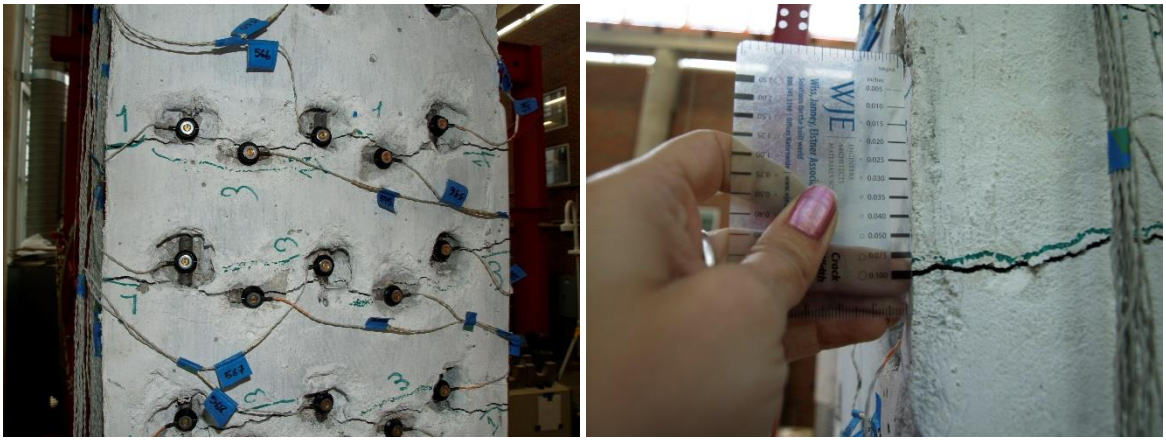

Figure A-251. Test 11: Propagation of damage at 8 εy

Figure A-252. Test 11: Propagation of damage at 9 εy

Figure A-253. Test 11: Propagation of damage at 10 εy

Figure A-254. Test 11: Bar buckling observed upon compressive loads during the 10 εy cycle

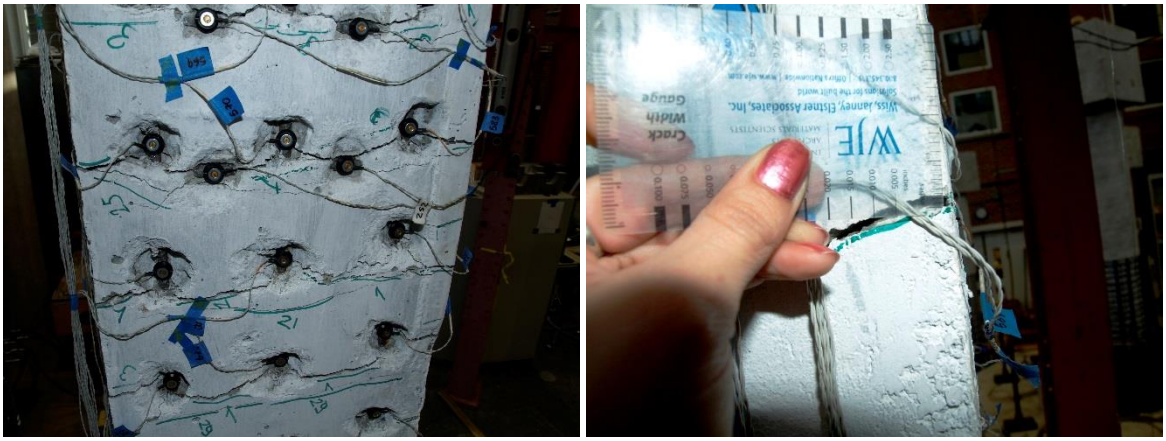

Figure A-255. Test 11: Propagation of damage at 13 εy

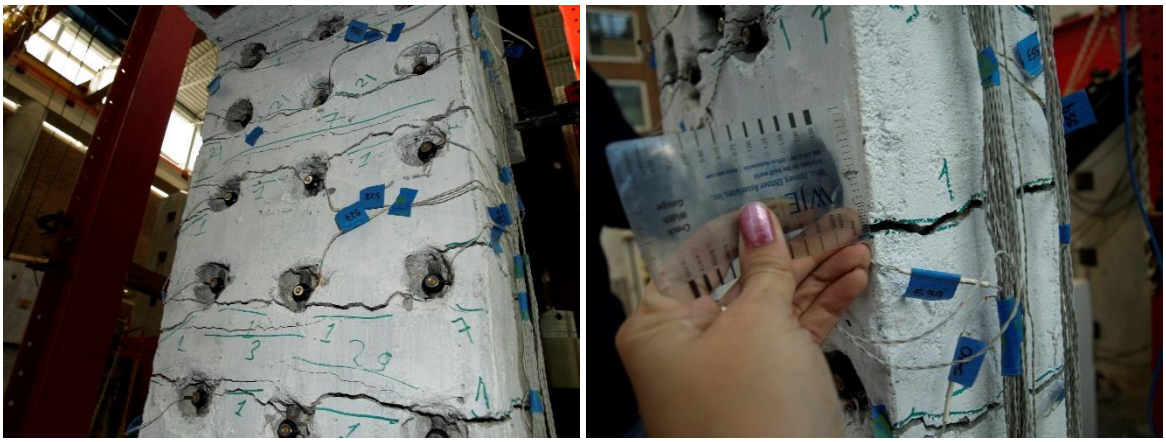

Figure A-256. Test 11: Propagation of damage at 16 εy

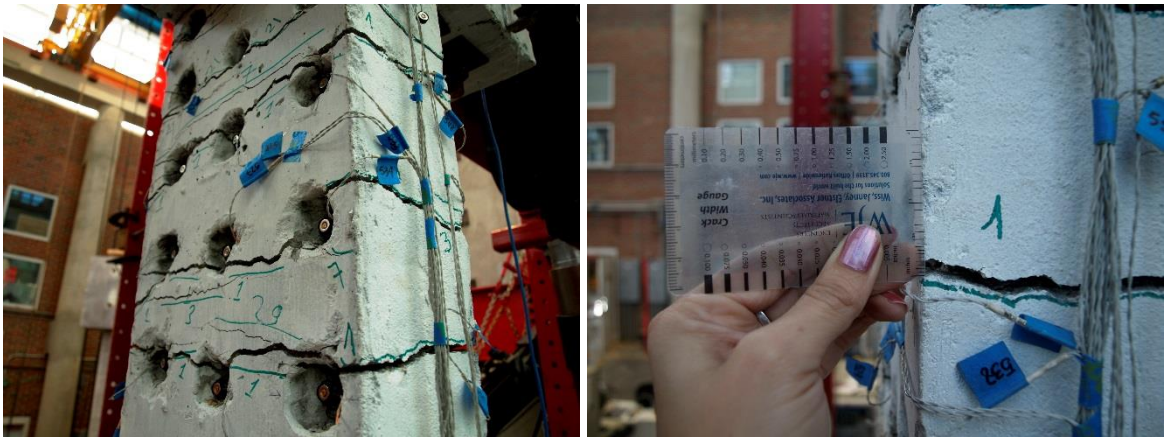

Figure A-257. Test 11: Propagation of damage at 24 εy

Out-of-plane buckling deformations were more evident during 13ε_y and 16ε_y, which implies that as tensile demands increased during these cycles, the out-of-plane buckling mechanism developed upon compressive loading. In this scenario, where the out-of-plane deformation is relatively small, the compression force developed to resist the overturning moment, can be fully reached as cracks close and consequently, the prism returns to a fairly straight and stable position. When compressive forces were acting on the specimen after reaching the maximum tensile demand at 24εy, instability occurred as illustrated in Figure A-258. The end of the test showing local concrete crushing at midheight is displayed in the same figure.

Figure A-258. Test 11: Instability captured upon compressive loads for 24εy

Figure A-259 depicts the entire structural response of P3-P11 as a function of axial forces captured from the vertical components of the actuators and axial displacements calculated from the Optotrak system. After the 13εy cycle, a zero stiffness region is developed by the time the axial compressive load approaches -35 kips. At these phases, the specimen is still extended. These points are associated with the onset of out-of-plane buckling. Due to the intrinsic eccentricity in the developed compressive

force, one side of the wall end region closes first resulting in out-of-plane deformations. Once the cracks close, the prism gains stiffness and is able to carry the same axial load as in previous compressive stages. In the last stage associated with 24εy and upon compressive loads, instability was captured since the prism was not able to recover its strength and original configuration. The maximum applied compressive load at this stage was -109 kips, equivalent to 37% of the axial design compressive capacity, *Po*.

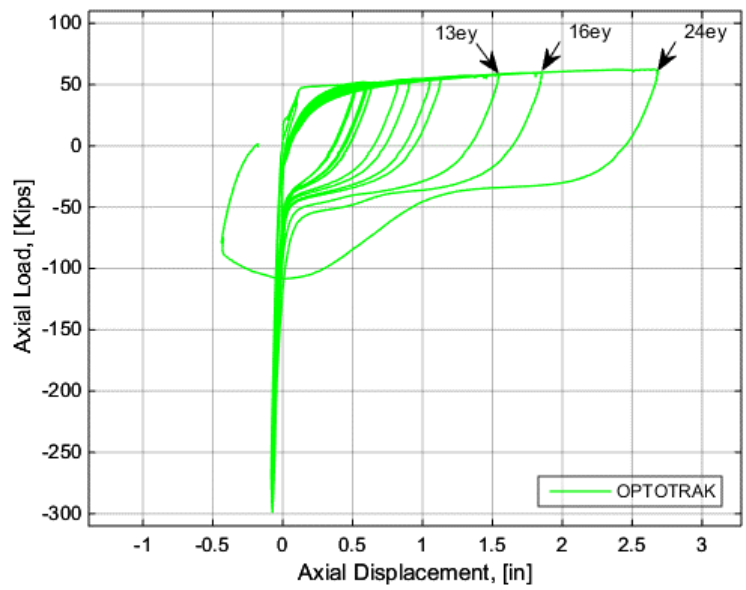

Figure A-259. Test 11: Axial structural response of prism P3-P11

Figure A-260 shows strain profiles established during the last cycle for 24ε_y under tensile forces. The average of the strains in the left and right faces is 5%, close to the value established as target value equivalent to 24ε_y = 5.2%.

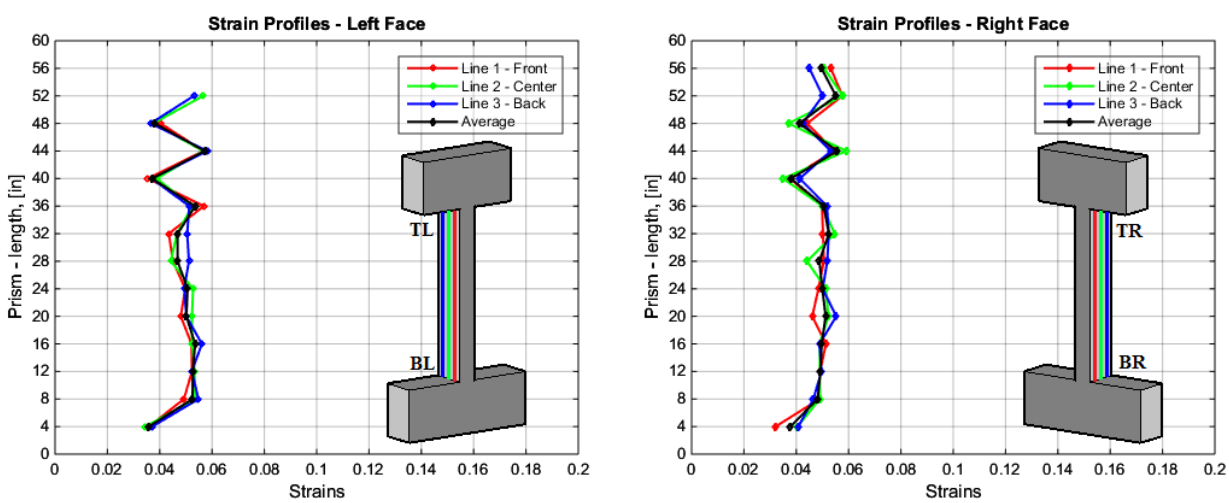

Figure A-260. Test 11: Strain profiles at 24εy

In order to analyze the bar buckling mechanism detected during the test, the upper and lower gages adjacent to the location where this phenomenon was significant are considered to establish their strain responses, Figure A-261. Notice that during the cycles corresponding to $10\varepsilon_y$, $13\varepsilon_y$, and $16\varepsilon_y$ when the specimen was subjected to maximum compressive loads, tensile strains are captured on the upper gage, and higher compressive strains on the lower gage. From this analysis it is concluded that the bar under study, certainly experienced bar buckling at earlier stages and became more severe at the time the specimen failed due to out-of-plane inelastic buckling. The damage observed at the end of the test showed a combination of the two failure modes.

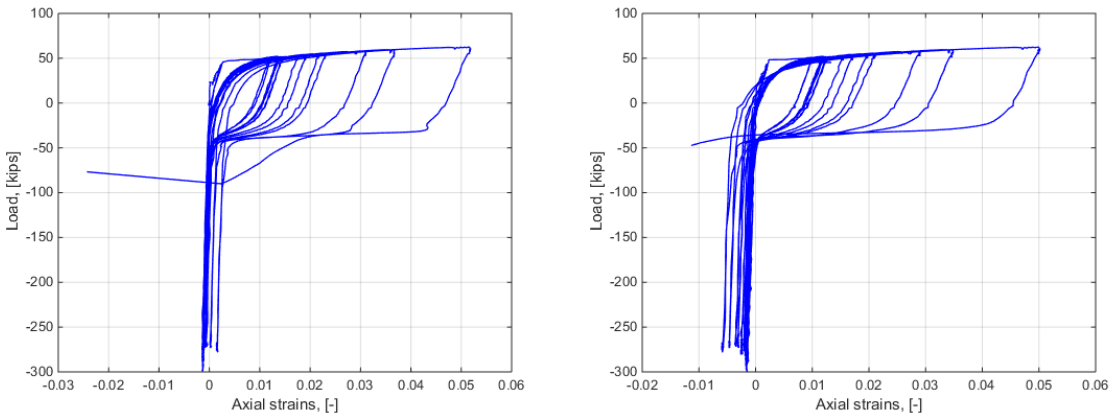

(a) (b)

Figure A-261. Test 11: Strain history response of two gages adjacent to the location where bar buckling was captured: (a) upper gage; (b) lower gage

Figure A-262 illustrates the evolution of the nominal axial strain captured from gage 22 at the center of the specimen on the right face versus the normalized out-of-plane deformation and the axial force. The compressive strain measured at the onset of instability reached a value of -0.56%. Figure A-263 shows the variation of strains computed from gage 67 located at the center of the prism on the left face. The tensile strain captured during the onset of instability is 4.3%. Notice a stable response of the prism at low levels of axial tensile strains.

The normalized out-of-plane displacements increased upon compressive loading during the $13\varepsilon_y$ and the first $16\varepsilon_y$ stages. A sudden increment on this deformation took place during the last cycle associated with $24\varepsilon_y$ at the time the compressive load was -67 kips, which represents 23% of the axial design compressive capacity, *Po=294 kips*. The onset of instability is captured at the time the relative normalized out-of-plane displacement reaches -0.49. Yielding forces, *AsFy*, in tension and compression are also plotted in Figure A-262 and Figure A-263, where *As* is the area of the longitudinal reinforcement.

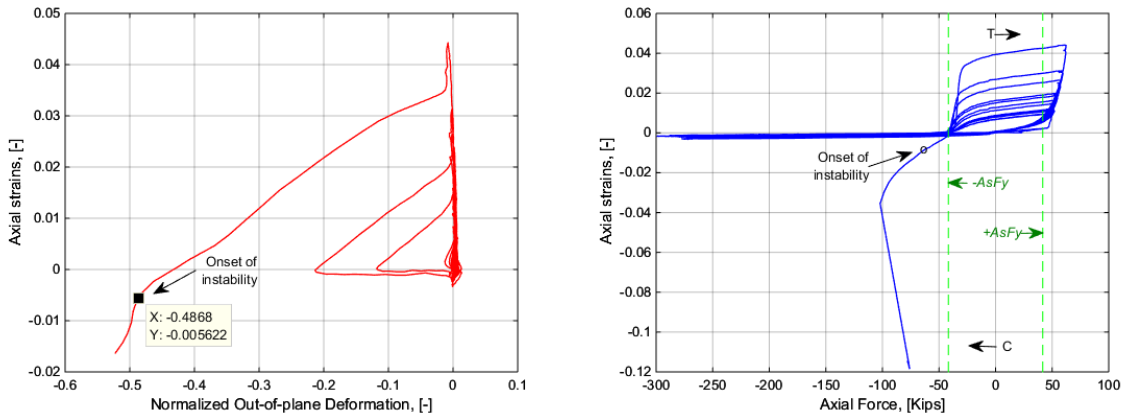

Figure A-262. Test 11: Response of specimen P3-P11 captured from a midheight gage on the right face

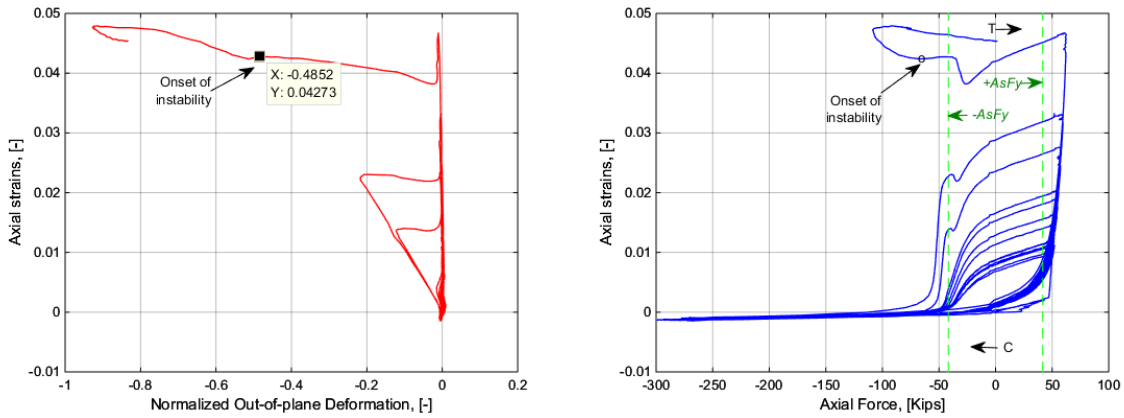

Figure A-263. Test 11: Response of specimen P3-P11 captured from a midheight gage on the left face

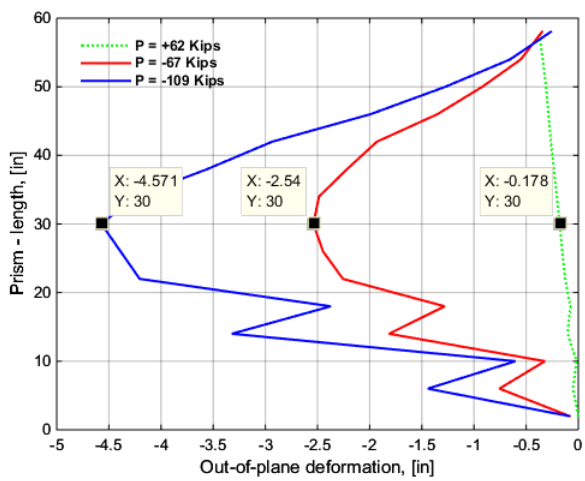

Figure A-264. Test 11: Evolution of the buckling shape during the last cycle under compressive loads

The evolution of the buckling shape during the last cycle of the test when the prism was subjected to compressive forces is plotted in Figure A-264. Three stages were considered: maximum tensile demand, onset of instability, and maximum out-of-plane deformation, which is in total 4.571 - 0.178 = 4.393 in., located at midheight.

5. Conclusions

Specimen P3-P11 was tested during four hours where it was subjected to axial cyclic tensile displacements and compressive loads generated from a cyclic protocol created to account for the effects of inelastic cycles and cumulative damage demands of subduction megathrust earthquakes.

The progressive cyclic axial loads/strains that were applied to the specimen reached maximum values close to the axial design capacity, Po = -294 kips in compression, and $24\varepsilon_y$ in tension. The specimen presented a stable response at low levels of axial tensile demands. First signs of out-of-plane deformations and bar buckling were noticed under compressive loads during the cycle associated with $10\varepsilon_y$. These mechanisms became more severe in the following cycles until instability was observed during the last cycle associated with $24\varepsilon_y$. The large out-of-plane buckling deformation led to concrete crushing and spalling in the central region of the prism. The axial compressive force at this stage was 37% of the compressive force applied in a previous cycle.

Bar fracture was not detected during or after the test. The stirrups remained as originally constructed. Analysis of the data from this test will continue, as a consequence the material presented here should be considered preliminary. Further experiments will reveal more information about the effectiveness of the reinforcement detailing recommended in guidelines to prevent lateral instability in RC structural walls.

Stability of Ductile RC Structural Walls – Assessment of the Local Buckling Failure Mode

Test 12

October – 12 – 2016

Summary Report

Prepared for:

Alaska Department of Transportation

Prepared by:

RA – Ana Gabriela Haro

PIs – Mervyn Kowalsky and Rob Chai

North Carolina State University

Raleigh – NC

1. Executive Summary

Test 12 was conducted at the Constructed Facilities Laboratory on Wednesday, October 12th, 2016, as part of the third phase related to the load path project. The specimen was designed and built simulating boundary elements from prototype walls. An axial cyclic load generated from a seismic historic record from 1994 Northridge earthquake (Sylmar station) was applied to the specimen to capture its structural performance and to determine additional critical parameters associated with lateral instability of RC walls. The first part of the results are presented in this report. Further analyses will be elaborated.

2. Introduction

Recent earthquakes in New Zealand and Chile have illustrated the importance of out-of-plane stability of concrete wall elements due to in-plane loading. Pier walls are occasionally employed by Alaska DOT for their in-plane lateral stiffness. While these walls are normally thicker than the walls typically found in building applications, their clear heights are also larger, giving rise to height-to-thickness ratios which may be larger than that of buildings. Some analyses have demonstrated that walls as thick as 20 in. may be prone to buckling, depending on their length and height.

Noticing the concentration of damage in the boundary elements of rectangular reinforced concrete structural walls due to higher stress and strain demands, some past investigations by others have been carried out on prisms, which was found to be an economical way to study the inelastic instability of structural walls. In general, the main objective of these tests focuses on subjecting specimens to cyclic tension and compression actions to simulate vertical components of actual seismic loading.

While past tests on prisms has shown existing models to be promising, missing from the models is the interaction with out-of-plane loading. The existing models correlate tensile strain from in plane loading to out-of-plane deformation, assuming a prescribed curvature distribution. If loading occurs in the out-of-plane direction, the relationship between tensile strain and out-of-plane deformations must be adjusted to reflect this. In its simplest form, this would be an addition of an out-of-plane displacement to the existing equation. However, out-of-plane displacement may impact the distribution of curvature with height, thus requiring additional adjustments to the models.

A total of 12 prisms are being experimentally tested in the Constructed Facilities Laboratory (CFL) during this project. The support conditions for the 12 prisms are conceived as fixed-fixed. The first testing phase involved controlled load paths where the specimens were subjected to tension/compression cycles in addition to lateral loading to mimic the effects of out-of-plane displacements. In the second and third phases, longitudinal reinforcement ratios varied to consider the typical values employed by Alaska DOT for pier walls. The details associated with the two phases are presented in Table A-23.

This first phase consisted of testing six 1/2-scale identical specimens. The thickness of the prisms was 5 in. since the cover was excluded from the construction. The geometry used was 5x12x60 in., corresponding to an aspect ratio (*h/b = height/thickness*) of 10 (including the missing cover). The longitudinal reinforcement ratio was 2.6% (6 bars #5). Transverse reinforcement consisted of #3 diameter rebar spaced at 2 in. and was placed as shown in Figure A-265.

Table A-23. Test 12: Description of the experimental phases

Phase	Tests	Geometry	Reinforcement	Loading
1	6	Thickness and Height (based on prototype wall). (6”x12” ; actual geometry = 5”x12”)	Longitudinal (6 bars **#5**) and transverse (#3@2in) reinforcement ratios similar for the 6 specimens.	Controlled 3D load path
2	3	Same as phase 1 (Based on actual pier walls formerly used by the Alaska DOT)	Longitudinal reinforcement ratio varies. (3 specimens 6 bars **#4**)	Controlled 3D load path
3	3	Same as phase 2 (Based on actual pier walls formerly used by the Alaska DOT)	Longitudinal reinforcement ratio varies. (3 specimens 6 bars **#3**)	Controlled 3D load path

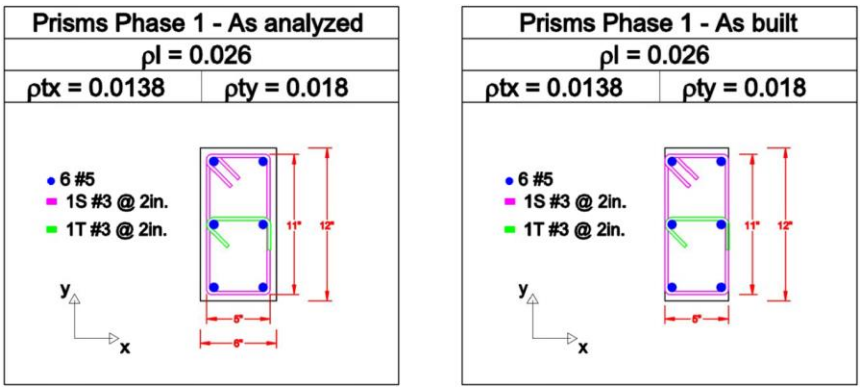

Figure A-265. Test 12: Phase 1 - Cross section of the prisms

The first phase concluded in June 2016. For the second phase, three more specimens were tested following similar load protocols and concluded in August 2016. During the third phase, three additional specimens are being tested considering equivalent parameters than the previous phases. The geometry of the specimens built for phases 2 and 3 was the same as the one adopted during the first phase, 5x12x60 in. The three specimens related to phase 2 included 6 #4 longitudinal bars and the three specimens related to phase 3 consist of 6 bars #3, corresponding to reinforcement ratios of 1.7% and 0.9%, respectively. The distribution of transverse reinforcement is similar to the one used for the first phase, Figure A-266.

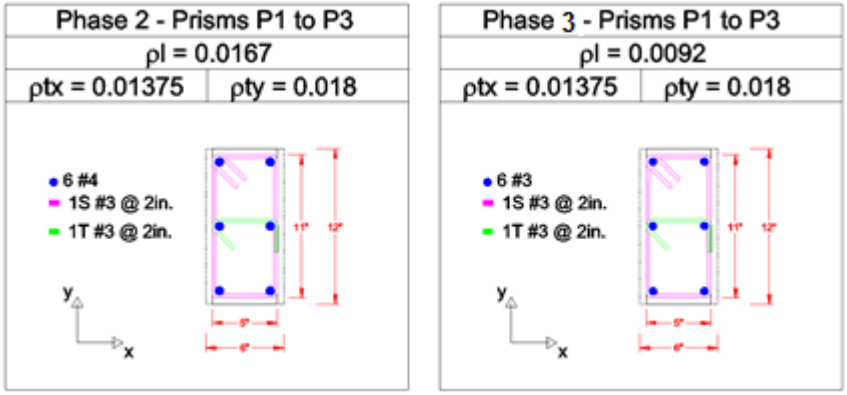

Figure A-266. Test 12: Phase 2 And Phase 3 - Cross section of the prisms

Regarding the material properties, an unconfined concrete strength of 5 ksi and reinforcement yielding strength of 62.9 ksi were considered as design values to define the load/displacement history for the test. Table A-24 shows the steel tensile test properties for the #3 bars associated with the three specimens of the third phase. The reinforcement detailing was established according to the ACI 318 and NEHERP guidelines for ductile columns and boundary elements.

Table A-24. Test 12: Phase 3 - Steel tensile test properties for bars #3 (longitudinal and transverse reinforcement)

Sample No.	Bar #	fy (ksi)	εy = fy/Es	fu (ksi)	εu
1	3	63.1	0.0022	89.0	0.1088
2	3	62.9	0.0022	89.7	0.1280
3	3	63.3	0.0022	90.3	0.1120
4	3	63.4	0.0022	90.2	0.1200
5	3	62.9	0.0022	90.1	0.1393
6	3	62.0	0.0021	89.8	0.1245
#3 Average long.		**62.9**	**0.00217**	**89.9**	**0.1221**
1	3	68.7	0.0024	100.1	0.0909
2	3	69.3	0.0024	101.2	0.0796
3	3	71.4	0.0025	100.9	0.0764
4	3	68.1	0.0023	100.6	0.1035
5	3	69.8	0.0024	100.5	0.1119
6	3	71.6	0.0025	100.9	0.1021
#3 Average transv.		**69.8**	**0.00241**	**100.7**	**0.0941**

3. Test Setup

The test setup consisted of a 14 ft long steel loading beam placed on the top of the specimen and connected to three actuators: two vertically inclined 440 kips actuators which induce axial loads and one horizontal 55 kips actuator to apply out-of-plane displacements. Two steel frames are used to

restrain torsion in the loading beam. Two concrete blocks attached to the strong floor support the specimen to reach the required height associated with the effective length of the 440 kips actuators. Figure A-267 displays the test setup drawings and Figure A-268 shows a picture of the area where the components of the project are placed.

The horizontal actuator is controlled by displacements. The vertically inclined actuator located at the left hand side of the specimen, Figure A-267, is controlled by rotations captured throughout an inclinometer attached to the loading beam. The actuator placed at the right hand of the specimen is controlled by a combination of forces and displacements. Loads and strokes in the actuators are measured through integrated LVDTs and loads cells.

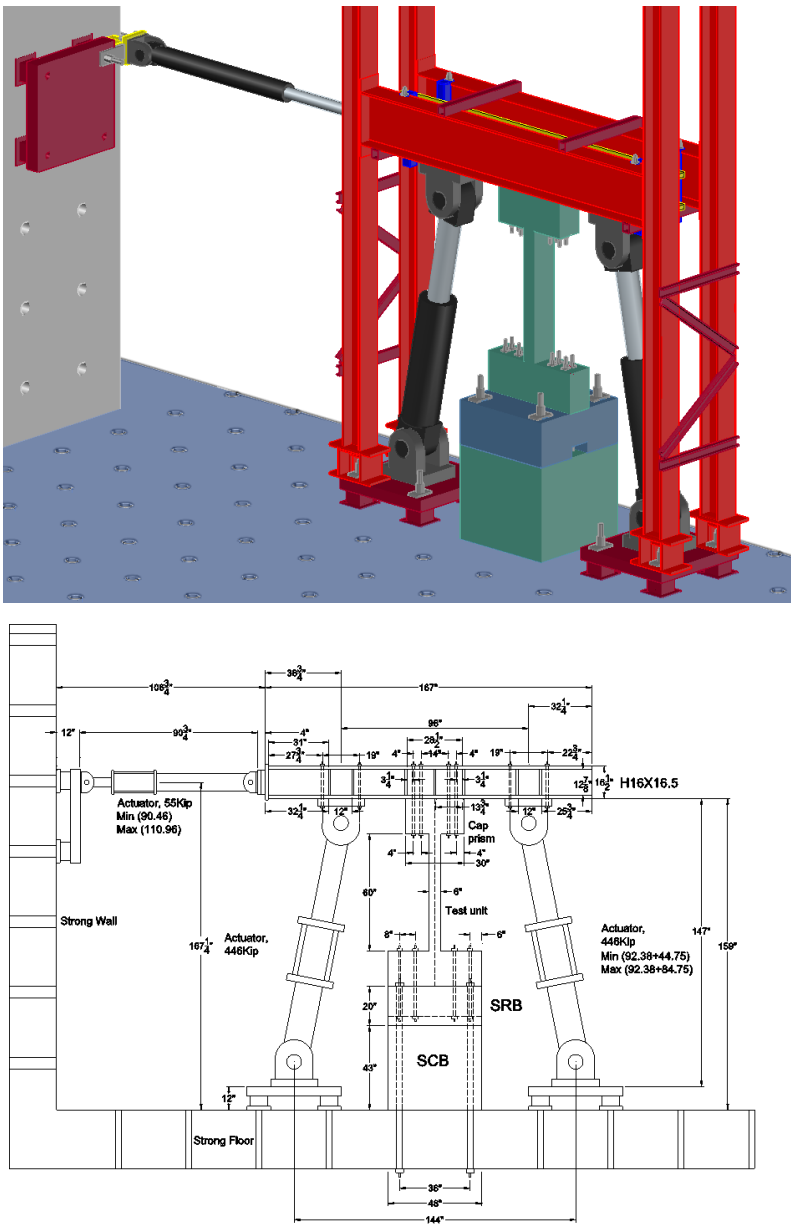

Figure A-267. Test 12: Test setup drawings

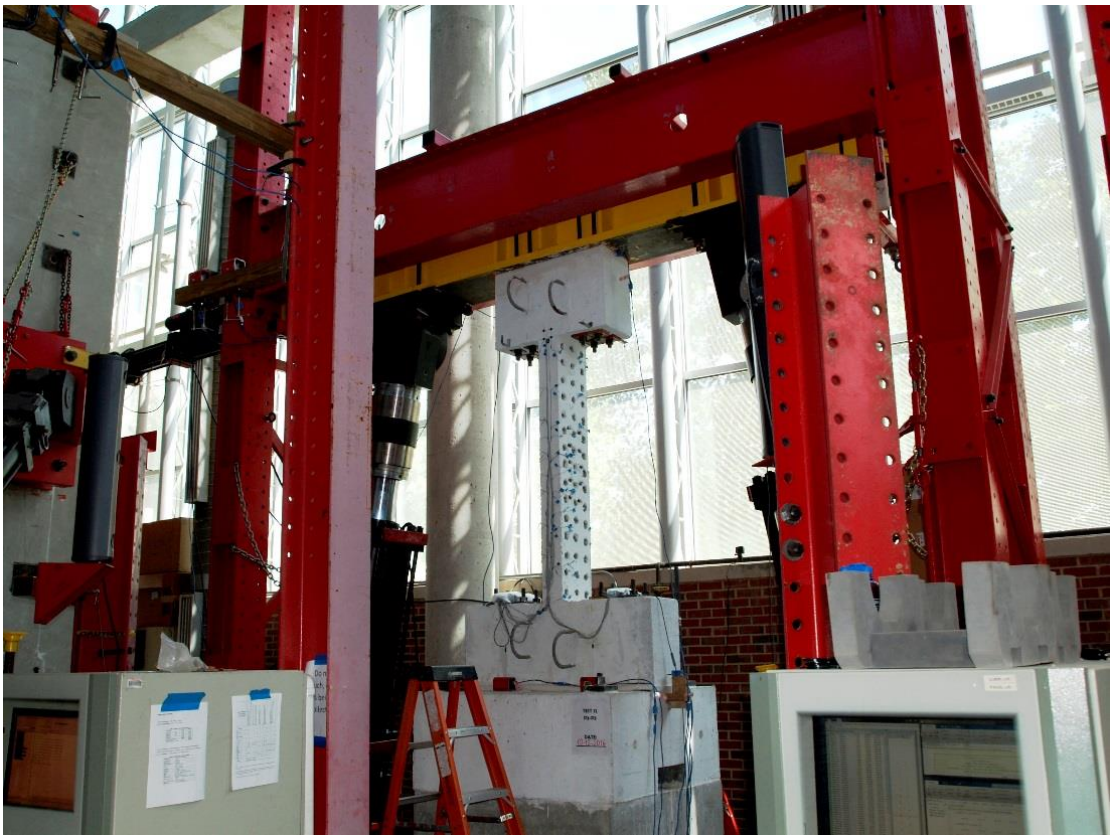

Figure A-268. Test 12: Test setup in the CFL at NC State

Relative displacements resulting from the interaction between the specimen and the connecting concrete block were obtained through two linear potentiometers. In addition, axial deformations of the prism were registered through four string potentiometers. Another string potentiometer was used to capture the lateral displacement of the loading beam.

A total of 110 infrared LEDs from the optical tracking system Optotrak Certus developed by Northern Digital Inc. were placed directly on the steel reinforcement of the prism. The objective is to establish longitudinal and transverse strains in real time throughout the MATLAB code "REALSTRAIN", created during the first phase of the project. Four additional infrared LEDs were positioned on the front face of the prism cap as a plane of reference. For the second phase, REALSTRAIN was modified to capture, in addition, real time displacements of the prism cap. Figure A-269 shows the distribution of the LEDs on the right face of the prism and the overall allocation of the markers obtained from the Optotrak spatial coordinate output.

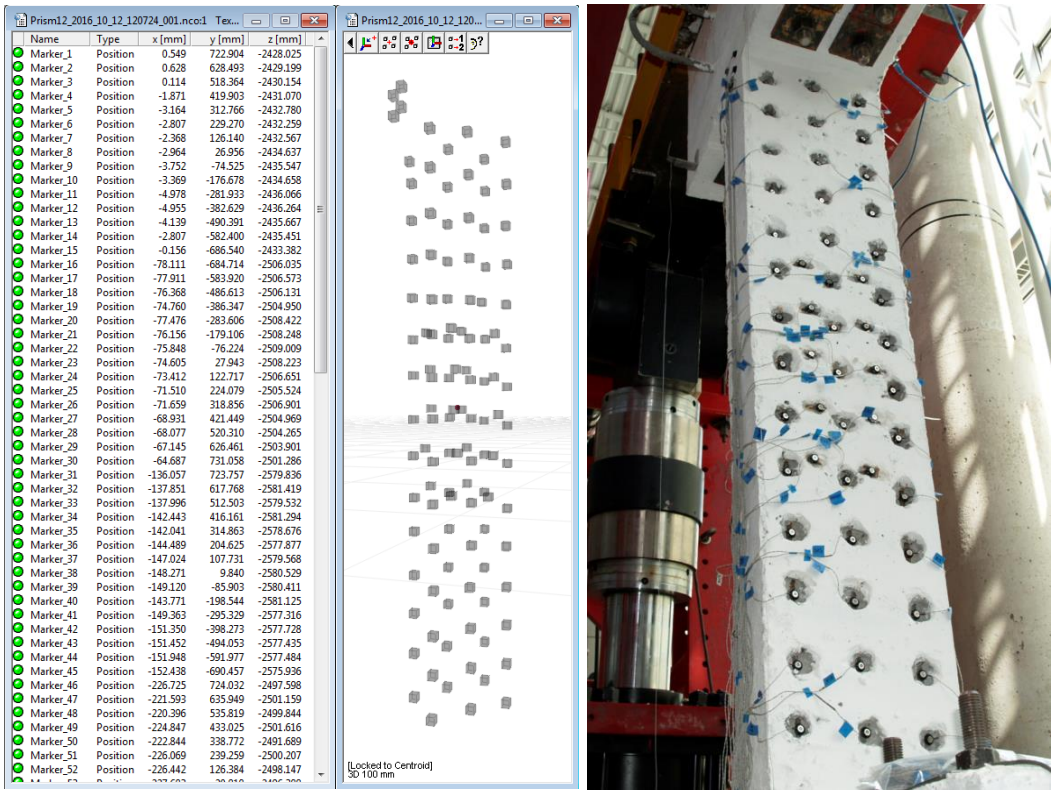

Figure A-269. Test 12: Instrumentation – Optotrak LEDs distribution on right face of the specimen and Spatial coordinate output

4. Test Summary

Specimen P3-P12 (Phase 3 – Prism 12) was subjected to a seismic axial displacement history based on the structural response of a prototype RC wall subjected to an actual in-plane horizontal earthquake record. The earthquake is characterized for a long duration pulse, consequently a record from the 1994 Northridge earthquake (Sylmar station) was selected. The main purpose of subjecting the specimen to this kind of demands, is to consider the effects of near-field records that contain long duration pulses. With this aim, a time history analysis was conducted using SEISMOSTRUCT. Figure A-270 shows the Sylmar earthquake horizontal accelerations applied to the prototype wall. The geometry of the wall consists of a total height of 21 meters (69 ft), a length of 4 meters (13 ft) and a thickness of 0.15 meters (5 in.). Figure A-271 presents the strain response history of a data point that corresponds to a longitudinal reinforcement 12 mm diameter steel bar located at the base of the wall in one of the boundary elements.

Subsequently, the seismic axial displacements to be applied during test #12 were defined as stages considering the 60 in. height of the prism P3-P12 and the strains already determined in a previous step. A total of 6 stages were established for each input data. The first axial displacement history was scaled as a function of a maximum tensile displacement associated with $16\varepsilon_y$, and the second one was scaled

to 18ε_y, see Figure A-272. The unique compressive target load considered during the entire test was the maximum axial design compressive capacity of the prism, *Po* = -294 kips.

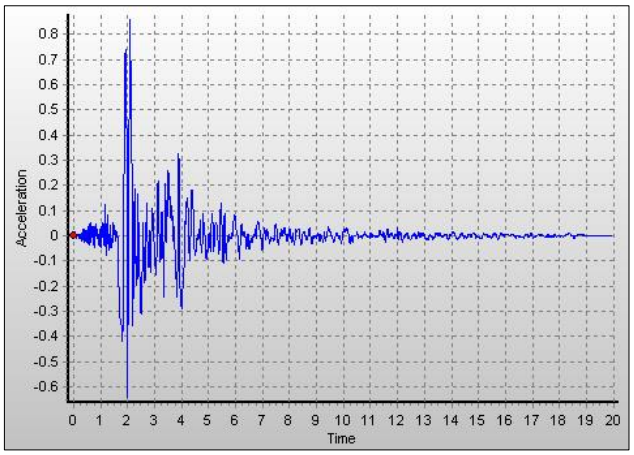

Figure A-270. Test 12: 1994 Northridge earthquake - Sylmar station accelerations record

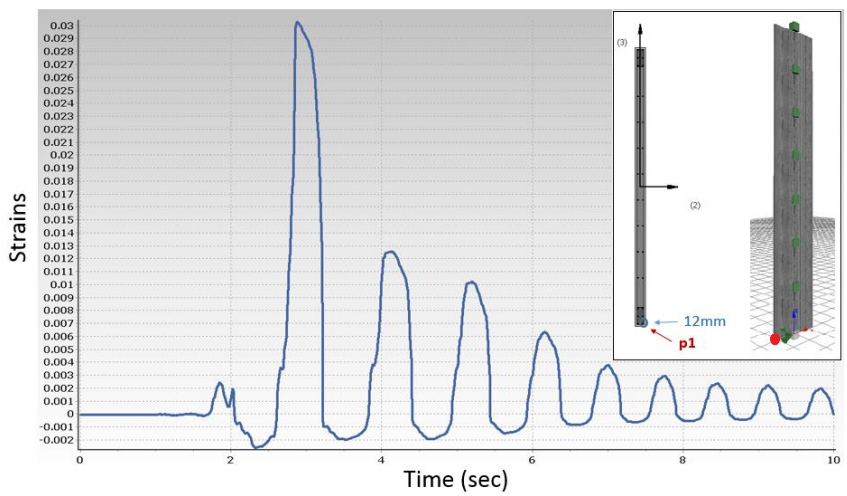

Figure A-271. Test 12: Strain time history response of a longitudinal reinforcement data point located at the base of an RC wall

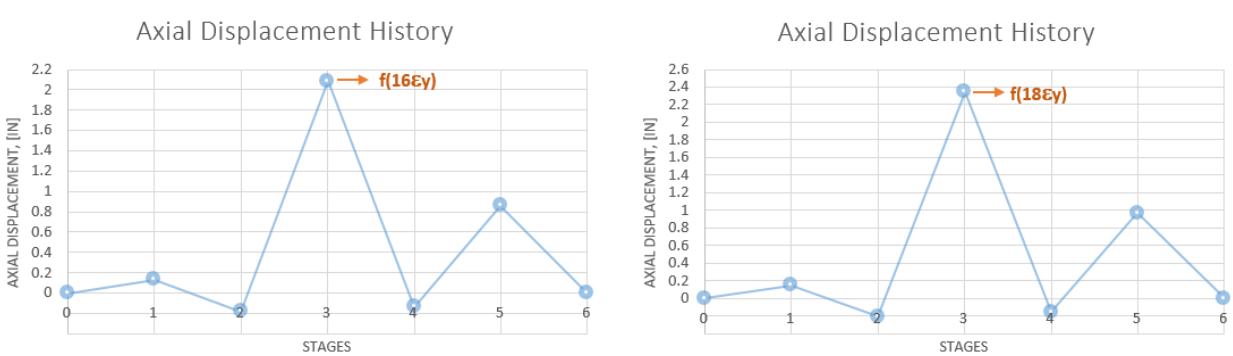

Figure A-272. Test 12: Axial displacement history inputs applied during test #12

During the first stage corresponding to the first 16εy seismic axial displacement history input, horizontal cracks appeared along the length of the prism where crack widths close to 0.005 in. were measured at midheight, Figure A-273. Upon compressive loads, cracks uniformly closed. This phenomenon was observed during the following stages until instability was captured at the end of the test.

Damage propagation at $16\varepsilon_y$ (1), where (1) implies the first seismic axial displacement input, is presented in Figure A-274. Crack widths close to 3/16 in. were captured on the region close to the footing. The distribution of cracks was nearly uniform along the height of the prism. The out-of-plane buckling mechanism was observed upon compressive loading. In this scenario, where the out-of-plane deformation is relatively small, the compression force developed to resist the overturning moment, can be fully reached as cracks close and consequently, the prism returns to a straight and stable position. Throughout the next cycle, out-of-plane buckling deformations were not evident. At the end of the stage # 6, signs of concrete flacking were observed, Figure A-275.

Two more complete load histories associated with $16\varepsilon_y$ were applied to the specimen, where out-of-plane deformations were only captured upon compressive loads right after the maximum tensile target equal to $16\varepsilon_y$ was achieved. More damage related to concrete spalling was accumulated during these cycles. In addition signs of bar bucking appeared during the second load history input. However since inelastic buckling was not captured up to this point, then the load history related to 18εy were applied. New and wider cracks only manifested at the time the specimen was subjected to the maximum tensile demand equivalent to $18\varepsilon_y$, Figure A-276. Crack widths close to 1/4 in. were captured at midheight. Concrete spalling propagated in the bottom region (BR). The out-of-plane buckling mechanism was visually captured upon compressive loading, but the prism returned to a fairly straight and stable position. Concrete cover fell down on the front face of the prism and the transverse reinforcement was exposed within a length of 40 in. Before resuming the test, debris was removed to protect the instrumentation and subsequently the next target tensile displacement was reached.

Once the 6 stages were completed, the same displacement history related to $18\varepsilon_y$ was applied. Upon tensile displacements and on the way to $18\varepsilon_y$ (2), two bars located in the midheight right face region fractured before reaching the tensile target, Figure A-277. Subsequently, the prism was subjected to a last compressive load and during this stage out-of-plane instability combined with bar buckling were observed. Figure A-278 presents the final state of the specimen P3-P12.

Figure A-273. Test 12: Propagation of cracks during the first axial tensile displacement [Stage 1 - 16εy (1) displacement history input]

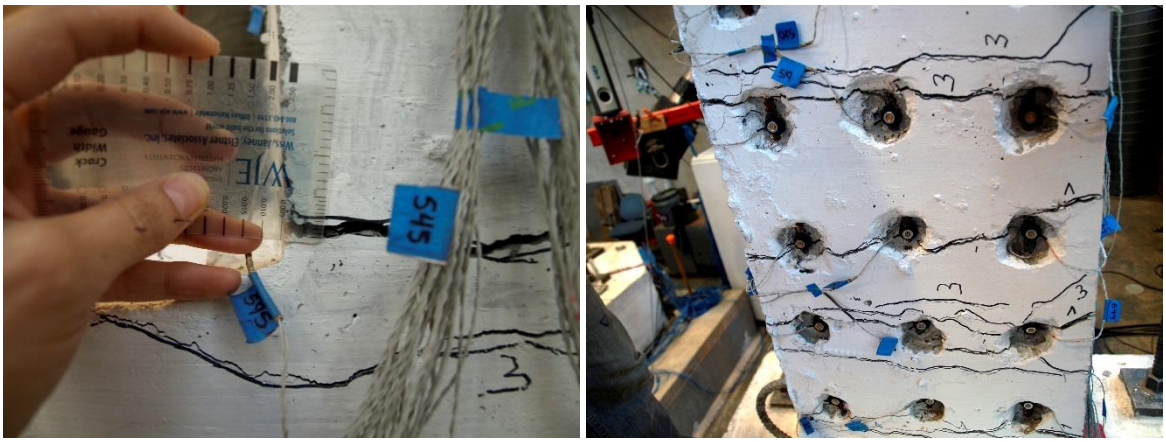

Figure A-274. Test 12: Propagation of damage at 16 εy [Stage 3 - 16εy (1) displacement history input]

Figure A-275. Test 12: Damage captured at the end of the first displacement history input

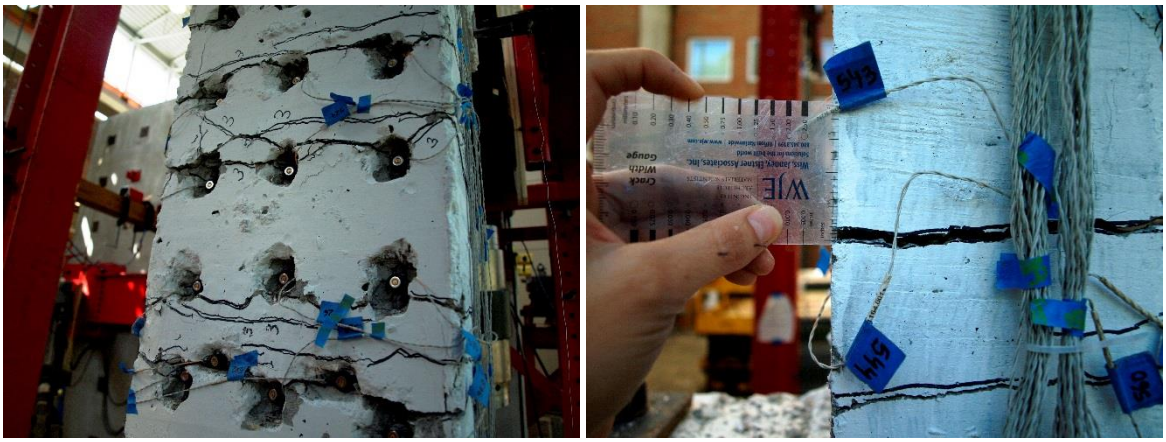

Figure A-276. Test 12: Propagation of damage at 18 εy [Stage 3 - 18εy (1) displacement history input]

Figure A-277. Test 12: Propagation of damage on the way to 18 εy [Stage 3 - 18εy (2) displacement history input]

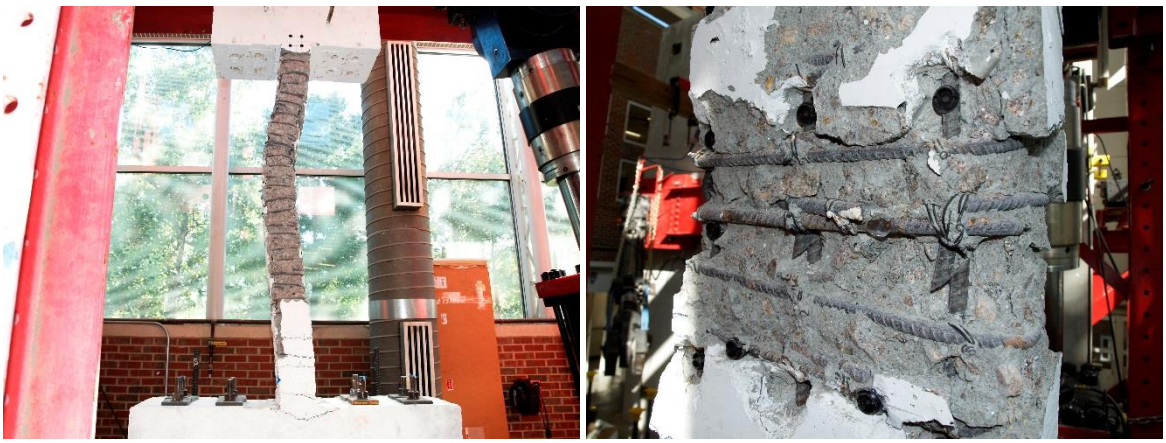

Figure A-278. Test 12: Out-of-plane instability captured upon compressive loads [Stage 4 - 18εy (2) displacement history input]

Figure A-279 and Figure A-280 show strain profiles established at 16ε_y (1) and 18ε_y (1), respectively. The average of the strains in the left and right faces is 3.6% and 4.0%, close to the values established as targets equivalent to 16ε_y=3.5% and 18ε_y=3.9%.

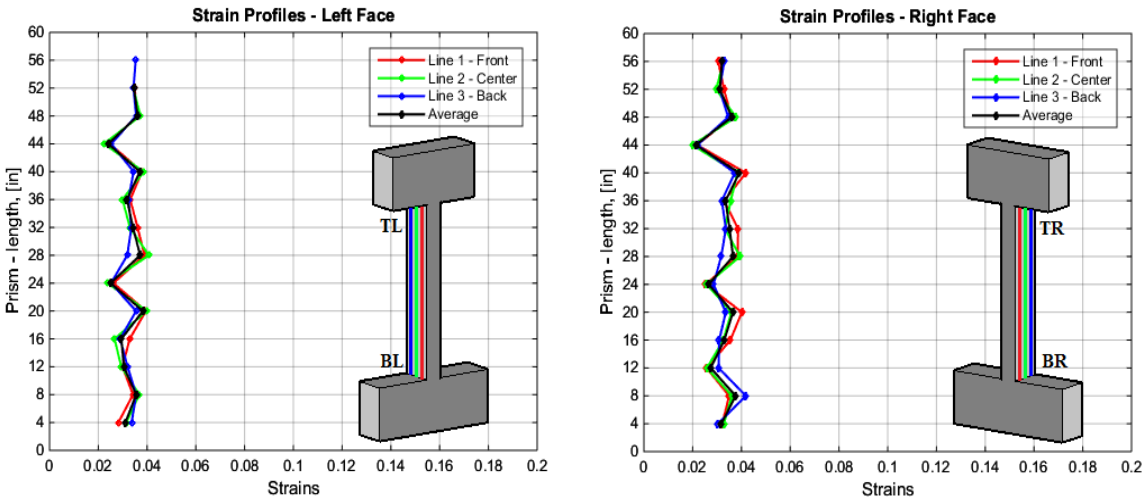

Figure A-279. Test 12: Strain profiles at 16εy (1)

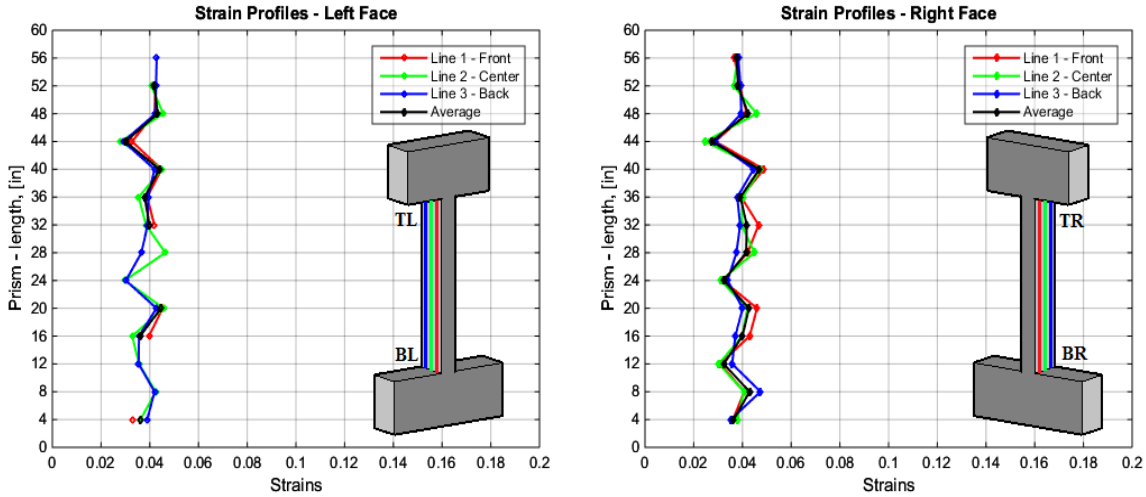

Figure A-280. Test 12: Strain profiles at 18εy (1)

Figure A-281 depicts the entire structural response of P3-P12 as a function of axial forces captured from the vertical components of the actuators and axial displacements calculated from the four spring potentiometers. The prism stiffness reduces during the cycles corresponding to 16ε_y and 18ε_y by the time the axial compressive load approaches -20 kips. At these phases, the specimen is still extended. Once the cracks close, the prism gains stiffness and is able to carry the same axial compressive load as in previous cycles. In the last cycle, bar fracture occurred under tensile displacements. Subsequently, upon compressive loads out-of-plane instability accompanied with bar buckling

occurred. The maximum applied compressive load at this stage was -95 kips, equivalent to 32% of the axial design compressive capacity, *Po*.

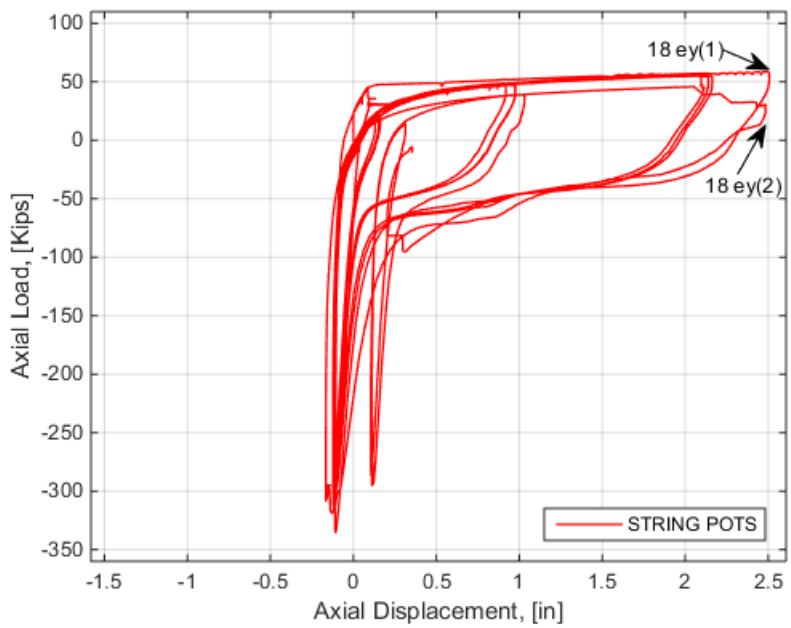

Figure A-281. Test 12: Axial structural response of prism P3-P12

Figure A-281 also shows that after 18ε_y (1), the axial tensile force capacity of the prism decreased from 59 kips to 39 kips, which represents a reduction of about 34%. This variation is attributed to accumulated local damage due to bar buckling that occurred upon compressive loads after reaching 18ε_y (1).

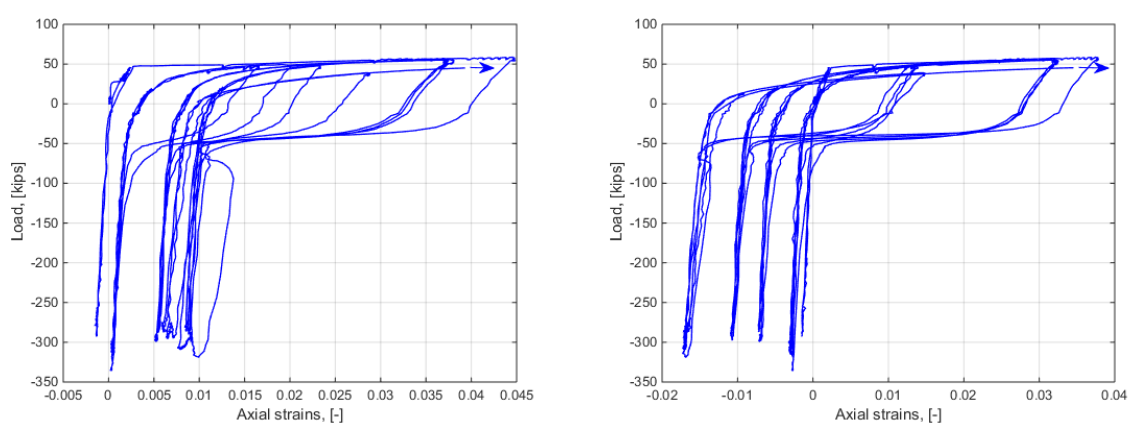

(a) (b)

Figure A-282. Test 12: Strain history response of two gages adjacent to the location where a longitudinal bar (b1) fractured;
(a) upper gage; (b) lower gage

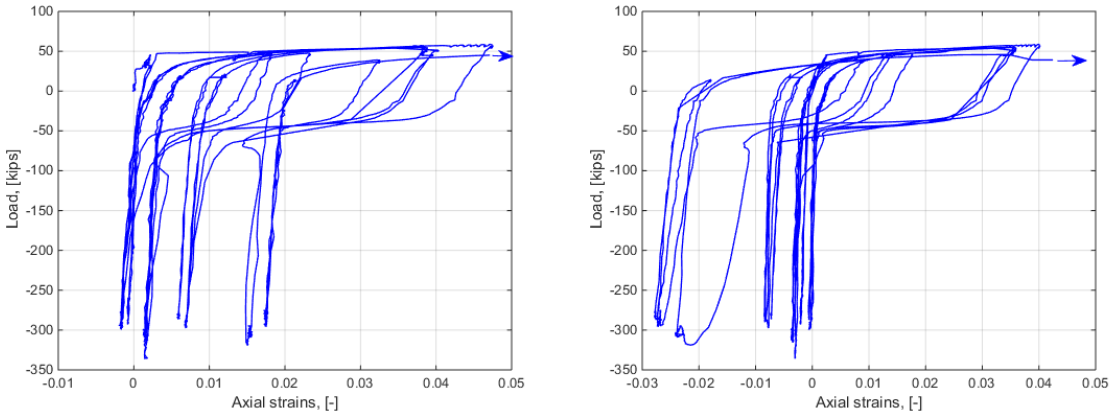

(a) (b)

Figure A-283. Test 12: Strain history response of two gages adjacent to the location where a longitudinal bar (b2) fractured; (a) upper gage; (b) lower gage

In order to analyze this phenomenon, the upper and lower gages adjacent to the location where the two bars fractured are considered to establish the strain responses during the test, see Figure A-282 and Figure A-283. After 16ε_y (2), when the prism was subjected to compression loads, the strains reached higher tensile values on the upper gage, and lower compressive values on the lower gage. From this analysis it is concluded that the bars that fractured, certainly experienced bar buckling at earlier stages which led to a reduction in the tensile capacity of the prism and the subsequent bar rupture.

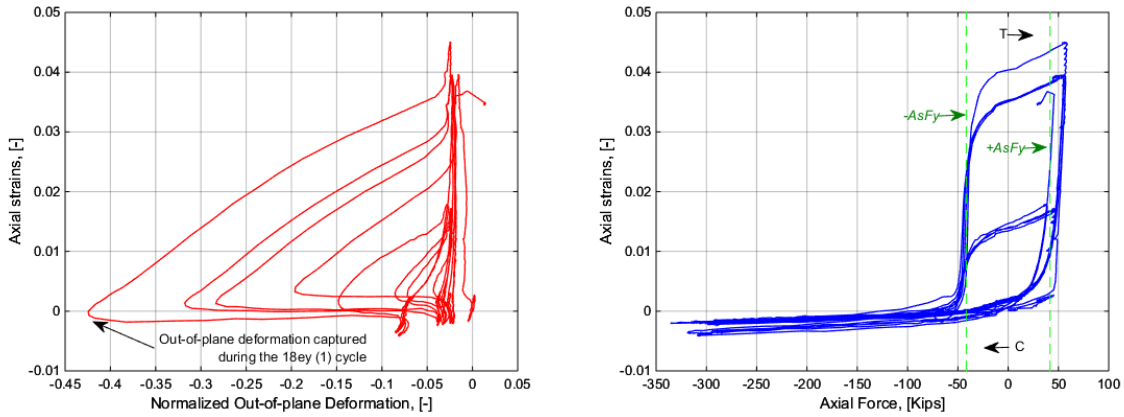

Figure A-284. Test 12: Response of specimen P3-P12 captured from a midheight gage on the right face

Figure A-284 illustrates the evolution of the nominal axial strain captured from gage 22 at the center of the specimen on the right face versus the normalized out-of-plane deformation and the axial force. Figure A-285 shows the variation of strains computed from gage 67 located at the center of the prism on the left face. Notice a stable response of the prism at low levels of axial tensile demands. The maximum normalized out-of-plane displacement developed upon compressive loading during the cycle associated with 18ε_y (1), before bar fracture occurred, is 0.42. Yielding forces, *AsFy*, in tension

and compression are also plotted in Figure A-284 and Figure A-285, where *As* is the area of the longitudinal reinforcement.

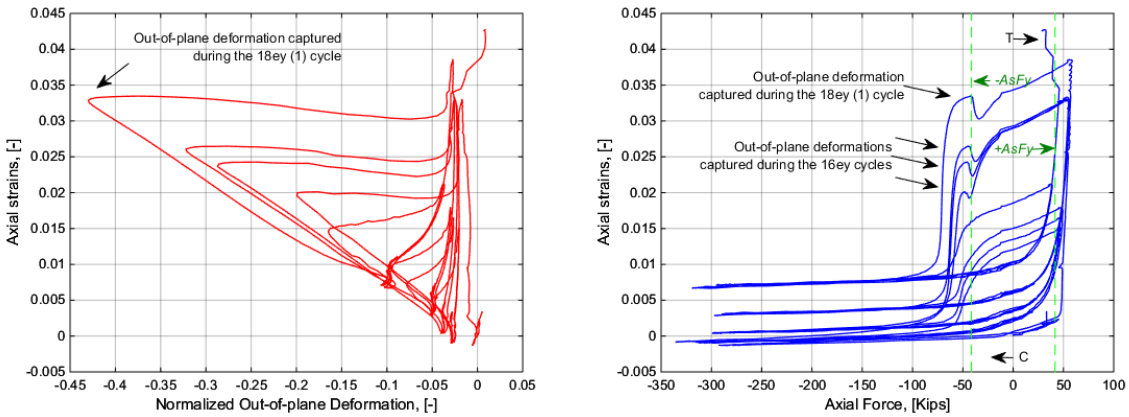

Figure A-285. Test 12: Response of specimen P3-P12 captured from a midheight gage on the left face

The evolution of out-of-plane buckling deformations measured during the 16ε_y (3), 18ε_y (1) and 18ε_y (2) cycles is plotted in Figure A-286. The prism returned to a fairly straight position after the 16ε_y (3), and 18ε_y (1) cycles. During the last cycle, as it was mentioned previously, the prism was able to develop an inelastic out-of-plane buckling deformation, with a maximum value equal to 2.71 in., located 4 in. above midheight. Figure A-286 also shows the corresponding compressive loads that the prism sustained at the time the buckled shape was developed.

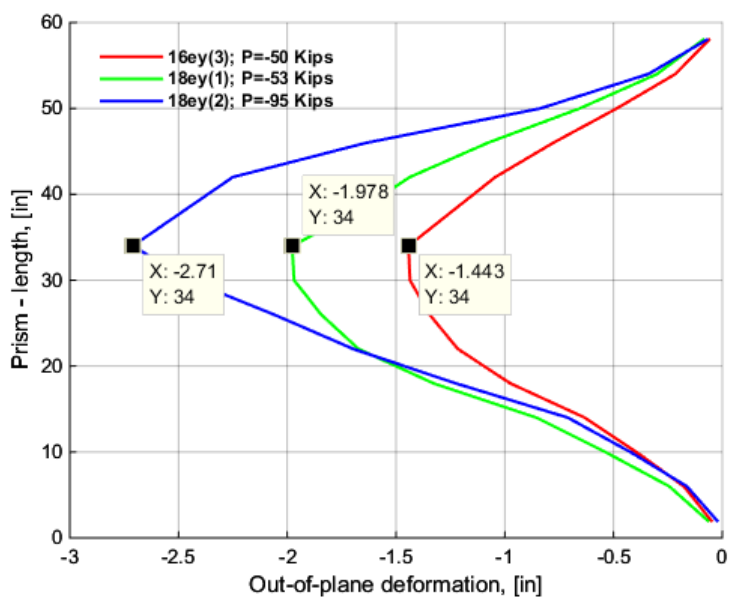

Figure A-286. Test 12: Evolution of the buckling shape during the last cycle under compressive loads

5. Conclusions

Specimen P3-P12 was tested during three hours where it was subjected to axial cyclic tensile displacements and compressive loads generated from the 1994 Northridge earthquake (Sylmar station) in order to consider the effects of near-field records that contain long duration pulses.

The cyclic axial loads/strains that were applied to the specimen reached maximum values close to the axial design capacity, Po = -294 kips in compression, and $18\varepsilon_y$ in tension. The specimen presented a stable response at low levels of axial tensile demands. Signs of out-of-plane deformations were noticed under compressive loads during the cycles associated with $16\varepsilon_y$ and $18\varepsilon_y$. The onset of bar buckling was detected during $16\varepsilon_y$ (2) upon compressive demands. The latter mechanism became more severe in the following cycles until bar fracture occurred during the last cycle associated with $18\varepsilon_y$ (2). Subsequently, instability related to inelastic out-of-plane buckling deformations developed upon compressive loads, which also led to concrete crushing and spalling in the central region of the prism. The axial compressive force at this stage was 32% of the compressive force applied in a previous cycle.

The stirrups remained as originally constructed. Analysis of the data from this test will continue, as a consequence the material presented here should be considered preliminary. Further experiments will reveal more information about the effectiveness of the reinforcement detailing recommended in guidelines to prevent lateral instability in RC structural walls.